INVESTIGATING METABOLIC AND INFLAMMATORY RELATIONSHIPS IN TWO DISTINCT MODELS OF RIGHT-SIDED CARDIAC STRESS

SHIVAM GANDHI

A DISSERTATION SUBMITTED TO THE FACULTY OF GRADUATE STUDIES IN PARTIAL FULFILLMENT OF THE REQUIREMENTS FOR THE DEGREE OF DOCTOR OF PHILOSOPHY

GRADUATE PROGRAM IN Kinesiology and Health Sciences
YORK UNIVERSITY
TORONTO, ONTARIO

November 2024

Abstract

This thesis summarizes data generated from two distinct models with unrelated underlying etiology that both implicate metabolic- and inflammatory-mediated adaptations in right-sided cardiac stress.

The first model, Duchenne muscular dystrophy (DMD), is a neuromuscular disease caused by mutations in the X-linked *DMD* gene that encodes the sub-sarcolemmal protein, dystrophin. While current standards of care –glucocorticoid administration and gene-editing therapies – provide promise for skeletal muscle impairments, the effects of these interventions on dystrophic cardiomyopathy are unclear. The purpose of this thesis was to characterize chamber-specific remodeling in young D2.B10-DMD^{mdx}/2J (D2.*mdx*) mice, while concurrently exploring if an adiponectin peptidomimetic (ALY688) could alleviate underlying chamber-specific pathology.

Our results demonstrated that right ventricular (RV) fibrosis and cardiomyocyte hypertrophy in 4-week-old D2.*mdx* mice were related to lower mitochondrial respiration and increased complex I-stimulated mitochondrial H_2O_2. ALY688 prevented RV fibrosis and cardiomyocyte hypertrophy, concurrent with macrophage sub-population shifts towards an anti-inflammatory phenotype. Our findings identified that the dystrophic heart is heterogeneously affected, while ALY688 represents a viable intervention aimed at addressing secondary contributors to dystrophic cardiac remodeling.

The second model, on-pump coronary artery bypass grafting (CABG) surgery, is a common intervention for treatment of coronary artery disease. Key to this surgery is infusion of cardioplegia, which temporarily arrests the heart so surgeons can anastomose grafts around occluded coronary arteries while blood supply is maintained by cardiopulmonary bypass. The combination of ischemia and reperfusion remains a precipitator of post-operative complications.

To date, repeated-measures mitochondrial stress responses associated with CABG have never been explored in a study design that compares right atrial appendage (RAA) samples from the same patient at multiple time-points.

Therefore, the purpose of this study was to investigate if post-CABG RAA exhibited alterations to mitochondrial stress responses (perturbed mitochondrial substrate-specific respiration and reactive oxygen species (ROS)-mediated protein adaptations) that correlated with patient discharge times.

Preliminary findings demonstrated that CABG is associated with increased fatty acid-supported respiration on the post-CABG RAA. It is unknown if this is a protective mechanism or a detrimental mitochondrial stress response. Correlative statistics suggest that the increase in fatty acid-supported respiration and ROS-mediated adaptations do not improve patient discharge times.

Acknowledgements

As my PhD journey comes to a bittersweet end, I often find myself reflecting on the fortunate years I have been afforded being a member of the Perry Lab. While I can write an entire chapter in this dissertation about the lessons I have learned during my PhD (both science and life related), it is the special people I have met and leaned on throughout this process that I would like to acknowledge.

At the top of this list is Dr. Christopher Perry, who will forever remain among the most influential and awe-inspiring people I've had the privilege to work with in my life. Although I entered my PhD a nervous, self-deprecating course-work Master's graduate who admittedly had no idea what he was getting himself into, meeting with Chris for the first time dissipated all feelings of self-doubt and apprehension almost immediately. Instead, a soft, reassuring smile quickly became a permanent fixture that I associated with Chris. The time, effort, and faith that has been invested in me by Chris is a debt that cannot be repaid. Words are not enough to express my gratitude and appreciation, but I'll give it a shot. Chris, you've transformed me into not only a better scientist, but also a better person, and I can only hope to leave an impact in science and society the way you have so effortlessly. I'll never take for granted the new and exciting places you enabled me to visit, the achievements + accomplishments we celebrated, and the unforgettable memories that can never be replaced. Any day that we share a beer and an unnecessarily long dad joke with a subpar punchline is a good science day in my books.

To members of the Perry Lab, past and present. It's weird to think that I've spent more time with you than I have with my own family and fiancé. Truthfully, I couldn't have asked for a better bunch to spend the long days and nights in lab with. Through the high and lows, every one of you has inspired me to be better in all facets of my life. If I wasn't crying in lab because one of my experiments failed, the tears were probably from all the laughter (re: the infamous Perry Lab quote board). I wish each and every one of you the best in your future endeavours and have no doubt that you will all accomplish great things in your lives.

To all the scientific mentors who have contributed to my journey: Drs. Ali Abdul-Sater, Peter Backx, Ola Adegoke, Ian Dixon, Jeremy Simpson, Gary Sweeney, David Wright, Arthur Cheng, and David MacLean. Whether you know this or not, you have all provided me with invaluable insight, guidance, and supervision throughout my degree and have inspired me to be the best version of myself. You have challenged me on countless occasions and have encouraged critical thinking, whether it was at the end of a conference presentation or during an innocent hallway conversation. I consider each of you a scientific force to be reckoned with who has played a significant transformative role in my life.

Last, but certainly not least, to the most important people in my life: my parents (Sanjay and Leena Gandhi), my sister Shreya, and my loving fiancé Sarina. Simply put, this dissertation and degree would not have materialized if you were not there to pick me up every time I fell (and believe me, I fell a lot). During this journey, I realized that you are the people I do this for. You are the ones who inspire me every day to work harder, dig deeper, and fight tooth and nail to achieve my dreams. I hope you know how much you mean to me. This is not an accomplishment to be celebrated in my lonesome - let this dissertation be a reminder that we did this together.

Table of Contents

List of Tables

Chapter 8 (CABG)

List of Figures

Chapter 1 (Introduction; DMD)

Chapter 2 (Literature Review; DMD)

Chapter 4 (DMD)

Chapter 5 (Introduction; CABG)

Chapter 6 (Literature Review; CABG)

Chapter 8 (CABG)

Chapter 9 (Summary of Findings)

List of Supplemental Figures

Chapter 4 (DMD)

Chapter 8 (CABG)

List of Abbreviations (DMD + CABG)

αSMA: Alpha Smooth Muscle Actin
-Creatine: Without creatine
+Creatine: With creatine
ACBP: Acyl CoA binding protein
ACC: Acetyl CoA carboxylase
ACE: Angiotensin-converting enzyme
ACS: Acyl CoA synthetase
ACT: Acetyl CoA transferase
ARB: Angiotensin receptor blocker
AdipoR: Adiponectin receptor
ADP: Adenosine diphosphate
ApN: Adiponectin
ATP: Adenosine triphosphate
A.U.: Arbitrary units
BW: Body weight
CABG: Coronary artery bypass graft
CAD: Coronary artery disease
CPB: Cardiopulmonary bypass
CPTI/II: Carnitine palmitoyl transferase I/II
CRC: Calcium retention capacity
Cr: Creatine
DCM: Dilated cardiomyopathy
DMD: Duchenne muscular dystrophy
ECM: Extracellular matrix
ETC: Electron transport chain
ETF: Electron transport flavoprotein
$FADH_2$: Flavin adenine dinucleotide
FET: Forward electron transfer
FFA: Free fatty acid
GLUT: Glucose transporter
HD: High dose
H&E: Hematoxylin and Eosin
HSC: Hematopoietic stem cell
IF: Immunofluorescence
IL-6/10: Interleukin 6/10
IMA: Internal mammary artery
IMTG: Intramuscular triglyceride
IRI: Ischemia-reperfusion injury
LA: Left atrium
LCA: Left coronary artery
LD: Low dose
LDH: Lactate hydrogenase
LPM: L-carnitine + Palmitoyl CoA + Malate
LV: Left ventricle

MCD: Malonyl CoA decarboxylase
mH_2O_2: Mitochondrial hydrogen peroxide
MFI: Mean fluorescent intensity
MFD: Minimal feret diameter
MI: Myocardial infarction
mPT: Mitochondrial permeability transition
mtCK: Mitochondrial creatine kinase
NADH: Nicotinamide adenine dinucleotide
OXPHOS: Oxidative phosphorylation
PBS: Phosphate buffered saline
PCI: Percutaneous coronary intervention
PCr: Phosphocreatine
PDC: Pyruvate dehydrogenase complex
PDH: Pyruvate dehydrogenase
PDK: Pyruvate dehydrogenase kinase
PFK: Phosphofructokinase
PM: Pyruvate + malate
PmFB: Permeabilized fiber bundles
PPP: Pentose phosphate pathway
Prx3: Peroxiredoxin 3
PSR: Picrosirius red
RET: Reverse electron transfer
RAA: Right atrial appendage
RA: Right atrium
RCA: Right coronary artery
RCR: Respiratory control ratio
ROI: Regional of interest
RV: Right ventricle
SERCA: Sarco/endoplasmic reticulum calcium ATPase
STAT3: Signal transducer and activator of transcription 3
SV: Saphenous vein
TGFβ: Transforming Growth Factor β
Trx: Thioredoxin
VEH: Vehicle
WAT: White adipose tissue
WGA: Wheat germ agglutinin
WT: Wildtype

1 INTRODUCTION

Duchenne muscular dystrophy (DMD) is a debilitating, progressive neuromuscular disease caused by X-linked recessive mutations to the *DMD* gene, which is responsible for encoding the sub-sarcolemmal anchor protein, dystrophin [1,2]. DMD is the most common inherited muscular dystrophy diagnosed in childhood, with a global birth prevalence of 1 in 5000 live male births [3], although variations have been reported elsewhere [4–6]. Since DMD is X-linked, it primarily affects males, while the occurrence in females (which would require two copies of the recessive mutation) is extremely rare. Mutations to the *DMD* gene result in a deficiency of functional dystrophin protein and subsequent loss of myofiber integrity in skeletal (locomotor and respiratory) and cardiac muscles, thus leaving muscle fibers susceptible to contraction-induced damage [7]. As DMD progresses, muscle turnover and repair cannot keep pace with the constitutive cellular damage and membrane micro-tears that arise, resulting in cell death and replacement with fibrotic and/or fatty tissue (reviewed in [8]).

Phenotypically, dystrophin deficiency is characterized by progressive skeletal, respiratory, and cardiac muscle weakness, resulting in a loss of ambulation, ventilatory complications, and cardiomyopathy [9–12]. Notably, pathologic cardiac manifestations occur in nearly every DMD patient, with the development of cardiomyopathy inevitable by adulthood [13,14] and ultimately progressing to heart failure and mortality in 44–57% of patients [15]. Functional measurements in dystrophin deficiency-induced cardiomyopathy are often confounded by skeletal muscle weakness given that typical heart failure symptoms, such as exercise limitations and dyspnea, are masked in this population, thus making cardiac impairments difficult to diagnose early in disease progression (reviewed in [9]). Due to early pharmacological intervention and advancements in respiratory care

for DMD patients (such as assistive ventilatory devices), cardiomyopathy is now the leading cause of death in persons with DMD [16,17].

While there is no cure for DMD, ongoing pre-clinical research seeks to restore the normal genetic sequence through emerging gene editing technologies (e.g. CRISPR) or produce truncated dystrophin transcripts with exon-skipping and micro-dystrophin gene therapies [18–20]. Exon-skipping therapy was recently approved by the FDA in the USA for certain mutations, but the technology must be individually adapted for each of the 70 unique mutations to be considered efficacious across the full spectrum of pathology. The ability of exon-skipping therapy to only partially improve muscle dysfunction underscores the importance of maintaining glucocorticoid therapy as a major standard of care, given that systemic inflammation is a major contributor to muscle dysfunction [21–23] for virtually all persons with DMD. While the effectiveness of glucocorticoids in slowing the decline of muscle function demonstrates the value of targeting secondary contributors to this disease, the eventual decline in muscle function and unwanted side effects (i.e., attenuated growth, obesity, mood disorders, other) [24] underscores the importance of developing additional treatments that provide benefits for most patients regardless of the specific underlying mutation. Additionally, many of the current pre-clinical interventions in development have yielded variable results for treating dystrophin deficiency-induced cardiac remodeling and cardiomyopathy.

While prevailing hypotheses of underlying mechanisms that perpetuate dystrophic cardiac remodeling include sarcolemmal weakening [25], inflammation [26], unregulated expansion of cardiac fibrosis that mediates a gradual enlargement of the ventricular wall [27], and perturbed calcium (Ca^{2+}) homeostasis [28,29], mitochondrial stress responses have been viewed as a potential key contributor in concert with the abovementioned mechanisms [12,30,31].

It is important to note that the relationship between muscular dystrophy-induced cytosolic Ca^{2+} elevations and muscle-cell necrosis was first proposed 40 years ago (long before the discovery of dystrophin) and represents a major link between mitochondria, sarcolemmal tearing, and muscle fiber degeneration [32,33]. It was originally hypothesized that elevated cytosolic Ca^{2+} triggers a 'vicious cycle' of downstream mitochondrial Ca^{2+} overload, resultant functional and structural damage to mitochondria, and ultimately, impairments to ATP synthesis, which further exacerbates cytoplasmic Ca^{2+} levels by compromising essential ATPase-dependent Ca^{2+} re-uptake pumps, leading to the hypercontraction of muscle fibers and subsequent cell necrosis [32]. While the precise mechanisms regulating excess mitochondrial Ca^{2+} overload require more investigation, current theories posit that Ca^{2+} overload triggers cell death through mitochondrial permeability transition (mPT) in conjunction with impaired oxidative phosphorylation and elevated mitochondrial reactive oxygen species (ROS) emission.

With the discovery of the D2.B10-DMD^{mdx}/2J (D2.*mdx*) dystrophin deficient mouse, reduced mitochondrial pyruvate oxidation and increased mitochondrial ROS emissions have been identified in the left ventricle (LV) at an early age (4-week-old) where cardiac fibrosis or functional echocardiographic impairments have yet to manifest [34]. This is particularly important because cardiac fibrosis is thought to be one of several histopathological remodeling programs that are initiated in the dystrophic heart after repeated damage as a means of preventing additional, more detrimental consequences by replacing dead or dying cells with collagenous scar tissue [35–37]. The observation of mitochondrial stress responses in the dystrophic LV that is not affected by cardiac fibrosis or overt cardiac dysfunction led to unanswered questions about the complex relationship between dystrophin deficiency-induced damage and the histopathological remodeling

process, especially pertaining to other chambers of the heart such as the right ventricle, which plays a crucial role along pulmonary circulation pathways.

Therefore, this study was separated into three major objectives: to determine if 1) young D2.*mdx* mice exhibit chamber-specific heterogeneity in histopathological cardiac remodeling signatures beyond what is already known in the LV; 2) chamber-specific remodeling signatures correspond to shifts in inflammatory macrophage sub-populations or elevations to indices of mitochondrial stress responses; and 3) administering an anti-inflammatory adiponectin receptor agonist could attenuate symptoms of dystrophic histopathological cardiac remodeling by improving the inflammatory and mitochondrial stress response profile.

Four distinct phases of in-house animal breeding and drug injections (D2.*mdx* mice) were required to obtain sufficient tissue for the four-chamber histopathological, mitochondrial, and inflammatory characterizations that were conducted in 4-week-old mice. While a comprehensive examination (to this magnitude) of chamber-specific responses has never been conducted in any pre-clinical or clinical DMD trial before, the design provided invaluable insight towards progression of dystrophic cardiomyopathy beyond the left ventricle, and accordingly, informs prospective guided therapy development for the heart.

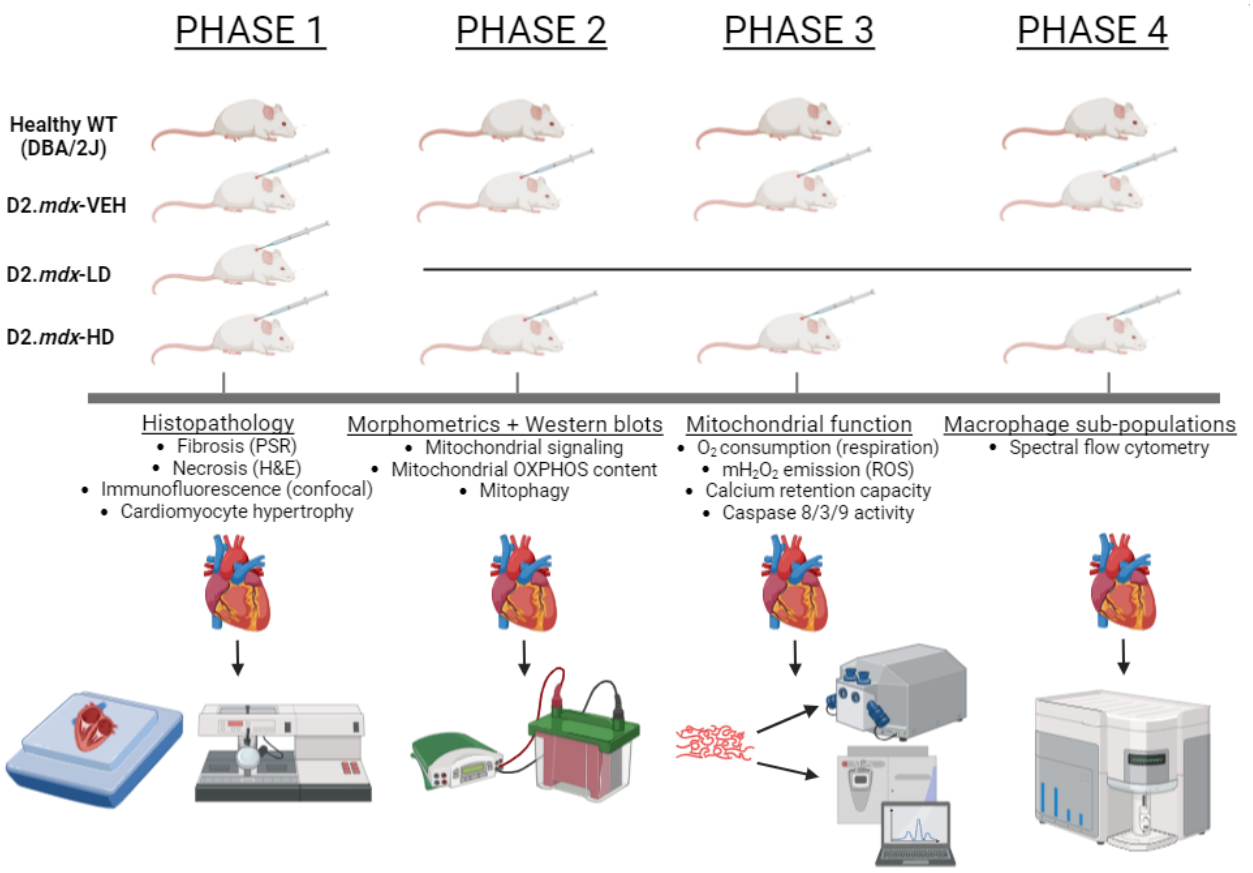

Figure 1-1. Schematic representation of a study design implemented to comprehensively characterize four-chamber histopathological, mitochondrial, and inflammatory remodeling signatures in 4-week-old D2.mdx mice. In order to gain invaluable insight towards previously unexplored determinants of dystrophic cardiomyopathy progression, four independent phases of animal breeding were required to acquire four-chamber data from D2.*mdx* hearts that were no larger than 90 milligrams on average. Healthy WT (DBA/2J) and three groups of injected mice (D2.*mdx*-VEH, D2.*mdx*-LD (dropped after phase 1 for logistical reasons), and D2.*mdx*-HD) were examined with a sample size of n = 10-12 for most measures through each phase. While WT mice were ordered from Jackson Laboratories due to difficulties of in-house breeding, all other mice were bred in York University's vivarium and injected daily for 3 weeks per phase. Several experimental methods, including mitochondrial bioenergetics, spectral flow cytometry, and histopathology, had to be modified, adapted, or optimized to reflect the small tissue sample sizes. This figure has been adapted from *SFigure 4-1*. Figure created using www.BioRender.com.

The following Literature Review (***Chapter 2***) has been adapted from two published Review papers authored by Shivam Gandhi (first author), alongside world renowned pioneers in the fields of Duchenne muscular dystrophy and adiponectin biology: (Drs. Gary Sweeney, Christopher Perry; *Biomedicines*) and (Drs. Lee Sweeney, Cora Hart, Renzhi Han, Christopher Perry; *Cells*). Schematics that have been adapted from these papers have been identified in their respective Figure Captions.

1) **Gandhi, S**, Sweeney, G, and Perry, CGR (2024). Recent Advances in Pre-Clinical Development of Adiponectin Receptor Agonist Therapies for Duchenne Muscular Dystrophy. *Biomedicines.* **12**(7):1407. DOI: 10.3390/biomedicines12071407

2) **Gandhi, S**, Sweeney, HL, Hart, CC, Han, R, and Perry, CGR (2024). Cardiomyopathy in Duchenne Muscular Dystrophy and the Potential for Mitochondrial Therapeutics to Improve Treatment Response. *Cells.* **13**(14):1168. DOI: 10.3390/cells13141168

2 LITERATURE REVIEW

2.1. Brief Overview of DMD

Duchenne muscular dystrophy (DMD) is a rare neuromuscular disease caused by X-linked recessive mutations to the dystrophin gene (*DMD*) located on chromosome Xp21.2 [1,2]. The mutation results in a deficiency of functional dystrophin protein and subsequent loss of myofiber integrity in skeletal and cardiac muscle, thus leaving muscle fibers susceptible to contraction-induced damage [7]. As DMD progresses, muscle turnover and repair cannot keep pace with the constitutive cellular damage that arises, resulting in cell death and replacement with fibrotic and/or fatty tissue (reviewed in [8]).

Phenotypically, dystrophin deficiency is characterized by progressive locomotor-skeletal, respiratory-skeletal, and cardiac muscle weakness, ultimately resulting in a loss of ambulation as well as respiratory and cardiac failure [9–12]. Pathologic cardiac manifestations occur in nearly every DMD patient, with the development of cardiomyopathy inevitable by adulthood [13,14] and ultimately progressing to heart failure and mortality in 44–57% of patients [15]. Due to early pharmacological intervention and advancements in respiratory care for DMD patients, cardiomyopathy is now the leading cause of death in this patient population [16,17]. While timely detection and management are essential to slow the progression of dystrophin deficiency-induced cardiomyopathy, uncovering appropriate diagnostic and treatment modalities remains a challenge due to the early cardiac abnormalities that are often difficult to detect. Additionally, functional measurements in dystrophin deficiency-induced cardiomyopathy are confounded by skeletal muscle weakness, given that typical heart failure symptoms, such as exercise limitations and dyspnea, are masked in this population (reviewed in [9]).

No cure exists for DMD - therefore, treatment is aimed at delaying disease progression and alleviating symptoms. A comprehensive appreciation of the pathophysiological mechanisms that underlie cardiomyopathy is of the utmost importance to develop targeted treatments. It is worth noting that no singular mechanism can explain the multifactorial pathogenesis of dystrophin deficiency-induced cardiomyopathy; rather, it is a result of several interrelated mechanisms that will be discussed in detail later. While prevailing hypotheses of underlying mechanisms include sarcolemmal weakening, upregulation of pro-inflammatory cytokines, metabolic impairments, and perturbed calcium homeostasis, mitochondrial stress has been viewed as a potential key contributor [12,30]. Currently, there are several experimental compounds targeted at the skeletal muscle pathology of dystrophin deficiency that are in development, which will ultimately determine whether changes in mitochondrial functions are contributing to dystrophin deficiency-induced myopathy. For now, the effects of these agents on cardiac function remain unclear.

2.1.1. Genetics

The *DMD* gene is the largest in the human genome [38,39], spanning 2.4 Mb in the Xp21.2 region [40]. It consists of 79 exons and has several internal promoters that produce an array of dystrophin isoforms expressed in striated and smooth muscles, brain, retina, and the kidney [40]. Thousands of mutations in the *DMD* gene have been found to cause dystrophin deficiency [6].

Deletions account for approximately 70% of mutations causing DMD and typically result in an altered reading frame that produces a premature stop codon [41,42]. Roughly 20% of dystrophin mutations are point mutations, small deletions, or insertions, whereas duplications make up the remaining 5–15% of mutations [43,44]. Deletions and duplications tend to cluster in hotspot regions, located at exons 45–55 and 3–9 on the *DMD* gene [45]. *De novo* mutations are responsible for one-third of DMD cases [41]. Mutations that disrupt the reading frame or introduce a premature

stop codon cause the absence of dystrophin. Mutations that maintain the reading frame allow for truncated dystrophin to be produced, resulting in the phenotype of Becker muscular dystrophy (BMD) [46]. Certain mutations may circumvent dystrophin deficiency-induced dilated cardiomyopathy (DCM) (exons 51–52) [47], perpetuate cardiomyopathy (exons 12, 14–17, 31–42, 45, 48–49, and 79) (reviewed in [48]), or be neutral. As mutations can affect different exons on the *DMD* gene, it is unlikely that a single genetic therapy will benefit patients across the spectrum of mutations that cause this disease.

Dystrophin is a rod-shaped protein located beneath the muscle fiber membrane that acts as a molecular shock absorber by transmitting forces generated by sarcomere contraction to the extracellular matrix (ECM) [49] **(Figure 2-1)**. Dystrophin consists of four major functional domains: an amino-terminal actin-binding domain, a large central rod domain, a carboxyl-terminal domain, and a cysteine-rich domain that binds dystroglycan (reviewed in [50]). Dystrophin is an integral part of the dystrophin-glycoprotein complex (DGC) that connects the intracellular actin cytoskeleton to the ECM [51] and provides structural support to the sarcolemma **(Figure 2-1)**. Aside from structural support, dystrophin also serves as a scaffold for proteins involved in various signaling cascades, including sarcolemmal ion channels [52]. In cardiomyocytes, the Dp427 isoform of dystrophin is expressed and located at the cardiac sarcolemma as well as in the cardiac T-tubules [53]. DMD-induced cardiomyopathy appears to be predominantly attributed to the loss of the Dp427 isoform [53].

In skeletal muscle, dystrophin mutations also lead to perturbed microtubule organization and oxidized actin, which contributes to weakness and is thought to contribute to mitochondrial stress and other abnormalities [54–59], but the degree to which this occurs in the heart remains unknown.

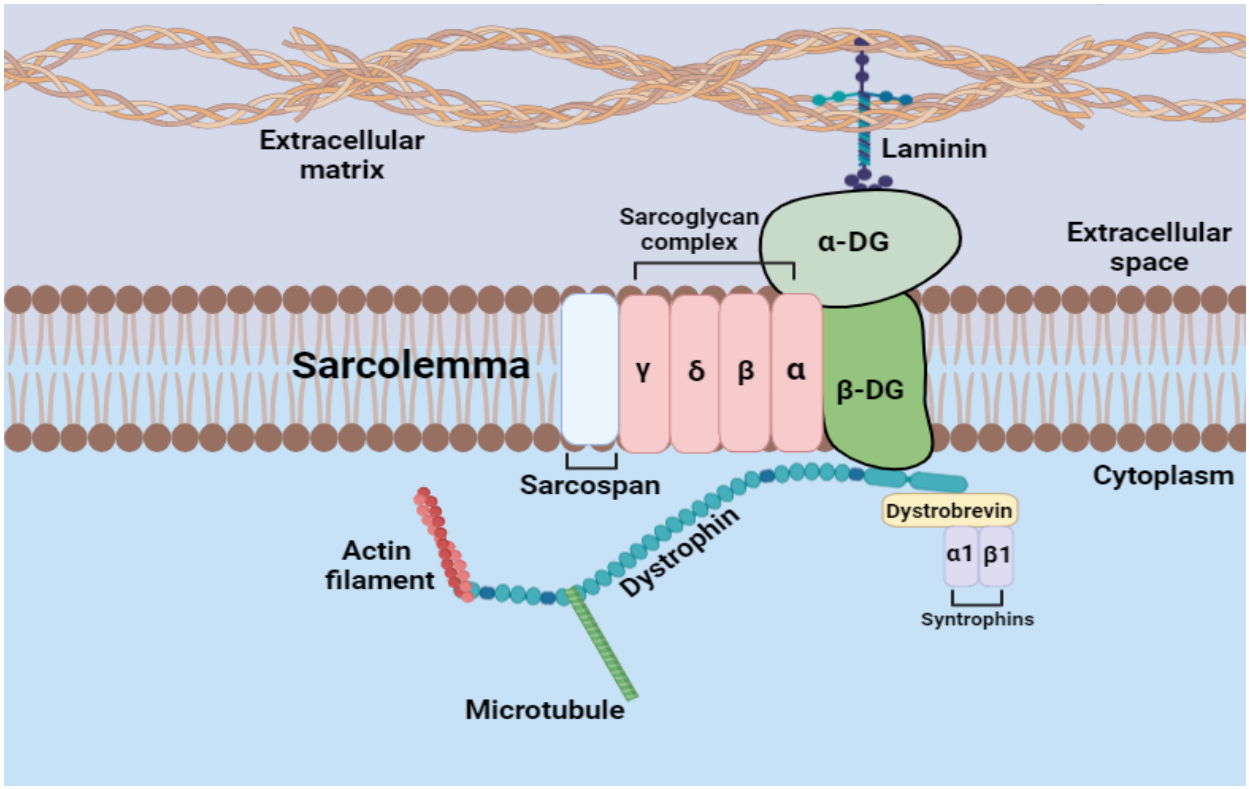

Figure 2-1. Structural configuration of the dystrophin-glycoprotein complex (DGC), including key components indispensable for upholding cellular architecture in skeletal and cardiac muscles. Dystrophin is a rod-like protein that is responsible for providing structural support to the cell by anchoring components of the intercellular cytoskeleton to the extracellular matrix via laminin. Several transmembrane proteins comprise the DGC, including α-dystroglycan (α-DG), β-dystroglycan (β-DG), the sarcoglycan complex (comprised of γ, δ, β, α subunits), and sarcospan, among other non-transmembrane proteins located throughout the cytoplasm, sarcolemma, and extracellular space. Figure created using www.BioRender.com.

2.1.2. Epidemiology

DMD is the most common inherited muscular dystrophy diagnosed in childhood, with an incidence of approximately 1 in 5000 newborn males [3], although variations have been reported elsewhere [4–6]. Since DMD is X-linked, it primarily affects males. Approximately 25% and 59% of DMD patients develop cardiomyopathy by 6 and 10 years of age, respectively, with electrocardiogram (ECG) abnormalities and sinus tachycardia (ST) representing the primary early clinical manifestations [9,13,60,61]. By 18 years of age, cardiomyopathy occurs in 98% of patients and progresses to heart failure in 40% of patients [1,62,63]. A higher mortality is linked to dystrophin deficiency-induced cardiomyopathy than to other cardiomyopathies [9].

The prevalence of DMD in females (two copies of the recessive mutation) is extremely rare. Interestingly, one study conducted on aged 22-month-old female C57BL/10.*mdx* mice demonstrated impairments to LV hemodynamic function that was more severe compared to age-matched males and wild-types (WTs) in the absence of differences to cardiac fibrosis, ECG abnormalities, and lifespan between sexes [64,65]. In these mice, it was observed that female *mdx* exhibited heavier heart weight compared to male *mdx* when normalized to body weight [64]. Despite these findings, male *mdx* mice of the DBA/2J background appeared to have heavier hearts compared to age-matched female *mdx* at 8 months old, meaning that the genetic background, sex, and age likely all contribute to the disparate cardiac phenotype that has been observed in *mdx* mice [66]. The clinical relevance of these findings is uncertain, given that the prevalence of DMD in females is extremely rare. However, female carriers can be either asymptomatic or demonstrate mild to severe skeletal muscle weakness and cardiomyopathy that, like affected males, can worsen with age [67,68].

2.1.3. Clinical Phenotypic Manifestations

The earliest symptoms in DMD patients typically present between 1 and 5 years of age and include a waddling gait, Gower's maneuver, difficulty climbing stairs, and frequent falls [4,69,70]. Calf hypertrophy tends to develop during early childhood due to the localized accumulation of fatty and fibrotic tissue [71]. Motor skills deteriorate at 6 to 8 years of age when lordosis and scoliosis advance [72]. Scoliosis increases the risk of respiratory failure [73]. Most DMD patients are wheelchair-bound at approximately 13 years of age [74]. Cognitive impairments are observed in roughly one-third of all DMD patients [75]. Secondary to progressive muscle degradation and the leakage of myofiber contents, elevated creatine kinase (CK) levels are detected early, with

levels being about 10 times higher in newborns with DMD and approximately 50 to 100 times higher in children with DMD as compared to healthy age-matched boys [68,76].

During disease progression, cardiac symptoms advance from diastolic dysfunction to myocardial remodeling and fibrosis, leading to contractile weakness and subsequent DCM with decreased systolic function [60,61]. Heart failure and arrhythmias develop gradually, increasing the risk of sudden cardiac death [12]. Largely attributable to advancements in respiratory interventions, such as assistive breathing devices (ventilators), the predominant cause of death has shifted from respiratory failure towards cardiomyopathy (reviewed in [17]), and resultantly, patients may survive well into their third and fourth decades [16,77].

2.1.4. Preclinical Models

Animal models have been critical in delineating the pathophysiologic mechanisms of dystrophin deficiency and for subsequently trialing therapeutic candidates. The C57BL/10.*mdx* mouse, a genetic and biochemical homolog of human DMD, is the most widely used animal model of dystrophin deficiency and has been invaluable in providing knowledge for therapeutic strategies [78]. The C57BL/10.*mdx* mouse lacks full-length dystrophin due to a nonsense point mutation in exon 23 of the *DMD* gene [78]. This model only exhibits a mild cardiomyopathy late in life that never fully advances into heart failure [79]. Additionally, cardiac fibrosis and dysfunction present very late, if at all, in this model [80]. Although the milder skeletal muscle phenotype and subtle nature of cardiac involvement limit translation to human disease progression (reviewed in [9]), some features, such as cardiomyopathy, can be unmasked in C57BL/10.*mdx* mice via cardiac stressors, such as ischemia–reperfusion (IR) insults [81,82]. Due to the ease of breeding and maintaining, with a long life expectancy, the C57BL/10.*mdx* mouse models remain a common tool in dystrophin deficiency research [83]. Other mouse models exist with a variety of backgrounds

and mutations, but the majority result from the crossing of the C57BL/10.*mdx* mouse with different mutations to worsen the dystrophin deficiency phenotype [84,85]. However, the natural history of cardiomyopathy in each model remains largely uncharacterized.

The DBA/2J-*mdx* (D2.*mdx*) and utrophin–dystrophin double-knockout (STOCK *Utrn*^{tm1Ked} *Dmd*^{mdx}/J) mice have drawn attention as representing better models of DMD-induced cardiomyopathy, including earlier-onset cardiac deficits [78]. In the D2.*mdx* mouse, cardiac fibrosis and calcinosis affecting the RV is noted at 18 weeks of age [86], however, the degree to which cardiac remodeling or dysfunction occurs in this ventricle has never been characterized at a young time-point better reflective of early disease progression. Several mouse models for dystrophin deficiency have been developed, but none of the models completely recapitulates the phenotype and disease progression seen in humans. However, more severe models have a reduced lifespan, are more difficult to breed, and carry an additional mutation not affected in humans, which causes difficulty in reliably extrapolating data to the human phenotype [78,83].

To bridge the gap between small rodent (mouse) DMD models and the human phenotype, several different rat DMD models have been investigated. To date, the majority of rat DMD models have been developed to genetically target the genomic region that spans exons 3–26 [87–89]. This is a major limitation in the model, given that a major mutation hotspot for the classical, progressive DMD phenotype is between exons 45 and 55 [87]. For this reason, a new rat DMD model was generated with a deletion mutation in exon 52 on the rat *DMD* gene, known as the R-DMDdel52 rat [87]. In comparison to the *mdx* mouse model, the R-DMDdel52 rat exhibits remodeling of the entire striated musculature, including both the heart and diaphragm, which culminates leading to premature lethality between 10 and 14 months of age [87].

The golden retriever muscular dystrophy (GRMD) model offers remarkable resemblance to the progressive locomotor, respiratory, and cardiac muscular phenotype observed in human DMD patients [90]. Similar to humans, these canines are characterized by highly variable cardiomyopathy progression, making the assessment of therapies challenging [91,92]. Unfortunately, high costs, limited supply, and difficulty in maintaining a colony preclude the widespread use of GRMD models [83].

In order to more closely recapitulate the human DMD phenotype (in comparison to small rodent models) without limitations imposed by the financial burden of large mammals (e.g., GRMD), a DMD rabbit model was developed by cytoplasmic microinjections of Cas9 mRNA and single-guide RNA (sgRNA) [93]. The rabbit DMD model was developed by targeting exon 51 (commonly mutated in human DMD patients) to disrupt the open reading frame of *DMD* in rabbits, thereby generating *DMD* KO (knock-out) rabbits [93]. This model exhibits many hallmark pathologies of DMD, including elevated serum creatine kinase, impaired mobility/ambulation, muscle necrosis and regeneration, and, importantly, cardiomyopathic manifestations (increased cardiac fibrosis, impaired function, etc.) [93]. Although further research is still required to comprehensively validate and characterize this model, the clear evidence of cardiomyopathy at 4 months of age (demonstrated by reduced left ventricular ejection fraction and fractioning shortening), paired with the close resemblance to its human DMD counterpart, makes this an attractive model for preclinical drug screening studies [93].

A dystrophin-deficient pig model that is characterized by a targeted deletion of *DMD* exon 52 has also been recently developed to recapitulate human size, anatomy, and physiology more closely [94]. Of relevance, pigs with deletions to *DMD* exon 52 do not express dystrophin in skeletal muscle and have elevated serum CK, impaired function including mobility, muscle weakness, and

a maximum life expectancy of 3 months due to severe deteriorative respiratory impairments [94]. This model is also noted for its cardiac dystrophin deficiency, with several notable downregulations to components of the dystrophin-associated protein complex that have been observed [95].

Aside from mammalian models that provide integrative insight into the pathophysiology of DMD, work from the nematode worm *Caenorhabditis elegans* can also provide invaluable information regarding disease progression. This double-mutant model contains a combination of a dystrophin homologue (*dys-1*) null mutation and a weak mutation to *hlh-1*, which encodes for a MyoD homologue [96,97]. These worms are interesting given that they exhibit a time-dependent loss of motility as well as muscle degeneration, which are similar observations to those seen in *mdx* mouse mutants [96]. The worms are typically used to identify new components of the DGC and also unidentified suppressors of muscle degeneration [96].

Induced pluripotent stem cells (iPSCs), another preclinical model for dystrophin deficiency, are reprogrammed from patient-specific somatic cells and carry the same genetic defects as DMD patients [98]. These cells make it possible to obtain functional cardiomyocytes from DMD patients and offer an important complement to animal models in studying dystrophin deficiency (reviewed in [99]). However, iPSCs do not manifest a fully mature phenotype, which may limit their utility in pre-clinical research [100]. Collectively, most of the research demonstrating mitochondrial dysfunctions in response to dystrophin mutations has been conducted in the C57BL/10.*mdx* and D2.*mdx* mouse, as well as some literature in males with DMD.

2.2. Current Standard of Care and the Need for New Therapies

No cure exists for DMD or its associated cardiac abnormalities, and therefore, most interventions are aimed at treating the symptoms and delaying the progression of dystrophic

cardiomyopathy. Unfortunately, cardiac transplantation is generally contraindicated in DMD patients due to muscular weakness and respiratory insufficiency [101]. Left ventricular assist devices (LVAD), if implemented as a destination therapy rather than a bridge to transplantation, can be considered as a therapeutic option in DMD patients [102]. While novel therapies have been in development to specifically address defects resulting from dystrophin deficiency, their effectiveness with respect to cardiac function has been limited due to the diverse range of genetic mutations in DMD and the complex risks of each prospective therapy (reviewed in [103]). For example, certain small molecule-based therapies used in practice target secondary cellular dysfunctions that are common in most, if not all, DMD patients and therefore have the potential for widespread use. Such therapies tend to focus on symptom management and delaying the development of cardiomyopathy and heart failure. Other gene-based treatments that focus on restoring dystrophin expression in a truncated or complete sequence must be customized to each unique mutation that occurs in DMD.

The most widely used intervention in DMD are glucocorticoids, which have been proven to reduce inflammation, prolong strength, and delay the loss of ambulation by 1 to 3 years in DMD patients [104]. Glucocorticoid therapy most often involves up to daily dosing of either prednisone or deflazacort initiated around 2 to 5 years of age [42]. Although it is unknown how glucocorticoids delay disease progression, likely mechanisms include reduced cytokine production and the activation of insulin-like growth factors, decreased myocardial inflammation and fibrosis, cell membrane stabilization, increased myoblast proliferation, improvements to skeletal muscle function, and upregulation of proteins that support dystrophin [105,106]. Studies in DMD patients have collectively revealed the protective benefits of glucocorticoid treatment in dystrophic hearts, including decreased fibrosis, preserved ventricular function, and better survival [106–111].

When glucocorticoid therapy is initiated prior to the onset of cardiomyopathy and remodeling, delayed development of cardiac dysfunction has been observed [112]. Data from a surveillance program demonstrated that a longer duration of glucocorticoid use correlates with a greater improvement in LV function [106]. Furthermore, the duration of glucocorticoid treatment has been proven to be inversely correlated with the incidence of cardiomyopathy in DMD patients [106]. Long-term glucocorticoid treatment beyond the loss of ambulation in DMD led to improvement in all-cause mortality secondary to improved cardiac outcomes [107]. On a molecular level, a study in 7-week-old C57BL/10.*mdx* mice demonstrated that glucocorticoids prevented calcium-induced mitochondrial permeability transition (mPT) and restored ADP-stimulated respiration as the result of enhanced expression of mitochondrial complex III, complex IV, and complex V protein content markers in skeletal muscle [113], but further work on cardiac muscle is required in this area.

More recent studies have suggested that pulsed steroid regimens may limit the adverse effects while maintaining the benefits of daily steroid dosing in DMD patients [114,115]. Preclinical studies have demonstrated that steroids may worsen the progression of cardiomyopathy in the heart of C57BL/10.*mdx*, with findings including decreased cardiac function, increased dilation, and increased cardiac fibrosis [116–118], consistent with similar findings in the diaphragm [79]. It should be noted that these studies used a more continuous method of drug delivery than is equivalent to the single daily dose therapies administered in DMD patients [110].

Chronic steroid use may activate mineralocorticoid receptors (MR), which likely cause adverse effects, including reduced bone density, obesity, hypertension, adrenal insufficiency, and increased muscle catabolism [119–121]. MR antagonists, such as Eplerenone and Spironolactone, are treatments for heart failure with reduced left ventricular ejection fraction (LVEF) and are used in some cases of DMD-induced cardiomyopathy [40].

Additional therapeutic options such as angiotensin inhibition, beta-adrenergic receptor blockers, and Tamoxifen—which is a first-generation selective estrogen receptor modulator (SERM)—have demonstrated some potential for DMD but are not approved for clinical use, while gene-targeted therapies are limited. Angiotensin II and angiotensin II type 1 receptors induce many harmful cardiac effects, including increased fibrosis, remodeling, ROS production, and cardiomyocyte death [122–124]. The two angiotensin-inhibiting drug classes used in heart failure and DMD patients are angiotensin receptor blockers (ARBs) and angiotensin-converting enzyme inhibitors (ACEIs). ACEIs prevent an enzyme from converting angiotensin I to angiotensin II, which decreases the activation of genes that enhance fibrosis and scarring of the myocardium [125] and block the action of angiotensin II, allowing veins and arteries to dilate. The activation of beta-adrenergic receptors enhances heart rate elevations and increases contractility through its action on the calcium transients in the cardiomyocyte [126]. Beta-blockers may limit these adverse effects through inhibition of beta-receptor binding and subsequent catecholamine binding [126]. Beta-blockers are considered a second-line candidate for cardiac-related therapy in DMD patients, typically administered in addition to an angiotensin-inhibiting agent [9,127].

2.3. Dystrophin Deficiency in the Heart

2.3.1. Cellular Diagnostic Indicators of DMD-induced Cardiomyopathy

As previously noted, typical cardiac symptoms of exercise intolerance and dyspnea are masked in DMD patients due to the influence of skeletal muscle weakness on these same parameters [9]. Nonetheless, the detection of early changes in the structure and function of the heart is crucial to initiating timely treatment in hopes of yielding better outcomes. Current guidelines recommend yearly cardiac screening at diagnosis [68].

2.3.1.1. Hemodynamic Biomarkers

Biomarkers indicative of DMD are suspected to be released into circulation because of sarcolemmal tearing, a phenomenon that occurs in response to the mechanical stress of contraction caused by compromised membrane integrity arising from the dystrophin mutation. Cardiac troponin I (cTnI) and T (cTnT) are proteins that comprise the contractile unit of myocardial cells and are biomarkers for damage to the myocardium [128]. Serum cTnT can be elevated in the setting of neuromuscular disease and has been shown to correlate better with creatine kinase and myoglobin levels than with cTnI [129,130]. Therefore, cTnI is more specific for myocardial injury in DMD as it is not expressed in skeletal muscle during regenerative processes [131,132]. Cases of acutely elevated cTnI in DMD patients have been reported with abnormal ECGs but no evidence of coronary artery disease [133–138]. Heterogeneity of cTnI levels has also been reported throughout the literature [128]. Significantly elevated levels of cTnI have been reported in DMD patients with mild late gadolinium enhancement (LGE) compared to those without LGE. However, cTnI levels were not elevated in patients with moderate-to-severe LGE. Since LGE is representative of cardiac fibrosis on cardiac magnetic resonance (CMR) imaging, this finding is likely due to increased cell death and fibrofatty tissue replacement in early disease and decreased enzyme leak at later stages of the disease when fibrofatty tissue has replaced most of the myocardium [139]. Elevated troponin levels have also been reported in asymptomatic patients prior to the development of cardiac disease [139], which may represent the necrosis and fibrosis resulting from subclinical or early cardiac remodeling. Decreased cTnI was observed in dystrophic dogs treated with membrane sealant, which was thought to ameliorate cardiac injury [140]. No current recommendations exist for routine monitoring of cTnI in DMD patients. Therefore, only

symptomatic patients tend to undergo testing, making unbiased assessment of the distribution of troponin levels difficult [128].

In addition to troponin, B-type natriuretic peptide (BNP) is a well-known serological marker of cardiac dysfunction; however, studies have revealed that BNP levels are inconsistent and thus are not appropriate measurements of cardiomyopathy in DMD patients [141]. Despite this, lower BNP levels have been reported in patients with DMD-induced cardiomyopathy versus those with idiopathic cardiomyopathy [142]. Only a mild elevation of BNP levels is seen, typically only in the presence of severe cardiac dysfunction [143,144].

Other potential biomarkers and indicators include plasma alpha-atrial natriuretic peptide (ANP), CK-MB, and diastolic abnormalities. Elevation of plasma alpha-ANP levels may be an indication of poor prognosis in DMD patients as it is correlated with congestive heart failure and respiratory failure [145]. Since CK-MB, which is present in both skeletal and cardiac muscle types, can be seen during skeletal muscle regeneration, this protein is not a good marker for cardiac involvement in DMD patients as it can also be indicative of damage to other muscles in the body [146]. Furthermore, DCM and systolic dysfunction are preceded by diastolic dysfunction in DMD, and therefore, diastolic abnormalities may serve as early indicators for early cardiac decompensation [108].

2.4. Structural, Functional, and Histopathological Indicators of DMD-induced Cardiomyopathy

2.4.1. Systolic and Diastolic Dysfunction

Several studies have reported the presence of systolic and diastolic dysfunction in patients with DMD. It is hypothesized that the calcium dysregulation resulting from the absence of dystrophin presents phenotypically as sustained ion-driven myocyte contraction, which appears as underfilling of the LV and impaired relaxation prior to the development of DCM [108,147]. The

authors of [147] described the heart in this phase as “tonic contraction”, a term describing the abnormally increased tone without the ability to relax. Although the LV appears smaller due to its inability to relax, the mass is unaltered. These changes likely lead to a decrease in stroke volume, which may be correlated with the resting tachycardia often present in DMD patients [147]. Furthermore, impaired relaxation (which may be attributed to increased myocardial fibrosis, leading to stiffness of the ventricular walls), diminished the LV cavity size at the end of diastole (a possible outcome of impaired calcium handling to be discussed later), and thickened myocardium have been observed in DMD animal models [147–150]. In a recent study utilizing CMR in DMD patients, LV atrioventricular plane displacement (LVAPD), a marker of systolic and diastolic dysfunction, was decreased in patients with DMD, indicating reduced atrioventricular (AV) plane displacement [151]. Decreased AV displacement correlates to a reduction in contractility and relaxation of the heart, resulting in reduced diastolic filling pressure and diastolic volume [151]. This study found that LV end-diastolic volume (LVEDV) was significantly lower than controls, an observation supported well by the literature [152–154]. Other significant findings in the study by [151] included a reduced LV end-diastolic index (LVEDI) and changes in LV mass and LV end-systolic volume (LVESV).

2.4.2. Cardiac Fibrosis

Since the mammalian heart has a limited ability to replenish dead or dying cardiomyocytes (both in the presence and absence of pathology), a transient phenomenon in response to cardiac damage stimulates pro-fibrotic activity to reinforce zones of damage, while maintaining structural and functional integrity, with collagenous scar formation **(Figure 2-2)**. Cardiac fibrosis is defined as a protective response with immune-mediated etiology in which inflammation, tissue remodeling, and repair processes occur simultaneously [155]. While cardiac fibrosis aims to assist

in preservation of structure and function, if it occurs aberrantly without the appropriate regulatory mechanisms in place to limit its expansion, it can ultimately reduce tissue compliance and accelerate progression to heart failure due to ventricular chamber dilation, stiffness, cardiomyocyte hypertrophy, and aberrant apoptosis [156] **(Figure 2-2)**.

The deterioration of cardiomyocytes observed during dystrophin deficiency-induced cardiomyopathy activates an inflammatory cascade that results in macrophages clearing damaged cells and fibroblasts invading the compromised area to form fibrotic (collagenous) scar tissue. In DMD, a prolonged subclinical phase of myocardial fibrosis is typically observed, beginning early in life [108].

The death of cardiomyocytes and subsequent development of cardiac fibrosis initially presents in the posterobasal segment of the LV [157,158] and extends to the outer third and ultimately the entire LV and septum in human cases of DMD [159]. Interestingly, fibrotic lesions are more prominent in the subepicardium and spare the muscle fibers nearest to the chambers in GRMD [160]. Additionally, fibrosis of the papillary muscles and posterobasal area contributes to mitral valve regurgitation in human DMD [161]. Fibrosis is prevalent from a young age, as evidenced by LG-enhanced CMR [110,162], where cardiac fibrosis was identified in 17% of patients under 10 years, 34% of patients between 10 and 15 years, and 59% of patients over 15 years [163]. Cardiac fibrosis occurs prior to the onset of decreased systolic function, which has also been demonstrated with LG-enhanced CMR [162]. Myocardial fibrotic changes typically exhibit a heterogeneous distribution, according to evidence of regional wall motion abnormalities determined via imaging modalities [164]. While widespread scarring leads to stretching and thinning of the myocardial walls, focal fibrosis increases the risk of sudden death [165].

It should be noted that several studies in *mdx* have investigated the presence of cardiac fibrosis across various time-points (See Section 2.4.2.), with the vast majority of studies exclusively examining the LV) [86,166–170], however, no study has investigated chamber-specific differences (including RV and atria) at any age younger than 6 weeks.

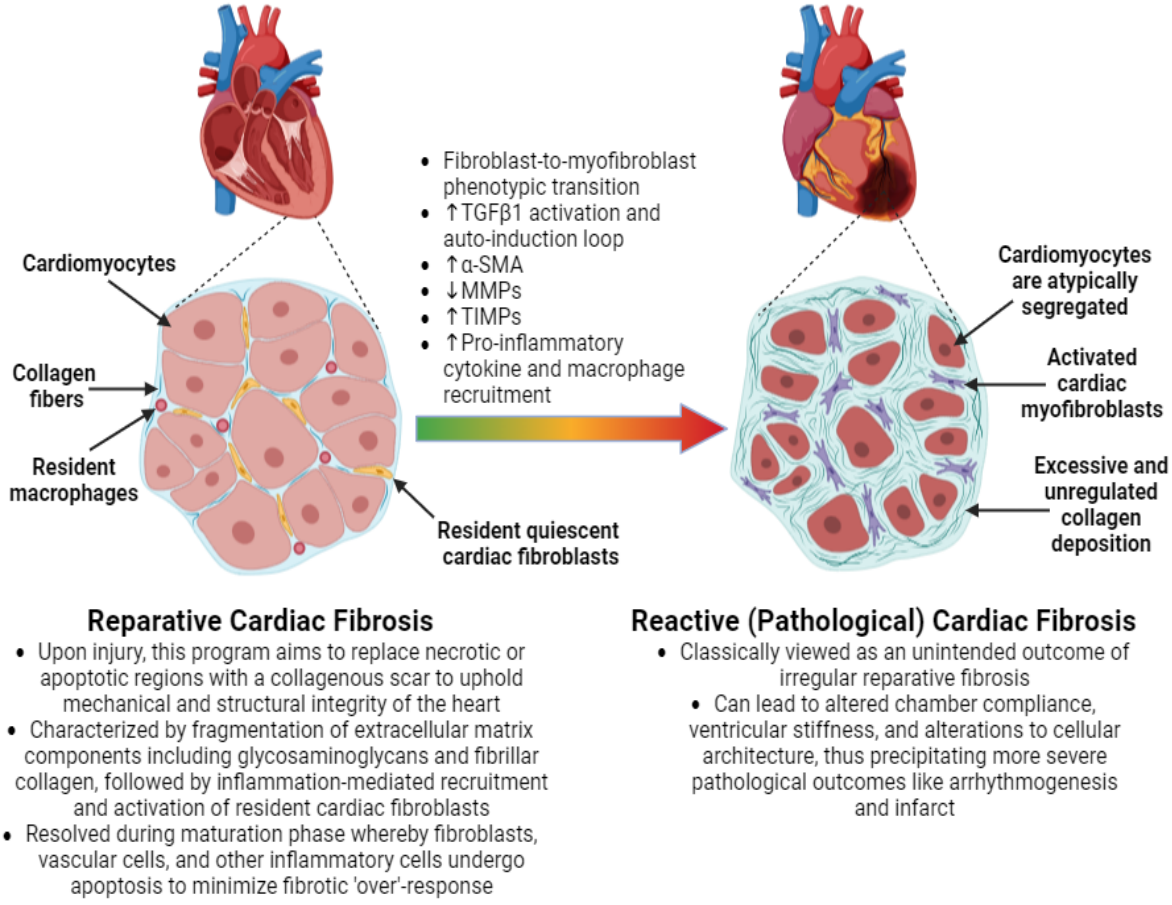

Figure 2-2. Graphical representation of reparative versus reactive (pathological) cardiac fibrosis, with specific mechanisms regulating the transition outlined. While cardiac fibrosis is often classically viewed as a negative histological remodeling signature, in actuality, it is necessary during early stages of damage to maintain mechanical and structural integrity of the heart. When signals to resolve cardiac fibrosis programs are perturbed or overridden, collagen deposition can aberrantly expand beyond the damage zones to unaffected areas, thus leading to altered chamber compliance and ventricular stiffness, ultimately exacerbating the pathology. TGFβ1 – transforming growth factor β1; α-SMA – α-smooth muscle actin; MMP – matrix metalloproteinase; TIMP – tissue inhibitor of matrix metalloproteinase. Figure created using www.BioRender.com.

2.4.3. Dilated Cardiomyopathy

As myocardial fibrosis increases with disease progression, the fibrotic region of the heart gradually stretches and thins, losing its contractility and resulting in DCM (reviewed in [50]). This may involve dilation of the LV or both ventricles, although right ventricle (RV) function tends to be relatively preserved in the setting of improved respiratory interventions [171]. Dystrophin deficiency-induced cardiomyopathy is different than other types of cardiomyopathy in that the LV dilatation is less prominent, while the prognosis is worse [101]. DCM typically occurs in the second decade of life in DMD patients, although it has been reported in children under six years of age [13]. The clinical signs of DCM in DMD patients include increased LV diameter and volume, reduced FS, decreased LVEF, and development of mitral valve regurgitation [50].

2.4.4. Arrhythmia

Frequent ECG changes detected in DMD after the development of cardiac fibrosis consist of ST, short PR interval, left atrial abnormality, and right axis deviation [172]. In addition to dystrophin deficiency-induced cardiac fibrosis, calcium transients, and elevated ROS, ECG abnormalities may be secondary to dysregulated sodium, calcium, and potassium channels, kinases, and nitric oxide synthase (nNOS) triggered by the absence of dystrophin [173]. Briefly, dystrophin is thought to play an important role in scaffolding voltage-dependent sarcolemmal ion channels in the heart via syntrophin binding, which is an adaptor protein that binds directly to two sites in dystrophin's carboxyl-terminal region [173]. Dystrophic cardiomyocytes have demonstrated considerable sodium channel loss-of-function, while the activity of some potassium channels may also be reduced [173]. It is hypothesized that sarcolemmal ion channel abnormalities may occur prior to the onset of cardiomyopathy in the dystrophic heart and may represent a primary effect of the *DMD* mutation [173]. QRS duration appears to increase with age, regardless of

systolic function [174]. The onset of resting ST is typically seen in DMD patients by 5 years of age, and conduction changes are observed by 10 years of age [50]. Cellular mechanisms, including altered calcium homeostasis and elevated ROS, are hypothesized to cause arrhythmias in these patients. More serious arrhythmias, such as atrial fibrillation, AV block, ventricular tachycardia, and ventricular fibrillation, have been reported in the presence of advanced fibrosis [50,175]. One study estimated that approximately 44% of DMD patients had arrhythmias, including frequent atrial (3%) or ventricular premature contractions (22%), atrial (16%) or ventricular couplets (32%), supraventricular tachycardia (SVT) (9%), and ventricular tachycardia (VT) (13%) [176]. Arrhythmias have been shown to be significantly correlated with decreased systolic function [176,177], and an age older than 17 years was significantly associated with the development of SVT or VT [176]. Sudden death does occur in DMD patients, but the percentage due to arrhythmias is unknown [178]. Continuous Holter recordings have shown resting ST, loss of cardiac circadian rhythm, and heart rate variability [179]. Although one study showed that ECG abnormalities frequently precede cardiac dysfunction by several years [180], no differences were noted in the ECG of DMD patients with cardiomyopathy compared to those in the subclinical stages [181]. These inconsistencies suggest that ECG is not a useful diagnostic tool; however, periodic Holter monitoring is recommended in this population [68].

2.5. Cardiac Chamber-Specific Differences in DMD

To date, most of the research in the hearts of DMD patients and/or dystrophin-deficient pre-clinical models has been conducted in the LV or, albeit less commonly, in the unspecified "whole heart". A limited data set now suggests that dystrophic cardiomyopathy may affect the heart heterogeneously, with differing data on histopathology (e.g., fibrosis, calcification, etc.), function (e.g., echocardiography, invasive hemodynamics, etc.), and other related remodeling

parameters observed across ventricles **(Figure 2-3)**. Metabolic and/or mitochondrial data comparing the two ventricles is surprisingly virtually non-existent across all time-points and models. Several studies across both human and pre-clinical DMD models have determined differences in ejection fraction, fractional shortening, and other related functional measurements between ventricles [162,182,183]. While systolic dysfunction is evident in both ventricles of the aged D2.*mdx* heart, it was determined that RV function was slightly better than LV despite the elevated fibrosis [184]. The authors of [86] demonstrated that 18-week-old D2.*mdx* hearts exhibit thick epicardial fibrotic-calcinosis layers that are limited and restricted to the RV, but such changes are not detectable in the LV or septum [184] **(Figure 2-3)**. Together, these data suggest that RV remodeling potentially precedes the onset of significant cardiac complications [184]. One study conducted on 4-week-old C57BL/10.*mdx* determined using LG-enhanced MRI and dobutamine stress that RV abnormalities were present at this young age (demonstrated by elevated end systolic volume compared to control) while unchanged in the LV, albeit in the absence of cardiac fibrosis [185], thus suggesting that the association between RV remodeling and function differs by model **(Figure 2-3)**.

Historically, the role of the RV in dystrophin deficiency-induced cardiomyopathy has been underappreciated in place of the larger, more physiologically demanding LV. For this reason, literature comparing pathology across ventricles is limited. Although, to date, some work has been conducted to elucidate RV function and its role in dystrophin deficiency, further research is required to investigate parameters such as hemodynamics and echocardiography in dystrophin-deficient rodent models (ideally mice aged >24 weeks), specifically in D2.*mdx* where early cardiac remodeling is more prominent. Additionally, there is an abundance of conflicting data about ventricle-specific disease progression due to the use of different dystrophin-deficient models and

time-points. Future research should seek to track the time-course progression of ventricular abnormalities in an established dystrophin-deficient pre-clinical model to determine the order in which these pathologies arise. Additionally, the field would invariably benefit from building on pre-existing literature that examines how LV metabolic and mitochondrial perturbations correspond to LV functional differences by extending experiments to the RV for chamber-specific comparisons using similar time-points and models.

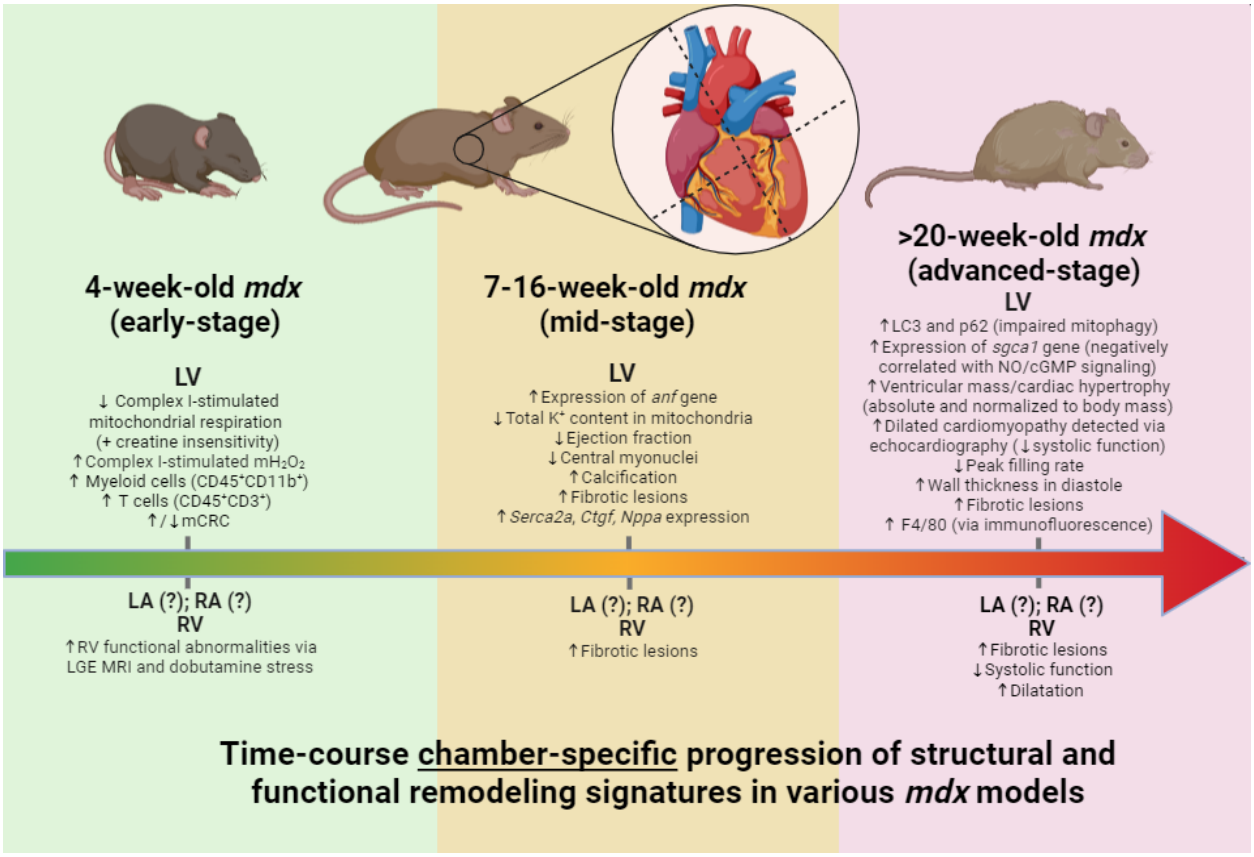

Figure 2-3. Time-course chamber-specific progression of structural and functional remodeling signatures in various mdx models. While the left ventricle has been extensively investigated from early-to-advanced stages in dystrophin deficient *mdx* mice, significantly less is known about the other chambers of the heart, including the atria and right ventricle. Understanding time-course progression of histological and metabolic remodeling signatures in the whole heart could provide invaluable insight towards manifestation of cardiac functional impairments that develop at later ages. This could ultimately improve the ability of clinicians to develop early therapeutic interventions aimed at delaying cardiomyopathy progression. LV – left ventricle; RV – right ventricle; LA – left atrium; RA – right atrium; LGE MRI – late gadolinium enhanced magnetic resonance microscopy. Figure created using www.BioRender.com.

2.6. Secondary Physiological Dysfunctions: Inflammation, Calcium Dysregulation, and Their Contributions to Stress Responses in DMD

2.6.1. Inflammation and the Immune Response

Although inflammation is necessary to heal from injury, it can also be damaging if it occurs aberrantly. In mammalian systems, inflammatory and immune infiltrate are responsible for clearing damaged muscle cells and are often present prior to the onset of cardiac remodeling systems. Since the heart has a limited ability to regenerate its cardiomyocytes, macrophages will secrete chemokines (such as transforming growth factor beta (TGF-β)) in response to injury, to activate resident homeostatic fibroblasts and endothelial cells, thus increasing the ratio of nascent myofibroblasts to homeostatic fibroblasts **(Figure 2-4)**. Fibroblasts are activated into collagen-secreting myofibroblasts and enhance ECM deposition at the injury site, forming fibrocollagenous scar tissue within the wall of the ventricular myocardium [186,187]. Accordingly, muscle biopsies from DMD patients demonstrated that elevated TGF-β expression is associated with skeletal muscle fibrosis [188]. The immune infiltrate primarily consists of macrophages and T cells in young (2 to 8 years of age) DMD patients [189,190]. Furthermore, a high concentration of macrophages and T lymphocytes has been reported in pooled dystrophic muscles (quadriceps, hamstrings, and gastrocnemius) beginning early in disease progression, suggesting that these cells play a crucial role in the pathology of dystrophic muscle [190,191] **(Figure 2-4)**. Of note, it has been demonstrated in dystrophic diaphragms of 6- and 12-week-old C57BL/10.*mdx* mice that the inflammatory macrophage serotype $CD45^{+}CD11b^{+}F4/80^{+}$ is elevated compared to WT, while mRNA expression reveals elevated CC chemokine receptor 2 (CCR2) mRNA expression (representative of pro-inflammatory macrophage polarization) in both diaphragm and TA muscles at both time-points [192]. Interestingly, this study determined that CCR2 loss-of-function (both genetically and pharmacologically) helped to restore macrophage polarization towards an anti-

inflammatory phenotype, which ameliorated indices of histopathological remodeling and also increased muscle strength in the diaphragm, suggesting that CCR2 plays an imperative role in the pathogenesis of DMD-induced inflammation and remodeling [192].

Sarcolemmal lesions in dystrophic skeletal muscles initiate calcium leakage and inflammatory cytokine upregulation, produce and release tumor necrosis factor alpha (TNF-α) and histamine, and contribute to mast cell degranulation and elevations to eosinophils [190,193,194]. A combination of these cytokines contributes to a proinflammatory environment and consequently promotes muscle necrosis [190]. While inflammatory mechanisms have been discovered in dystrophic skeletal muscle, these pathways have not been extensively examined in the dystrophic heart, thus representing a future avenue of research.

Two main inflammatory pathways are involved in dystrophic skeletal muscle: the nuclear factor kappa-light-chain-enhancer of activated B cells (NF-κB) pathway and the nucleotide-binding oligomerization domain (NOD)-like receptor family pyrin domain containing 3 (NLRP3) pathway. NF-κB, a transcription factor that regulates the expression of chemokines and cytokines, may be activated by dystrophin deficiency-induced mechanical stretch **(Figure 2-4)**. Increased activation of NF-κB is seen in dystrophic skeletal muscle [190,195]. The overexpression of chemokines is hypothesized to occur prior to initial disease onset (defined as the initial mechanical damage that results from the absence of the membrane-stabilizing effects of dystrophin) and induce macrophage and T-cell infiltration [190,196]. It has been previously determined that the inhibition of NF-κB in utrophin/dystrophin-deficient mice improves cardiac contractile function [197].

Inflammatory cytokines like IL-6 are elevated in both pre-clinical models [198] and humans [190,199,200] with DMD, specifically in various skeletal muscles. The potential relationships between inflammation and mitochondrial dysfunction are notable given that TNF-α

and IL-6 are examples of cytokines that induce decreases in mitochondrial oxidative phosphorylation and elevations in mitochondrial superoxide production in a variety of cell types and models unrelated to dystrophin mutations [201–203]. Indeed, the current standard of care involves immunosuppression with glucocorticoids [104], which slows the progress of the disease through mechanisms that are thought to be related, in part, to reduced inflammation [115]. Nonetheless, the remaining influence of inflammation is thought to contribute to mitochondrial dysfunctions in muscle [30], although this is not fully characterized in the context of disease and glucocorticoid interactions.

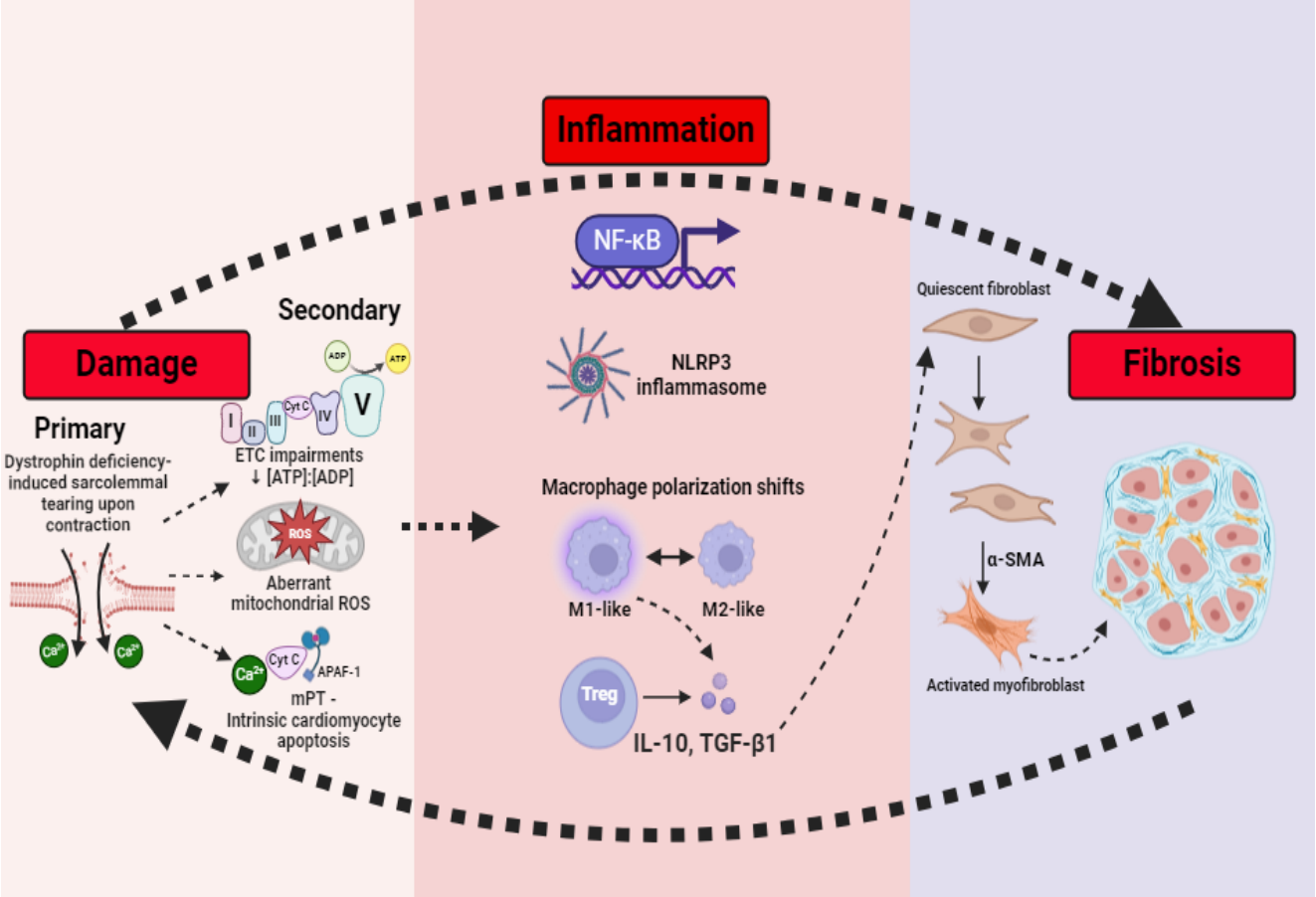

Figure 2-4. Schematic representation of a proposed signaling pathway from dystrophin deficiency-induced muscle damage to inflammation-mediated fibrosis. Mutations to the dystrophin protein cause its functional absence in the cell, thus leading to dystrophin deficiency-induced sarcolemmal tearing with each contraction and representing the primary pathology in DMD. Such sarcolemmal tears perpetuate secondary contributors to dystrophic pathology, such as mitochondrial electron transport chain impairments, aberrant mitochondrial reactive oxygen species emissions, and perturbed calcium handling leading to intrinsic mitochondrial-mediated apoptosis. Dystrophin deficiency precedes and contributes to a robust inflammatory response, which is a hallmark characteristic of DMD. Incomplete resolution of the inflammatory phase can stimulate a fibrotic response, thus representing the final and possibly most detrimental outcome of dystrophic pathology. *Important to note:* while most, if not all of these proposed mechanisms have been extensively investigated in dystrophic skeletal muscle, more research is required to elucidate this cascade in the dystrophic heart, especially with chamber-specific considerations. ROS – reactive oxygen species; ETC – electron transport chain; I-V – mitochondrial ETC complexes; Cyt C – cytochrome *c*; Ca^{2+} - calcium; mPT – mitochondrial permeability transition; APAF-1 – apoptotic peptidase activating factor; NLRP3 - NOD-, LRR- and pyrin domain-containing protein 3; NF-κB – Nuclear factor kappa-light-chain-enhancer of activated B cells; IL – interleukin; TGF-β – transforming growth factor β; α-SMA – α-smooth muscle actin. Figure created using www.BioRender.com.

2.6.2. Calcium-Handling Dysregulation, Ionic Perturbations, and Cell Death

In healthy cardiac muscle, contraction and relaxation are driven by the cycling of calcium between the sarcoplasmic reticulum (SR) (the intracellular storage site of calcium) and cytosol. Briefly, this process involves plasma membrane depolarization that subsequently activates the L-type calcium channels (LTCC), which allows calcium to flow into the cell and subsequently causes a larger calcium flux from the SR through the ryanodine receptor 2 (RyR2), resulting in muscle contraction. This process is termed calcium-induced calcium release (CICR). It is imperative to note that the relationship between muscular dystrophy-induced elevations to net intracellular influx of calcium and muscle-cell necrosis was first proposed 40 years ago [32,33]. It was hypothesized that this increased intracellular calcium concentration triggers a vicious cycle of downstream mitochondrial calcium overload and eventual insufficient ATP synthesis, which further perpetuates cytosolic calcium levels by impairing calcium pumps, leading to the hypercontraction of muscle fibers and subsequent cell necrosis [32] **(Figure 2-5)**. Interestingly, Wrogemann and colleagues were among the first to determine that calcium chelators such as EDTA could ameliorate the depressed respiration in dystrophic mitochondria, at least from skeletal muscle, by lowering mitochondrial calcium concentrations [32]. Although this observation was not originally established in dystrophic cardiac tissue, it is still a seminal finding that highlights the importance of intracellular calcium balance in dystrophic tissue and how calcium handling can be targeted in pursuit of a therapy.

Multiple mechanisms are believed to contribute to calcium overload and disrupted calcium homeostasis. Increased calcium influx and resting levels of mitochondrial calcium have been observed in myocytes from C57BL/10.*mdx* mice [204]. In addition to the extracellular calcium that leaks through the sarcolemmal membrane tears, ion channels and calcium handling proteins

likely contribute to the excessive calcium found in dystrophic myocytes (See Section 2.7.1.1.). Stretch-activated calcium influx differences, increased diastolic calcium levels, altered calcium transient kinetics, and changes in calcium-handling protein expression, activation, or post-translational modifications have been observed in cardiomyocytes of C57BL/10.*mdx* mice [28,29,205,206].

Excessive cytosolic calcium may activate calcium-dependent proteases, such as calpains, contributing to apoptosis [207]. A study investigating single ventricular myocytes from C57BL/10.*mdx* proposed that calcium-activated calpains degrade troponin I, resulting in contractile dysfunction and decreased calcium sensitivity [28]. A separate study assessing calpains in 4-week-old C57BL/10.*mdx* mice determined that total concentrations of calpains were elevated in necrotic hind limb muscle from dystrophic mice compared to controls; however, further research on the heart is required [208].

Another possible source of calcium overload in dystrophic cardiomyocytes is through transient receptor potential channels (TRPC) and the LTCC $Ca_v1.2$ [209–212]. TRPCs are hypothesized to engage in the augmented stretch-activated cation influx seen in C57BL/10.*mdx* cardiomyocytes, and overexpression of these channels has been observed in dystrophic cardiomyocytes [209–212]. A decrease in excessive calcium was demonstrated in C57BL/10.*mdx* cardiomyocytes using inhibitors of TRPC, stretch-activated channels, and transient receptor potential vanilloid (TRPV2) [28,211]. Redox modifications of $Ca_v1.2$ alpha1 subunit that occur during periods of elevated oxidative stress lead to increased channel-mediated calcium influx [173,213,214]. Resultantly, ROS may partly explain the gain-of-function calcium channel abnormalities observed in dystrophic cardiomyocytes [173]. Indeed, communication between LTCC and mitochondria has proven to be crucial in healthy cells for metabolic function, and this

communication was disrupted in C57BL/10.*mdx* cardiomyocytes [204,215]. Studies in mice lacking either dystrophin alone or dystrophin and utrophin demonstrated increased calcium influx through the LTCC in cardiomyocytes [28,211] **(Figure 2-5)**. The LTCC pathway to calcium overload is also suspected to play a role in the calcium-dependent arrythmias seen in DMD [216].

RyR2 and sarcoplasmic/endoplasmic reticulum calcium ATPase (SERCA) may enhance the release of store-operated calcium in cardiomyocytes of DMD patients [83,217–219]. It has been observed that in C57BL/10.*mdx* hearts, RyR2 levels are 2 to 3 times greater compared to those of WT mice [28]. Also, protein kinase A (PKA)- or calcium/calmodulin-dependent protein kinase II (CaMKII)-mediated hyperphosphorylation and S-nitrosylation of RyR2 have been demonstrated in dystrophic cardiomyocytes and lead to dissociation from the stabilizing-protein calstabin2 and subsequent increased release of calcium from the SR [83,217–219]. This is supported by studies demonstrating that agents blocking RyR2 phosphorylation result in the normalization of cytosolic calcium levels as well as improvement in cardiac pathology and arrythmias [218–221]. SERCA2a activity is significantly reduced in the C57BL/10.*mdx* dystrophic hearts due to lower SERCA2a expression and impaired regulation by inhibitory proteins phospholamban (PLN) and sarcolipin [28,220,221]. Phosphorylation of PLN via PKA or CaMKII is mostly regulated by β-adrenergic signaling [222,223]. Inositol trisphosphate (IP_3) receptors, which are calcium-release channels on the SR, are activated by the downstream product of phospholipase C (PLC) [209]. PLC inhibitors have demonstrated normalization of intracellular calcium levels in C57BL/10.*mdx* cardiomyocytes to WT levels [224]. It should be noted that calcium-dependent phospholipase A_2 (PLA_2) can also be activated when dystrophic cell membranes permit excessive calcium influx, thus resulting in destabilization of muscle membrane structure, at least in dystrophic myofibers [61,225,226].

Sodium ions can also affect mitochondrial–cytoplasmic calcium exchange through the Na^+-Ca^{2+} exchanger (NCX), which drives calcium out of the mitochondria in exchange for sodium when cytosolic sodium begins to accumulate as a result of dystrophin deficiency-induced microtears. A significant increase in cytosolic sodium levels [227] and elevated levels of NCLX ($Na^+/Li^+/Ca^{2+}$) have been observed in cardiomyocytes of C57BL/10.*mdx* mice [228]. To decrease intracellular sodium and calcium overload caused by pathologic reversal of the NCX, a potent and selective sodium-proton exchanger isoform 1 (NHE-1) inhibitor known as rimeporide has been in development [229,230]. NHE-1 is a membrane transporter responsible for catalyzing the electroneutral counter transport of sodium and hydrogen ions through the plasma membrane [229]. Interestingly, when rimeporide was tested on *mdx* mice, protective effects against inflammation and accumulation of fibrosis were observed in the heart, but additional work in this field to identify potential side effects and dose–response curves is still required [229]. Additionally, previous work in gastrocnemius and longissimus dorsi muscles from 5- to 6-month-old C57BL/10.*mdx* mice demonstrated elevations in Na^+/K^+ ATPase content [231]. Albeit not in the heart, this further suggests that sodium regulation is abnormal in dystrophic muscle and potentially precedes cell death via abnormal regulation of the cell volume [231].

Alongside perturbed Na^+ regulation in dystrophic skeletal and cardiac muscle, the efficiency of cardiac K^+ ion transport and total cardiac K^+ content in 8-week-old C57BL/10.*mdx* mice is decreased [232] **(Figure 2-5)**. This is important because impairments to K^+ homeostasis have been implicated in the manifestation of dilated cardiomyopathy observed across several myopathies, including DMD [232,233]. Given that several calcium-dependent processes are impacted by dystrophin deficiency, mitochondrial K^+ channels represent a prospective therapeutic target due to their involvement in mitochondrial large-conductance Ca^{2+}-dependent K^+ channels

(mitoBK$_{Ca}$) [232]. Interestingly, it has been observed that the chronic administration of the benzimidazole derivative NS1619 (an activator of mitoBK$_{Ca}$) improved K^+ transport and content in cardiac mitochondria of 8-week-old C57BL/10.*mdx* mice while simultaneously alleviating lipid peroxidation, reducing cardiac fibrosis, and normalizing the cardiac mitochondrial ultrastructure [232]. This same group also tested a metabolic modulator known as uridine, which is thought to activate the mitochondrial ATP-sensitive K^+ channel through actions of the metabolite of uridine—UDP (uridine-5-diphosphate) [232,234]. It was revealed that daily administration of uridine for four weeks improved K^+ transport and content in cardiac mitochondria of 8-week-old C57BL/10.*mdx* mice, akin to NS1619, which was accompanied by elevations to the cardiac mitochondrial number and increases in the calcium retention capacity [232,234,235]. Collectively, these findings highlight opportunities for further investigation into the potential role of ion (e.g., Na^+, Ca^{2+}, Li^+, K^+, Cl^-, and H^+) dysregulation as a prospective driver of mitochondrial dysfunction.

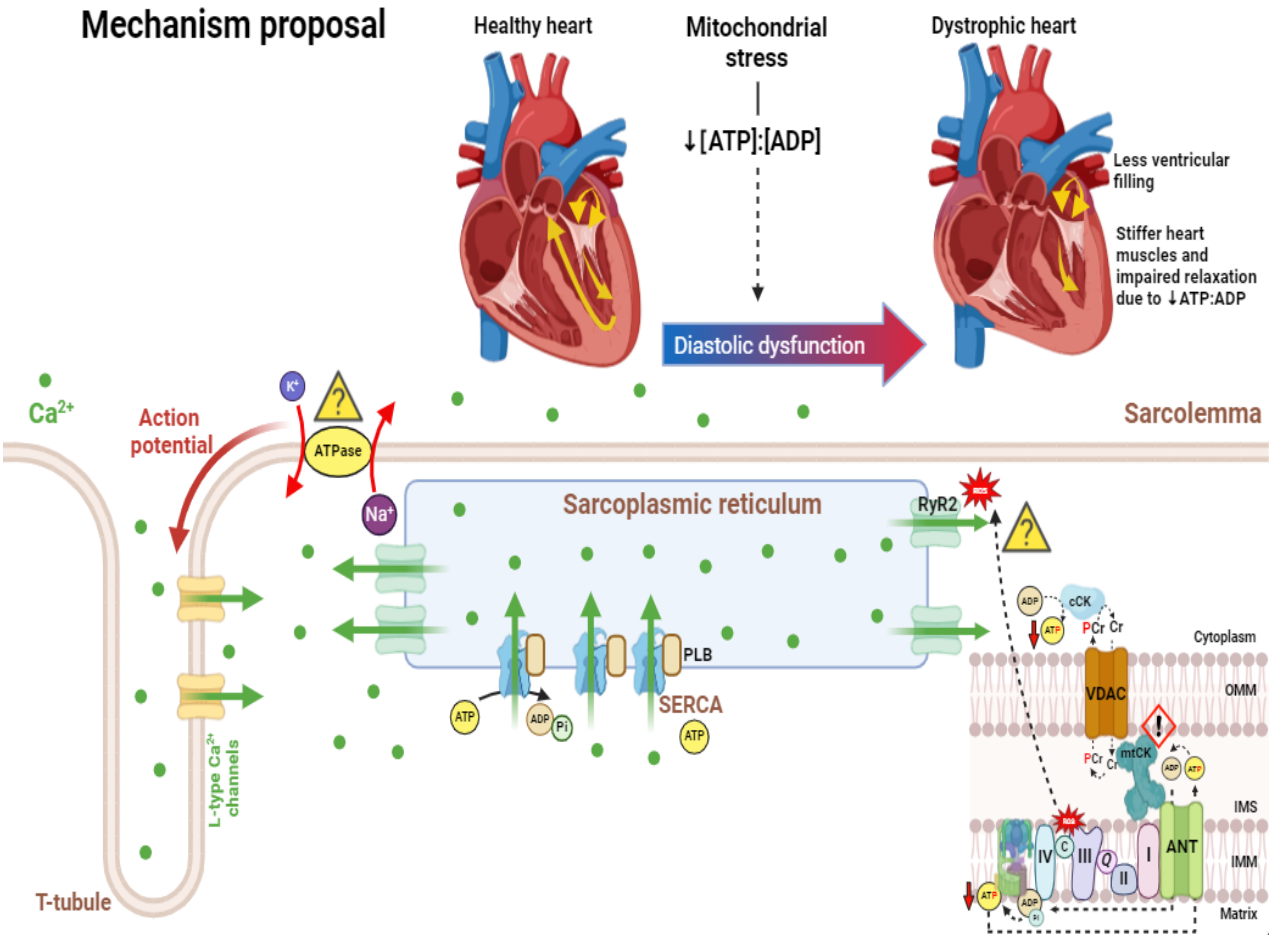

Figure 2-5. In this mechanism proposal, cardiac dystrophin deficiency may contribute to diastolic dysfunction through calcium-handling dysregulation, ionic perturbations, and mitochondrial stress responses. Yellow question marks denote pathways where ATP insufficiency and elevated mH_2O_2 may directly contribute to impaired muscle function, with hypotheses reflecting extensive previous literature. While these mechanisms have never been demonstrated in a singular model, this proposal combines published literature from studies across various DMD models. Dystrophin deficiency in the LV leads to lower [ATP]:[ADP] and elevated mH_2O_2 in *mdx* [31,228]. Additionally, work by the authors of [31] determined that loss of phosphate shuttling by creatine in the LV of D2.*mdx* may contribute to lower ATP export out of the mitochondria (possible impairment to mtCK denoted by exclamation mark symbol). Consequently, lower [ATP] may impact a myriad of pathways, including Na^+/K^+ ATPases along the t-tubule (which require ATP to maintain action potential charge balance and membrane excitability) [231], ATP-dependent SERCA (which requires ATP-mediated re-uptake of excess cytosolic Ca^{2+} to allow for cardiac relaxation) [28,220,231,593], and ROS-induced RyR2 oxidative stress (which may aberrantly 'leak' Ca^{2+} from its SERCA storage site) [218–220,593]. PLB - phospholamban; SERCA - sarcoplasmic/endoplasmic reticulum Ca^{2+}-ATPase; RyR - ryanodine receptor; PCr - phosphocreatine; Cr - creatine; Pi - inorganic phosphate; cCK - cytosolic creatine kinase; mtCK - mitochondrial creatine kinase; VDAC - voltage-dependent anion channel; ANT - adenine nucleotide translocase; IMM - inner mitochondrial membrane; IMS - intermembrane space; OMM - outer mitochondrial membrane; I - complex I; II - complex II; Q - coenzyme Q/ubiquinone; III - complex III; *c* – cytochrome *c*; IV - complex IV; K^+ - potassium ion; Na^+ - sodium ion; Ca^{2+} - calcium ion; ATP - adenosine triphosphate; ADP - adenosine diphosphate; ROS - reactive oxygen species. Figure has been published in *Cells*. Figure created using www.BioRender.com.

The disruption of ions could theoretically induce mitochondrial dysfunction. While the relationship between sodium and mitochondrial dysfunction in DMD has not been examined in detail, the link to calcium stress has been investigated extensively. This is an important relationship to consider given that cardiac mitochondria do not typically act as a significant dynamic buffer of cytosolic calcium in healthy hearts; however, prolonged elevations of intracellular calcium substantially enhance mitochondrial calcium uptake [236,237]. Recently, increased calcium uptake has been observed in the mitochondria of C57BL/10.*mdx* cardiac muscle, likely due to enhanced expression of the channel-forming MCU subunit and reduced expression of the dominant-negative MCUb subunit [228]. While the precise mechanisms regulating excess mitochondrial calcium uptake require more investigation, current theories posit that calcium overload triggers cell death through mitochondrial permeability transition activity in conjunction with impaired oxidative phosphorylation and elevated ROS production, as described in detail below **(Figure 2-6)**.

2.7. Introduction to Mitochondrial Bioenergetics

The mitochondrion, colloquially referred to as the 'powerhouse of the cell', is a cellular organelle present in eukaryotes that is characterized by its double membrane system, which is comprised of the ion-permeable outer mitochondrial membrane (OMM), the intermediary intermembrane space (IMS), and the relatively impermeable inner mitochondrial membrane (IMM), which separates the mitochondrial matrix from the IMS. Most notably, mitochondria are recognized for their indispensable role in ATP-generating processes, whereby mitochondria are responsible for up to 95% of the total ATP generated in the cell for imperative physiological functions through a process known as oxidative phosphorylation [238]. Key to oxidative phosphorylation is the presence of the electron transport chain (ETC) within the IMM, which consists of five transmembrane protein complexes (I-V), two reducing equivalents that supply

electrons to complex I and II (NADH and $FADH_2$, respectively) generated through the catabolism of fuel sources (primarily carbohydrates and fat), and two intermediate electron carriers (coenzyme Q and cytochrome *c*) which work collectively to transfer electrons sequentially through the complexes in a series of redox reactions to generate free energy [239]. This system, which was eventually coined the chemiosmotic theory of oxidative phosphorylation by Peter Mitchell, demonstrates how inter-complex electron (anion) transfer via redox reactions is coupled to proton pumps within the ETC that simultaneously extrude protons (cations) from the negatively charged matrix into the positively charged IMS, thus generating a proton motive force, also known as electrochemical gradient, for ATP synthesis via complex V (ATP synthase) [240]. ATP synthase functions by synthesizing ATP from ADP and an inorganic phosphate (P_i), which requires the flow of protons against its electrochemical gradient back to the matrix through ATP synthase [239]. In addition to oxidative phosphorylation, mitochondria are also imperative for several other physiological processes which will be described below, including mitochondrial Ca^{2+}-uptake-induced swelling and apoptosis, and oxidative stress via ROS emission attributed to premature electron slip.

2.7.1. Mitochondrial Permeability Transition Pore and Intrinsic Apoptosis

Recent evidence supports a model whereby ATP synthase components dimerize to form the mitochondrial permeability transition pore (mPTP) in response to ROS and excessive calcium stress (mitochondrial calcium overload when matrix [calcium] is high) [241,242], which then leads to depolarization of the mitochondrial membrane, a loss of ATP synthesis, and rapid mitochondrial calcium efflux to the cytosol through an event known as mitochondrial permeability transition (mPT) **(Figure 2-6)**. mPTP formation is an event that fuses the IMM and OMM while increasing the permeability of the IMM to solutes, which is typically impermeable to most solutes and ions.

It is important to note that mPT can result in two important changes to the mitochondria. Firstly, the increased permeability of the IMM to solutes leads to a rise in osmotic pressure which can cause swelling of the mitochondria. Following the subsequent release of cytochrome *c* from the OMM due to swelling-induced rupture, caspases 9/3 are activated, which signal to proteases that contribute to intrinsic mitochondrial-mediated apoptosis [243] **(Figure 2-6)**. Secondly, since the IMM can become permeable to protons during mPT, oxidative phosphorylation processes can become uncoupled from ATP synthesis, leading to its hydrolyzation rather than synthesis [244]. Furthermore, there is evidence that the ADP/ATP antiporter, ANT, may be involved in mPT given that sarcoglycan-deficient mice were shown to develop mPT in an ANT-dependent manner [245].

2.7.1.1. Mitochondrial Permeability Transition in DMD

Myotubes cultured from C57BL/10.*mdx* demonstrate ~10-fold higher calcium in the matrix compared to the cytosol [246]. Calcium-induced PT was elevated following ischemia–reperfusion in young C57BL/10.*mdx* hearts and was accompanied by the release of proapoptotic factors (including cytochrome *c* into the cytosolic fraction), as well as enhanced activities of caspases 9/3 prior to the onset of cardiac dysfunction [81,82]. In LV of 4-week-old D2.*mdx* mice, no differences in calcium-induced PT or caspases 9/3 activities were observed [247] in contrast to increases in both measures seen in certain skeletal muscles [248]. As there were no reductions in the ejection fraction at this young age, the study concluded that mitochondria do not demonstrate PT in LV in early-stage disease. A separate study conducted on 7-month-old C57BL/10.*mdx* mice using mitochondria isolated from whole hearts demonstrated a greater propensity for calcium-induced mPT [249]. Collectively, these findings suggest that introducing physiological stressors such as ischemia–reperfusion or assessing more advanced disease states may be required to reveal an underlying mitochondrial propensity for PT, although the degree to which mPT exists across

specific regions of the heart is unknown. The contributions of mPT to cardiomyopathy at specific stages of disease requires further research.

It has been proposed that different analytical interpretations can be associated with the specific technique that is used to determine and quantify mPT. Techniques include quantifying the concentration of calcium required to trigger its opening via bolus titrations in a permeabilized fiber system versus the elapsed time that is required to trigger this opening in response to a single bolus of calcium. To this end, differing conclusions from studies have led to the belief that disease effects on time may not be mirrored by changes in the total calcium uptake by mPT (proposed and reviewed in [30]). In one such study, both approaches were compared and demonstrated no change in total calcium uptake despite a lower time for calcium to trigger mPT in C57BL/10.*mdx* mice [82]. This finding implies that a greater propensity for calcium-induced mPT may be due to greater velocities of calcium uptake independent of potential differences in total uptake. Such methodological considerations could be considered when assessing mPT in relation to cardiomyopathy in *mdx* models. Although this has not been studied extensively in the heart, pharmacological inhibitors of mPT in skeletal muscle have shown promise by improving indices of muscle function in C57BL/10.*mdx* mice [30,250,251]. Whether this can be attributed to the inhibitory effects on mPT itself or the indirect benefit of immunosuppression is still a contentious topic. This is important given that immunosuppressive glucocorticoids have been known to suppress mPT in C57BL/10.*mdx* skeletal muscle [113].

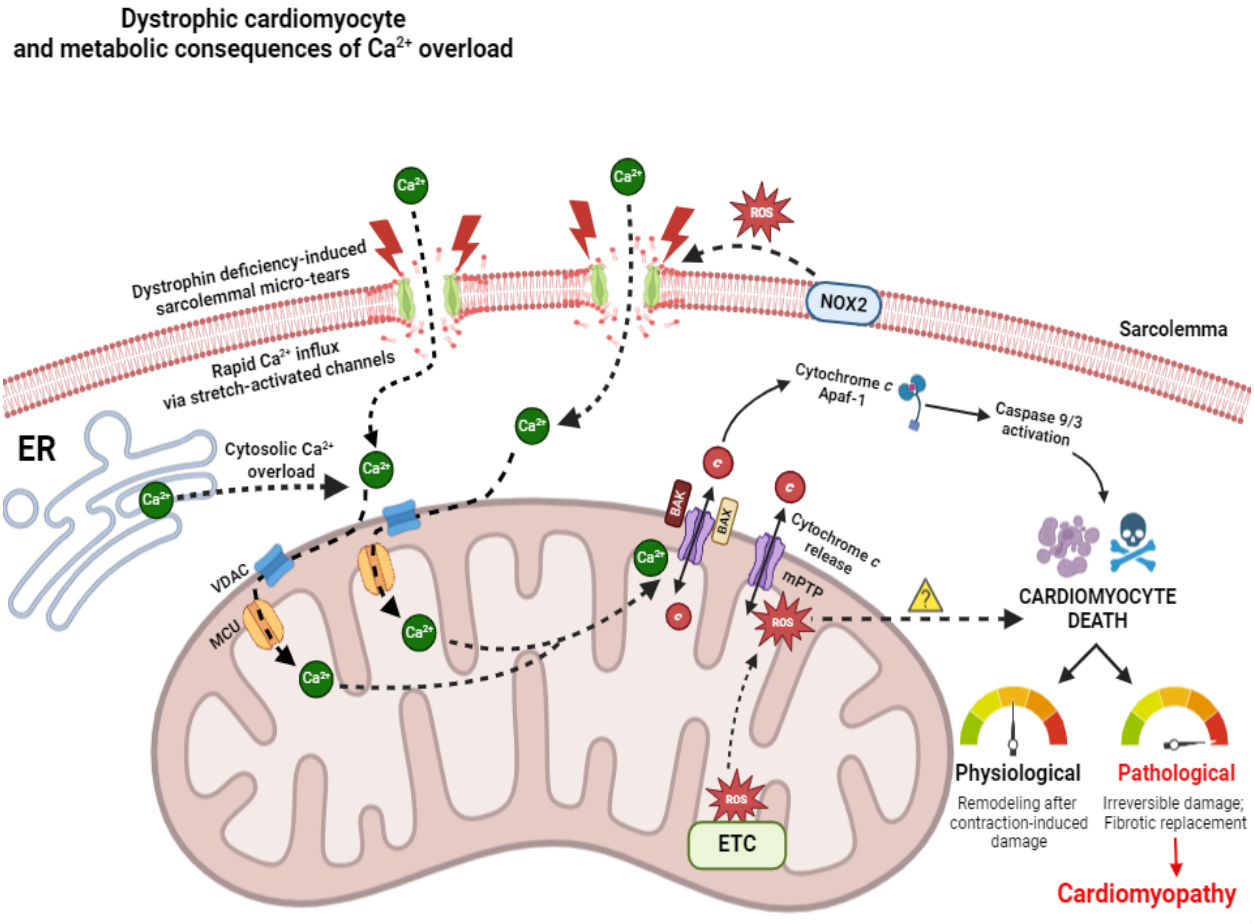

Figure 2-6. Schematic representation of intracellular pathological Ca^{2+} overload caused by dystrophin deficiency-induced micro-tears to the sarcolemmal membrane, and the potential for targeting mPT to attenuate dystrophic cardiac stress. Dystrophin deficiency-induced cytosolic Ca^{2+} overload via stretch-activated channels (SACs) on the sarcolemmal membrane is a hallmark characteristic of the dystrophic phenotype [28,29,205]. Pathological SACs-mediated Ca^{2+} influx into the cytosol is further exacerbated by NOX2-derived oxidative stress, which also occurs as an outcome of dystrophin deficiency [52,210]. During cytosolic Ca^{2+} overload that occurs in crisis, the mitochondrion takes up excess Ca^{2+} via voltage-dependent anion channel (VDAC) and mitochondrial calcium uniporter (MCU) channels along the OMM and IMM, respectively. Subsequent mitochondrial Ca^{2+} overload results in mPT, which expels cytochrome *c* into the cytosol [81]. It is also hypothesized that complex I and complex III-derived ROS damage stimulates mPT (insufficient data); however, further research is required to characterize the presence of complex III-derived ROS in *mdx* models [81,594]. It is also presently unknown if mitochondrial ROS directly triggers cardiomyocyte death in dystrophic hearts (denoted by yellow question mark). Cytochrome *c* release from the OMM interacts with the apoptosome-containing adaptor Apaf-1 and other initiator caspases (9/3) [82,243], which induce cardiomyocyte death downstream. In healthy physiological systems, tightly regulated control of cardiomyocyte death is required for remodeling events following contraction-induced damage; however, in pathological states, excessive cardiomyocyte death leads to irreversible damage and fibro-fatty tissue replacement. VDAC—voltage-dependent anion channel; MCU - mitochondrial calcium uniporter; ER - endoplasmic reticulum; ETC - electron transport chain; mPTP - mitochondrial permeability transition pore; Apaf-1 - Apoptotic protease activating factor 1; NOX2 - NADPH oxidase 2; $Ca2^{+}$ - calcium ion; ROS - reactive oxygen species; BAX - Bcl-2-associated X protein; BAK - Bcl-2 antagonist killer; *c* - cytochrome *c*. Figure has been published in *Cells*. Figure created using www.BioRender.com.

Overall, the specific importance and role of mPT-induced cell death in dystrophic cardiomyopathy is still not fully understood and requires more research. Insight may be gained by considering the effects of mPT inhibitors in the skeletal muscle of *mdx* mouse models **(Figure 2-6)**. For example, Debio 025 (D-MeAla^{3}EtVal^4-cyclosporin), an inhibitor of the mPT regulator cyclophilin, showed beneficial roles in locomotor and respiratory muscles of 3-week-old *mdx*^{5Cv} mice [252,253] but had no effect on echocardiograph assessments of heart function or fibrosis in 18-week-old D2.*mdx* mice [86]. Alisporivir, another cyclophilin inhibitor, is a cyclosporin A derivative that desensitizes the mPT without inhibiting calcineurin [254]. Albeit not in the heart, treatment of alisporivir in primary cultures obtained from muscle biopsies of DMD patients demonstrated that this compound could restore the maximal respiratory capacity in dystrophic muscle cells without interfering with basal oxygen consumption, therefore restoring physiological respiratory reserve [254]. In addition, treatment with alisporivir also recovered respiratory function, which matched improvements to muscle ultrastructure and survival in the *sapje* zebrafish model of DMD [254]. TR001, which is a metabolically stable triazole analog and inhibitor of mPT, improved markers of motility 6 days post-fertilization when administered in *sapje* zebrafish [255]. In addition to improving muscle structure and function recovery, as well as mitochondrial respiration and survival in these zebrafish, TR001 also improved respiration in skeletal muscle-derived myoblasts and myotubes from DMD patients [255]. The promise and efficacy of mPT inhibitor treatment modalities on dystrophic locomotor and respiratory muscle in various pre-clinical DMD models supports the need for these compounds to be tested on cardiac tissue and/or cardiomyocytes.

2.7.2. Mitochondrial Biogenesis in DMD

Mitochondrial biogenesis is regulated, in part, through the sequelae of transcriptional regulators that activate or repress promoters for genes encoding over 1500 mitochondrial proteins. Time-dependent decrements to peroxisome proliferator-activated receptor γ coactivator 1-α (PGC-1α) expression—transcriptional co-activator regulating numerous transcription factors—were identified in TA muscle of C57BL/10.*mdx* mice [256]. This finding corresponded to reduced expression of target genes. Several seminal papers have demonstrated that regulation of PGC-1α levels in the skeletal muscle of *mdx* mice may represent a potential avenue for reducing dystrophic muscle pathology given the beneficial effects that have been reported, including improvements to muscle histology, functional performance, and fatigue resistance [257–259]. Although studies have explored AMPK phosphorylation, which regulates PGC-1α in response to a variety of stimuli, and PGC-1α activation in TA muscle of C57BL/10.*mdx* mice using metformin to demonstrate upregulations in mitochondrial content [260], heart-specific data remain limited and represent a future avenue for research.

Contrary to these findings, a separate study assessing mitochondrial biogenesis in pre-necrotic 2-week-old C57BL/10.*mdx* mice revealed no differences in PGC-1α protein content in the quadriceps muscle [261]. These conflicting data suggest that the regulation of mitochondrial biogenesis in *mdx* mice may be complex and age- and muscle-specific, but the transient states of activity in this co-activator, as well as other transcriptional processes, requires careful consideration of time-point selection when relating mitochondrial adaptations to disease processes.

Changes in transcription factors and co-activators that govern mitochondrial biogenesis do not always predict mitochondrial functions. This is due to the complexity by which mitochondrial transporters and enzymatic pathways are regulated post-translationally and in response to other

factors, such as the morphology and structure of the mitochondrial membranes. Furthermore, transcriptional pathways are often induced in response to a stressor that signals a demand for altering mitochondrial content, as can occur under conditions of insufficient energy supply. In this way, simply measuring markers of transcription factors does not necessarily predict functional outcomes of mitochondria. As an example, the mitochondrial permeability transition pore inhibitor Alisporivir increased certain measures of mitochondrial respiration despite lowering the mRNA of PGC-1α [262]. While speculative, these findings may suggest that the improved mitochondrial function may have alleviated a stress signal that was driving the demand for mitochondrial biogenesis. In this way, contextualizing markers of mitochondrial biogenic pathways in relation to mitochondrial function, and ideally mitochondrial content markers, can provide additional insight into the way mitochondria do or do not contribute to myopathy.

Collectively, these data suggest that understanding the role of mitochondrial biogenesis in the context of dystrophinopathy is still incomplete and requires further research, with specific considerations that should be made for the time-point (age), muscle-type, and dystrophin-deficient model.

2.7.3. Oxidative Phosphorylation, Mitochondrial Creatine Kinase, and Substrate Catabolism

2.7.3.1. Oxidative Phosphorylation in DMD

Mitochondrial ATP synthesis occurs predominantly through oxidative phosphorylation within the ETC, a process vital for the energy-demanding heart. As previously mentioned, in healthy mitochondria, this process depends upon the governance of membrane potential across the IMM and is stimulated by temporary elevations to mitochondrial matrix calcium caused by contraction [239,263]. The early identification of mitochondrial deficits in muscular dystrophies using direct assessments of respirometry in isolated mitochondria in people with DMD was reported in 1967, albeit in skeletal muscle [264]. Other reports around this time focused on skeletal

muscle animal models of undefined muscular dystrophies [32,265–267] prior to the identification of the *mdx* mouse [80]. Numerous factors need to be considered when assessing the regulation of mitochondrial oxidative phosphorylation in muscle, including phenotype severity (due to the progressive nature of dystrophin deficiency) and the fact that not all mitochondrial protein markers uniformly change across a spectrum of muscle types, models, or age ranges [30]. This is important to note because mitochondrial protein content should not always be interpreted as being reflective of mitochondrial function (discussed in [30]).

While no study has performed functional assessments of cardiac mitochondrial oxidative phosphorylation in people with DMD, one study found that iPSC-derived cardiomyocytes from adults with DMD had significant reductions in oxygen consumption coupled with ATP synthesis [268]. Attenuations in the phosphocreatine (PCr) energy system indicated by lower PCr concentrations were also observed in these cells [268]. In the C57BL/10.*mdx* mouse heart, studies have shown significant reductions in the ratio of the PCr to ATP ratio, which reflects a compromised ability to maintain energy homeostasis prior to the development of significant hemodynamic or structural changes [269]. This observation is consistent with many reports of attenuated mitochondrial respiration in the dystrophin-deficient heart [30].

2.7.3.2. Mitochondrial Creatine-Dependent Phosphate Shuttling

Of interest, mitochondria can also export, or 'shuttle', PCr (specifically high-energy phosphate groups) in the presence of creatine as a method for maintaining high intracellular ATP:ADP when demand for ATP is high [270,271]. Regulated by mitochondrial creatine kinase (mtCK) located on the outer leaflet of the IMM that also binds to the voltage-dependent anion channel (VDAC) on the OMM, this model posits that when ATP is produced in the ETC during oxidative phosphorylation, it is first shuttled to the IMS by the adenine nucleotide translocase

(ANT) **(Figure 2-7)**. Thereafter, mtCK can trans-phosphorylate ATP (specifically, its phosphate group) and free Cr to produce ADP and PCr. While the ADP can be shuttled back to the matrix via ANT to restart this cycle, PCr is shuttled out of the IMS via VDAC on the OMM and recycled back to ATP by local ATP-hydrolyzing proteins through cytosolic creatine kinases (cCK) (located in the cytosol), which phosphorylates ADP to produce the aforementioned ATP using cytosolic PCr. As PCr diffuses at a rate several-fold faster than ATP, with the creatine product returning to mitochondria ~2000-fold faster than ADP, this fast 'high-energy phosphate shuttling' mechanism may be advantageous to maintaining energy homeostasis in cells that can experience very high rates of demand for ATP, such as the heart [271–273]. It is estimated that approximately 80% of energy transfer in cardiac muscle occurs through creatine-dependent high-energy phosphate shuttling through CK isozymes [274] **(Figure 2-7)**. It is important to note that despite the efficiency of this creatine-dependent pathway, in the absence of creatine (and accordingly mtCK), ADP and ATP can still freely diffuse through ANT and VDAC located on the IMM and OMM, respectively, albeit at a much slower rate than the creatine-dependent system.

2.7.3.3. Mitochondrial Creatine-Dependent Phosphate Shuttling in DMD

One study found that this faster creatine-dependent phosphate shuttling mechanism was more attenuated than the direct ATP export system when assessed with respirometry in permeabilized muscle fibers from the LV of 4-week-old D2.*mdx* mice [247], which has also been reported in skeletal muscle [248,275]. Such "creatine insensitivity" occurring early in the disease was suggested to be a potential unique mechanism preceding the eventual development of cardiomyopathy.

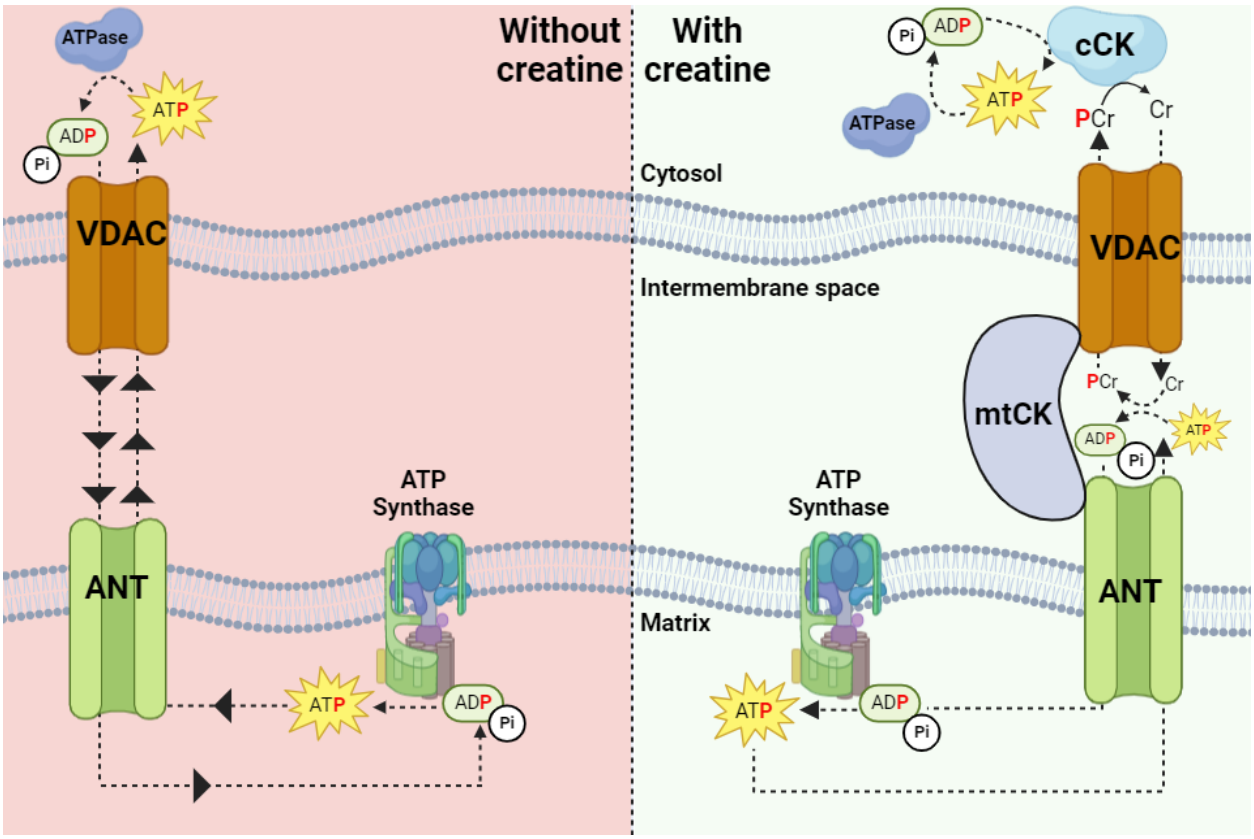

Figure 2-7. Energy transfer systems between the mitochondrion and cytosol in the presence and absence of creatine. On the left side of the image, in the absence of creatine, ADP/ATP transfer from the mitochondrion to cytosol occurs through diffusion across adenine nucleotide translocase (ANT) on the inner mitochondrial membrane (IMM) and voltage-dependent anion channel (VDAC) on the outer mitochondrial membrane (OMM). It is thought that only approximately 20% of energy transfer occurs through this process in cardiac muscle. On the right side of the image, ADP/ATP transfer occurs through the joint efforts of mitochondrial creatine kinase (mtCK) located in the intermembrane space (IMS) and cytosolic creatine kinase (cCK) located in the cytosol. mtCK facilitates the transfer of a phosphate group from ATP to creatine (Cr), thus producing phosphocreatine (PCr) and ADP. While PCr is exported to the cytosol via VDAC to reform ATP, ADP is recycled back into the matrix to restart the cycle via ANT. This process is thought to contribute up to 80% of energy transfer in cardiac muscle. ANT – adenine nucleotide translocase; VDAC – voltage-dependent anion channel; ATP – adenosine triphosphate; ADP – adenosine diphosphate; Pi – inorganic phosphate; mtCK – mitochondrial creatine kinase; cytosolic creatine kinase (cCK). Figure created using www.BioRender.com.

2.7.3.4. Substrate Catabolism in DMD

Additional work is required to address the fates of glucose and other substrates being utilized in dystrophic cardiac tissue. When assessing new therapeutic avenues, careful consideration should be given to designing experiments that consider the role of mitochondrial oxidative phosphorylation as part of an integrated perspective on substrate fates [30].

A variety of other metabolic changes occur in the dystrophic heart. For example, a shift in metabolism from fatty acid to carbohydrate oxidation was observed in vivo in C57BL/10.*mdx* hearts prior to cardiomyopathy, suggesting that altered mitochondrial metabolism is one of the first metabolic changes to occur [276]. In ex vivo perfused C57BL/10.*mdx* hearts, a shift in substrate selection from long chain fatty acids (LCFA) to carbohydrate (glucose) oxidation in C57BL/10.*mdx* hearts was demonstrated by a ~30% lower oleate flux ratio, ~120% higher pyruvate decarboxylation flux ratio, and ~80% increased glycolysis rate [276]. This shift is supported by evidence from cardiac positron emission tomography (PET) studies in DMD patients using ^{18}F-deoxyglucose or a radioiodinated branched fatty acid [277–280]. On the note of carbohydrate oxidation, glucose transporter type 4 (GLUT4) is the main transporter of glucose in cardiomyocytes [281,282] and glucose transport into muscle cells in response to insulin or contraction occurs via translocation of GLUT4 from the cytoplasm to the sarcolemma/T-tubules [282,283]. GLUT4 was observed to be abnormally localized in the sarcolemmal membrane and a trend toward elevated GLUT4 expression was observed in skeletal muscle of GRMD, but not in the LV [284]. Primary cardiac insulin resistance was also observed in the LV of GRMD [285]. Together, this data suggests that glucose/carbohydrate metabolism can potentially be used as a preclinical biomarker of the dystrophic phenotype in skeletal muscle of GRMD dogs, but whether this can be implemented in cardiac tissue remains to be determined [284].

Interventions that correct the substrate imbalance may lead to improvements or recovery of the cardiac contractile dysfunction (reviewed in [286]). Improved contractile performance was observed in C57BL/10.*mdx* hearts perfused with multiple substrates, including carbohydrates (glucose, lactate, and pyruvate) and a LCFA (oleate), in comparison to C57BL/10.*mdx* hearts with glucose as the sole substrate [81,287]. Another potential explanation for substrate shift is the p38 mitogen-activated protein kinase (MAPK) pathway, which is involved through the nuclear receptor peroxisome proliferator-activated receptor (PPARα), a transcriptional regulator of fatty acid oxidation enzyme expression [276]. A 2-fold decrease in p38 MAPK phosphorylation may account for the decrease in LCFA oxidation observed in the C57BL/10.*mdx* heart [81]. This emphasizes the importance of increased and balanced substrate supply to maintain adequate cellular energy in the C57BL/10.*mdx* heart.

It is also possible that certain metabolic stress responses are compensatory in nature. For instance, a shift from fat to carbohydrate oxidation could be beneficial given carbohydrate oxidation produces more adenosine triphosphate (ATP) for a given amount of oxygen consumption [288,289]. However, in DMD, competition for glucose, fatty acids, and proteins may exist for uses unrelated to bioenergetics, such as for membrane repair, as reviewed elsewhere [30]. For example, the degree to which dystrophic muscles downregulate mitochondrial oxidative phosphorylation to favor non-ATP related uses of glucose or fatty acids for structural roles as never been addressed. Such metabolic reprogramming occurs in other models, such as cancer [290], and represents a new avenue for research in DMD. Interestingly, greater levels of fatty acid biosynthesis enzymes that convert fatty acid constituents to acetyl-CoA for the tricarboxylic (TCA) cycle were observed in skeletal muscle from people with DMD [291]. Despite this finding, decreases in TCA pool size and lower aconitase activity were found in C57BL/10.*mdx* hearts [276,292] which could limit

oxidative phosphorylation. Likewise, lower mitochondrial respiratory sensitivity to ADP, reduced mitochondrial creatine metabolism, and attenuated complex I activity were reported in LV of 4-week-old D2.*mdx* mice [247]. Some of these metabolic changes [247,276,292] preceded the development of overt cardiac dysfunction, suggesting metabolic stress could be an initial event in the disease.

The relationship of such mitochondrial reprogramming and/or deficiencies to impaired nitric oxide (NO)/cyclic guanosine monophosphate (cGMP) signaling is relatively understudied in DMD, but several reports supporting continued investigation in this area are warranted. NO/cGMP is believed to regulate nuclear gene expression supporting mitochondrial biogenesis [293]. Increased expression of the atrial natriuretic factor (*anf*) gene, an activator of the NO/cGMP signaling pathway and marker of cardiac remodeling, was observed in C57BL/10.*mdx* hearts at 10–12 weeks of age [276]. Increased levels of the alpha unit of soluble guanylate cyclase ($sgc\alpha_1$) gene were observed in hearts of 25-week-old mice, a gene which typically negatively correlates with NO/cGMP [294]. These results suggest that an increase in *anf* expression may compensate for a defective NO/cGMP pathway in young mice, but this adaptive mechanism appears to diminish with age [276,294]. However, despite lower nNOS protein content, a study examining skeletal muscle in C57BL/10.*mdx* reported that nitrate supplementation (an approach used to increase NO) did not rescue mitochondrial oxidative phosphorylation, increased mitochondrial peroxynitrite, and promoted muscle damage [295]. Future research could consider whether nitrate supplementation is not effective in *mdx* mice given NO signaling is highly compartmentalized within cells while supplementation cannot mimic this compartmentalized delivery of NO and activation of specific signaling pathways [296]. Collectively, these data suggest that a defect in the NO/cGMP signaling pathway potentially contributes to the metabolic abnormalities in the

dystrophic heart [81,276] but negative effects of nitrate supplementation in skeletal muscle of *mdx* mice identify an incomplete understanding of this pathway's role in contributing to mitochondrial dysfunction in DMD.

Collectively, the regulation of mitochondrial substrate oxidation is altered in the heart during DMD. However, the degree to which such stress responses contribute to cardiomyopathy or serve as an intentional reprogramming to permit alternative fates of glucose or fatty acid substrates requires considerable attention given the latter possibility has rarely been considered (proposed in [30]).

2.7.4. Reactive Oxygen Species (ROS) and Mitochondrial Hydrogen Peroxide (H_2O_2)

Mitochondria are an important source of ROS emissions that govern oxidative stress cascades and are actively involved in redox signaling pathways which oversee both physiological and pathological processes. The major form of ROS generated within mitochondria is the highly reactive superoxide ($O_2^{\bullet-}$) radical, which is produced by premature electron slip (prior to complex IV; typically at complex I or III) that leads to one-electron reduction of O_2 (the final electron acceptor in the ETC located at complex IV) [297] **(Figure 2-8)**. In healthy mitochondria, $O_2^{\bullet-}$ is rapidly dismutated to H_2O_2 (a reaction catalyzed by manganese superoxide dismutase (MnSOD)), which is then converted to the harmless H_2O molecule by mitochondrial catalase **(Figure 2-8)**. In pathological states, endogenous mitochondrial antioxidant systems that work alongside MnSOD and catalase (such as glutathione peroxidase, peroxiredoxin/thioredoxin, etc.) can be impaired, resulting in elevated reactive oxidant and/or free radical generation and export out of the mitochondria with an attenuated ability of these reactive molecules to be scavenged.

There are several factors that can precipitate mitochondrial $O_2^{\bullet-}$ generation. If mitochondria are not generating ATP and therefore have a high proton motive force, the chance of

premature electron slip is higher because electrons are not being rapidly transferred towards complex IV to produce H_2O and minimal amounts of $O_2^{\bullet-}$ [297]. Likewise, this same fate is possible when the $NADH/NAD^+$ ratio is high in the mitochondrial matrix due to the buildup of electrons within the complexes. Interestingly, if ADP and P_i are absent, ATP synthesis will be blunted, however, reducing equivalents such as NADH and $FADH_2$ can still be oxidized without being coupled to ATP generation, thus leading to a buildup of the proton motive force and a reduction of coenzyme Q due to electron back pressure within the complexes [298,299]. This is another scenario in which premature electron slip can occur, resulting in elevated $O_2^{\bullet-}$ generation. Mitochondria that are actively generating ATP have lower proton motive forces and a lower $NADH/NAD^+$ ratio, thus ensuring electrons flow efficiently through the complexes with a lower risk of premature slip [297].

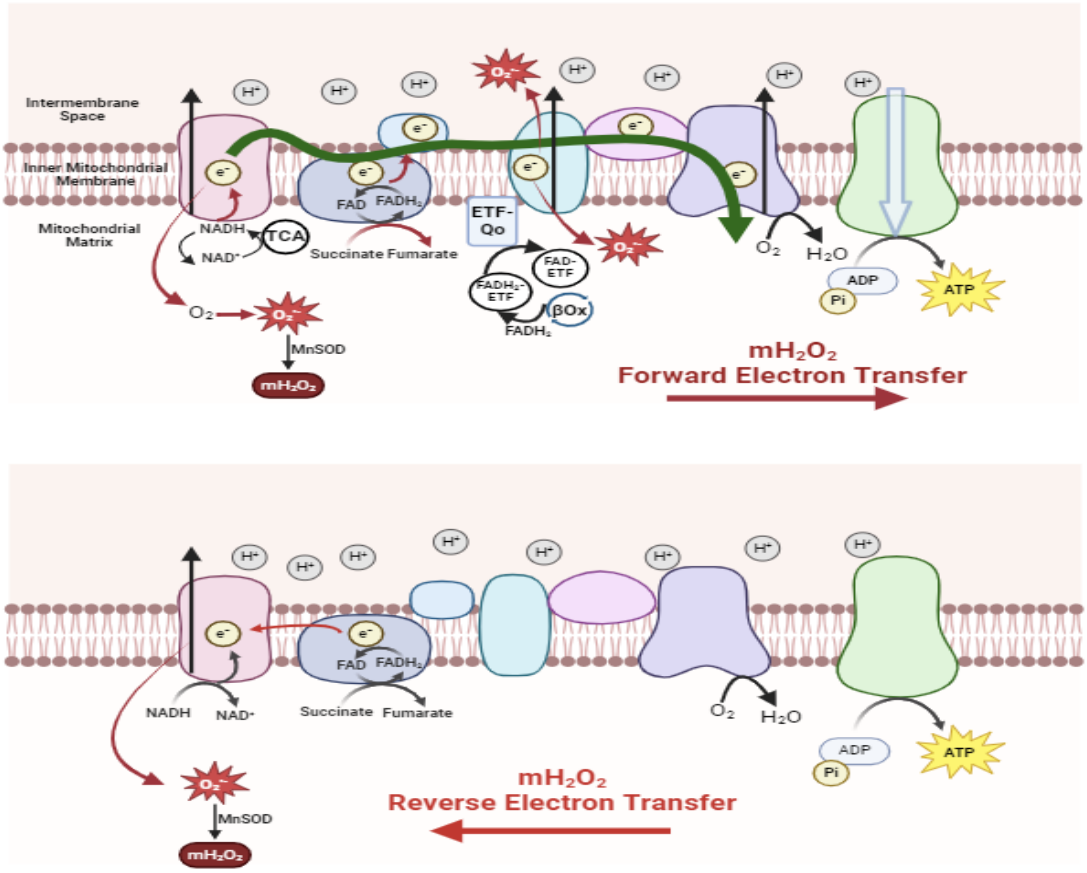

Figure 2-8. Schematic representation of forward and reverse electron transfer-mediated mitochondrial reactive oxygen species (ROS) production within the electron transport chain (ETC). The reducing equivalents NADH and $FADH_2$ supply electrons to complex I and II, respectively, which then transfer electrons sequentially through the remaining complexes and intermediate electron carriers in a series of redox reactions to generate free energy (ATP). Premature electron slip during forward electron transfer (FET) can occur at complex I and III, while complex II is a well-known site of ROS production during reverse electron transfer (RET) – both of which can contribute to oxidative stress if unregulated. The superoxide anion ($O_2^{\bullet-}$) is a highly reactive free radical formed in the mitochondrion that is dismutated to the less reactive, albeit still detrimental H_2O_2 molecule by MnSOD. It should be noted that complex I, II, and III are among 11 distinct sites in the mitochondrion where premature electron slip to oxygen can produce $O_2^{\bullet-}$ and/or H_2O_2 [595]. MnSOD – manganese superoxide dismutase; mH_2O_2 – mitochondrial hydrogen peroxide; $O_2^{\bullet-}$-superoxide anion; NADH – nicotinamide adenine dinucleotide; $FADH_2$ – flavin adenine dinucleotide; H^+ - hydrogen ion; e^- - electron; ATP – adenosine triphosphate; ADP – adenosine diphosphate; Pi – inorganic phosphate; ETF – electron transfer flavoprotein; TCA – tricarboxylic acid; βOX – beta oxidation. Figure created using www.BioRender.com.

2.7.4.1. Mitochondrial ROS in DMD

Many studies measuring ROS in *mdx* models used relatively non-specific fluorophores that do not permit definitive conclusions regarding the precise subcellular origin or type of ROS assessed [30]. In this regard, very few studies have used methodologies that isolated the source of ROS from mitochondria or other sources.

Increased pyruvate-stimulated, complex I-supported mH_2O_2 was observed during attenuated oxidative phosphorylation in permeabilized LV cardiac muscle fibres of dystrophin-deficient mice due to a reduced ability of ADP to suppress mH_2O_2, as normally occurs during oxidative phosphorylation [239]. As creatine normally accelerates mitochondrial ADP/ATP cycling [271], and has been shown to enhance ADP's ability to attenuate mH_2O_2 [300], the additional finding that mitochondrial ADP attenuation of mH_2O_2 was no longer sensitive in D2.*mdx* LV fibres suggests that mtCK may represent a unique mechanism of mitochondrial dysfunction in dystrophin deficient hearts [247]. The precise mechanisms by which this elevation in mH_2O_2/O_2 may contribute to cardiac dysfunction remains unknown, particularly given there were no changes in the glutathione equilibrium [247] or the ability of mitochondria to scavenge H_2O_2 in C57BL/10.*mdx* hearts [82], but such elevations in mH_2O_2/O_2 occurred during a time of apparent cardiac compensations as mice showed slight elevations in ejection fraction albeit before overt cardiac dysfunction [247].

Similar observations were made in isolated mitochondria from mixed hearts (rather than a specific chamber) in the C57BL/10.*mdx* mouse also at 4 weeks of age [228] as well as skeletal muscle of D2.*mdx* mice [54,248,275]. While various antioxidants that do not target mitochondria *per se* have been tested in C57BL/10.*mdx* mice for their potential cardioprotective properties, and have demonstrated discordant results [301], to our knowledge, there are no studies assessing the

effects of mitochondrial-targeted antioxidants on mitochondrial bioenergetics and cardiac function in *mdx* models.

The precise signaling mechanisms downstream of mH_2O_2 that may mediate cardiac dysfunction in dystrophin deficient hearts have not been explored extensively in *mdx* mice or DMD patients. Understanding how mitochondrial-derived ROS contributes to cardiac dysfunction with consideration of ROS-sensitive targets mediating cell membrane injury, metabolic dysfunction, calcium dysregulation, and cardiomyocyte degeneration could guide the development of ROS-specific targeted therapies.

The superoxide-generating enzyme Nicotinamide Adenine Dinucleotide Phosphate (NADPH) is a major source of non-mitochondrial ROS in skeletal and cardiac muscle [302,303], especially during mechanical stress and at early stages of disease progression [83,227]. NOX2-mediated ROS generation is significantly increased in C57BL/10.*mdx* hearts [28,302–304] **(Figure 2-6)**, which has been attributed to altered microtubule association with NOX2 [304,305]. Inhibiting NOX2-derived ROS [306,307] or using the non-specific ROS scavenger N-acetylcysteine (NAC) [28,302] restored calcium homeostasis in dystrophin-deficient muscle. NOX2 inhibition with the drug apocynin improved single sarcomeric shortening in isolated cardiomyocytes [303] while NAC improved fractional shortening [28]. However, the therapeutic potential of NAC is uncertain given it also reduces muscle weights in C57BL/10.*mdx* mice [308] although the degree to which this occurred because of attenuated superoxide is not clear.

2.7.5. Altered Mitochondrial Autophagy (Mitophagy)

In healthy tissue, defective mitochondria can be removed through mitochondrial autophagy, also known as mitophagy, in a process intended to uphold quality control of the healthy mitochondrial pool. This process mitigates damage that may be caused by dysfunctional

mitochondria [309] to maintain energy metabolism stability [310,311]. Mitophagy is regulated by PTEN-induced kinase 1 (PINK1) and Parkinson juvenile disease protein 2, (PARKIN) (reviewed in [275]). In a damaged mitochondrion, PINK1 is not degraded and is able to phosphorylate mitofusin 2 (Mfn2), which subsequently signals PARKIN to tag the mitochondria for degradation [309,312].

2.7.5.1. Mitophagy in DMD

Important mitophagy-related genes, including *PINK1*, *PARK2*, and *BNIP3* were decreased in DMD patients (dystrophic quadriceps) and dystrophin-deficient rodent models (12-month-old C57BL/10.*mdx* mice) [312,313]. One study showed a relationship between increased mitophagy and improved diaphragm force and histopathology, as well as reduced mPT, when activating AMPK with AICAR [314], but further research is required to develop mitophagy-specific therapeutics given AMPK regulates other processes that could contribute to the improved phenotype. Collectively, further research is required to elucidate if PINK/PARKIN pathways represent potential therapeutic targets in the dystrophic heart.

Given that loss of PINK1 increases the vulnerability of the heart to IR-injury, it appears to possess some cardioprotective properties [312]. Other common markers of mitophagy include light chain 3 (LC3) which is involved in the formation of mature autophagosomes, as well as the PINK1-PARKIN-adaptor protein sequestosome 1 (SQSTM1, p62), both of which are elevated in the hearts of 22-week-old C57BL/10.*mdx*, however, further data is required to elucidate chamber-specific and time-course progression of this elevated mitophagic response [315]. This study revealed that the co-localization of LC3 dots with fragmented mitochondria was significantly increased in hearts of 22-week-old C57BL/10.*mdx* mice compared to healthy controls, indicating that the elimination of damaged mitochondria via mitophagy was impaired and subsequent accumulation of damaged

mitochondria persisted. Other studies in skeletal muscle from C57BL/10.*mdx* mice and DMD patients demonstrated significantly reduced levels of autophagy [316], suggesting that the suppression of autophagy may be muscle-type dependent. Further, mitophagy is a dynamic process and therefore, changes to protein content and gene expression of common mitophagic markers may not always be proportional to mitophagic activity and/or flux. It is essential to understand phenotype severity, muscle-type, and age when considering mitophagy as a therapeutic target. Most of the research to date investigating the role of mitophagy in dystrophin deficient models has been conducted in skeletal muscle, thus, advancements in cardiac muscle remain to be addressed.

2.7.6. Altered Mitochondrial Content and Structure in DMD

iPSC-cardiomyocytes from DMD patients possess increased mitochondria with abnormal morphologies [268]. Degeneration of mitochondrial structure (swelling and loss of cristae) has been identified in dystrophic cardiomyocytes from hearts of 1-month-old and 3–4-month-old *mdx* mice prior to disease onset [227]. Furthermore, a significant increase in structurally abnormal mitochondria were observed in hearts of 12-month and older C57BL/10.*mdx* mice after developing DCM [312] which has also been reported as early as 4 weeks of age in this model [228]. Various mitochondrial proteins contents have been assessed in *mdx* mouse models with divergent responses observed depending on the pathway, age and model suggesting that altered control of oxidative phosphorylation could occur through post-translational modifications that have yet to be fully identified, and that compensations in the content of certain pathways may occurs [30,82,247].

2.8. Mitochondria as a Potential Therapeutic Target for DMD-induced Cardiomyopathy

2.8.1. Mitochondrial Calcium Overload

Given mitochondrial dysfunctions are thought to arise, in part, by elevated calcium uptake, preventing mitochondrial dysfunction could be achieved by improving cytoplasmic handling itself. For example, due to the hypersensitivity to excitation-contraction coupling in cardiomyopathy of DMD patients, targeting RyR2 may offer therapeutic benefit. PKA phosphorylation of RyR2 appears to contribute to increased calcium release from the SR, and therefore, PKA could be a potential therapeutic target. In dystrophic mice, inhibition of PKA-mediated phosphorylation of RyR2 reduced SR calcium leak and in turn prevented cardiomyopathy [317]. Oxidative stress can lead to the nitrosylation of RyR2 and subsequent disassociation of calstabin2 from RyR2, increasing SR calcium leak [218]. Treatment of C57BL/10.*mdx* mice with either NAC to inhibit RyR2 nitrosylation, or the RyR2 stabilizer Rycal, prevented depletion of calstabin2 and subsequent SR calcium leak, aberrant depolarization in cardiomyocytes, and arrhythmias [218].

The stretch-sensitive channel TRPV2 is another calcium channel target to consider, as increased TRPV2 has been documented in the cytoplasmic membrane of *mdx* cardiac and skeletal cells and the sarcolemmal membrane of DMD patients [318]. Treatment of DMD patients with the antiallergy drug Tranilast, which has anti-TRPV2 activity, resulted in reduction of heart failure biomarkers [319].

Enhancing SR calcium uptake through overexpression of SERCA or targeting its inhibitors can be considered in restoring calcium homeostasis. In C57BL/10.*mdx* mice 12 months of age, administration of AVV9-SERCA2a gene therapy significantly improved cardiac electrophysiology [320], whereas in 3-month-old *mdx* mice a similar therapy ameliorated DCM for at least 18 months [321]. Decreasing sarcolipin expression in *mdx* mice restored cardiac SERCA function and calcium cycling, thus preventing cardiomyopathy. Decreased LV internal diameter in diastole as well as

decreased fibrotic and necrotic tissue likely contributed to the improved cardiac function [221]. While targeting sarcolipin may be a promising approach, cardiac function worsened in phospholamban (PLN) knockout C57BL/10.*mdx* mice [322]. As described previously, frequent PT activity may contribute to calcium-dependent mitochondrial dysfunction and therefore, prevention of this opening could be beneficial. As discussed previously, inhibition of a key regulator of mPTP, cyclophilin, may impede opening of the pore and subsequent mitochondrial dysfunction [250,252].

2.8.2. Targeting Cellular/Mitochondrial Antioxidant Systems

Since cardiac mH_2O_2 is elevated early in DMD [228,247], mitochondrial-targeted antioxidant therapies could provide therapeutic benefit in DMD patients. Several general antioxidants, including MitoQ and SkQ1, are conjugated with the lipophilic cation triphenylphosphonin (TTP) to target the mitochondria [323]. The small 'SS' peptides are cell permeable agents that bind to cardiolipin on the IMM and can preserve oxidative phosphorylation, attenuate mH_2O_2, and prevent oxidative damage [324–326]. Furthermore, SS peptides can inhibit the dissociation of cytochrome *c* from cardiolipin, hindering the activation of cell death pathways [327]. To our knowledge, no publication has investigated the effects of any mitochondrial-ROS lowering compound in models of DMD.

2.8.3. Cardiolipin and Membrane Stability

Cardiolipin, a phospholipid enriched with unsaturated fatty acids located in the IMM, is essential to maintain mitochondrial structure and function. Through its binding to key modulators of energy exchange and subsequent proteolipid complex formation, cardiolipin plays a key role in mitochondrial bioenergetics [271]. This complex can regulate energy exchange, reduce mitochondrial ROS generation, and prevent opening of mPTP [271]. In the presence of oxidative stress, cardiolipin and the key regulator mtCK, lose their binding capacity, leading to dissociation

of the proteolipid complex [328,329]. Since mH_2O_2 generation is elevated in dystrophin deficient heart [228,247], a cardiolipin targeting agent, such as elamipretide, may be appropriate for targeting impaired mitochondrial bioenergetics. Although data on cardiolipin physiology in *mdx* is limited, the altered mitochondrial cristae structure mentioned above serves as a foundation for continuing the investigation on cardiolipin in various dystrophic models.

Albeit not published in a dystrophin-deficient model, SS-31, or elamipretide, is an agent that has demonstrated improvements to mitochondrial functions including reduction of mitochondrial ROS across several pathologies [330–332]. Elamipretide has also shown evidence of direct cardioprotective mechanisms, including the amelioration of apoptosis and fibrosis in preclinical models of heart failure [333,334].

Idebenone, a synthetic analogue of Coenzyme Q_{10} with electron-shuttling activity, can alter respiratory chain activity [335,336], although this may require very high micromolar doses [337,338]. Long-term idebenone therapy improved cardiac diastolic dysfunction, reduced cardiac inflammation and fibrosis, improved running performance, and limited mortality from cardiac pump failure induced by dobutamine stress testing in vivo in *mdx* mice [339]. Early clinical trials in patients with DMD revealed improved cardiac and respiratory function with idebenone treatment [340–342]. Specifically, a trend for increased peak systolic radial strain in the LV was seen in these patients [340]. However, no measures of mitochondrial bioenergetics were performed to verify that the drug was acting through a mitochondrial mechanism. As reviewed elsewhere, idebenone has a variety of effects on other organelles, which may not involve the antioxidant properties of the compound [343]. This suggests that the beneficial effects in some studies may not be due to alterations in mitochondrial functions despite claims to this effect. These factors might be consistent with a subsequent clinical trial in people with DMD that was unsuccessful

(NCT02814019). As such, no study to date has definitively tested the potential of mitochondrial-targeted therapies on cardiac dysfunction in pre-clinical models of dystrophin deficiency or in clinical studies.

Lastly, the potential for mitochondrial therapies to be combined with the current standard of care (glucocorticoids) or emerging gene-based and vector-mediated therapies requires extensive research to determine the potential for combinatorial treatments.

2.9. Adiponectin Receptor Agonists as an Alternative Therapeutic Option

2.9.1. Cellular and Structural Properties of Adiponectin and Relevance to DMD

Adiponectin (ApN) and its receptors (which exist as structurally related AdipoR1 and AdipoR2 isoforms) have been implicated in a myriad of functions, ranging from regulating cellular metabolism to anti-inflammatory effects in both skeletal muscle and cardiac tissue [344–346]. In addition to AdipoR1 and AdipoR2, T-cadherin (T-Cad) is another cell surface molecule that has a significant affinity for high molecular weight oligomers of ApN [347]. Although T-Cad can bind to ApN, its lack of intracellular signaling domain impedes its consideration as an ApN signaling receptor [347].

ApN is a 30-kDa multimeric protein, abundantly secreted by mature adipocytes within white adipose tissue (WAT), that consists of a globular C-terminal domain and a collagen-like N-terminal domain [347–349]. Although the collagenous domain allows ApN to be secreted into the bloodstream as three oligomeric complexes, including a low molecular weight (LMW) trimer form (67 kDa), middle molecular weight (MMW) hexamer form (140 kDa), and high molecular weight (HMW) (300 kDa) form [350], the HMW oligomer in particular elicits insulin-sensitizing and cardioprotective properties [351]. While the trimer is formed by hydrophobic interactions in its globular heads and is stabilized by non-covalent interactions of the collagen-like domains, the

hexamer and HMW forms of ApN require intermolecular disulfide bond formation between highly conserved cysteine residues [351,352]. This is particularly important because several post-translational modifications, including hydroxylation and glycosylation on conserved lysine residues, are vital for the assembly and secretion of HMW ApN [351].

While ApN is produced by WAT in its full-length (fAd) form, fAd can be proteolytically/enzymatically cleaved to the smaller globular (gAd) form by neutrophil elastase produced from monocytes or macrophages [353,354]. In addition to secretion by WAT, ApN can also be secreted by human and murine liver parenchymal cells [355], skeletal muscle myocytes [356], cardiac epithelial cells [357], endothelial cells [358], osteoblasts [348,359], and kidney tubular cells [360]. ApN can represent between 0.01 and 0.05% of total plasma protein (~2–20 μg/mL range) in humans, thus attesting to its abundance in circulation [347,361–363]. Despite being a stable protein in plasma, ApN has a relatively short half-life in circulation of only ~45–75 min in humans and is cleared primarily by the liver [364].

ApN is an attractive therapeutic candidate for a host of pathologies [365], given that its circulating levels have been negatively correlated with cardiovascular disease (CVD), cancer, and metabolic syndrome, while high circulating concentrations have been correlated with healthy physiological systems.

Although the mechanisms by which ApN contributes to improvements in cardiac pathology are multifactorial and generally implicate AMPK and cyclooxygenase-2 (COX2) signaling [366], limited data are available on the intersection between ApN, cardiac function, and DMD. This gap in knowledge represents an avenue for future research, where additional work is encouraged to explore the role of ApN on cardiac electrophysiology, alterations to echocardiographic parameters,

fibrosis, Ca^{2+} transients, and inflammation as common diagnostic indicators of DMD-induced cardiac remodeling.

ApN has long been recognized for its propensity to shift macrophage polarization toward an M2 anti-inflammatory phenotype, at least in murine peritoneal cavity and adipose tissue [367]. Of note, ApN induces the production of the anti-inflammatory cytokine IL-10 while also suppressing the growth and proliferation of bone marrow-derived macrophage progenitors in human leukocytes [347,368,369]. While macrophages from ApN-null mice demonstrate an M1 pro-inflammatory phenotype by releasing higher levels of tumor necrosis factor (TNF-α), monocyte chemoattractant protein (MCP-1), and IL-6 compared to WT mice, the elevations to these cytokines is reversed by exogenous recombinant ApN administration [367]. Accordingly, while ApN is able to suppress differentiation and classical activation of M1-like pro-inflammatory macrophages, it is also able to promote M2-like 'alternatively-activated' anti-inflammatory macrophage proliferation and expression of cytokines like IL-10, and the M2 macrophage markers Arg-1and Mgl-1 [367,368,370–372] **(Figure 2-9)**. To date, little is known about the role of ApN in regulating T cell and neutrophil function. Although previous studies have demonstrated that AdipoR1 receptors are expressed in murine Tregs [373], the mechanism through which this relationship confers anti-inflammatory effects requires further insight.

2.9.2. Synthetic Adiponectin Receptor Agonists

The discovery and design of AdipoR agonists that activate downstream signaling cascades have attracted great effort, given that it is difficult and expensive to produce biologically active recombinant ApN with an optimized dosage and route of administration for pre-clinical or clinical use [365] due to its large multimeric size and requirement for extensive post-translational

modifications [374]. Several molecules that activate AdipoR have been developed and explored in a variety of conditions including pre-clinical models of DMD.

2.9.2.1. AdipoRon

AdipoRon is a synthetic small-peptide AdipoR agonist that acts via both AdipoR1 and AdipoR2 to exert ApN-like effects [375,376]. It is the most studied AdipoR agonist available. Given that AdipoRon was the first orally active endogenous AdipoR agonist, many studies have been conducted to test its efficacy across different pathologies. Rodent models utilizing AdipoRon have determined that it has the ability to ameliorate insulin resistance, diabetes, and inflammation, in addition to its antiproliferative properties in various cancer models [376,377]. Subsequent studies demonstrated limited potency and specificity, which prompted the development of other AdipoR agonists [375,376].

2.9.2.2. ALY688

The 10 amino acid-long peptidomimetic ADP355 was developed following the identification of the critical receptor binding domain of ApN. This compound demonstrated high specificity for both receptor isoforms, was modified to be more resistant to proteolytic degradation, and demonstrated greater potency than ApN [374,378,379]. Now called ALY688, this small peptide was shown to lower inflammation in inflammatory disorders such as dry eye disease and reduce fibrosis in the liver [380–382]. Recent work using ALY688 has demonstrated its efficacy at increasing basal glucose uptake and enhancing insulin-stimulated glucose uptake in skeletal muscle cells while also improving glucose handling when administered to mice on a high-fat, high-sucrose diet [382]. Additionally, the same group also determined that daily subcutaneous ALY688 administration to 10–12-week-old C57BL/6 mice subjected to pressure overload attenuated

cardiac hypertrophy, cardiac remodeling, fibrosis, and several cytokines consistent with inflammation, including IL-6, TLR-4, and IL-1β [383].

2.9.3. Pre-Clinical Development of Adiponectin-Receptor Agonists for DMD

Boys with DMD have lower serum ApN concentrations [384], as do male *mdx* mice [385]. As such, several investigations have explored the potential of AdipoR signaling to prevent inflammation, metabolic dysfunction, and fibrosis in pre-clinical models of DMD.

Using C57BL/10.*mdx* mice, overexpression of ApN improved whole-body measures of muscle function, including grip strength, wire test, and treadmill activity, while reducing muscle damage and markers of inflammation [386]. AdipoRon treatment in this same model of DMD reduced inflammatory markers and muscle damage in skeletal muscle, stimulated markers of regeneration, lowered general marks of oxidative stress, and improved similar whole-body tests of muscle function [387]. This foundational work provides novel evidence to suggest that ApN signaling can beneficially influence whole-body indices of dystrophin deficiency-induced damage. Specifically, the work demonstrates a relationship between both genetically and pharmacologically elevated ApN in C57BL/10.*mdx* mice and attenuations of the dystrophic phenotype. These findings are important because they position ApN as a prospective therapeutic target and potential biomarker to aid in addressing DMD-induced cardiac remodeling **(Figure 2-9)**.

Two recent studies explored the potential for ALY688 to modify the disease process in mouse models of DMD. In one study, daily subcutaneous administration of ALY688 for 2 months beginning at 4 weeks of age in C57BL/10.*mdx* mice improved treadmill activity, wire test, and grip strength while lowering tibialis anterior necrosis and fibrosis [344]. Reductions in IL-1β and TNFα, the M1-type macrophage marker $CD68^{+}$, as well as the lipid peroxidation product 4-HNE (4-Hydroxynonenal) were reduced in the limb muscle gastrocnemius. ALY688 treatment increased

the expression of muscle differentiation and maturation factors and enhanced the myogenic program, leading to partial increases in revertant dystrophin-expressing fibers in the quadriceps. mRNA levels of *Mrf4*, a marker of late muscle differentiation, was halved in C57BL/10.*mdx* mice and partially restored with ALY688 as were other regeneration markers **(Figure 2-9)**. ALY688 also lowered fibrosis in quadriceps and the fibrotic regulators TGFβ and p-SMAD2 while activating adenosine monophosphate kinase (AMPK), which has been shown to mediate AdipoR-mediated reductions in inflammation and fibrosis and stimulate both glucose and fatty acid oxidation [388–390] **(Figure 2-9)**. Incubation of myotubes derived from DMD patients with ALY688 lowered IL-1β and TNFα and increased the expression of utrophin, a dystrophin homolog—the latter also being increased in the treated C57BL/10.*mdx* tibialis anterior muscle. As discussed by the authors [344], the collective results suggest a possible role for ALY688 in lowering inflammation and fibrosis through AMPK activation, given that this mechanism was previously demonstrated in C57BL/10.*mdx* mice [391].

In a second study, ALY688 was injected daily into D2.*mdx* mice—a more severe model of DMD than the C57BL10.*mdx* model—beginning at day 7 of age up to day 28 of age in order to determine the early effects of AdipoR agonism on muscle remodeling [392]. In the diaphragm, treatment reduced fibrosis in relation to lower IL-6 mRNA but increased IL-6 and TGFβ protein contents. ALY688 lowered mitochondrial complex I-stimulated H_2O_2 (a form of reactive oxygen species; ROS) without restoring pyruvate oxidation (a marker of glucose oxidation) that was shown to be lower in untreated D2.*mdx* mice assessed with high-resolution respirometry *in vitro*. Treatment lowered diaphragm force production assessed *in vitro* while quadriceps were not affected and remained lower compared to WT mice. Serum CK—a marker of sarcolemmal damage—was decreased by high doses of ALY688 and increased with low doses, while grip

strength, cage hang time, and voluntary wheel running were unaffected by treatment. No changes in AMPK phosphorylation were observed but it was noted that future studies could consider whether the signaling effects are rapid and transient and would be captured by assessing tissues shortly after the last drug injection. The early prevention of diaphragm fibrosis and markers of muscle damage at high doses of treatment in these 4-week-old mice suggests future studies could examine longer-term treatment into adulthood when complex muscle development during adolescence is complete.

A separate study (using a parallel study design) assessed the effects of daily ALY688 treatment on indices of recognition memory in D2.*mdx* mice [393]. Interestingly, ALY688 prevented impairments in recognition memory in D2.*mdx* mice, indicated by a lower discrimination index in the novel objection recognition test. Furthermore, decreased hippocampal mitochondrial pyruvate-supported respiration was also prevented by ALY688. Lastly, ALY688 completely prevented increases in protein contents of the neurofibrillary tangles marker total Tau, as well as protein contents of the upstream marker of tangles and autophagy, total Raptor. Together, the results indicate that ApN agonism improves recognition memory in D2.*mdx* mice through mechanisms that are not yet fully elucidated.

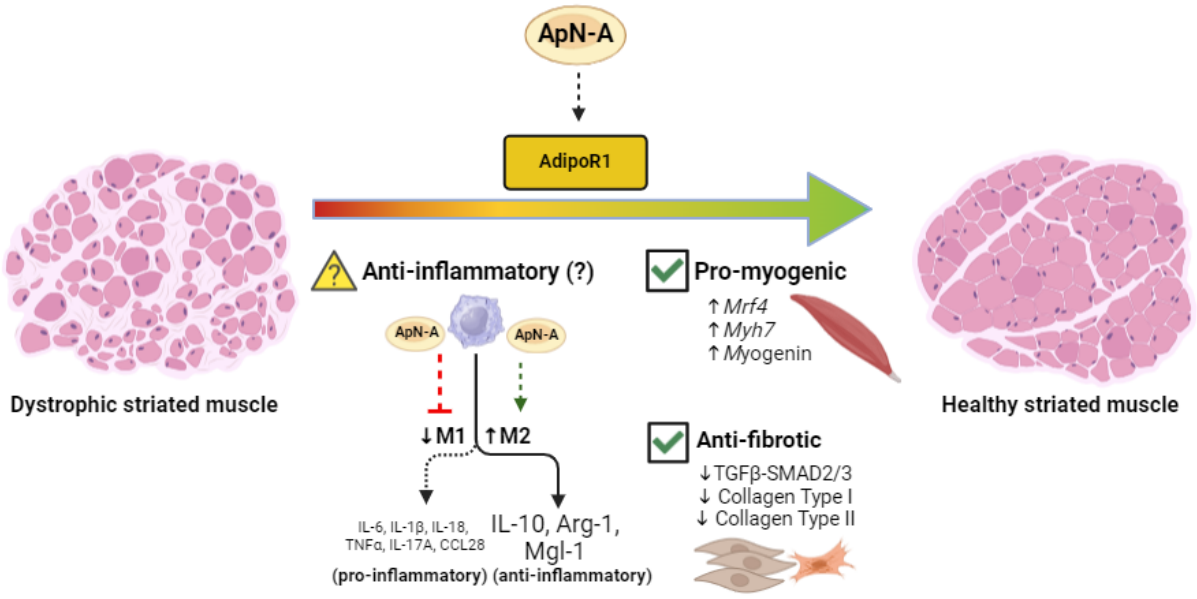

Figure 2-9. Mechanisms linking adiponectin receptor agonism to improved myogenic and fibrotic profile of striated muscle from dystrophin deficient mice. Dystrophic mice exhibit low circulating adiponectin levels [386], therefore, improving these levels with exogenous adiponectin receptor agonism may improve the myogenic profile of skeletal muscle by upregulating *Mrf4*, *Myh7*, and *Myogenin* while simultaneously attenuating fibrosis by downregulating TGFβ-SMAD2/3, Collagen Type I, and Collagen Type II [344]. Check mark denotes data previously published in *mdx*. Moreover, adiponectin agonists may also shift the pro-inflammatory macrophage polarization in dystrophic skeletal muscle [388] towards the anti-inflammatory polarization, characterized by elevations in IL-10, Arg-1, and Mgl-1, although this has yet to be proven in *mdx* mice (denoted by question mark) [367,368,371,372]. ApN-A – Adiponectin agonist. Figure has been published in *Biomedicines*. Figure created using www.BioRender.com.

Collectively, ALY688 demonstrates contrasting effects on inflammatory cascades that may be dependent on the age of assessments, the mouse model employed, the duration of treatment, or the muscles selected for analyses. While no studies of ApN/AdipoR agonists have been performed in humans, some work has assessed the effects of ApN on human DMD-derived myotubes separate from the lower IL-1β and TNFα responses to ALY688 treatments discussed above [344]. Specifically, ApN incubations reduced several pro-inflammatory cytokines, including TNFα, IL-17A, and CCL28 [388], while also decreasing the NLRP3 inflammasome [394]. ApN treatment in human DMD-derived myotubes increases IL-6 [388], similar to the findings of ALY688 treatment

in young D2.*mdx* mice discussed above [392], but in contrast to the effects seen with longer treatments and later ages in C57BL10.*mdx* mice [344]. The repression of NLRP3 is notable given that *mdx*/NLRP3-KO cross-bred mice reverse the increases in caspase-1 activity and contents of the pro-inflammatory cytokines IL-1β, IL-18, and TNFα seen in C57BL/10.*mdx* controls [394]. It should be noted that the effects of adiponectin receptor agonism on the dystrophic heart in *mdx* has never been explored.

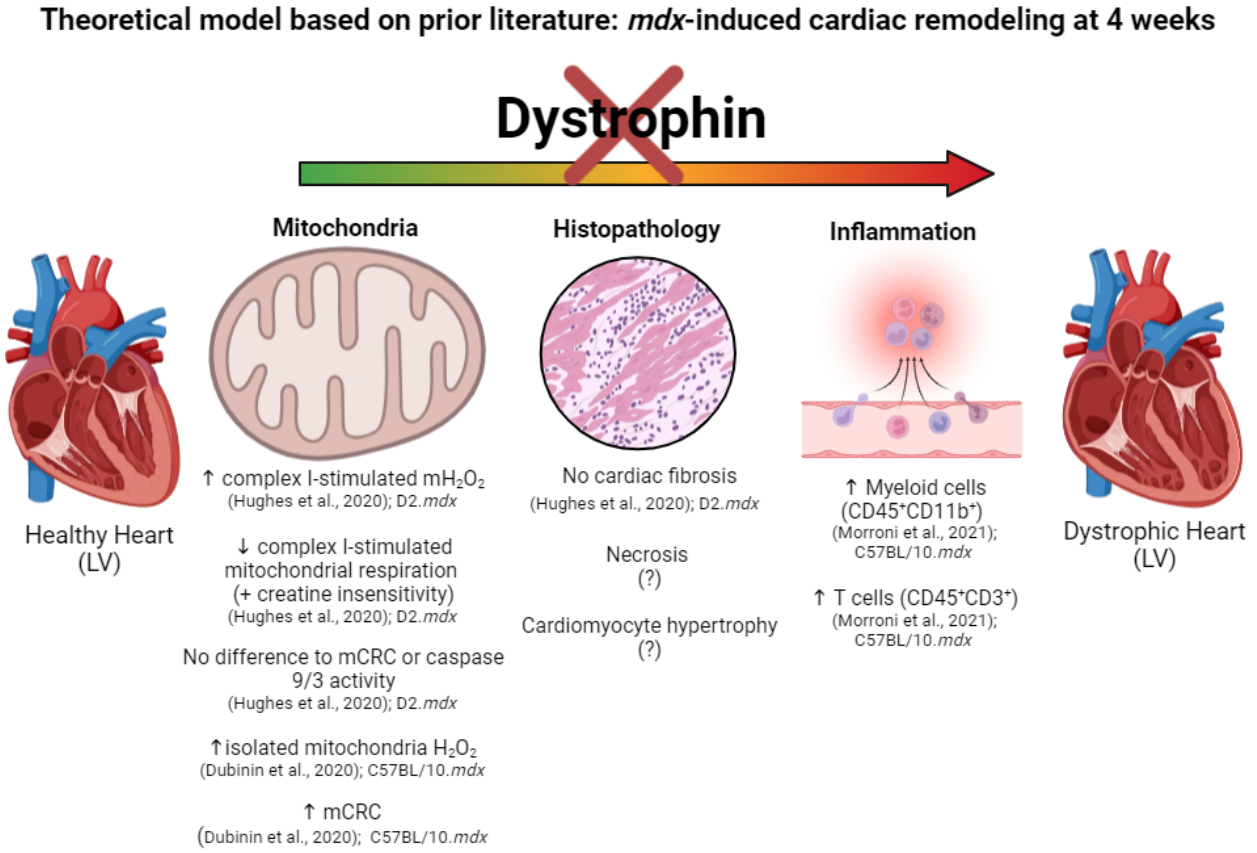

Figure 2-10. Theoretical model outlining the current known mitochondrial, histopathological, and inflammatory profile of the dystrophin deficient LV in mdx mice aged 4-weeks. While previous research has elucidated several noteworthy molecular signatures underpinning the dystrophin deficient LV of young *mdx* mice, comprehensive chamber-specific data is sparse and reflects a significant gap in knowledge for clinical therapy development. As demonstrated in the schematic above, atrial and right ventricular data is notably limited at 4-weeks and may lend insight towards the complex and atypical progression of cardiomyopathy in DMD. Figure created using www.BioRender.com.

3 OBJECTIVES AND HYPOTHESES

3.1. Overview of Thesis

While there are several unique 'stress paradigms' in which cardiac mitochondria and inflammation have demonstrated involvement, the nature of why mitochondrial reprogramming and inflammation occurs across these diverse conditions with unrelated underlying etiology remains unclear. In this regard, the focus of this thesis is to examine myofiber mitochondrial stress response relationships to systemic and tissue-specific inflammation in two distinct models of cardiac remodeling, including in dystrophin deficient mice (Duchenne muscular dystrophy; DMD) and elective coronary artery bypass graft (CABG) surgery in humans. The first part of this thesis will focus on DMD, while the second part will focus on on-pump CABG in humans.

There are two underlying goals of Study 1 (*Chapter 4)* (DMD):

1) to comprehensively explore the contributions of mitochondrial stress response pathways and shifts in inflammatory macrophage sub-populations to chamber-specific dystrophin deficiency-induced histopathological cardiac remodeling in a young mouse model of DMD (D2.*mdx* mice).

2) to determine if daily administration of a novel adiponectin receptor agonist in D2.*mdx* mice influences indices of chamber-specific histopathological cardiac remodeling through mitochondrial or inflammation-mediated mechanisms.

3.2. Objectives and Hypotheses for Study 1 (Chapter 4) (DMD)

The current standards of care for DMD - glucocorticoid administration and gene-editing therapies - provide promise for patients, however, they can often be overshadowed by unwanted side effects and lack of applicability to the full spectrum of mutations that cause this debilitating disease. Moreover, the effects of these therapies on the dystrophic heart have yielded variable results. Cardiomyopathy - which is the leading cause of premature death among DMD patients -

remains relatively understudied compared to the skeletal (locomotor and respiratory) impairments that impact this patient population. While it has been established previously in our lab that mitochondrial stress responses - including impairments to bioenergetics - precede overt dystrophin deficiency-induced left ventricular dysfunction and histopathological remodeling in young D2.*mdx* mice, the current literature on the remaining chambers of the heart is scarce. Furthermore, all four chambers of 4-week-old D2.*mdx* mice have never been comparatively and comprehensively characterized using a combination of methods that assess histopathology, inflammation, and mitochondrial stress responses. Therefore, the primary objective of this chapter was to understand how the dystrophic hearts of young D2.*mdx* mice, beyond just the LV, are impacted by dystrophin deficiency. The secondary objective of this chapter was to implement a therapeutic intervention – specifically daily subcutaneous administration of a novel anti-inflammatory adiponectin receptor agonist – to determine if this compound represents a viable alternative treatment option for addressing secondary contributors to dystrophin deficiency-induced cardiac remodeling across chambers of the heart.

Hypotheses for Study 1 (*Chapter 4*)

1) 4-week-old D2.*mdx* mice will demonstrate robust, chamber-specific heterogeneity in histopathological cardiac remodeling signatures compared to healthy WT mice
2) Chamber-specific histopathological remodeling will correspond with elevated pro-inflammatory macrophage sub-populations and indices of aberrant mitochondrial stress
3) Daily administration of an adiponectin receptor agonist will improve the histopathological phenotype of affected chambers in D2.*mdx* mice via anti-inflammatory and anti-apoptotic mechanisms, while also improving indices of mitochondrial stress

4 The novel adiponectin receptor agonist ALY688 completely prevents a unique right ventricular fibrosis in the dystrophic heart through anti-inflammatory and metabolic-enhancing effects

This chapter is currently in preparation for submission to an academic journal.

Authors Contributions: All four phases of this study were principally carried out by Shivam Gandhi from July 2020 to May 2024. Shivam Gandhi: conceptualization, methodology, validation, formal analysis, investigation, writing - original draft, writing – review & editing, visualization, project administration; Luca J. Delfinis: investigation and writing – review & editing; Parashar D. Bhatt: formal analysis, methodology (spectral flow cytometry), investigation, and writing – review & editing; Madison C. Garibotti: methodology and writing – review & editing; Catherine A. Bellissimo: conceptualization, methodology, validation, and investigation; Amireza N. Goli: methodology (immunofluorescence); Brooke A. Morris: methodology; Aditya N. Brahmbhatt: methodology; Laura N. Castellani: methodology and validation; Simona Yakobov-Shimonov: methodology; Brittany A. Edgett: methodology; Fasih A. Rahman: methodology (caspase activity assay); Joe Quadrilatero: methodology; Jeremy A. Simpson: methodology, validation, formal analysis, and writing – review & editing; Gary Sweeney: methodology, validation, formal analysis, and writing – review & editing; Ali-Abdul Sater: methodology, validation, formal analysis, and writing – review & editing; Peter H. Backx: methodology, validation, formal analysis, and writing – review & editing; Henry H. Hsu: conceptualization and visualization; Christopher G.R. Perry: conceptualization, methodology, validation, formal analysis, investigation, writing -original draft, writing – review & editing, visualization, project administration. All persons designated as authors qualify for authorship, and all those who qualify for authorship are listed.

The novel adiponectin receptor agonist ALY688 completely prevents a unique right ventricular fibrosis in the dystrophic heart through anti-inflammatory and metabolic-enhancing effects

Authors: Shivam Gandhi[1], Luca J. Delfinis[1], Parashar D. Bhatt[2], Madison C. Garibotti[1], Catherine A. Bellissimo[1], Amireza N. Goli[1], Brooke A. Morris[1], Aditya N. Brahmbhatt[1], Laura N. Castellani[1], Simona Yakobov-Shimonov[2], Brittany A. Edgett[3], Fasih A. Rahman[4], Joe Quadrilatero[4], Jeremy A. Simpson[5], Gary Sweeney[2], Ali-Abdul Sater[2], Peter H. Backx[2], Henry H. Hsu[6], and Christopher G.R. Perry[1]†.

Affiliations:

[1]School of Kinesiology & Health Science, Muscle Health Research Centre, York University, Toronto, ON, Canada

[2]Department of Biology and Muscle Health Research Centre, York University, Toronto, ON, Canada

[3]Faculty of Kinesiology, University of Calgary, Calgary, AB, Canada

[4]Department of Kinesiology & Health Sciences, University of Waterloo, Waterloo, ON, Canada

[5]Department of Human Health and Nutritional Sciences, University of Guelph, Guelph, ON, Canada

[6]Allysta Pharmaceuticals Inc., Bellevue, Washington, United States

Email Addresses: shivamg@yorku.ca, delfinis@yorku.ca, bhattparashar@hotmail.com, mgarib@yorku.ca, catherine.bellissimo@uhn.ca, amireza@qmed.ca, brookeam@yorku.ca, anbrahm4@yorku.ca, laura.castellani03@gmail.com, simonayakobov@gmail.com, brittany.edgett@ucalgary.ca, fasih.rahman@uwaterloo.ca, jquadrilatero@uwaterloo.ca, jeremys@uoguelph.ca, gsweeney@yorku.ca, aasater@yorku.ca, pbackx@yorku.ca, hhsu@allysta.com, cperry@yorku.ca

Key words: Duchenne muscular dystrophy, cardiac, fibrosis, adiponectin, mitochondria

†Address for Correspondence:

Christopher Perry, PhD

School of Kinesiology and Health Science Muscle Health Research Centre

344 Norman Bethune College

York University

4700 Keele Street

Toronto, Ontario M3J 1P3

(P) 416 736 2100 ext. 33232

cperry@yorku.ca

Conflict of Interest: The authors have declared that no conflict of interest exists.

Highlights

1. D2.*mdx* exhibit chamber-specific heterogeneity in cardiac fibrosis and hypertrophy

2. RV fibrosis and cardiomyocyte hypertrophy are prevented by an adiponectin-receptor agonist

3. Shifts in macrophage polarization underpin improvements to cardiac fibrosis

4. Some mitochondrial stress responses are restored with improvements to fibrosis

Abstract

Cardiac fibrosis during Duchenne muscular dystrophy arises from cycles of cellular damage and inflammation and is often associated with cardiomyocyte hypertrophy and mitochondrial stress. Glucocorticoids may slow this pathology, but their numerous side effects underscores an unmet need for new therapies. Here, we explored the potential of a novel adiponectin receptor agonist, ALY688, with anti-inflammatory and mitochondrial enhancing properties to prevent cardiac fibrosis, tissue disorganization, fibre size, inflammation, and mitochondrial stress in both right and left sides of the heart during early disease stages of the D2.*mdx* mouse. To overcome considerable limitations in heart sizes, we pooled cardiac chambers by quadrupling the typical breeding strategy and discovered that 4-week-old D2.*mdx* mice are defined by a unique right ventricular and left atrial cardiac fibrosis that is absent in the right atrium and left ventricle. Moreover, cardiomyocyte hypertrophy was seen in both the right and left ventricle. Short-term daily treatment of ALY688 from 7-28 days-of-age completely prevented fibrosis in the right ventricle and left atrium and prevented right ventricular hypertrophy. Tissue disorganization assessed with H&E stains was present in all chambers except the right atrium which was not prevented by ALY688. Using a sophisticated and robust strategy for isolating macrophage sub-populations, we identified an increase in a specific right ventricular infiltrating pro-inflammatory macrophage sub-population, $CD11b^{+}CD45^{+}CD64^{+}F4/80^{+}CCR2^{+}$, that was prevented by ALY688 consistent with its anti-fibrotic effects in this chamber. The diseased right ventricle also demonstrated reduced mitochondrial oxidation of carbohydrate, fatty acid, and other substrates and mitochondrial-linked apoptotic caspase-3 signaling that were all prevented by ALY688. These discoveries reveal a unique right ventricular fibrosis linked to distinct inflammatory and metabolic signatures in young dystrophin-deficient mice. The tissue preservation effects of

ALY688 that are mediated by attenuated infiltrating macrophages and preserved mitochondrial metabolism warrant further investigation for therapeutic development in Duchenne muscular dystrophy.

Introduction

Duchenne muscular dystrophy (DMD) is a devasting X-linked recessive neuromuscular disease with an approximate global birth prevalence of 19.8 per 100,000 live male births [395]. It is caused by mutations to the *DMD* gene, which encodes the subsarcolemmal protein dystrophin [34,396,397]. Absence of dystrophin in cardiomyocytes can hinder the cardiac extracellular matrix (ECM) from anchoring to the actin and microtubule [58] cytoskeleton networks – a process critical in providing stability to the sarcolemmal membrane during contraction-relaxation cycles. This can lead to contraction-induced membrane damage that leads to repeated cycles of systemic inflammation, necrosis, and fibrosis [398]. Although the hallmark phenotypic manifestations of DMD, including locomotor impairments and respiratory failure, contribute to dependence on assistive devices, it is the dilated cardiomyopathy (DCM) that determines patient lifespan, and remains to be addressed with therapy development.

Key to the development of DMD-induced DCM - which precedes a loss of contractility and ultimately heart failure - is the progressive, unregulated spreading of ventricular fibrosis that mediates a gradual enlargement of the ventricular wall [27]. Aberrant cardiac fibrosis development is one of several programmes that are initiated in the dystrophic heart after repeated injury or damage as a means of preventing additional, more detrimental consequences by replacing dead or dying tissue with collagenous scar tissue [35–37]. In addition to aberrant cardiac fibrosis development (which occurs when the scar tissue begins to interfere with normal physiological processes), cardiac necrosis (degeneration) and cardiomyocyte hypertrophy collectively encompass the cellular, molecular, and interstitial changes associated with cardiac remodeling in DMD [35,37,399,400]. These indicators of cardiac remodeling, which are usually assessed with histopathological and/or immunofluorescent methods (especially in younger

dystrophic models where tissue size is limiting), are paramount for identifying early signs of cardiac pathology that often precede functional impairments and other symptomatic manifestations.

Current standard of care for DMD primarily relies on immunosuppression via glucocorticoid administration to prolong ambulatory function and slow disease progression [111]. However, glucocorticoids are often accompanied by deleterious side effects, such as attenuated growth, obesity, behavioural disorders, and other detriments [24]. The limited cardio-protection offered by emerging gene therapies [103] further underscores the remaining unmet need to develop additional cardioprotective therapies in DMD. In this regard, adiponectin (ApN)-based therapies offer a potential new avenue for consideration given ApN has been shown to be cardioprotective in other models of cardiovascular dysfunction through pleiotropic functions including anti-inflammatory and anti-oxidative stress properties [401,402]. Furthermore, the D2.B10-DMD^{mdx}/2J (D2.*mdx*) mouse model of DMD exhibits decreased plasma ApN levels due to reduced secretion by adipose tissue [403]. Additionally, previous work demonstrated that transgenic overexpression of ApN in C57BL10.*mdx* mice improved locomotor activity thus suggesting ApN may have therapeutic potential role in DMD [403]. Other beneficial effects of ApN on skeletal muscle in C57BL10.*mdx* mice were observed in models utilizing AdipoRon, which is an orally administered synthetic small-molecule (non-peptide) ApN receptor (AdipoR) agonist [403]. Given that ApN turns over quickly and ideally should be injected rather than orally administered to produce its effects (like most large multimeric peptides), ADP355 was pharmacologically developed to overcome these limitations. ADP355, now known as ALY688, is a small peptidomimetic of ApN that activates both AdipoR1 and R2 receptors to induce ApN-like effects, and has exhibited potent anti-fibrotic phenotypes in liver, kidney, and skin fibrosis

models [378]. It is noteworthy that ALY688 has been developed with pharmacokinetics enabling once-daily injection (unpublished observation).

Recent findings demonstrate that ALY688 preserves certain aspects of mitochondrial bioenergetics in skeletal muscle [392]. These effects further supports consideration of this compound as a therapeutic intervention for the dystrophin deficient heart. This is important given that mitochondrial stress response pathways represent a potential contributor to cardiac fibrosis development that occurs following a sustained inflammatory response [310]. Indeed, reduced mitochondrial pyruvate oxidation and increased mitochondrial reactive oxygen species occurs in the left ventricle of D2.*mdx* at an early age (4-week-old) where fibrosis has yet to manifest [34]. Exploring the degree to which adiponectin receptor agonism exerts cardioprotective effects through mitochondrial metabolism in addition to anti-inflammatory and anti-oxidative stress effects is therefore warranted.

The development of new therapeutics to treat cardiomyopathy in DMD could be better informed by considering chamber-specific responses to this disease. In this light, the first purpose of this investigation was to examine the degree to which histopathological characteristics develop in all four chambers of the heart in early stages of the disease process in D2.*mdx* mice. The second purpose of the study was to determine the relationship between histopathology, inflammation, and mitochondrial metabolism and whether this differed between the right and left sides of the heart. The final purpose of this investigation was to determine the adiponectin receptor agonist ALY688 prevented fibrosis and other indices of histopathology in relation to anti-inflammatory effects and mitochondrial reprogramming. We chose to investigate early stages of disease progression by using 4-week-old D2.*mdx* mice given disease symptoms often manifest in young children [404]. Our discoveries uncover right ventricular fibrosis and

hypertrophy as an early event in cardiac remodeling that is completely prevented by short-term treatment of ALY688 through apparent anti-inflammatory and mitochondrial preservation actions.

Results

Fibrosis is dominant in the right ventricle and left atrium in D2.mdx mice and is prevented by ALY688.

To determine if fibrosis is present at early stages of disease progression, collagen deposition was assessed by staining sagittal (four-chamber) cardiac tissue sections with picrosirius red dye.

Considerable heterogeneity between chambers was noted wherein the RV free wall (epicardial region) and LA of D2.*mdx*-VEH demonstrated increased collagen deposition (7.7-fold and 2-fold increase vs WT, respectively), in contrast to an absence of fibrosis in the LV free wall and RA of D2.*mdx* compared to WT (**Figure 4-1A, B**). Both drug doses significantly prevented collagen deposition along the RV free wall (LD, 2-fold decrease vs VEH; HD, 5-fold decrease vs VEH). In the LA, both drug doses significantly prevented collagen deposition (LD, 1.6-fold decrease vs VEH; HD; 3-fold decrease vs VEH) (**Figure 4-1A, B**).

D2.*mdx*-LD mice were excluded from subsequent analyses given that HD was more effective at preventing fibrosis in the affected chambers.

Figure 1

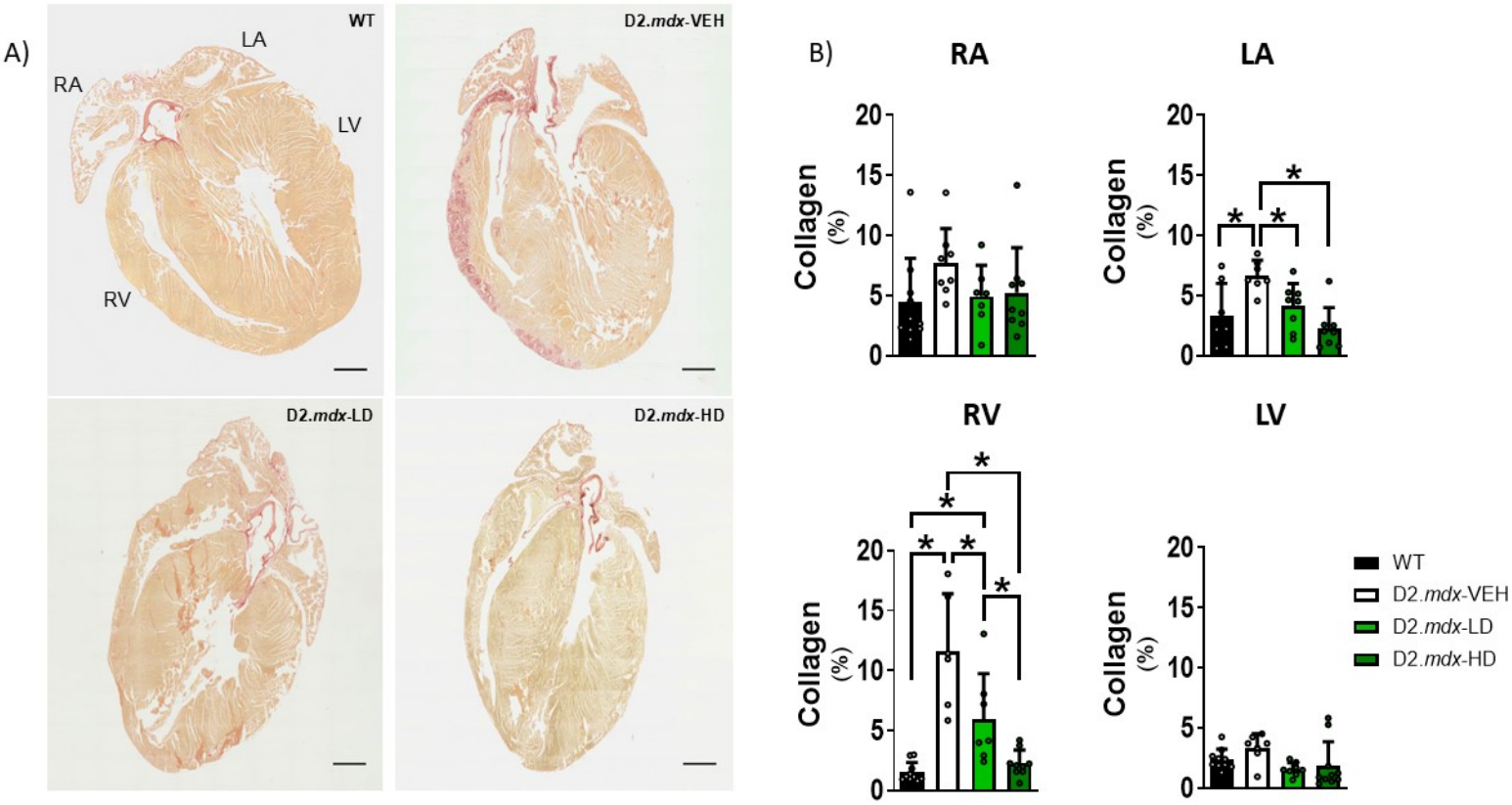

Figure 4-1. 4-week-old D2.*mdx* mice exhibit robust, chamber-specific cardiac fibrosis, which is prevented by daily ALY688 administration. A) 5 µM thick sagittal sections of cardiac tissue were stained with picrosirius red dye, which selectively binds collagen fibres. B) Epicardial RV and LA of D2.*mdx*-VEH exhibit increased collagen deposition compared to WT. ALY688 administration prevents collagen deposition along epicardial RV and LA in D2.*mdx*-LD and D2.*mdx*-HD. Images were taken with EVOS M7000 Imaging System at 4x magnification. Dark red segments denote collagen. Results represent mean ± SD; n=6-10. Scale bars are 1 mm. All *p* values are FDR-adjusted by Benjamini, Krieger, and Yekutieli *post-hoc* analyses. **p*<0.05 denotes significance. WT = Wildtype mouse; D2.*mdx*-VEH = vehicle (saline)-treated *mdx*; D2.*mdx*-HD = high dose (ALY688)-treated *mdx*; RA = right atrium; LA = left atrium; RV = right ventricle; LV = left ventricle.

Right ventricular cardiomyocyte hypertrophy is prevented by ALY688, while myocardial disorganization occurs in a chamber-specific manner in D2.mdx mice.

D2.*mdx*-VEH demonstrated larger cardiomyocyte diameter in both ventricles' vs WT (RV, 16% larger; LV, 15% larger) assessed by average Minimal Feret Diameter indicating that cardiomyocyte hypertrophy may occur early in this model. D2.*mdx*-HD exhibited a complete prevention of this hypertrophy in RV (HD, 14% smaller vs VEH) while MFD remained unchanged in the LV (**Figure 4-2A**). When assessing morphometrics between groups from hearts collected over two phases, WT heart weights were significantly larger than both D2.*mdx* groups (VEH, 12% smaller than WT; HD, 14% smaller than WT), however, when normalizing heart weights to tibia length, no significant differences were observed between groups (**Figure 4-2B**). D2.*mdx* mice also demonstrated significantly smaller body weights when combining data from both phases (VEH, 25% smaller than WT; HD, 26% smaller than WT) (**Figure 4-2B**). Four phases of in-house breeding and daily injections were required to collect chamber-specific data for all measures with a sufficient sample size (**SFigure 4-1A**). Morphometrics were collected from phase one and four, including ventricle-specific weights during phase four, which were unchanged between groups (**SFigure 4-1B**).

H&E staining was used to identify myocardial disorganization. Loss of nuclear detail and the presence of coalescing nuclei were used as determinants of cardiac muscle damage. In D2.*mdx*-VEH, increased myocardial disorganization was observed in the RV (4.4-fold increase vs WT), LV (1.8-fold increase vs WT), and LA (1.4-fold increase vs WT) (**SFigure 4-2A, B**). This disorganization was not prevented by ALY688 in any chamber (**SFigure 4-2A, B**).

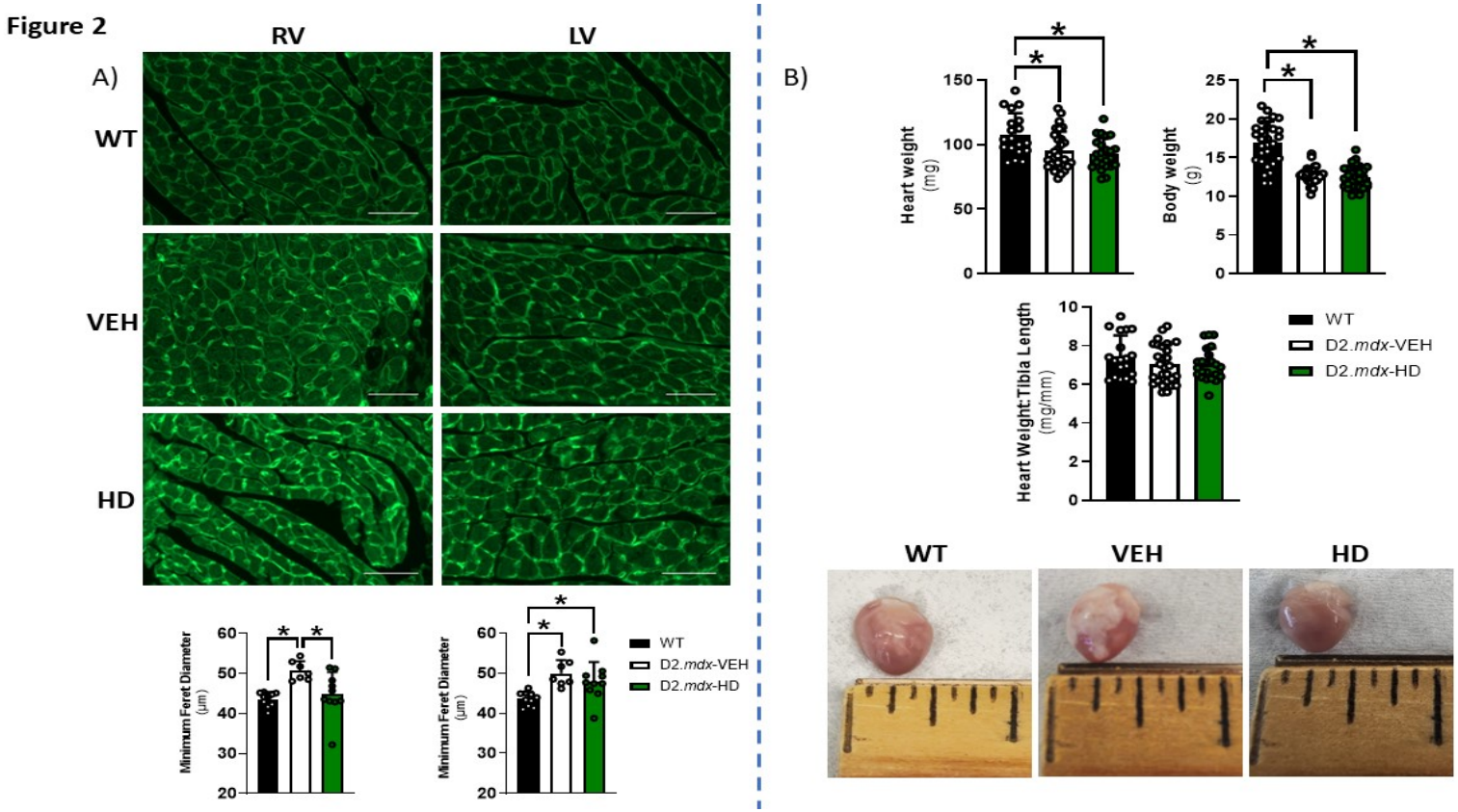

Figure 4-2. Ventricular cardiomyocytes are hypertrophied in D2.*mdx* mice but this is prevented by ALY688 in the RV. A) Sagittal sections of both ventricles were stained with wheat-germ agglutinin and imaged using immunofluorescence. Results represent mean ± SD; n=7-10. Scale bars are 50 μm. All *p* values are FDR-adjusted by Benjamini, Krieger, and Yekutieli *post-hoc* analyses. *$p<0.05$ denotes significance. B) Morphometric data comparing heart weight (mg), body weight (g), and heart weight-to-tibia length (mg/mm) between WT, D2.*mdx*-VEH, and D2.*mdx*-HD, with representative images of perfused whole-heart with the RV oriented frontward. Results represent mean ± SD; n=23-35 (combined phases 1+4). All *p* values are FDR-adjusted by Benjamini, Krieger, and Yekutieli *post-hoc* analyses. *$p<0.05$ denotes significance. WT = Wildtype mouse; VEH = vehicle (saline)-treated *mdx*; HD = high dose (ALY688)-treated *mdx*; RV = right ventricle; LV = left ventricle.

Fibrosis markers are elevated in RV of D2.mdx mice.

The RV of D2.*mdx*-VEH demonstrated significant elevations to TGF-β1 (an index of collagen) (30% increase vs WT) (**Figure 4-3A, B**). In D2.*mdx*-VEH, α-SMA was significantly elevated in both the RV and RA (RV, 30% increase; RA, 42% increase vs WT). In the RA, D2.*mdx*-HD had elevated α-SMA (36% increase vs WT). In the LA, α-SMA was elevated in both D2.*mdx*-VEH and D2.*mdx*-HD (VEH, 47% increase; HD, 34% increase vs WT), but in the LV, it was only elevated in D2.*mdx*-HD mice (38% increase vs WT) (**SFigure 4-3A, B**).

No significant differences between groups were revealed when comparing mean fluorescent intensity of TGF-β1 and α-SMA within the septum (**SFigure 4-4A**). While only two mice treated with ALY688 demonstrated fibrosis in the RV, we noted reduced markers of both TGF-β1 and α-SMA in the epicardial region (see representative image, **SFigure 4-4B**).

Inflammatory cytokines are heterogeneously altered between chambers in D2.mdx

In D2.*mdx*-VEH, the anti-inflammatory cytokine IL-10 was significantly elevated in all four chambers (41-58% increase vs WT). IL-10 was further increased in D2.*mdx*-HD in the LV (31% increase vs VEH) (**SFigure 4-5A, B**). When assessing the pro-inflammatory cytokine IL-6 across chambers, it was observed that only the LA of D2.*mdx*-HD revealed elevations (31% increase vs WT) (**SFigure 4-6A, B**).

Atria were excluded from remaining measures given not all cryosections contained the atria due to their smaller size.

Figure 3

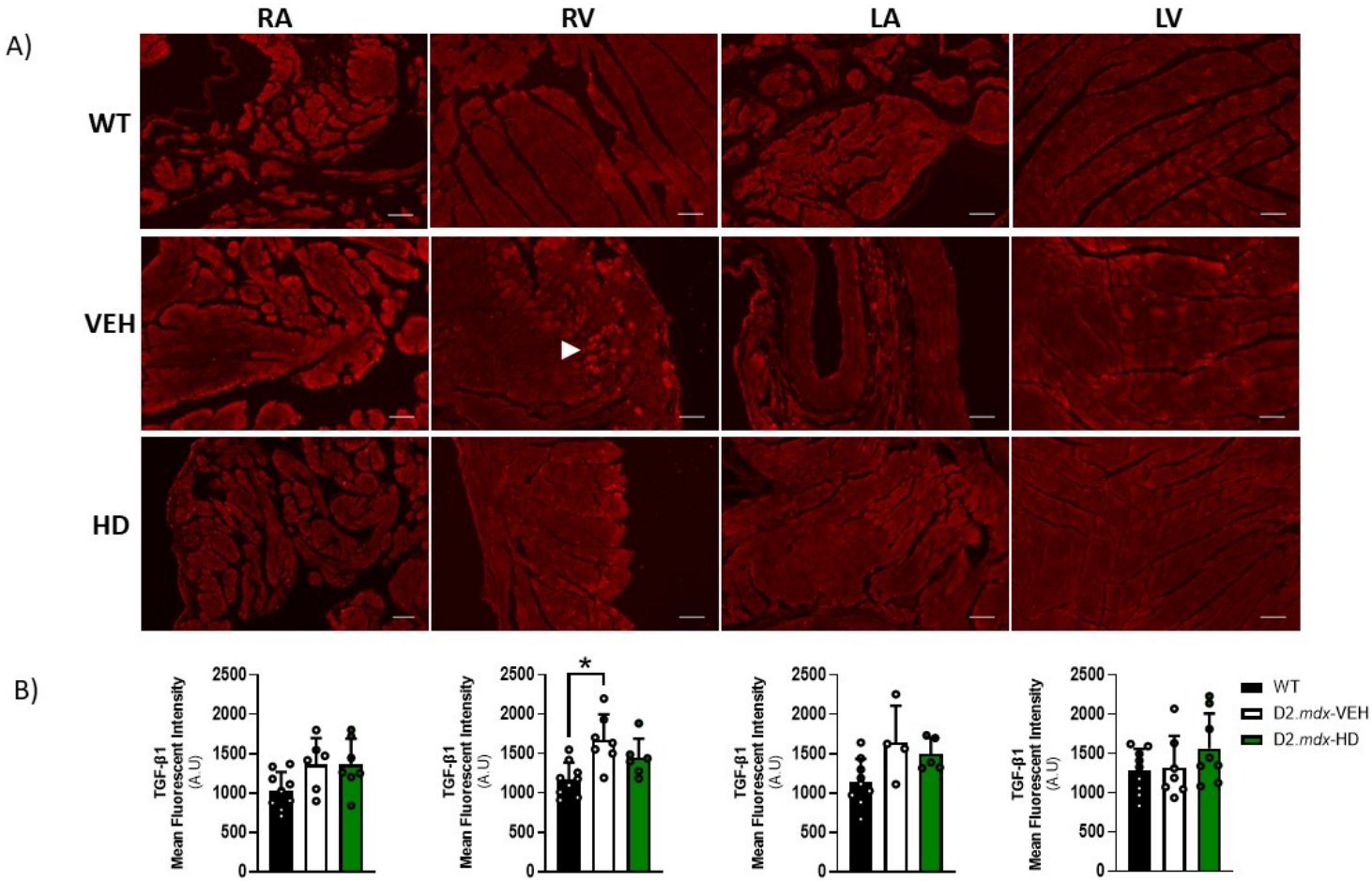

Figure 4-3. Chamber-specific immunofluorescent staining reveals that D2.*mdx*-VEH demonstrate elevated TGF-β1 compared to WT in the RV. A) TGF-β1 (denoted by white arrows) was quantified by Mean Fluorescent Intensity (A.U.) per region of interest (B). Whole atria and free-wall segments of the ventricles were analyzed. Stains were conducted on 5 µm thick paraffin-embedded sagittal sections and imaged by confocal microscopy at 20x magnification. Results represent mean ± SD; n=4-9. Scale bars are 100 µm. All *p* values are FDR-adjusted by Benjamini, Krieger, and Yekutieli *post-hoc* analyses. **p*<0.05 denotes significance. WT = Wildtype mouse; VEH = vehicle (saline)-treated *mdx*; HD = high dose (ALY688)-treated *mdx*; RA = right atrium; LA = left atrium; RV = right ventricle; LV = left ventricle.

Spectral flow cytometry reveals significant elevation to an infiltrating macrophage population in RV of D2.mdx-VEH which is restored in D2.mdx-HD mice.

In the RV, $CD11b^{+}CD45^{+}CD64^{+}F4/80^{+}CCR2^{+}$ cells, which represent an infiltrating (pro-inflammatory) macrophage population, are elevated in D2.*mdx*-VEH (16-fold increase compared to WT when examining cells normalized per mg tissue), but this is restored back to WT levels in D2.*mdx*-HD (**Figure 4-4A**). No differences were detected between groups when examining the same serotype in the LV. When examining $CD11b^{+}CD45^{+}CD64^{+}F4/80^{+}CCR2^{-}$ cells, which represent a resident (anti-inflammatory) macrophage population, no differences were detected between groups in either ventricle (**Figure 4-4B**). A sample gating scheme retrieved from a D2.*mdx*-HD RV demonstrates how cell populations were carefully selected, or 'gated', with special considerations taken for excluding cellular aggregates and debris which may contribute to fluorescent artefact (**SFigure 4-7**).

Figure 4

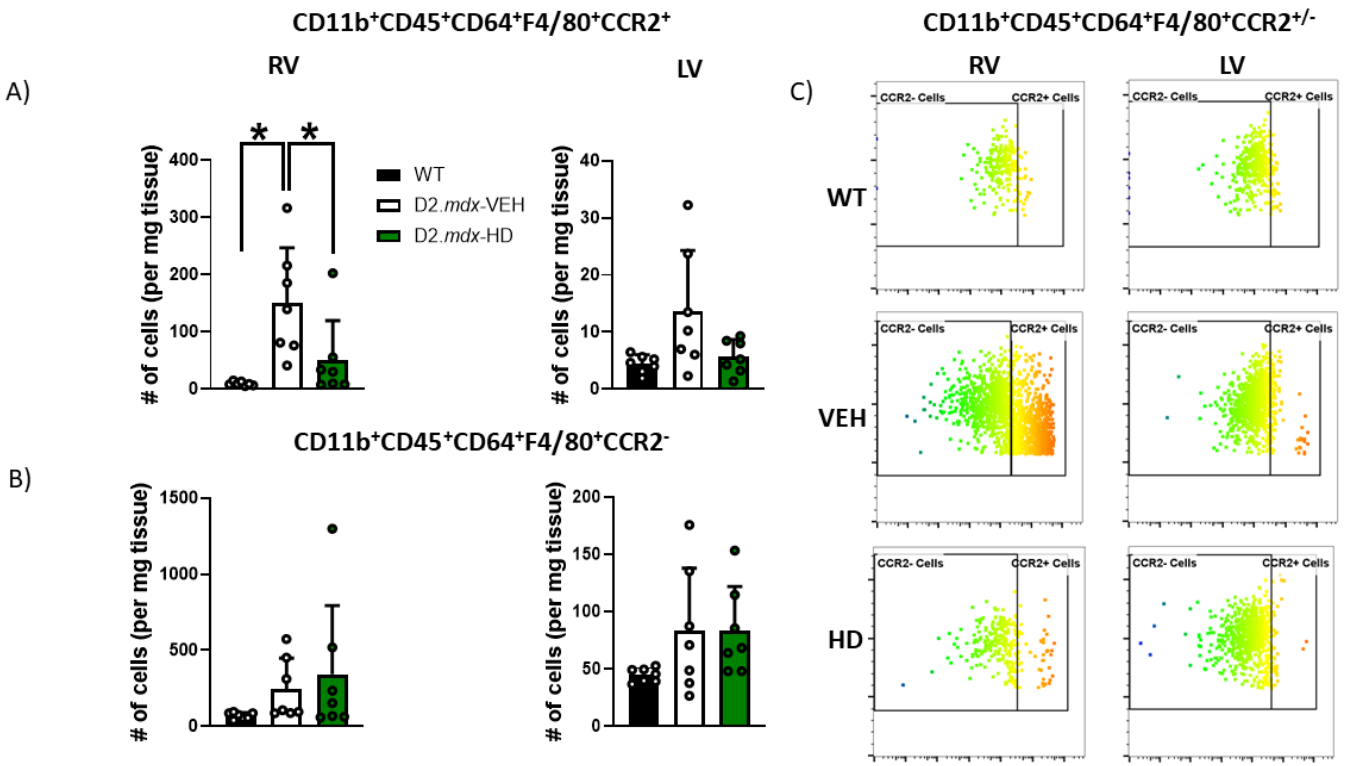

Figure 4-4. Ventricle-specific spectral flow cytometry analysis of infiltrating and resident macrophage populations in D2.*mdx*. A) In the RV, compared to WT, D2.*mdx*-VEH demonstrated elevated $CD11b^{+}CD45^{+}CD64^{+}F4/80^{+}CCR2^{+}$ cells (representative of an infiltrating macrophage population), which is restored by ALY688. In the LV, no differences were detected. B) When examining $CD11b^{+}CD45^{+}CD64^{+}F4/80^{+}CCR2^{-}$ cells (representative of a resident macrophage population), no differences were detected between groups in either ventricle. C) Representative gating scheme of $CCR2^{+/-}$ cells in all three groups between ventricles. Results represent mean ± SD; n=7. All *p* values are FDR-adjusted by Benjamini, Krieger, and Yekutieli *post-hoc* analyses. **p*<0.05 denotes significance. WT = Wildtype mouse; VEH = vehicle (saline)-treated *mdx*; HD = high dose (ALY688)-treated *mdx*; RV = right ventricle; LV = left ventricle.

D2.mdx-VEH exhibit indices of mitochondrial stress responses in the RV, but this is only partially prevented by ALY688 administration.

In the RV, caspase 3 and 9, whose activities are both involved in apoptotic pathways, are elevated in D2.*mdx*-VEH (caspase 3, 3-fold increase compared to WT; caspase 9, 2-fold increase compared to WT), but are both prevented in D2.*mdx*-HD (caspase 3, 1.7-fold decrease compared to VEH; caspase 9, 1.8-fold decreased compared to VEH) (**Figure 4-5A**). No differences were detected in caspase 8 activity, which is involved in extrinsic non-mitochondrial-mediated apoptotic pathways, thereby demonstrating a unique apoptotic signature. In the LV, no differences were detected between groups in any caspase activity.

As a complimentary measure to caspase 9/3 activity, mitochondrial calcium retention capacity was examined to determine the ability of mitochondria to uptake calcium prior to triggering permeability transition (mPT), which precedes mitochondrial-mediated apoptosis. In the RV, D2.*mdx*-HD exhibited a significantly elevated capacity to uptake calcium prior to mPT compared to both WT and D2.*mdx*-VEH, which corresponds with caspase 9/3 activity data. However, disease effects were not detectable at this low sample size (**Figure 4-5C**). It should be noted that only PmFBs that demonstrated a clear sign of calcium efflux (a sign of mPT) were included. **Figure 4-5D** demonstrates traces that exhibit mPT versus traces without clear mPT. When pooling traces with a clear opening and traces without clear mPT together, it was determined that D2.*mdx*-VEH had a significantly lower calcium retention capacity compared to WT, which was subsequently prevented in D2.*mdx*-HD (**SFigure 4-8D**). No differences were detected in the LV using either analytical technique (data reflecting only PmFBs with mPT versus pooled data) indicating that a heightened probability of calcium-induced mPT is unique to the RV.

By titrating pyruvate (5 mM) and malate (2 mM) with 20 mM creatine across increasing submaximal ADP concentrations to model metabolic demands close to physiological conditions (25, 100, and 500 μM) in the RV, it was observed that D2.*mdx*-VEH and D2.*mdx*-HD had elevated mH_2O_2 (denoted as a % of State II) (D2.*mdx*-VEH, 27-58% increase vs WT; HD, 28-51% increase vs WT) (**Figure 4-5B**). As this measure was performed in the presence of ADP, which stimulates oxidative phosphorylation and attenuates mH_2O_2 due to its effects on lowering membrane potential and considering that data were expressed relative to maximal H_2O_2, the results indicate that the elevated mH_2O_2 in the RV are due specifically to a lower mitochondrial responsiveness to ADP. In the LV, it was observed that D2.*mdx*-VEH had elevated mH_2O_2 (14-29% increase vs WT) due to lower mitochondrial responsiveness to ADP's attenuating effects on mH_2O_2, but interestingly, this was prevented in D2.*mdx*-HD (17-29% decrease vs D2.*mdx*-VEH) (**Figure 4-5B**).

By titrating pyruvate (5 mM) and malate (2 mM) (1st protocol) with saturating creatine, absolute mH_2O_2 was decreased in D2.*mdx*-VEH (PM, 31% decrease vs WT) in RV. Surprisingly, absolute mH_2O_2 was elevated in D2.*mdx*-HD (PM, 61% increase vs D2.*mdx*-VEH) in RV (**SFigure 4-8E**). No differences were observed in the LV. By titrating succinate (10 mM) exclusively (2nd protocol) in the presence of saturating creatine, mH_2O_2 was decreased in *mdx* compared to WT (Succ, 44.2% decrease vs D2.*mdx*-VEH; 29.7% decrease vs D2.*mdx*-HD), but interestingly, was elevated in D2.*mdx*-HD compared to D2.*mdx*-VEH (Succ, 26.5% increase) in the RV. No differences were observed in LV (**SFigure 4-8F**).

Figure 5

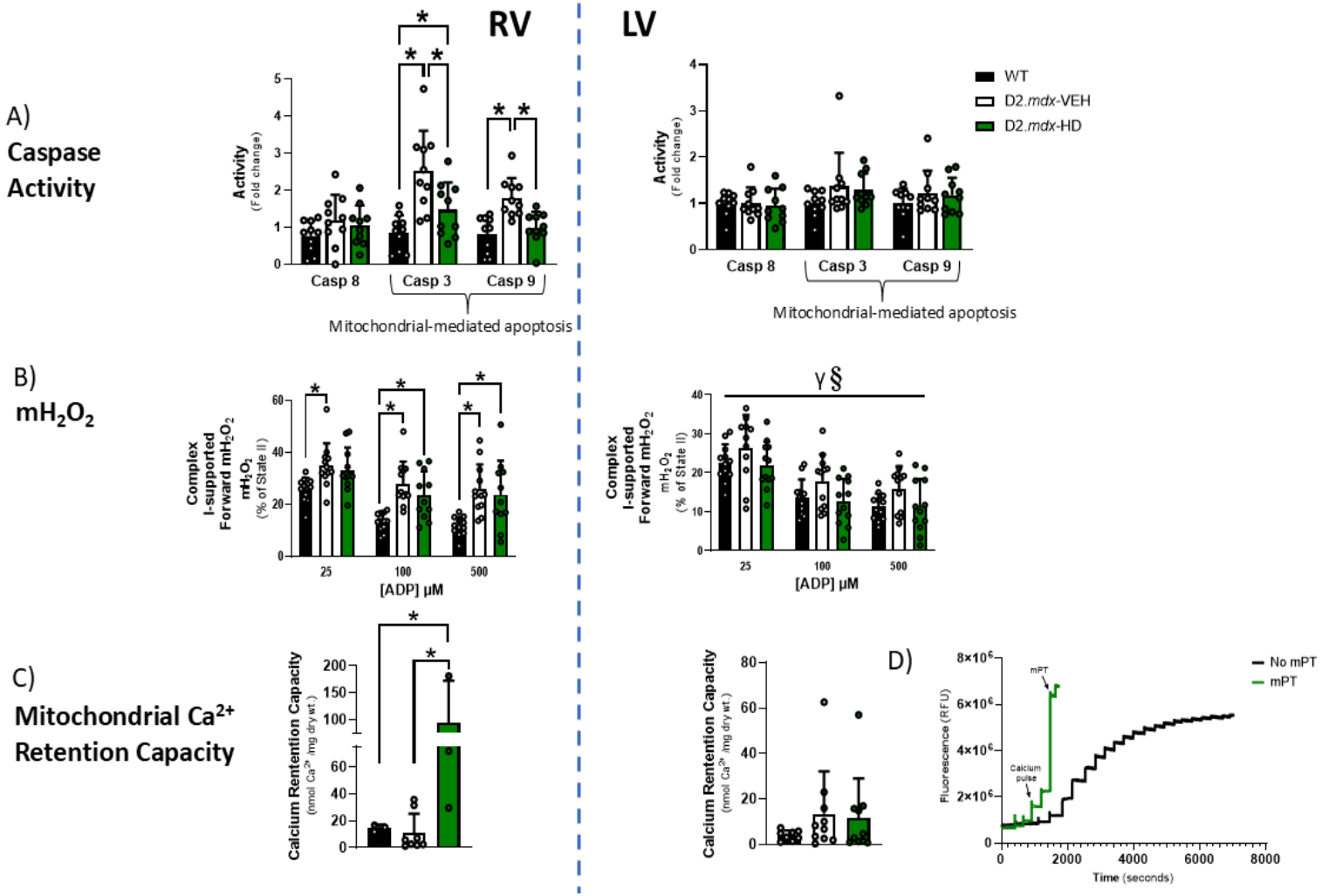
A)
Caspase Activity
RV
LV
WT
D2.mdx-VEH
D2.mdx-HD
Activity (Fold change)
Casp 8
Casp 3
Casp 9
Mitochondrial-mediated apoptosis
B)
mH2O2
Complex I-supported Forward mH2O2 (% of State II)
[ADP] µM
γ §
C)
Mitochondrial Ca2+ Retention Capacity
Calcium Rentention Capacity (nmol Ca2+ /mg dry wt.)
D)
No mPT
mPT
Calcium pulse
Fluorescence (RFU)
Time (seconds)

Figure 4-5. D2.*mdx* exhibit indices of mitochondrial stress primarily in the RV that are partially prevented by daily ALY688 administration. A) Caspase 3 and 9 activities are elevated in D2.*mdx*-VEH and prevented by ALY688, but only in the RV. No differences were detected in caspase 3 and 9 activity in the LV. Caspase 8 activity, which is involved in extrinsic (non-mitochondrial-mediated) apoptotic pathways, is unchanged in both ventricles. Results represent mean ± SD; n=10-12. *p<0.05 denotes significance. B) D2.*mdx*-VEH mice exhibit elevated mitochondrial Complex I-Supported (pyruvate + malate) forward electron transfer mH_2O_2 (represented as % of State II) in the presence of creatine in both ventricles across metabolic demands (25, 100, 500 μM ADP), but this is only prevented by ALY688 in the LV. Results represent mean ± SD; n=10-12. RV: *p<0.05 denotes significance; LV (main effects are denoted by horizontal bar): γp<0.05 WT vs D2.*mdx*-VEH; §p<0.05 D2.*mdx*-VEH vs D2.*mdx*-HD. C) Mitochondrial calcium retention capacity (CRC) to trigger mPT (which precedes mitochondrial-mediated apoptosis) is elevated in the RV of D2.*mdx*-HD compared to WT and D2.*mdx*-VEH, but disease effects are not detectable at this low sample size. No differences were observed in the LV. D) Representative CRC trace demonstrating ventricular PmFB with distinct mPT, compared to PmFB without mPT. Results represent mean ± SD; n=3-10. All p values are FDR-adjusted by Benjamini, Krieger, and Yekutieli *post-hoc* analyses. *p<0.05 denotes significance. Casp = caspase; mH_2O_2 = mitochondrial H_2O_2 emission; WT = Wildtype mouse; D2.*mdx*-VEH = vehicle (saline)-treated *mdx*; D2.*mdx*-HD = high dose (ALY688)-treated *mdx*; Ca^{2+} = calcium; mPT = mitochondrial permeability transition.

Blunted Pyruvate-supported Complex I, and Complex II, -stimulated respiration in RV of D2.mdx is prevented by ALY688.

In the RV, when assessed between groups, mitochondrial oxygen consumption using the NADH-generating substrates pyruvate (5 mM) and malate (2 mM) with saturating (20 mM) creatine was significantly lower in D2.*mdx*-VEH across a spectrum of metabolic demands (25 μM to 5000 μM ADP) (35-53% decrease vs WT) but was prevented in D2.*mdx*-HD (36-46% increase vs D2.*mdx*-VEH) (**Figure 4-6B**). Similar conclusions were also observed between groups without creatine (D2.*mdx*-VEH, 19-43% decrease vs WT; D2.*mdx*-HD, 7-24% increase vs D2.*mdx*-VEH) (**SFigure 4-8A**) which indicates that mitochondrial creatine-dependent phosphate shuttling may not be modified. The ability of creatine to stimulate respiration was further assessed by comparing respiration rates at submaximal ADP (100, 500 μM) with (20 mM Cr) and without (-Cr) creatine between groups. A complex relationship was identified whereby D2.*mdx*-HD exhibit elevated mitochondrial creatine sensitivity compared to D2.*mdx*-VEH in the RV with 500 μM ADP, while in the LV at 100 μM ADP, creatine sensitivity in D2.*mdx*-HD is significantly decreased compared to both WT and D2.*mdx*-VEH and only significantly decreased compared to WT at 500 μM ADP (**SFigure 4-8B**). When examining 10 mM glutamate (further NADH generation) and 10 mM succinate ($FADH_2$ generation; Complex II stimulation) it was observed that lower mitochondrial oxygen consumption in D2.*mdx*-VEH (glutamate, 52% decrease; succinate, 42% decrease vs WT) was prevented in D2.*mdx*-HD (glutamate, 44% increase; succinate, 39% increase vs D2.*mdx*-VEH) (**Figure 4-6C, D**).

No differences were detected in the LV in pyruvate/malate-, glutamate-, or succinate-supported respiration between any groups in the presence of saturating creatine (**Figure 4-6B**). In the absence of creatine, differences were only detected in pyruvate/malate-supported respiration in

D2.*mdx*-VEH and D2.*mdx*-HD (D2.*mdx*-VEH, 5-30% increase vs WT; HD, 18-36% increase vs WT) (**SFigure 4-8A**). In the same protocol, D2.*mdx*-HD demonstrated elevated mitochondrial oxygen consumption (5-21% increase vs D2.*mdx*-VEH) (**SFigure 4-8B**).

ALY688 prevents attenuations in fatty acid-supported mitochondrial respiration in D2.mdx.

We also examined fatty acid (beta) oxidation in both ventricles by titrating 10 μM L-Carnitine, 20 μM Palmitoyl-CoA, and 500 μM malate, across increasing ADP concentrations, with creatine. In the RV, when assessed between groups, mitochondrial oxygen consumption was lower in D2.*mdx*-VEH (30-39% decrease vs WT) but prevented by D2.*mdx*-HD (30-40% increase vs D2.*mdx*-VEH) (**Figure 4-6E**).

In the LV, there were no differences in L-carnitine/palmitoyl-CoA/malate-supported respiration between any groups without creatine (**Figure 4-6E**).

Electron transport chain complex-II subunit SDHB protein content may explain improvements to respiration in D2.mdx-HD.

Collectively, the lower respiration under all substrate conditions seen in the RV of the disease group, and the preventative effect of the drug, suggests that a common feature of these metabolic pathways may be universally modified. In order to gain more insight into this pattern, we recognized that the normalization of respiration per mg of tissue could be influenced by potential shifts in the contents of electron transport chain proteins, particularly those that are common and downstream of Complex I and II stimulation.

However, no changes in subunits of Complex III, IV or V (ATP Synthase) were seen in the RV. Of interest, complex-II subunit SDHB was significantly elevated in D2.*mdx*-HD (16% increase vs D2.*mdx*-VEH) which may have contributed to the higher succinate-stimulated respiration in

this group. No changes in the measured ETC proteins were observed in the LV. Total ETC content was also pooled together, but there were no differences between groups in either ventricle (**SFigure 4-8C**).

Figure 6

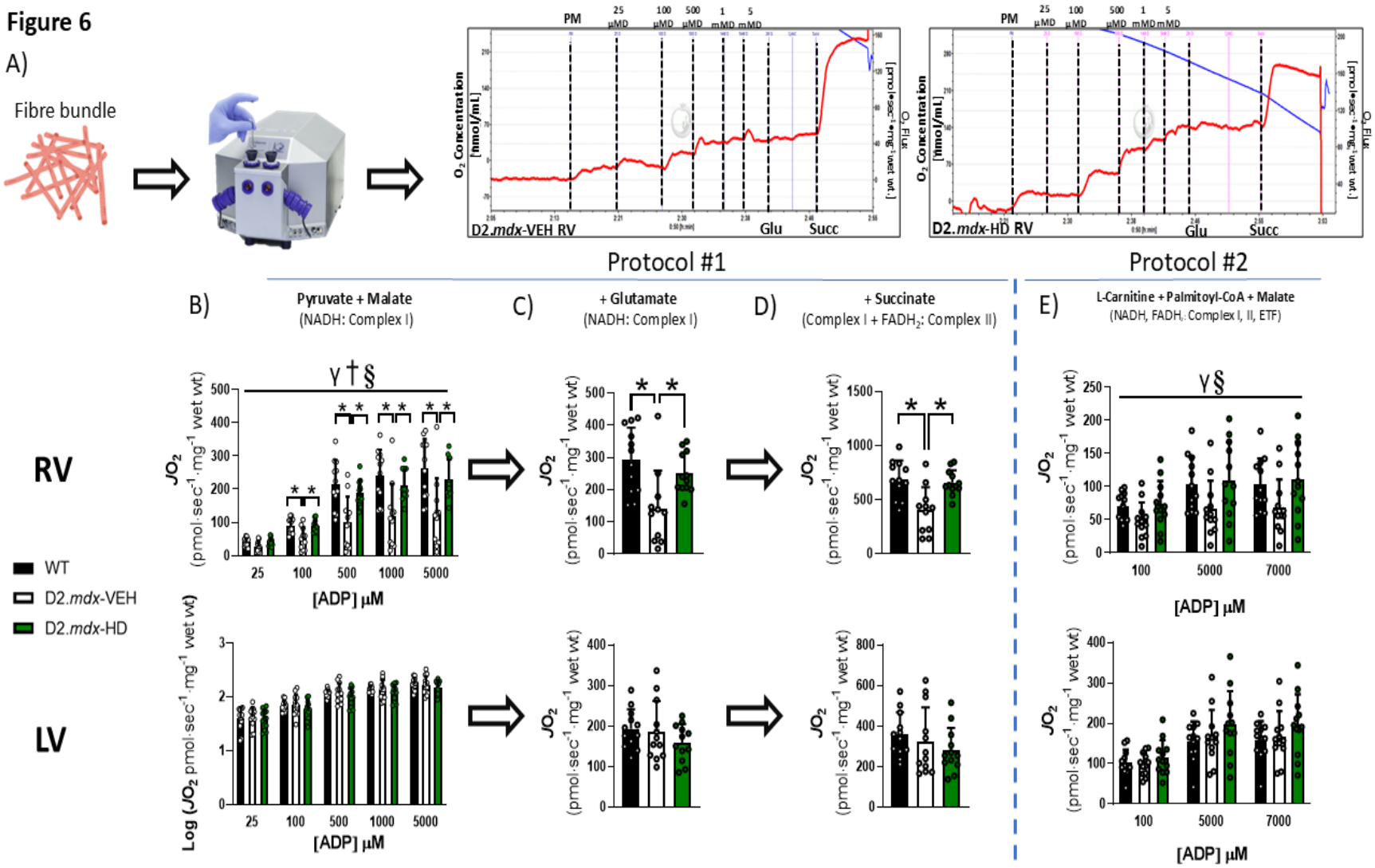
A)
Fibre bundle
PM
25 µMD
100 µMD
500 µMD
1 mMD
5 mMD
O2 Concentration [nmol/mL]
O2 Flux [pmol•sec-1•mg-1 wet wt.]
D2.mdx-VEH RV
Glu
Succ
D2.mdx-HD RV
Protocol #1
Protocol #2
B) Pyruvate + Malate (NADH: Complex I)
C) + Glutamate (NADH: Complex I)
D) + Succinate (Complex I + FADH2: Complex II)
E) L-Carnitine + Palmitoyl-CoA + Malate (NADH, FADH: Complex I, II, ETF)
RV
LV
WT
D2.mdx-VEH
D2.mdx-HD
JO2 (pmol·sec-1·mg-1 wet wt)
Log (JO2 pmol·sec-1·mg-1 wet wt)
[ADP] µM
25
100
500
1000
5000
7000

Figure 4-6. Substrate-specific stimulation of mitochondrial respiration in right and left ventricle of D2.*mdx* mice. A) Representative trace of high-resolution respirometry data demonstrating oxygen consumption that is calculated as the change in slope of oxygen consumption in the respirometry chamber (left trace, VEH RV - pyruvate + malate, ADP titration, glutamate, succinate protocol; right trace, HD RV - pyruvate + malate, ADP titration, glutamate, succinate protocol). B) ADP-stimulated respiration was supported by pyruvate (5 mM) supplemented with malate (2 mM) (NADH, Complex-I stimulation) as an index of carbohydrate oxidation. C) After the final addition of ADP (5000 µM) in 'A', glutamate (10 mM; NADH, Complex-I stimulation) was added as an index of amino acid oxidation, followed by D) succinate (10 mM) ($FADH_2$, Complex-II stimulation). E) Palmitoyl CoA (20 µM, supplemented with 10 µM L-Carnitine, 500 µM Malate and 100-7000 µM ADP; NADH and $FADH_2$) was added to a separate permeabilized fibre bundle as an index of fat oxidation. $FADH_2$ from the TCA cycle transfers its electrons at complex-II while $FADH_2$ from beta oxidation provides electrons for ETF. NADH = Nicotinamide adenine dinucleotide; $FADH_2$ = Flavin adenine dinucleotide; ETF = Electron transport flavoprotein; RV = right ventricle; LV = left ventricle; PM = pyruvate + malate; 'D' (from Panel A) = ADP. Results represent mean ± SD, n=10-12; a 2-way ANOVA was used to determine the difference between WT, D2.*mdx*-VEH and D2.*mdx*-HD across ADP concentrations in 'B' and 'E' while a 1-way ANOVA was used in 'C' and 'D'. All *p* values are FDR-adjusted by Benjamini, Krieger, and Yekutieli *post-hoc* analyses. LV data was log-transformed given that it did not pass parametric testing. *$p<0.05$ denotes significance. Main effects are denoted by horizontal bar over 'B' and 'E': γ$p<0.05$ WT vs D2.*mdx*-VEH; §$p<0.05$ D2.*mdx*-VEH vs D2.*mdx*-HD; †$p<0.05$ WT vs D2.*mdx*-HD. Oroboros image in Panel A obtained from https://www.oroboros.at/.

Mitochondrial signaling and mitophagy protein content does not explain divergent bioenergetic responses in the RV.

We examined mtCK due to its involvement with ATP/ADP cycling, however, no significant differences were observed between groups in either ventricle (**Figure 4-7A**) which is consistent with the observations that changes in respiration in disease and drug-treated groups were similar whether creatine was present or absent in the assay. Collectively, this suggests that creatine-dependent phosphate shuttling was not modified by either group. Total and phosphorylated protein content of AMPK were also examined, which are thought to be activated by adiponectin-receptor agonism [405]. In the RV, both D2.*mdx*-VEH and D2.*mdx*-HD mice had elevated phosphorylated AMPK (D2.*mdx*-VEH, 21% increase vs WT; HD, 27% increase vs WT; (**Figure -4-7A**). In the LV, D2.*mdx*-VEH mice demonstrated elevated phosphorylated AMPK (32% increase vs WT) which was prevented by the drug (**Figure 4-7A**). Lastly, the redox-sensitive apoptosis-activating protein p38 MAPK, which can be phosphorylated in response to mH_2O_2 [406] and activated by adiponectin as demonstrated in other studies [407–409], was examined to determine if it was altered between groups [406,410]. No differences were detected in total or phosphorylated p38 MAPK between groups in either ventricle (**Figure 4-7A**).

Mitophagy can preserve or restore mitochondrial function in cardiac tissue. Impairments to mitophagic processes can induce mitochondrial dysfunction, which can exacerbate cardiomyopathy [411]. Protein content of the autophagosome-ubiquitination adaptor proteins SQSTM1/p62 and LC3BII/I were investigated, however, the only difference detected was in LC3B-I, where D2.*mdx*-HD was significantly elevated compared to WT in the RV (**Figure 4-7B**).

Figure 7

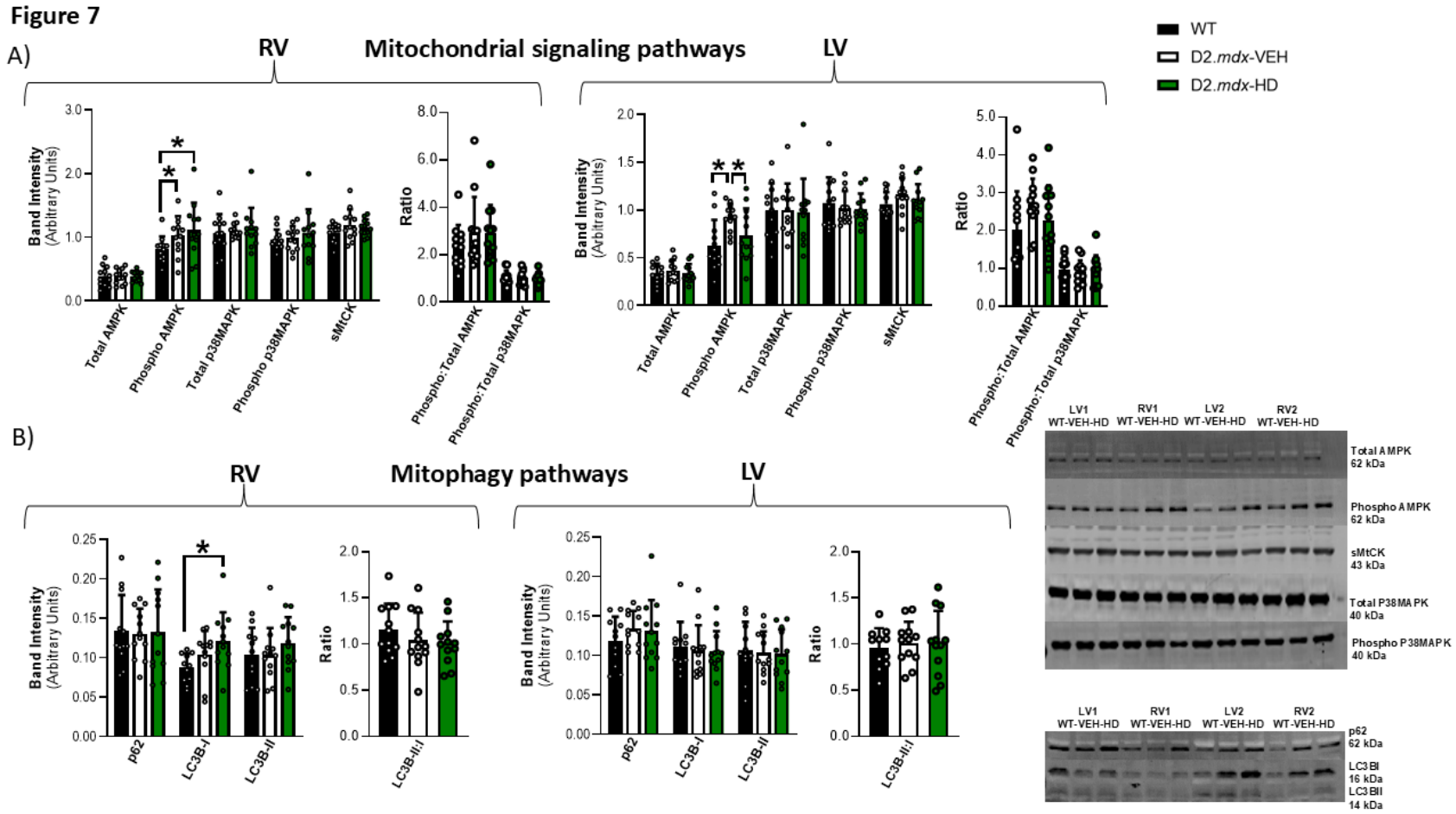

Figure 4-7. Western blotting of mitochondrial signaling and mitophagy markers reveals that D2.*mdx* exhibit elevated phosphorylated AMPK in both ventricles, but this is only prevented in the LV by ALY688. Top panel (A) Ventricle-specific mitochondrial signaling markers, while bottom panel (B) represents ventricle-specific mitophagic markers. Results represent mean ± SD; n=11-12. All *p* values are FDR-adjusted by Benjamini, Krieger, and Yekutieli *post-hoc* analyses. The 'ratio' is defined as phosphorylated protein content divided by total protein content. **p*<0.05 denotes significance. RV = right ventricle; LV = left ventricle.

Figure 8

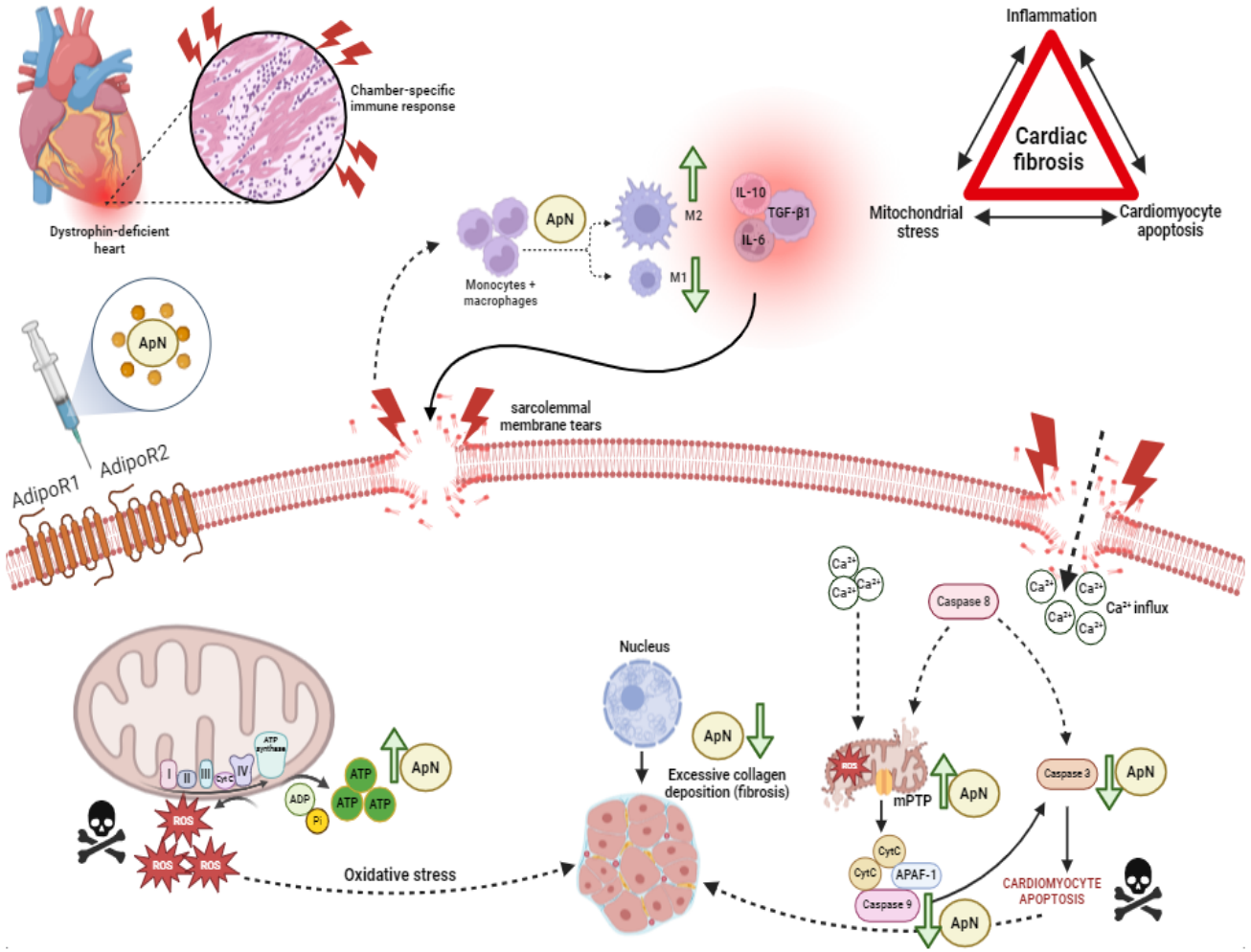
Inflammation
Cardiac fibrosis
Mitochondrial stress
Cardiomyocyte apoptosis
Chamber-specific immune response
Dystrophin-deficient heart
ApN
Monocytes + macrophages
M2
M1
IL-10
TGF-β1
IL-6
AdipoR1
AdipoR2
sarcolemmal membrane tears
Ca2+ influx
Caspase 8
Nucleus
Excessive collagen deposition (fibrosis)
mPTP
Caspase 3
ROS
ATP
ADP
Pi
Oxidative stress
CytC
APAF-1
Caspase 9
CARDIOMYOCYTE APOPTOSIS

Figure 4-8. Proposed mechanisms underlying dystrophin deficiency-induced cardiac fibrosis in 4-week-old D2.*mdx* mice that can be partially prevented by daily adiponectin-receptor agonism. Herein, we established that three major secondary contributors to dystrophin deficiency-induced cardiac fibrosis (inflammation, cardiomyocyte apoptosis, and mitochondrial stress) differentially impacted chambers of the heart. Our findings indicated that these secondary contributors demonstrated prevention effects when D2.*mdx* mice were injected daily with ALY688, ultimately leading to reduced cardiac fibrosis in the right ventricle (RV). To examine indices of mitochondrial stress, we investigated chamber-specific mitochondrial respiration and mH_2O_2, while intrinsic (mitochondrial-mediated) apoptosis was assessed by a combination of calcium retention capacity and caspase activity as complimentary measures. Inflammation was assessed by spectral flow cytometry to determine shifts in macrophage polarization (infiltrating versus resident populations) as well as by immunofluorescence of various inflammatory and fibrosis-linked cytokines. Our results indicate that daily adiponectin-receptor agonism may represent a viable therapeutic intervention for preventing RV fibrosis in young D2.*mdx* mice. Green arrows denote protective effects of ALY688 observed in the D2.*mdx*-HD RV across various remodeling signatures, including shifts to pro-/anti-inflammatory markers, mitochondrial stress responses, and cardiac fibrosis. Figure created using www.BioRender.com.

Discussion

A gap in knowledge exists whereby data examining chamber-specific dystrophin deficiency-induced cardiomyopathy is limited. Furthermore, there is an unmet need to address chamber-specific secondary contributors to damage in DMD with a therapeutic intervention that can slow progression to pathologic cardiomyopathy. Secondary contributors to DMD-induced cardiomyopathy include aberrant cardiac fibrosis [412], inflammation [26], and mitochondrial stress responses [31], some of which have been previously assessed, albeit primarily in the LV.

While there are numerous studies that have investigated inflammatory signaling and cardiac fibrosis development in both ventricles of DMD hearts (albeit at later time points of disease progression), data comparing mitochondrial stress responses between ventricles is limited. Our work identifies for the first time that hearts from 4-week-old D2.*mdx* mice are differentially impacted across chambers by fibrotic, inflammatory, and mitochondrial stress regulators. Specifically, we demonstrate that young D2.*mdx* mice exhibit robust, epicardial RV fibrosis and cardiomyocyte hypertrophy. Interestingly, the LA also exhibits fibrosis, while the RA and LV do not at this early time point. Notably, we posit a role for the novel anti-inflammatory adiponectin receptor agonist, ALY688, in serving as an intervention that prevents LA and epicardial RV fibrosis, and RV cardiomyocyte hypertrophy, while also attenuating elevations to infiltrating (pro-inflammatory) macrophage populations and some mitochondrial stress responses in 4-week-old D2.*mdx* mice.

4-week-old D2.*mdx* mice exhibit heterogeneity in chamber-specific cardiac fibrosis and cardiomyocyte hypertrophy that are prevented by daily adiponectin-receptor agonism

Robust collagen deposition in the heart, termed cardiac fibrosis, was detected with PSR staining in the LA and epicardial RV of young (4-week-old) D2.*mdx*-VEH, compared to age-matched healthy WT. Daily subcutaneous administration of ALY688 completely prevented this accumulation in D2.*mdx*-HD. Although the finding of robust RV fibrosis was previously demonstrated in 4–6-month-old C57BL/10ScSn-Dmd^{mdx}, which is a model of less severe cardiomyopathy, we provide novel evidence that this fibrosis may manifest at the earliest stages of life in D2.*mdx* mice - particularly affecting the RV free wall and the LA [184]. Additionally, using H&E staining, we provide evidence that both chambers affected by collagen accumulation (LA and RV) also demonstrate increased myocardial damage compared to WT, which is defined by loss of nuclear detail and presence of coalescing nuclei.

In the present study, cardiac functional parameters could not be assessed in the RV given the small ventricular size at this age. However, previous work by other groups has demonstrated that systolic dysfunction is evident in both ventricles at later stages of disease progression, with one study indicating LV functional impairments in D2.*mdx* mice present at 28 weeks [184,396]. Together, this data suggests that collagen accumulation occurring early in disease progression within the LA and RV precede the LV echocardiographic decrements that manifest at later ages.

Additionally, using H&E staining, we provide evidence that both chambers affected by collagen accumulation (LA and RV) also demonstrate increased myocardial disorganization compared to WT, which is defined by loss of nuclear detail and presence of coalescing nuclei. Although this myocardial disorganization is not prevented in D2.*mdx*-HD mice, we provide evidence that collagen accumulation may be a protective mechanism intended to uphold mechanical and structural integrity of the heart. Consistent with these findings, D2.*mdx*-VEH mice also exhibit hypertrophied cardiomyocytes compared to healthy WT. This increase in

cardiomyocyte diameter is preserved in D2.*mdx*-HD mice. Further investigations are required to established why collagen deposition is restricted to the epicardial RV free wall. We postulate that this is a finding best explained by echocardiography at an age where logistically feasible.

Elevated infiltrating macrophage populations in RV of D2.*mdx* are prevented by daily adiponectin-receptor agonism

Using spectral flow cytometry, we investigated differences to infiltrating and resident macrophage populations in enzymatically digested ventricular samples to determine if dystrophin deficiency impacted macrophage polarization shifts. Additionally, we were interested to see if daily adiponectin-receptor agonism could correspondingly restore balance to these inflammatory populations. Given that adiponectin is characterized by its anti-inflammatory properties, we hypothesized that protective effects to the heart (such as against fibrosis and/or cardiomyocyte hypertrophy) could be attributed to improvements in the inflammatory state of the ventricle. The major macrophage populations investigated in each ventricle were $CD11b^{+}CD45^{+}CD64^{+}F4/80^{+}CCR2^{+}$ (indicative of infiltrating macrophages; referred to as $CCR2^{+}$ cells) and $CD11b^{+}CD45^{+}CD64^{+}F4/80^{+}CCR2^{-}$ (indicative of resident macrophage; referred to as $CCR2^{-}$ cells) [413]. CCR2 signaling is of particular interest in dystrophin deficient mouse models given that previous literature has demonstrated elevations to CCR2 expression and its chemokine ligands, alongside macrophages excessively skewing towards a proinflammatory phenotype in *mdx* diaphragms [192]. Interestingly, the same group determined that CCR2 deficiency was linked to improvements in histopathological features and increased muscle strength in the diaphragm [192].

In alignment with the findings in the dystrophic diaphragm, our data indicates that D2.*mdx*-VEH exhibited elevated $CCR2^{+}$ cells in the RV, thus reflecting an increase in infiltrating

macrophage cells compared to healthy WT. This elevation was entirely prevented in D2.*mdx*-HD, which restored $CCR2^+$ cell levels back to baseline (WT). Additionally, we determined that no differences could be identified to $CCR2^-$ cell levels in either ventricle, meaning that levels of resident macrophages were unchanged. Given that these findings were localized to the RV, we hypothesized that dystrophin deficiency-induced damage to the RV led to the recruitment of proinflammatory macrophages to the site of damage (specifically the free wall epicardium), thus perpetuating the fibrotic response by upregulating the production of cytokines involved in fibrotic/collagen-producing processes.

Inflammatory and fibrotic cytokines underpinning cardiac fibrosis may be difficult to capture 24 hours post-drug administration

Inflammation is a hallmark component of whole-body DMD pathology and should be investigated in the context of macrophage polarization shifts. To understand the role of elevated $CCR2^+$ cells that was observed in the RV of D2.*mdx*-VEH mice, as well as the protective effects conferred in D2.*mdx*-HD mice, chamber-specific immunofluorescent staining of pro-, anti-inflammatory, and fibrotic cytokines was conducted.

We first assessed the relative abundance of IL-10, a pleomorphic anti-inflammatory cytokine, and determined that it was elevated ubiquitously throughout the heart in all D2.*mdx* mice (VEH and HD). IL-10 is thought to be produced by the activation of virtually all immune cells, including B cells, mast cells, granulocytes, macrophages, dendritic cells, and multiple T cell subsets [414,415]. It modulates the inflammatory immune response to damage by reducing M1-like macrophage production of pro-inflammatory cytokines such as Interferon (IFN)-γ, Tumour necrosis factor (TNF)-α, and IL-6 in inflamed tissue [416]. The finding that D2.*mdx*-HD mice exhibited elevated IL-10 compared to D2.*mdx*-VEH in the non-fibrosed LV is particularly

interesting given the well-established anti-fibrotic properties of IL-10 [415]. We hypothesize that IL-10 may be elevated in response to cardiac damage originating from dystrophin deficiency, but specifically remains elevated in the LV after drug treatment due to the importance of this ventricle in distributing blood throughout systemic circulation in place of 'less demanding' chambers.

In addition to IL-10, the pro-inflammatory cytokine IL-6 was also examined due to its indispensable role in immune response to injury. Given the low fluorescence observed in the IL-6 stain, the authors acknowledge that the findings may not reflect a true response given the difficulty of accurately capturing a transient cytokine with immunofluorescent staining methods.

Next, we examined a central regulator of cell differentiation, migration, proliferation, fibroblast activity, and gene expression which is extensively implicated in both reparative and reactive fibrotic responses, TGF-β1 [417]. At sites of injury, following an inflammatory response, many different cell types can produce and secrete TGF isoforms, including macrophages, lymphocytes, and cardiac fibroblasts [417]. Unsurprisingly, the RV of D2.*mdx*-VEH, which incidentally had the highest collagen deposition, demonstrated elevated TGF-β1 compared to WT. Although it was unusual that this elevation was not significantly restored by ALY688 (given that drug-treated mice demonstrated prevention against fibrosis), we postulate that TGF-β1 expression is transient, and it is possible that we missed a crucial timepoint in the immune response when expression is low. This possibility arises given that tissues were harvested 24 hours following the final ALY688 injection.

Finally, we investigated a widely used marker of mature myofibroblast (matrix-producing) cells in tissues, α-SMA [418–421]. During fibrotic expansion, a defining feature of myofibroblasts is the presence of a network of actin-myosin bundles that connect to the

surrounding matrix through focal adhesion proteins. Upon TGF-β stimulation, these contractile fibres become surrounded by α-SMA [417]. In our present study, we determined that in all chambers except the LV, α-SMA is elevated in D2.*mdx*-VEH compared to WT. Interestingly, it is also elevated in D2.*mdx*-HD compared to WT in all chambers except the RV. It is unusual that α-SMA was not lower in drug-treated mice compared to D2.*mdx*-VEH, however, future studies should test these same markers 1 hr post-drug injection to identify time-course relationships.

Mitochondrial carbohydrate- and fatty acid-stimulated respiration in the RV of D2.*mdx* are prevented by ALY688

4-week-old D2.*mdx*-VEH mice exhibited blunted mitochondrial oxygen consumption in the RV compared to healthy WTs, as assessed by high-resolution respirometry on PmFBs. This decrement in mitochondrial respiration is prevented in D2.*mdx*-HD when assessing oxygen consumption using complex-I-stimulating carbohydrate oxidation substrates (pyruvate, malate, glutamate (NADH), and succinate ($FADH_2$)) and β-oxidation (fatty acid-stimulating) substrates (L-carnitine, palmitoyl-CoA, malate; NADH/$FADH_2$) over various [ADP] (physiological to supraphysiological workloads) in saturating creatine-infused buffer. These effects are not observable in the LV. When repeating these experiments in buffer without creatine, ALY688 improves respiration compared to D2.*mdx*-VEH in both ventricles across increasing [ADP]. Although data was not normalized to OXPHOS protein content given that these measures were acquired from different hearts, the lack of changes to OXPHOS content proposes that the improved mitochondrial respiration may be attributed to quality rather than quantity of mitochondria.

Mitochondrial stress in the RV of D2.*mdx* are only partially prevented in D2.*mdx*-HD

Various techniques, including caspase 9/3 activity (indicator of intrinsic mitochondrial-mediated apoptosis), mitochondrial calcium retention capacity, and mH_2O_2 were assessed and compared across ventricles as indicators of mitochondrial stress responses to dystrophin deficiency.

Notably, our results indicated that caspase 9/3 activity, but not caspase 8 activity, was elevated in the RV of D2.*mdx*-VEH, and subsequently prevented in D2.*mdx*-HD. These effects were not observed in the LV. This data is particularly important given that caspase 9/3 activity are involved in mitochondrial-mediated apoptotic cascades whereas caspase 8 is primarily involved in extrinsic apoptosis pathways [422]. This data suggests that in the dystrophic RV, mitochondrial apoptosis is elevated and may be a contributing factor to the cardiac fibrosis that is observed in D2.*mdx*-VEH mice, while reductions to mitochondrial-mediated apoptosis, as observed in D2.*mdx*-HD, may prevent fibrosis development.

To further investigate the role of mitochondrial apoptosis in dystrophin deficiency-induced damage, we assessed ventricle-specific mitochondrial calcium retention capacity (CRC), which is defined as the maximal calcium that the mitochondria can uptake prior to formation of the mitochondrial permeability transition (mPT) pore. Sustained mPT leads to mitochondrial swelling, which can rupture the outer mitochondrial membrane (OMM) and subsequently lead to apoptotic cell death [423]. Our results indicated that D2.*mdx*-VEH had significantly lower CRC compared to D2.*mdx*-HD, however, there were no disease effects due to low sample size when bundles without mPT were excluded from the analysis. Interestingly, when pooling bundles that had clear mPT with bundles that did not have clear mPT, RV of D2.*mdx*-VEH demonstrated disease effects whereby CRC was significantly lower compared to WT, which was prevented in D2.*mdx*-HD. No effects were observed in the LV. Collectively, this data suggests that chamber-

specific CRC is influenced by the specific ventricles' ability to maximally uptake calcium prior to mPT - which appears to differ between RV and LV and has never been previously characterized in 4-week-old D2.*mdx* mice. Although the sample size was low in our non-pooled analysis, the data still suggests that ALY688 may be modifying the ability of the dystrophic ventricle to maximally uptake calcium prior to mPT that precedes apoptosis. Furthermore, given that these effects were not identifiable in the LV regardless of analytical method, the data also suggests that ALY688 does not alter the LV's capacity to uptake calcium in the same way it alters the RV's maximal calcium uptake capacity.

Chamber-specific mH_2O_2 were also assessed in D2.*mdx* mice to determine if elevated ROS could explain some of the cardiac remodeling that was observed. Two different protocols were used to assess ROS, including mitochondrial complex I-supported (pyruvate + malate) forward electron transfer mH_2O_2 and complex-I+II-supported (succinate) reverse electron transfer mH_2O_2.

Using the complex I-supported (pyruvate + malate) forward electron transfer protocol, our results indicated that both D2.*mdx* groups exhibited elevated mH_2O_2 (expressed as % of state II) compared to WT in the RV, however, preventative drug effects were not observed. Although this was not entirely expected, it is noteworthy that when assessing the same protocol in the LV, D2.*mdx*-VEH mice exhibited elevations to mH_2O_2 compared to WT which were prevented in D2.*mdx*-HD. Collectively, our findings suggest that the ability of ALY688 to quench mitochondrial ROS is complex and differs between chambers. Future research may seek to investigate other indices of redox stress in tandem with mH_2O_2, including chamber-specific reduced-to-oxidized glutathione ratio.

Protein content of mitochondrial signaling and autophagy markers do not explain changes to cardiac inflammatory or fibrosis outcomes 24 hours post drug administration

We used Western blotting techniques to determine if markers of mitochondrial signaling or mitochondria-specific autophagy (known as mitophagy) could explain some of the improvements to mitochondrial function and fibrotic state of the ventricles.

We first examined mitochondrial creatine kinase (mtCK) given that previous literature has implicated downregulated mtCK protein content and activity as a consistent feature of heart failure in several animal models [424–426]. In the presence of creatine, mtCK is vital in cardiomyocytes for trans-phosphorylating newly synthesized ATP to phosphocreatine (PCr), thus allowing PCr to be exported to the cytosol via VDAC to increase efficiency of ATP transport out of mitochondria, compared to the much slower ATP/ADP cycling process [424]. Previous work from our lab has demonstrated robust impairments to the ability of creatine to govern mitochondrial bioenergetics in the LV of 4-week-old D2.*mdx* mice [31]. Across a range of both low and high ADP concentrations, it was noted that in the presence of creatine, ADP's governance of mitochondrial bioenergetics was impaired, thus suggesting perturbations to mtCK-dependent energy exchange [31]. In this same study, mtCK content was unchanged in the LV. In the current study, we determined that there were no differences to mtCK protein content in either ventricle across all groups, suggesting that an impairment to the mitochondrial phosphate shuttling system, which is particularly important in the heart to maintain constant rhythmic contractions, may remain unperturbed. Further assessments, such as the oxidation state (among other post-translational modifications to mtCK) should be investigated.

Next, we examined total and phosphorylated protein content of AMPK. Previous literature has determined that in the heart, adiponectin signals to and activates AMPK – a process

thought to be mediated by upstream signaling through the cardiac cell surface receptors, AdipoR1 and AdipoR2 [427]. Although our results indicated elevations to phosphorylated AMPK in both D2.*mdx* mouse groups (VEH and HD) in the RV compared to WT, and only to D2.*mdx*-VEH mice in the LV compared to WT, no drug effects were observed in either ventricle. This is unusual given the previously published literature surrounding adiponectin's propensity to signal AMPK. We believe that by delaying sacrifice to 24 hours post-injection, we missed a crucial window of AMPK upregulation, which is especially probable considering that ALY688's half-life in rodent models is only 75 minutes (unpublished data).

The final mitochondrial signaling proteins we investigated were total and phosphorylated p38 MAPK. It is well known that p38 MAPK is activated following ischemic cardiac events such as myocardial infarction, and its activation has been correlated with both cardiomyocyte apoptosis and oxidative stress [428,429]. Furthermore, upon activation, p38 MAPK has shown to contribute to LV remodeling, and heart failure development which is encompassed by inflammation, fibrosis, and hypertrophy [429,430]. Given that pharmacological inhibition and genetic knockout of p38 MAPK demonstrated improvements to LV function and attenuations to morphological alterations caused by myocardial infarction, there was value in determining if the improved fibrosis and mitochondrial function could be attributed to ALY688's upregulation of p38 MAPK. Ultimately, no drug effects were detected in either ventricle.

Mitophagic markers like p62 and LC3BII/I were both investigated to determine if the cell's inherent ability to eliminate dysfunctional mitochondria was disrupted. In healthy tissue, defective mitochondria are selectively removed in a process intended to uphold quality control of the healthy mitochondrial pool. Decreases in mitophagy have been previously published in older C57BL/10 *mdx* mice. While Kang et al. determined that hearts of 12-month-old C57BL/10 *mdx*

exhibited lower mitophagy attributed to decreased expression of PINK1/PARKIN, Kuno et al. also published lower mitophagic capabilities in hearts of 22-week-old C57BL/10 *mdx* mice, instead demonstrated by increased colocalization of LC3 dots [312,315]. Despite these findings, we did not detect any changes to the mitophagic ability of either ventricle at this early time point.

Perspectives, Limitations, and Conclusion

The data suggests that D2.*mdx* mice exhibit robust, chamber-specific fibrosis and cardiomyocyte hypertrophy as early as 4-weeks of age. Herein, we present novel data demonstrating that the affected chambers (RV and LA) are protected against fibrosis by daily administration of the anti-inflammatory adiponectin-receptor agonist, ALY688. RV epicardial fibrosis observed in D2.*mdx*-VEH mice corresponds with increased myocardial disorganization and cardiomyocyte hypertrophy, of which the latter is prevented by ALY688. The use of spectral flow cytometry and immunofluorescent staining identifies a role of inflammation (specifically shifts in infiltrating versus resident macrophage populations) that may be contributing to the RV cardiac fibrosis that is observed in D2.*mdx*-VEH mice given that it is resolved by ALY688. Lastly, mitochondrial stress responses, including blunted mitochondrial oxygen consumption, elevated mH_2O_2, and caspase 9/3 activity, are partly restored in a chamber- and substrate-specific manner by ALY688.

The authors acknowledge that there are several limitations of the model. Firstly, given the extremely small hearts in all three groups of mice, obtaining chamber-specific functional data via echocardiography proved to be challenging. Although we have previously assessed left ventricular function using echocardiography in this model, right ventricular function in particular was difficult to assess given the anatomical limitations imposed by the size and morphology of the ventricle. Although this data would have strengthened our model, future research may

consider alternative techniques for assessing cardiac function such as invasive hemodynamics or using larger mice. Secondly, immunofluorescent staining of inflammatory and fibrotic cytokines yielded variable, and generally inconclusive results. Given that these cytokines are transient, capturing them with RT-qPCR rather than immunofluorescence would be favourable. This was once again difficult for us to accomplish in a chamber-specific manner given the tissue size limitation on the RV in particular. An additional 5th phase of breeding would be required to satisfy this additional measurement whereby whole RV would be flash frozen specifically for this experiment. Lastly, we believe that waiting 24 hours following the final injection prior to sacrificing the animals may explain the absence of AMPK detection via Western blot in the drug-treated animals. Given that adiponectin is known to signal AMPK, we believe that future study designs should consider sacrificing animals 1 hr following the final injection to capture the effects of adiponectin before it is washed out due to its relatively short half life in rodents.

Collectively, our results support further investigation into adiponectin-receptor agonists for their roles in alleviating some of the secondary contributors of DMD-induced cardiomyopathy. Given that current generation treatment options, including gene therapy and glucocorticoid administration cannot, at this stage, correct the whole-body deficiency of dystrophin and are also accompanied by unwanted side effects, alternative therapy development that addresses DMD-induced inflammation, fibrosis, and mitochondrial stress responses are paramount. Furthermore, this work warrants investigation into other chambers of the heart, particularly the RV (which we have established as highly susceptible to damage), as a predictor of cardiomyopathic outcomes alongside the well-researched LV.

Methods

Animal care

Male D2.*mdx* mice were bred from an in-house colony established at York University's rodent facility (Toronto, Ontario). Mice were housed with littermates in standard vivarium cages and aged to four weeks until sacrifice (aged 28-32 days), in a room maintained on a 12:12-h light-dark cycle with *ad libitum* access to standard chow and water. Due to low in-house breeding success, 3-week-old DBA/2J Wildtype (WT) mice were ordered directly from Jackson Laboratories (Bar Harbor, USA) and allowed to acclimate for one week prior to sacrifice. Experiments, procedures, and personnel were all approved in accordance with both the Animal Care Committee at York University (AUP Approval Number 2016-18) and with the Canadian Council on Animal Care.

Breeding regimen and ALY688 drug treatment

Two groups of D2.*mdx* mice were treated with ALY688 (Allysta Pharmaceuticals) formulated at different dosages: low dose (LD; 3 mg/kg body weight/day) and high dose (HD; 15 mg/kg body weight/day) – both of which were dissolved in saline. A separate group of D2.*mdx* mice (VEH, vehicle) were treated with saline. Mice were treated starting at 7-days of age (until 28-32 days of age) via subscapular subcutaneous injection at a dosage of 1 μL/g body weight. WT mice did not receive injections.

Due to limited tissues in each chamber of the heart, four mice per 'n' were needed to generate all data (**Figure S1A)**. Accordingly, four breeding phases of D2.*mdx* mice were required to obtain sufficient tissue for all analyses. During phase 1, hearts from each group of mice were processed for tissue histology and immunofluorescence. Given that LD and HD yielded similar fibrotic

responses, as assessed by picrosirius red staining, it was decided that LD would not be pursued for analyses beyond phase 1. During phase 2, hearts from each group of mice (now WT, D2.*mdx*-VEH, and D2.*mdx*-HD) were flash frozen for Western blot analyses. During phase 3, hearts from each group of mice were incubated in preservation buffer and subsequently processed for mitochondrial bioenergetic assays. Phase 4 was conducted to obtain additional morphometric data, additional mitochondrial bioenergetics data, caspase activities, and spectral flow cytometry data. Sample sizes are indicated in figure legends where appropriate.

Surgical procedure

Hearts were carefully excised while the animal was anesthetized with medical-grade isoflurane. For phase 1, whole-hearts were preserved in 10% neutral-buffered formalin (Millipore Sigma, Burlington, MA, USA) and processed for histology. Morphometric data such as heart weight was also collected during this phase. For phase 2, hearts were carefully separated into 4 chambers under a microscope with surgical-grade scissors and were then frozen in liquid N_2 and stored at -80°C for Western blots. For phase 3, ventricles were removed and placed in ice-cold BIOPS preservation buffer containing (in mM) 50 MES Hydrate, 7.23 K_2EGTA, 2.77 CaK_2EGTA, 20 imidazole, 0.5 dithiothreitol, 20 taurine, 5.77 ATP, 15 PCr, and 6.56 $MgCl_2$•$6H_2O$ (pH 7.1), before being separated into fibre bundles for mitochondrial bioenergetic assays (see below). During phase 4, hearts with either placed in ice-cold BIOPS preservation buffer or processed for spectral flow cytometry.

Histological and immunofluorescent staining

Preparation of microscope slides: Hearts were immediately submerged into a 15 mL canonical Falcon tube containing 10% neutral-buffered formalin and stored for 24 hours at room

temperature. Following a 24-hour incubation period in formalin, hearts were transferred to a separate 15 mL conical centrifuge tube containing 70% ethanol and stored at 4°C thereafter.

Once ready for tissue processing, hearts were individually placed in plastic paraffin-embedding cassettes (Simport Scientific, Saint-Mathieu-de-Beloeil, QC) where they were dehydrated using a gradient of ethanol concentrations (70% to 99%), followed by two 100% xylene incubations. Cassettes were placed overnight in an oven heated to 54-57°C, which contained melting Type H paraffin wax (Thermo Fisher Scientific, USA), in a process intended to allow paraffin wax to penetrate and embed the samples. The following morning, after cassettes were removed from the oven and the paraffin wax had solidified at room temperature, paraffin within the cassettes was again heated to melting point, and samples were transferred to disposable base molds. Following this, paraffin was once again re-introduced to the cassettes and left to solidify at room temperature before the samples were ready to be sectioned at 5 μM thickness on a sagittal (4-chamber) plane using a microtome and hot water bath. Finally, sections were carefully placed onto Fisherbrand SuperFrost Plus positively charged microscope slides (Thermo Fisher Scientific) for microscopy.

Picrosirius Red (PSR): Fibrosis was assessed on formalin-fixed paraffin-embedded sections with PSR, which stains collagen [431]. Sections were deparaffinized with xylene incubations and subsequently rehydrated with ethanol incubations (100% to 70%, followed by distilled water). Sections were then incubated with PSR for 1 hour at room temperature, followed by washes in acidified water. Prior to mounting, sections were submerged in ethanol concentrations (95% to 100%), followed by xylene incubations, and then subsequently mounted with Permount mounting medium (Thermo Fisher Scientific). Sections were imaged with Brightfield microscopy on the EVOS M7000 imaging system (Thermo Fisher Scientific). Fibrotic

(collagenous) regions were expressed as a percentage against standardized total regions of interest (anatomically consistent between all samples), which included whole atria and a central region of the ventricular free wall. Artefacts (such as irregular tissue folds) were avoided during the blinded analysis. Fibrosis was quantified using ImageJ (National Institute of Health).

Hematoxylin and Eosin (H&E): Cardiac tissue disorganization was quantified using H&E staining, as previously described in our lab [432]. Disorganized cardiac tissue was defined by loss of nuclear detail and the presence of coalescing nuclei. Sections were imaged with Brightfield microscopy on the EVOS M7000 imager. Cardiac tissue disorganization was calculated by dividing areas containing coalesced nuclei or lost nuclear detail by total region of interest (artefacts and dead space subtracted) and expressed as a percentage. Regions of interest were kept consistent anatomically between samples. Blinded analyses were completed using ImageJ.

Immunofluorescence: To assess inflammatory cytokine presence, and markers of fibrosis, tissue sections were incubated with primary antibodies and imaged against corresponding fluorescent secondary antibodies. Sections were deparaffinized with xylene incubations, rehydrated with gradient ethanol incubations (100% to 70%, followed by distilled water), and then incubated in boiling Tris-EDTA (TE) buffer pH 9.0 for antigen retrieval. Sections were incubated with equal parts pre-conjugated wheat germ agglutinin (WGA) (AlexaFluor 488; Cat. No. W11261; 1:1000) and multiplexed primary antibodies for IL-6 (rabbit; Cat. No. P620; 1:100) and IL-10 (mouse; Cat. No. ARC9102; 1:100) or TGF-β1 (rabbit; Cat. No. PA5-120329; 1:100) and α-SMA (mouse; Cat. No. 14-9760-82; 1:100) (Thermo Fisher Scientific), on duplicate sections per set of antibodies. The following morning, primary antibodies were rinsed off with PBS-T and sections were incubated with the following fluorescent secondary antibodies: AlexaFluor 594 (Goat Anti-

Rabbit; Cat. No. ab150080; 1:1000), or Alexafluor 647 (Donkey Anti-Mouse; Cat. No. ab150107; 1:1000) (Abcam, Cambridge, UK) corresponding to the primary antibody for 1 hour at room temperature. Sections were mounted using an aqueous Fluoroshield DAPI mounting medium (Abcam) with edges sealed using clear nail polish. Slide microscopy was conducted using a fluorescence slide scanner (Zeiss AxioScan) at 20x magnification. Sections were analyzed using the QuPath-0.4.0 software. While blinded, the analyzer selectively avoided tissue folds and other fluorescent artefacts that influenced data, across all experimental groups. Entire atria were analyzed, while ROIs were kept consistent between ventricles. Endocardial, fibrotic epicardial, and septal regions were analyzed. Data was interpreted as Mean Fluorescent Intensity (MFI) corresponding to each of the four channels: AF408, AF488, AF594, and AF647, and expressed as Arbitrary Units (A.U.). The MFI from each channel of arbitrarily selected background ROIs (or neutral non-tissue sections) were averaged and subtracted from the MFI of each channel from the four chambers as a method for normalizing each section to its slide.

Minimal Feret Diameter: To quantify individual cardiomyocyte size, a blinded analysis was conducted using the WGA (cellular membrane) filter on sagittal IF sections. Twenty arbitrarily selected cardiomyocytes from the top (mitral annulus), middle, and bottom (near-apex) portions of each ventricle (endocardial/non-fibrotic region) were free hand traced (ImageJ), pooled together, and averaged to obtain a mean cardiomyocyte diameter (μm) for each ventricle.

Western blotting

Hearts were excised, promptly weighed, and subsequently flash frozen in liquid nitrogen. Heart weights were normalized to both body weight and tibial length. Western blotting was performed using standard SDS-PAGE procedures. A frozen section of each ventricle (~10-15 mg in size for RV and ~20-25 mg for LV) was homogenized using plastic microcentrifuge tubes and an

ultrawave Sonic Dismembrator Model 500 (Thermo Fisher Scientific) in ice-cold lysis buffer containing (in mM) 20 Tris/HCl, 150 NaCl, 1 EDTA, 1 EGTA, 2.5 $Na_4O_7P_2$, 1 Na_3VO_4, and 1% Triton X-100, supplemented with protease and phosphatase inhibitors (Millipore Sigma) (pH 7.0), as previously published [433,434]. Protein concentrations were determined using a bicinchoninic acid (BCA) assay (Life Technologies, Carlsbad, CA, USA). Denatured and reduced protein was subjected to SDS-PAGE on 10-14% gels followed by transfer onto 0.2 μm low-fluorescence polyvinylidene difluoride membrane (Bio-Rad, Mississauga, Canada) and blocked with Li-COR Intercept Blocking Buffer for 1 hour (LI-COR, Lincoln NE, USA). Membranes were then immunoblotted overnight (4°C) with the specific primary antibodies listed below.

To quantify mitochondrial electron transport chain complex subunits (including V-ATP5A (55 kDa), III-UQCRC2 (48 kDa), IV-MTCO1 (40 kDa), II-SDHB (30 kDa), and I-NDUFB8 (20 kDa)), a commercially available monoclonal rodent OXPHOS cocktail was used (Cat. No. ab110413; 1:1000) (Abcam). Commercially available polyclonal antibodies were used to detect AMPKα (Cat. No. 2532; 62 kDa; 1:500), p-AMPKα (Thr172) (Cat. No. 2535; 62 kDa; 1:500), p38MAPK (Cat. No. 9212; 40 kDa; 1:500), p-p38MAPK (Thr180/Tyr182) (Cat. No. 9211; 43 kDa; 1:500), LC3BII/I (Cat. No. 2775S; 14/16 kDa; 1:500), and a monoclonal antibody was used to detect SQSTM1/p62 (Cat. No. 23214S; 62 kDa; 1:500) (Cell Signaling Technology, Whitby, Ontario).

Following an overnight primary antibody incubation, membranes were washed 3x5 minutes in TBS-T, and incubated at room temperature with the appropriate infrared fluorescent secondary antibody (LI-COR IRDye 680nm (Cat. No. 925-68020) or 800nm (Cat. No. 925-32214)) at previously optimized dilutions (1:10,000 to 1:20,000). Immunoreactive proteins were detected

using infrared imaging (LI-COR CLx; LI-COR, Lincoln, NE, USA) and quantified on ImageJ by densitometry. All images were normalized to total protein from the same corresponding membrane using Amido Black total protein stain (Cat. No. A8181) (Millipore Sigma).

Preparation of permeabilized muscle fibre bundles

Mitochondrial bioenergetic assays were performed using permeabilized muscle fiber bundle (PmFB) preparations from heart tissue as we have described previously [34,432,435]. Upon sacrifice, the heart was immediately submerged in ice-cold ATP-containing media (BIOPS buffer) designed to mimic the extracellular environment. Tissue was carefully separated with precision forceps into small (0.6-1.6 mg) bundles that were blotted dry using a Kimwipe and weighed in 1.5 mL tared ice-cold BIOPS. Respiration values were normalized to fibre bundle wet weight. Extra precaution was taken when separating the tissue such that collagenous (non-respiring) regions were avoided when preparing bundles, however, some bundles may have had larger non-respiring regions than others. Bundles were permeabilized in BIOPS that contained saponin (40 μg/ml) for 30 mins at 4°C on a rotator, which digests the cell membrane and allows the cytosol to be washed out by selectively permeabilizing the sarcolemma and leaving other intracellular organelles intact.

Mitochondrial respiration

High-resolution respirometry (measure of mitochondrial oxygen consumption) was performed on heart PmFBs using the Oroboros Oxygraph-2k (OROBOROS Instruments, Corp., Innsbruck, Austria). PmFBs were submerged in 2 mL Buffer Z containing (in mM) 105 K-MES, 30 KCl, 10 KH_2PO_4, 5 $MgCl_2 \bullet 6H_2O$, 1 EGTA, and 5 mg/mL BSA, in the respirometer chambers in the presence of 5 μM blebbistatin to prevent contraction of PmFBs by rigor in response to ADP

while stirring at 750 RPM and 37°C [435]. Chambers were manually oxygenated with 100% O_2 to an initial concentration of ~350 μM and experiments were completed prior to chamber [O_2] dropping past 150 μM to prevent oxygen limitations to respiration.

Oxygen consumption was measured in either Buffer Z devoid of creatine (Cr) to prevent activation of mitochondrial creatine kinase (mtCK) (creatine-independent), or in Buffer Z with 20 mM Cr to saturate mtCK and promote phosphate shuttling through this complex (creatine-dependent) as performed previously [436].

For each heart, one PmFB from each ventricle was used to assess complex-I supported respiration using pyruvate (5 mM; carbohydrate substrate) and malate (2 mM) (NADH; State II respiration) followed by titrations of basal (25 μM), sub-maximal (100 and 500 μM), and saturating ADP (1000 and 5000 μM) to assess mitochondrial responsiveness to ADP across a range of metabolic demands (State III coupled respiration) [437]. Following ADP titrations, 10 mM glutamate was added to further saturate complex-I with NADH generation. Next, 10 μM cytochrome *c* was added to test mitochondrial outer membrane integrity. Anomalous cytochrome *c* responses (over 15%), where ADP-stimulated respiration was correspondingly low, were selectively removed. 10 mM succinate ($FADH_2$-stimulating) was then added to support complex-II respiration [437].

In a separate PmFB from each ventricle, a fatty acid-based protocol was implemented with 10 μM L-Carnitine, 20 μM Palmitoyl-CoA, and 500 μM malate to shuttle electrons through beta-oxidation pathways [438]. This protocol generates NADH (Complex I stimulation) and $FADH_2$ from β-oxidation (ETF stimulation) and the TCA cycle (Complex II stimulation). A similar ADP titration protocol was then performed as described above. Following ADP titrations, 10 μM cytochrome *c* was added.

Mitochondrial H_2O_2 Emission (mH_2O_2)

mH_2O_2 emission was detected spectrofluorometrically (QuantaMaster 40, HORIBA Scientific, Irvine, CA, USA) as previously described [432]. Assays were conducted in Buffer Z supplemented with 10 μM Amplex Ultra Red (AUR) (an H_2O_2 fluorogenic probe) (Life Technologies), 1 U/mL horseradish peroxidase (HRP), 1 mM EGTA, 40 U/mL Cu-Zn SOD1, 5 μM blebbistatin, and 20 mM Cr.

Two protocols were implemented in separate PMFBs, as follows. In protocol 1, maximal mH_2O_2 in the absence of ADP (State II), was induced using the complex I-supporting substrates pyruvate (10 mM) and malate (2 mM) (NADH; forward electron flow). Next, stepwise ADP concentrations (25-100 μM (physiological ranges) and 500 μM (saturating for suppression of mH_2O_2) were titrated progressively to determine ADP's ability to suppress mH_2O_2 and in the presence of 20 mM Cr [437]. In protocol 2, (separate PmFB), 10 mM succinate (State II) was added to stimulate mH_2O_2 by reverse electron flow from complex-II ($FADH_2$) to complex-I followed by ADP titrations as performed in Protocol 1. To assess the effects of creatine-dependent cycling of adenylates (ADP/ATP) on mH_2O_2 attenuation, the succinate protocols were repeated in a separate PmFB in the absence of creatine in the buffer given creatine enhances the ability of ADP to attenuate mH_2O_2 [300].

At culmination of the protocol, bundles were collected and lyophilized in a freeze-dryer (Labconco, Kansas City, MO, USA) for ~4 hours and weighed using a microbalance (Sartorius Cubis Microbalance, Gottingen, Germany). Rate of mH_2O_2 was calculated using a standard curve in identical assay conditions. Values were normalized to fibre bundle dry weight.

Calcium retention capacity

Mitochondrial calcium retention capacity (CRC) was performed as previously described [392]. Prior to commencing each experiment, a cuvette lined with 10 mM EGTA in ~500 uL deionized water was placed on a stir plate at room temperature for at least 10 mins. Water was aspirated without rinsing to allow EGTA to coat the cuvette, thus ensuring that residual Ca^{2+} in the assay buffer (Buffer Y) would be chelated. Experiments were measured spectrofluorometrically (QuantaMaster 80, HORIBA Scientific) at 37°C and continuous stirring in a cuvette with 300 µL Buffer Y containing 1 µL Calcium Green-5N (Invitrogen) as a fluorescent probe specific to Ca^{2+}, 2 µM thapsigargin (to inhibit SERCA), 5 µM blebbistatin, and 40 µM EGTA. For each experiment, minimum fluorescence (Fmin) was obtained by first adding 5 mM glutamate, 2 mM malate, and 500 µM ADP to Buffer Y containing the PmFB. Following these additions, a single 8 nmol bolus of $CaCl_2$ was titrated into the cuvette, followed by subsequent 4 nmol boluses until mitochondrial permeability transition (mPT) occurred, as reflected by an increase in fluorescence representing Ca^{2+} release from saturated mitochondria. Once mPT was established, two additional saturating boluses of 0.5 mM $CaCl_2$ were titrated to saturate the fluorophore and establish a maximum fluorescence (Fmax). To calculate changes in free Ca^{2+} in the cuvette as an outcome of mitochondrial Ca^{2+} uptake, the known Kd for Calcium Green-5N and equations for calculating free ion concentration were utilized [432]. Once an Fmax was established, PmFBs were carefully recovered and lyophilized in a freeze-dryer overnight and weighed on a microbalance for dry weight trace normalization.

Caspase activity assay

Caspase activity was measured in whole-muscle lysates that were prepared in the absence of protease inhibitors, as described elsewhere [439]. Lysis buffer consisted of (in mM): 20 HEPES,

10 NaCl, 1.5 MgCl2, 1 DTT, 20% glycerol, and 0.1% Triton X-100. Briefly, samples were incubated at room temperature in 20 μM Ac-DEVD-AFC (caspase-3), Ac-LEHD-AFC (caspase-9), or Ac-IETD-AMC (caspase-8) in assay buffer containing 20 mM HEPES, pH 7.4, 10 mM DTT, and 10% glycerol. Fluorescence was measured at room temperature using a Cytation 5 Imaging Multi-Mode Reader with excitation (400 nm) and emission (505 nm) wavelengths for AFC substrates (Caspase-3 and Caspase-9). Excitation (360 nm) and emission (440 nm) wavelengths were utilized for AMC substrates (Caspase-8). Values were normalized to protein concentration of samples and expressed as a fold change in fluorescence.

Flow cytometry

Heparinized mice were anesthetized with isoflurane and placed into a nose cone with continuous vaporization. The RV was perfused with 7 mL pre-warmed (37°C) EDTA buffer (pH 7.8) to chelate calcium and prevent aggregation of cells. The heart was then removed and placed into a shale plate containing EDTA buffer, followed by perfusion into the LV with 10 mL EDTA to remove remaining blood. The heart was then perfused with 3.5 mL pre-warmed perfusion buffer (pH 7.8) to arrest the heart in diastole. Upon taking whole heart weight, RV and LV were surgically separated, washed with remaining perfusion buffer, and were subsequently dried and weighed. Finely minced pieces of each ventricle were digested for 60 mins at 37°C on a 140 RPM shaker in DMEM containing DNase I (60 U/mL) (Sigma; Cat no. 11284932001), collagenase type II (450 U/mL) (Worthington; Cat no. LS004176), and hyaluronidase (60 U/mL) (Sigma; Cat no. h3506). Digested chamber-specific tissue was then filtered through 100 μM cell strainers (Miltenyi Biotec) and washed with 5 mL DMEM + 20% FBS into 15 mL conical tubes. Samples then underwent centrifugation for 5 mins at 4°C and 500 RCF. With only 2 mL remaining in the conical tubes, the pellets were resuspended, and fractions were separated into

'unstained' and 'full stained' 1.5 mL tubes. Following another identical centrifugation protocol, pellets were resuspended in FACS buffer (DPBS containing 2 mL FBS stock and 1 mM EDTA). FC block (Thermo Fisher; Cat no. 14-0161-85) was added to all tubes to prevent auto-antibody binding, and tubes were incubated on a shaker at room temperature for 15 mins. Additional FACS buffer was added to all unstained tubes while equal volume cell surface marker antibody master mix was added into the full stained tubes. All tubes were kept away from light and were incubated for 30 mins at 4°C on a shaker. Samples were then centrifuged again (same protocol), resuspended in FACS buffer and intracellular (IC) fixation buffer (Thermo Fisher; Cat no. 00-8222-49), and were once again incubated for 30 mins at 4°C on a shaker. After one final centrifugation (same protocol), pellets were resuspended in 1 mL FACS buffer and stored in a dark, humidity-controlled 4°C fridge for subsequent processing using the Cytek Aurora 5-laser spectral flow cytometer (CytekBio).

Cell surface marker antibody master mix
CD45 – 1:1200 – Thermo Fisher Cat no. 64-0451-82 – 30-F11 AF700
CD11b – 1:1000 – Thermo Fisher Cat no. 63-0112-82 – M1/70 SB600
CD64 – 1:800 - Thermo Fisher Cat no. 17-0641-82 - X54-5/7.1 APC
F4/80 – 1:600 – BioLegend Cat no. 10630 – BV650
CCR2 – 1:100 – BioLegend Cat no. 13354 - FITC

Statistics

All results are expressed as mean ± SD. Outliers were identified and excluded in accordance with ROUT testing (Q=0.5%). Subsequently, the D'Agostino-Pearson Omnibus normality parameters were performed to determine if data resembled a Gaussian (normal), or lognormal distribution (GraphPad Prism 9.3.0 Software, La Jolla, CA, USA). Complex I-stimulated respiration in both 20 mM Cr and No Cr conditions in the LV failed normality – therefore, relevant datasets were log-transformed, and we subsequently conducted standard parametric two-way ANOVA testing.

All other datasets passed normality. A two-way ANOVA was used for ADP-stimulated mitochondrial respiration and ADP-suppression of mH_2O_2, followed by Benjamini, Krieger, and Yekutieli's *post hoc* analysis to correct for false discovery rate when a significant interaction was observed [440]. A one-way ANOVA was conducted for morphometric, Western blot, histopathology (fibrosis and myocardial disorganization), and immunofluorescence, followed by *post hoc* analyses where relevant. Significance was established at $p < 0.05$ for all statistics. While corrected *p*-values are typically reported as q-values with the Benjamini, Krieger, and Yekutieli's *post-hoc* analysis, we herein report them as *p*-values.

Acknowledgements

ALY688 was provided by Allysta Pharmaceuticals.

Funding was provided to C.G.R.P. by Allysta Pharmaceuticals, the National Science and Engineering Research Council (no. 436138-2013) and an Ontario Early Researcher Award (C.G.R.P., no. 2017-0351) with infrastructure supported by Canada Foundation for Innovation, the James. H. Cummings Foundation, and the Ontario Research Fund. S.G. was supported by an Ontario Graduate Scholarship.

Supplementary Data – To be included in publication

SFigure 1

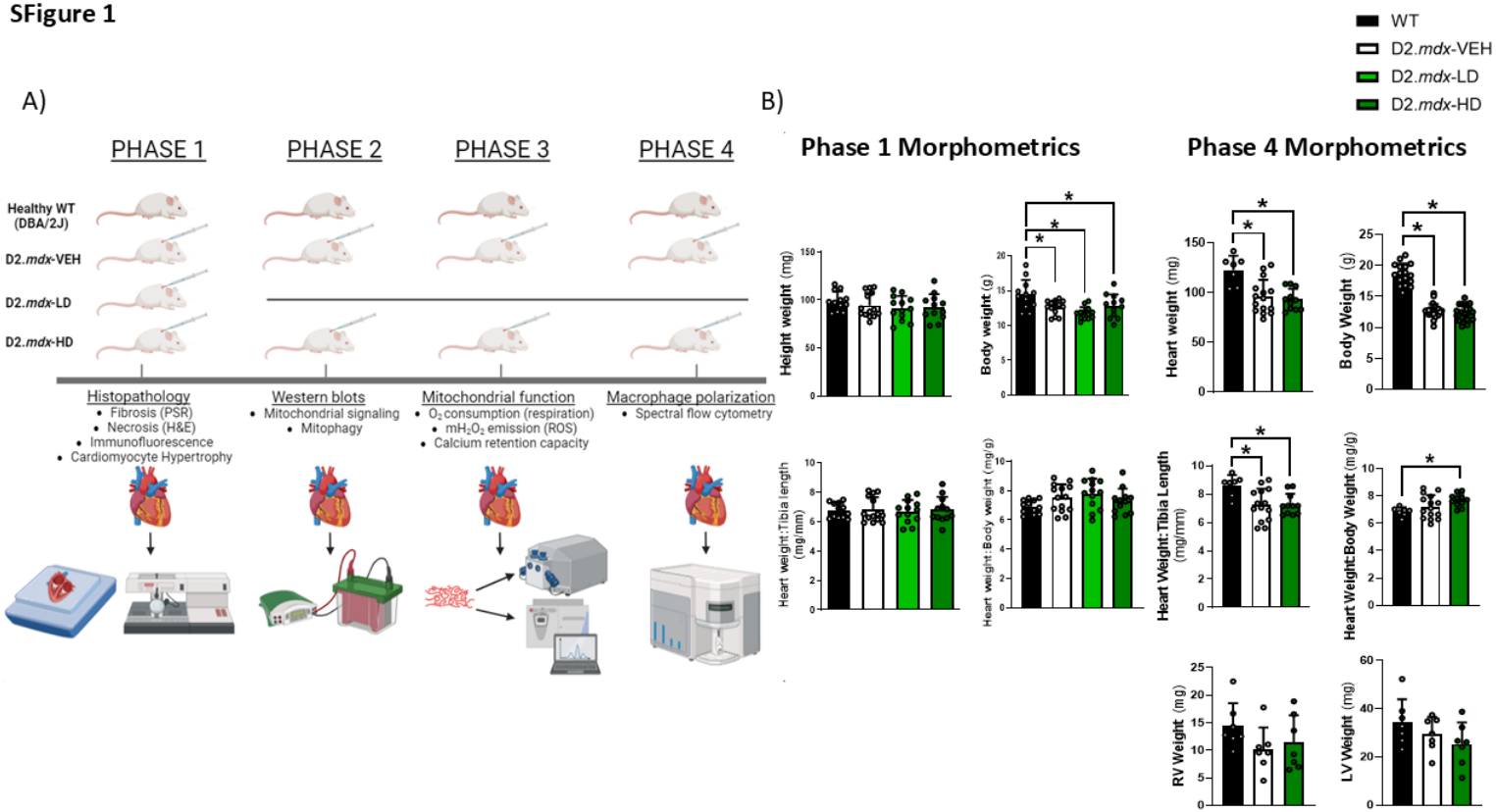

SFigure 4-1. Study design and corresponding timeline of data collection phases, with morphometric data from 4-week-old WT, D2.*mdx*-LD (phase 1 only), D2.*mdx*-VEH, and D2.*mdx*-HD. A) To collect chamber-specific data for all measures with a sufficient sample size, four phases of in-house breeding and daily injections were required. D2.*mdx*-LD mice were dropped following the first phase due to logistical considerations. B) Specific comparisons include heart weight (mg), body weight (g), heart weight normalized to tibia length (mg/mm), heart weight normalized to body weight (mg/g), and ventricle-specific weights (phase 4 only). Results represent mean ± SD; n=7-14. All *p* values are FDR-adjusted by Benjamini, Krieger, and Yekutieli *post-hoc* analyses. **p*<0.05 denotes significance. Figure (SF 4-1A) created using www.BioRender.com.

SFigure 2

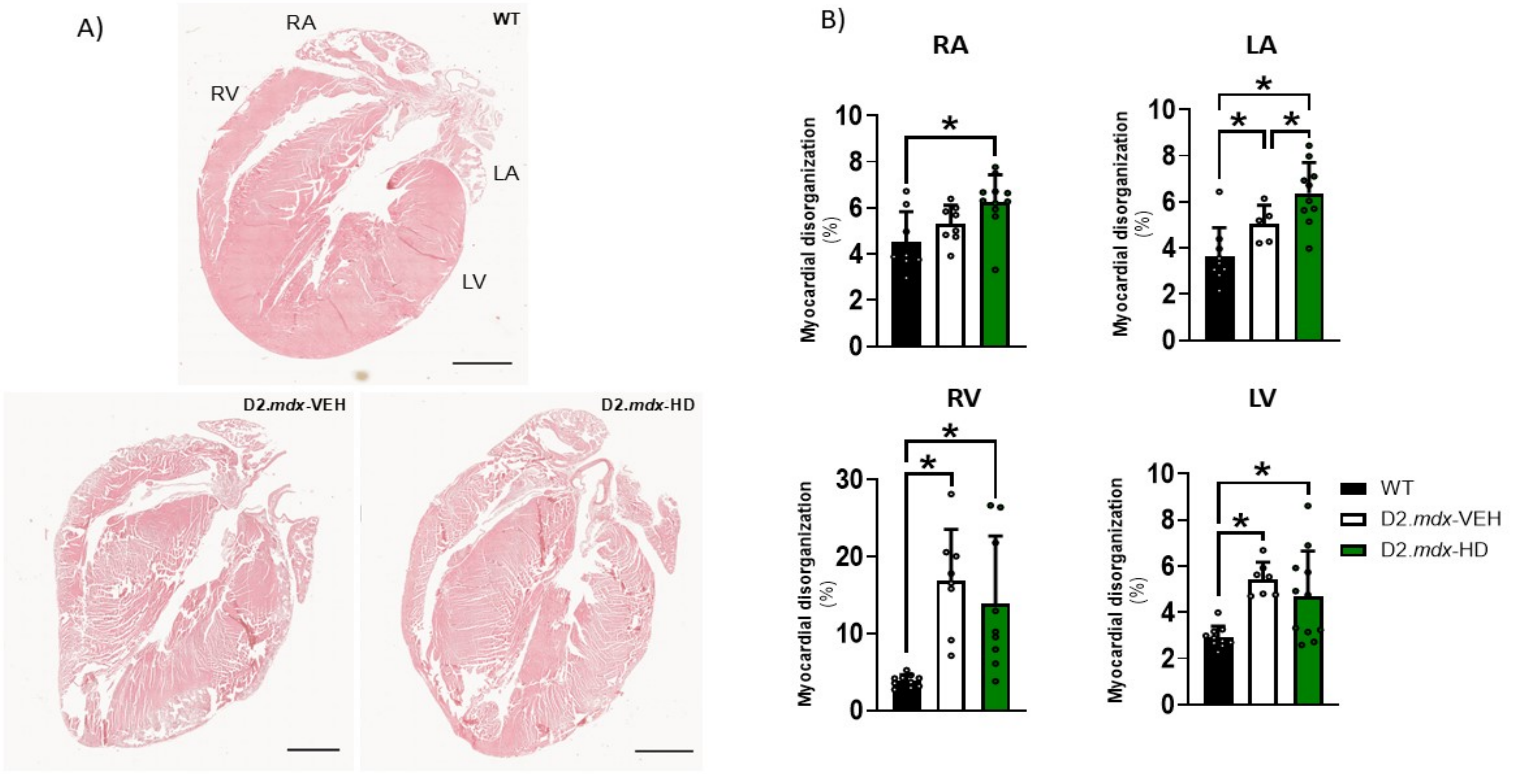

SFigure 4-2. D2.*mdx* mice demonstrate robust myocardial disorganization across various chambers which is not prevented by ALY688. A) D2.*mdx* mice exhibit myocardial disorganization (represented as a % of total tissue), which is defined by loss of nuclear detail and the presence of coalescing nuclei as detected with H&E staining. B) D2.*mdx*-VEH exhibit increased myocardial disorganization in the RV, but this was not protected by ALY688. Comparable results were demonstrated within the LV in D2.*mdx*-VEH. Images were taken with EVOS M7000 Imaging System at 4x magnification. Results represent mean ± SD; n=5-11. Scale bars are 1 mm. All *p* values are FDR-adjusted by Benjamini, Krieger, and Yekutieli *post-hoc* analyses. *$p<0.05$ denotes significance.

SFigure 3

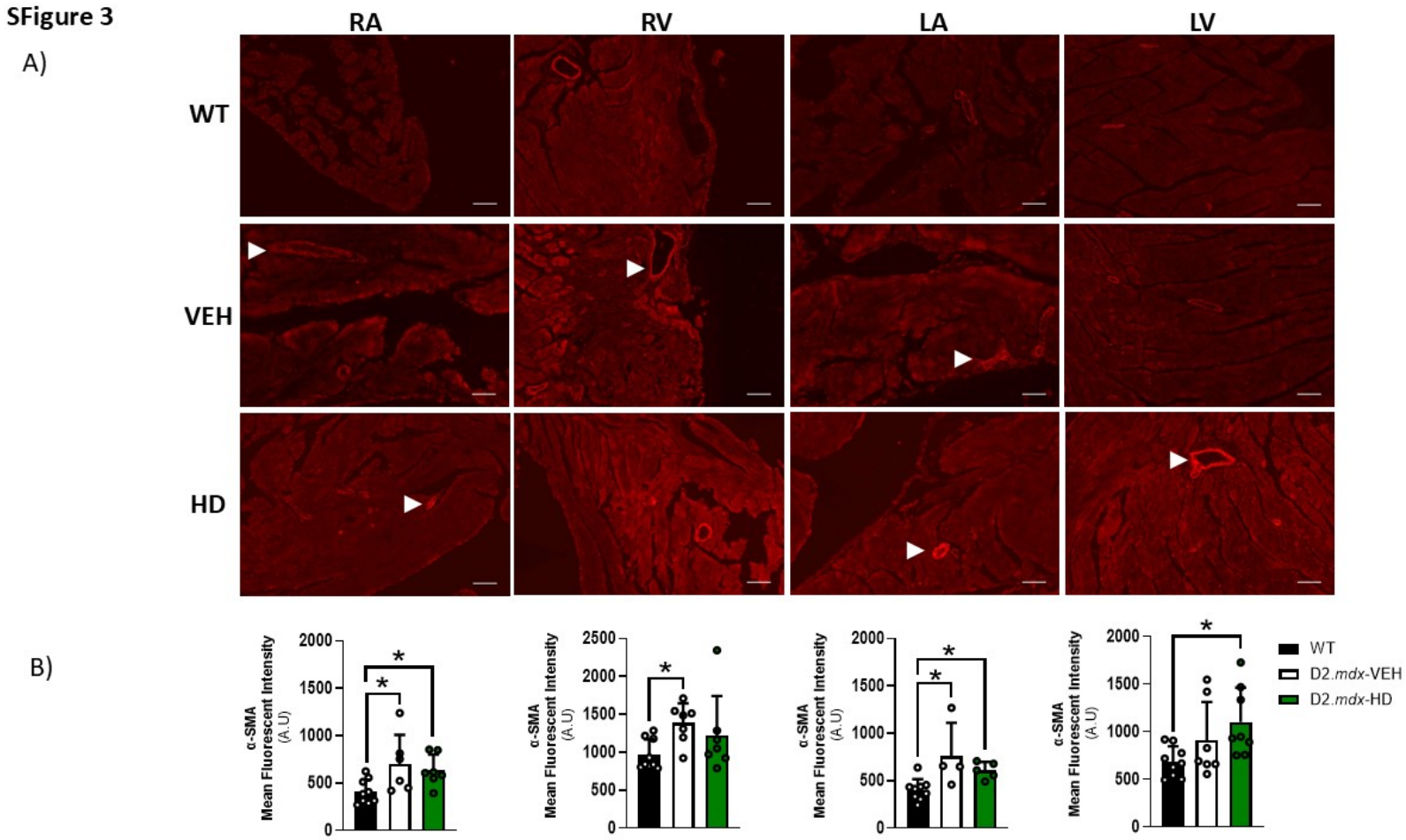

SFigure 4-3. Chamber-specific immunofluorescent staining reveals distinct differences in α-SMA across groups in D2.*mdx* mice. A) D2.*mdx*-VEH demonstrate elevated α-SMA compared to WT in the RA, RV, and LA. D2.*mdx*-HD demonstrate elevated α-SMA in the RA, LA, and LV. α-SMA (denoted by white arrows) was quantified by Mean Fluorescent Intensity (A.U.) per region of interest (B). Whole atria and free-wall segments of the ventricles were analyzed. Stains were conducted on 5 µm thick paraffin-embedded sagittal sections and imaged by confocal microscopy at 20x magnification. Results represent mean ± SD; n=4-9. Scale bars are 100 µm. All *p* values are FDR-adjusted by Benjamini, Krieger, and Yekutieli *post-hoc* analyses. *$p<0.05$ denotes significance. WT = Wildtype mouse; VEH = vehicle (saline)-treated *mdx*; HD = high dose (ALY688)-treated *mdx*; RA = right atrium; LA = left atrium; RV = right ventricle; LV = left ventricle.

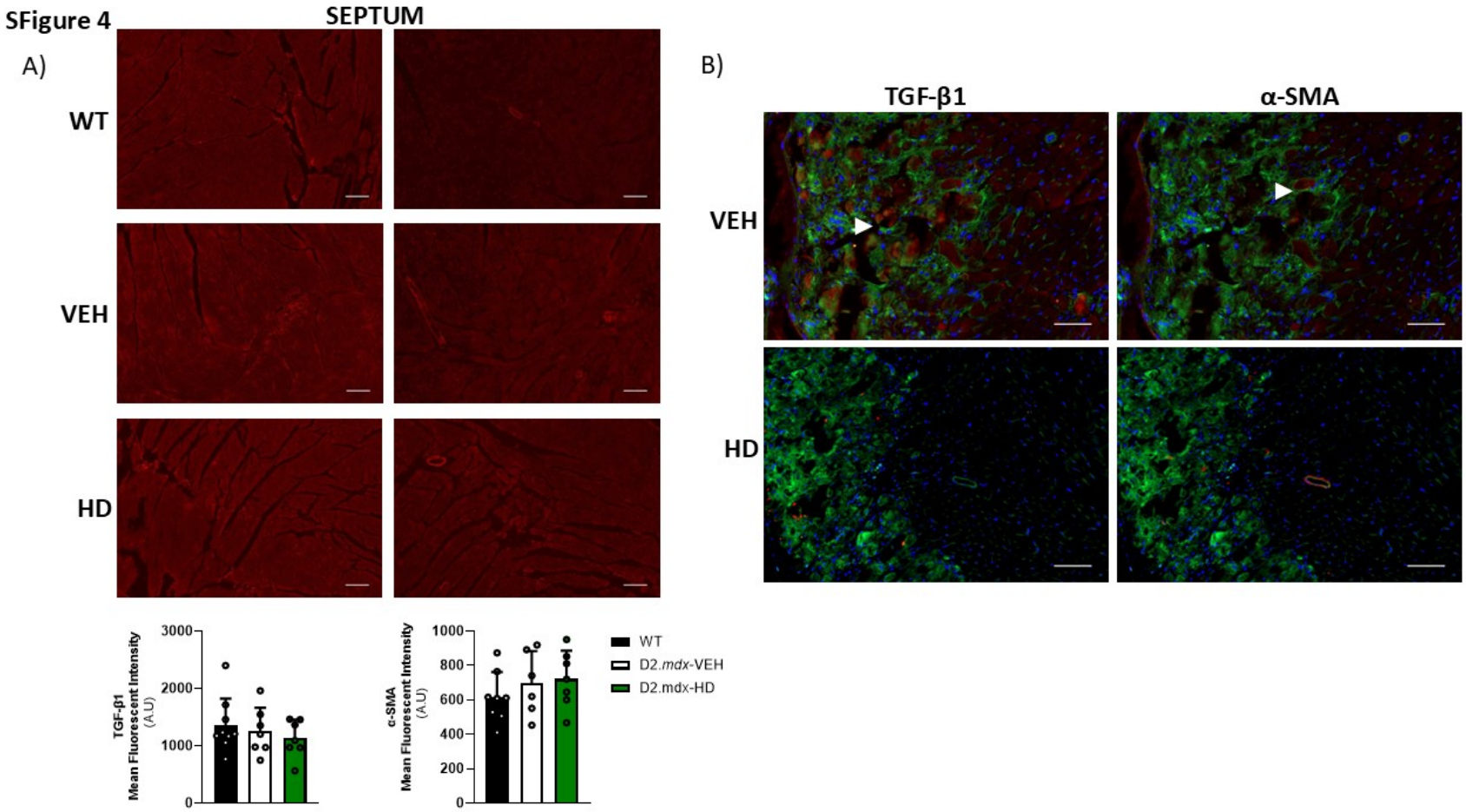

SFigure 4-4. Septum-specific immunofluorescent staining reveals no differences in TGF-β1 or α-SMA between any of the groups. B) When examining presence of TGF-β1 or α-SMA in the fibrotic (epicardial RV) regions of D2.*mdx*-VEH and D2.*mdx*-HD, it was determined qualitatively that VEH mice exhibited more of both compared to HD. Statistics could not be tested due to low sample size. n=6-10 (septum). Scale bars are 100 μm. WT = Wildtype mouse; VEH = vehicle (saline)-treated *mdx*; HD = high dose (ALY688)-treated *mdx*.

SFigure 5

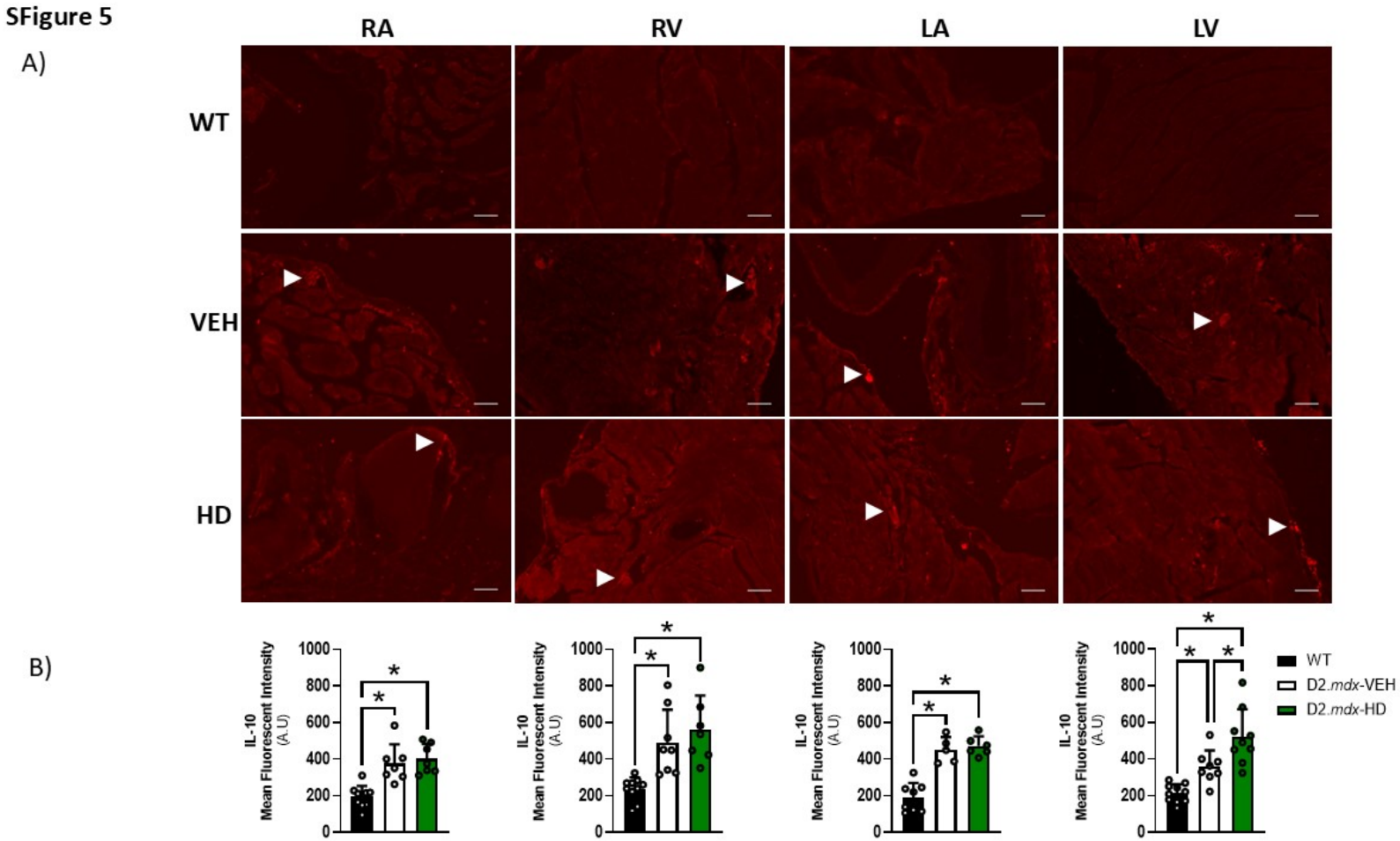

SFigure 4-5. Chamber-specific immunofluorescent staining reveals that dystrophin deficiency causes elevated IL-10 compared to WT mice, which is further elevated by ALY688 in LV of D2.*mdx* mice. A) IL-10 (denoted by white arrows) was quantified by Mean Fluorescent Intensity (A.U.) per region of interest (B). Whole atria and free-wall segments of the ventricles were analyzed. Stains were conducted on 5 µm thick paraffin-embedded sagittal sections and imaged by confocal microscopy at 20x magnification. Results represent mean ± SD; n=5-10. Scale bars are 100 µm. All *p* values are FDR-adjusted by Benjamini, Krieger, and Yekutieli *post-hoc* analyses. *$p<0.05$ denotes significance. WT = Wildtype mouse; VEH = vehicle (saline)-treated *mdx*; HD = high dose (ALY688)-treated *mdx*; RA = right atrium; LA = left atrium; RV = right ventricle; LV = left ventricle.

SFigure 6

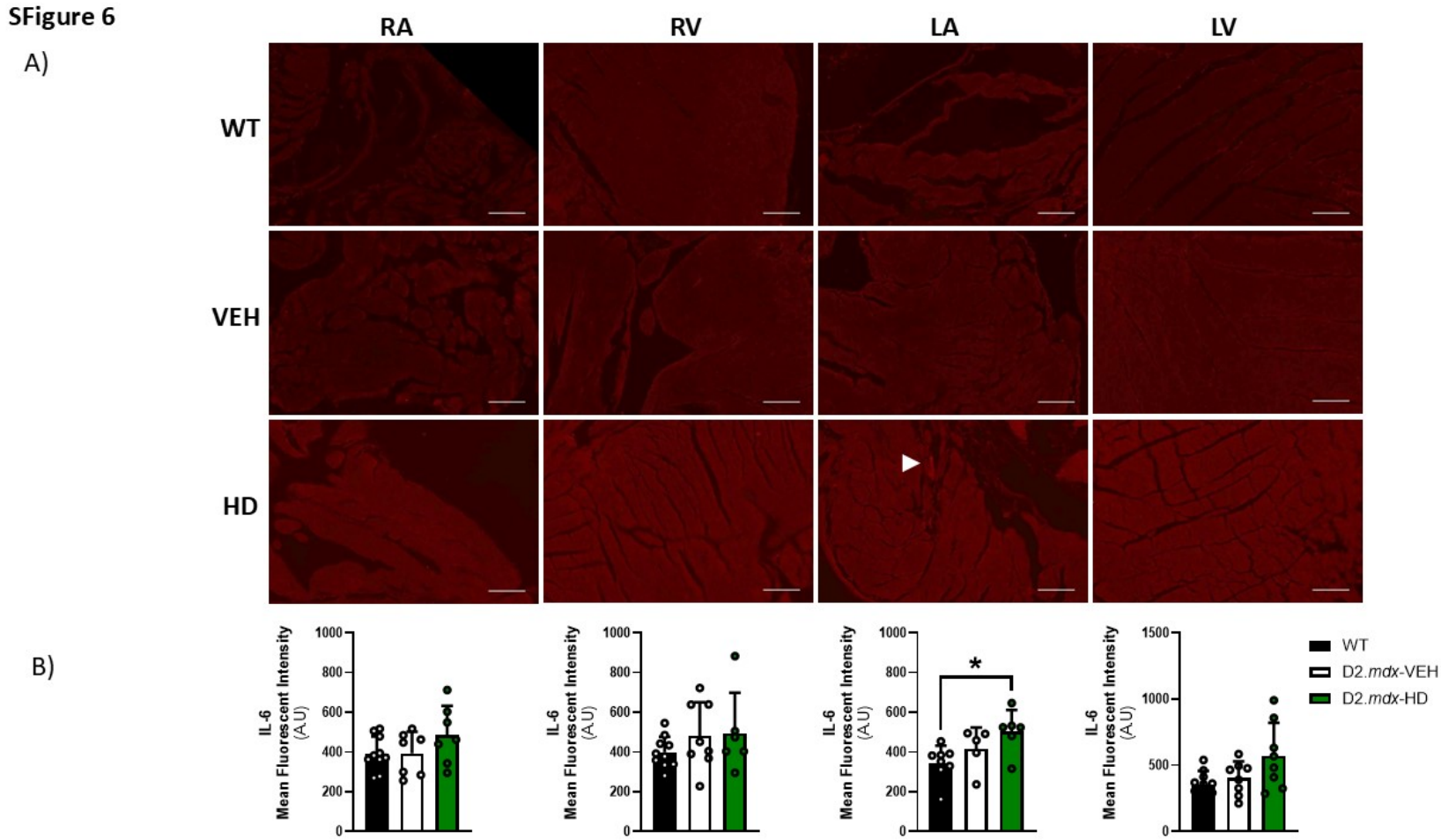

SFigure 4-6. Chamber-specific immunofluorescent staining reveals that D2.*mdx*-HD mice demonstrate elevated IL-6 compared to WT in the LA. A) IL-6 (denoted by white arrow) was quantified by Mean Fluorescent Intensity (A.U.) per region of interest (B). Whole atria and free-wall segments of the ventricles were analyzed. Stains were conducted on 5 μm thick paraffin-embedded sagittal sections and imaged by confocal microscopy at 20x magnification. Results represent mean ± SD; n=5-10. Scale bars are 100 μm. All *p* values are FDR-adjusted by Benjamini, Krieger, and Yekutieli *post-hoc* analyses. *$p<0.05$ denotes significance. WT = Wildtype mouse; VEH = vehicle (saline)-treated *mdx*; HD = high dose (ALY688)-treated *mdx*; RA = right atrium; LA = left atrium; RV = right ventricle; LV = left ventricle.

SFigure 7

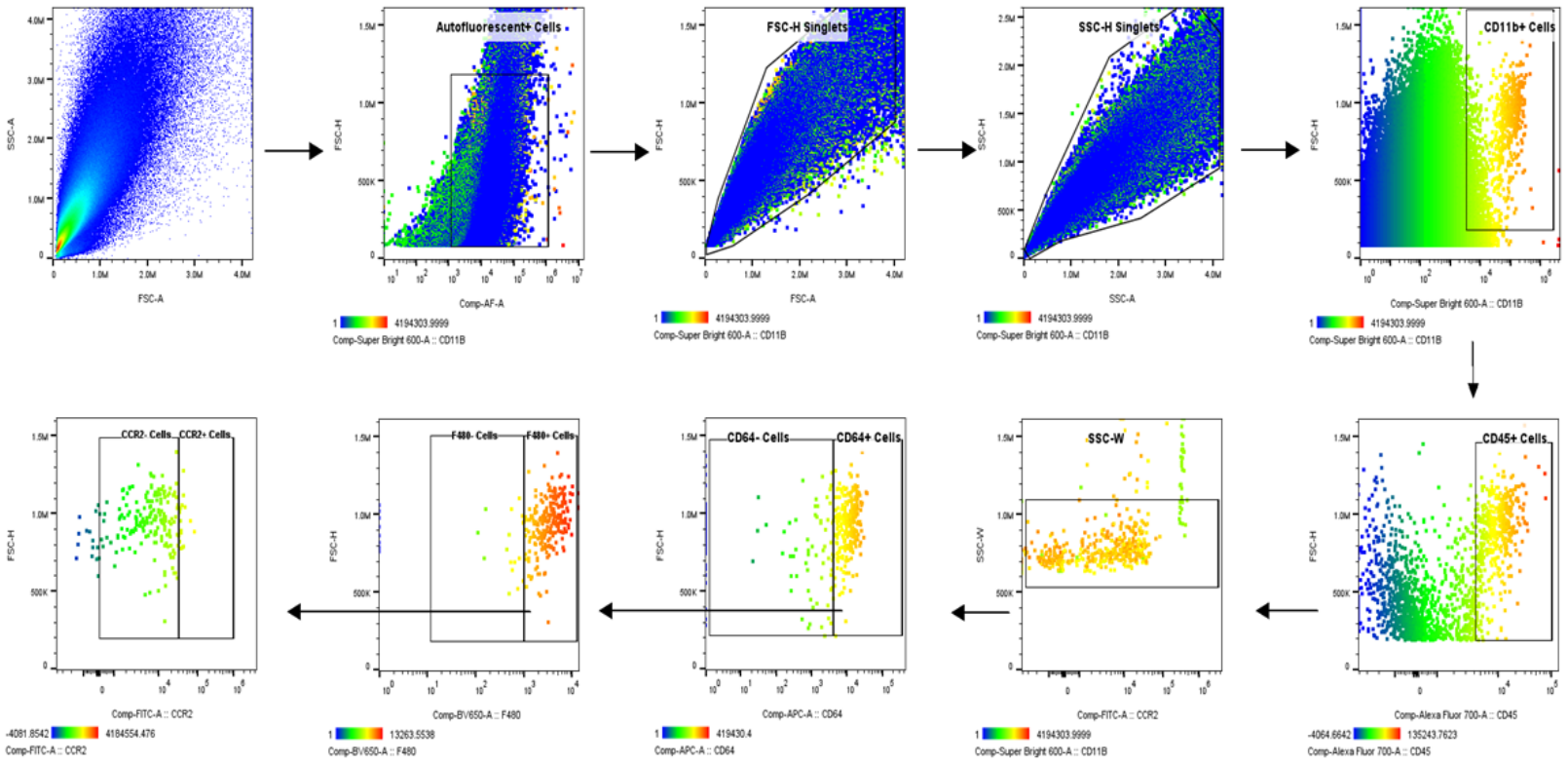

SFigure 4-7. Representative spectral flow cytometry gating scheme demonstrating how specific immune cell populations were gated. Gating scheme includes several quality control checks to exclude cell aggregates and debris which may contribute to artefacts in cell count. Corresponding serotype for this gating scheme is CD11b^{+}CD45^{+}CD64$^{+/-}$F4/80$^{+/-}$CCR2$^{+/-}$, retrieved from a D2.*mdx*-HD RV.

SFigure 8

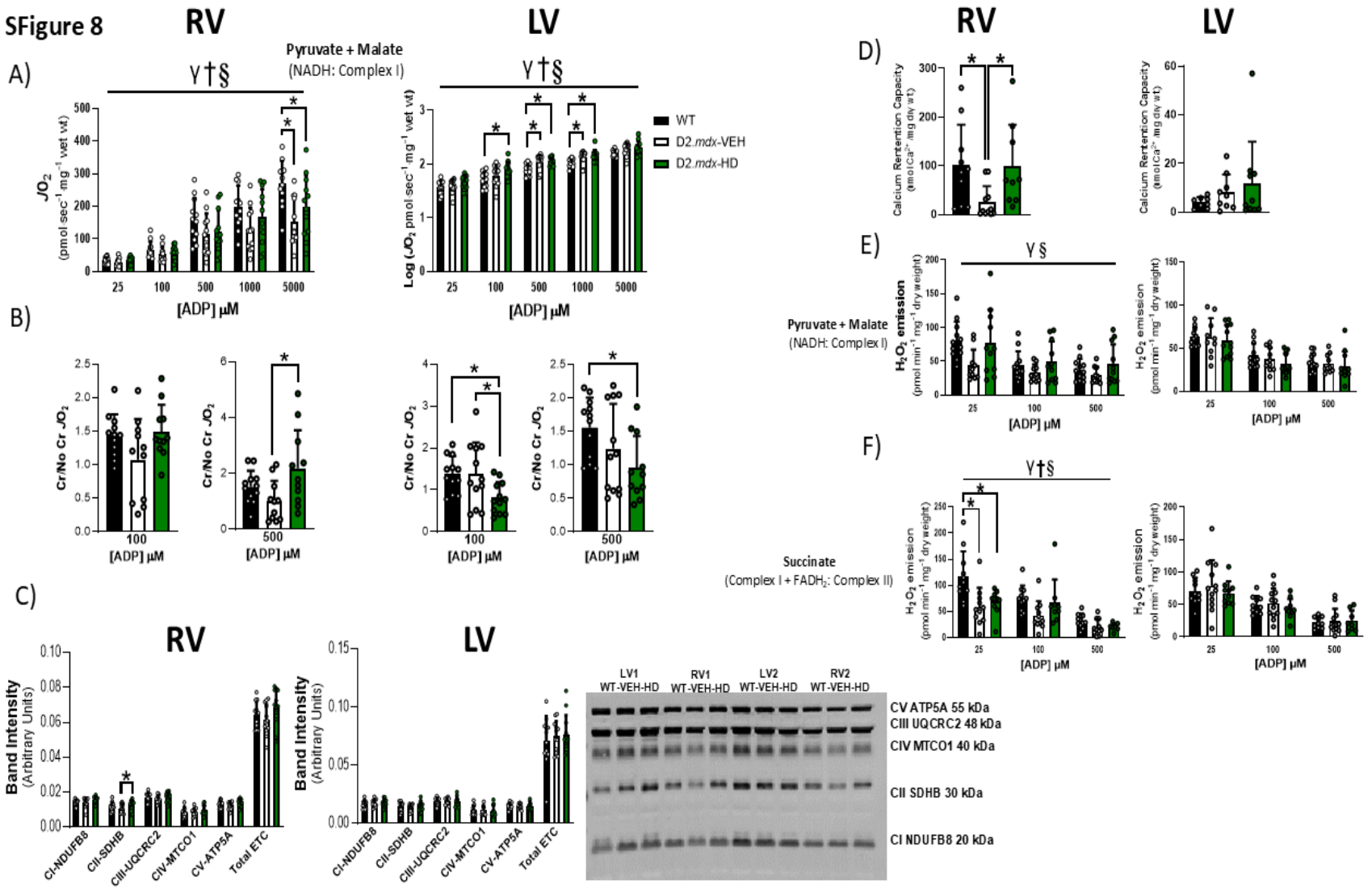
RV
LV
A)
Pyruvate + Malate
(NADH: Complex I)
γ†§
WT
D2.mdx-VEH
D2.mdx-HD
[ADP] µM
B)
C)
Band Intensity
(Arbitrary Units)
CI-NDUFB8
CII-SDHB
CIII-UQCRC2
CIV-MTCO1
CV-ATP5A
Total ETC
LV1 WT-VEH-HD
RV1 WT-VEH-HD
LV2 WT-VEH-HD
RV2 WT-VEH-HD
CV ATP5A 55 kDa
CIII UQCRC2 48 kDa
CIV MTCO1 40 kDa
CII SDHB 30 kDa
CI NDUFB8 20 kDa
D)
Calcium Retention Capacity
E)
Pyruvate + Malate
(NADH: Complex I)
F)
Succinate
(Complex I + FADH2: Complex II)

SFigure 4-8. Mitochondrial respiratory control by ADP during oxidative phosphorylation is prevented by ALY688 in the absence of creatine, while mitochondrial stress responses (indicated by CRC and H_2O_2) differ between ventricles and are only partially prevented by ALY688. A) Across various metabolic demands, oxygen consumption by mitochondria that is blunted in D2.*mdx*-VEH is prevented in D2.*mdx*-HD in the RV. In the LV, D2.*mdx*-VEH demonstrate elevated mitochondrial oxygen consumption compared to WT, and this is further elevated in D2.*mdx*-HD compared to D2.*mdx*-VEH. All experiments were conducted using the Complex-I-stimulating (NADH-generating substrates 5 mM pyruvate and 2 mM malate) in the absence of creatine. Results represent mean ± SD; n=10-12. LV data was log-transformed given that it did not pass normality testing. **p*<0.05 denotes significance. Main effects are denoted by horizontal bar - γ*p*<0.05 WT vs D2.*mdx*-VEH; §*p*<0.05 D2.*mdx*-VEH vs D2.*mdx*-HD; †*p*<0.05 WT vs D2.*mdx*-HD. B) Ventricle-specific creatine sensitivity using 100 and 500 μM ADP reveals a complex relationship whereby the D2.*mdx*-HD exhibit elevated Cr/No Cr JO_2 compared to D2.*mdx*-VEH in the RV using 500 μM ADP, while in the LV at 100 μM ADP, creatine sensitivity in D2.*mdx*-HD is significantly decreased compared to both WT and D2.*mdx*-VEH and only significantly decreased compared to WT at 500 μM ADP. n=10-12. **p*<0.05 denotes significance. C) OXPHOS content Western blot reveals differences whereby lower Complex-II subunit SDHB protein content in D2.*mdx*-VEH is prevented by ALY688 only in RV. No differences in other subunit or pooled ETC was detected in either ventricle. N=11-12. Results represent mean ± SD. **p*<0.05 denotes significance. D) In the RV, D2.*mdx*-VEH demonstrate significantly blunted mitochondrial CRC compared to WT, which is prevented in D2.*mdx*-HD, when examining pooled data of mPT and no mPT PmFBs. No differences were detected in the LV. Results represent mean ± SD; n=8-11. **p*<0.05 denotes significance. E) D2.*mdx*-VEH mice exhibit decreased mitochondrial Complex I-supported (pyruvate + malate) forward electron transfer mH_2O_2 compared to WT exclusively in the RV in the presence of saturating creatine, which is surprisingly elevated in D2.*mdx*-HD compared to D2.*mdx*-VEH across various metabolic demands but is not different compared to WT. N=10-12. Results represent mean ± SD. Main effects are denoted by horizontal bar - γ*p*<0.05 WT vs D2.*mdx*-VEH; §*p*<0.05 D2.*mdx*-VEH vs D2.*mdx*-HD. F) When assessing mitochondrial Complex I+II-supported (succinate) reverse electron transfer H_2O_2 emission in the presence of saturating creatine, it was again observed that D2.*mdx*-VEH had lower mH_2O_2 compared to WT, which was also decreased in D2.*mdx*-HD at 25 μM ADP. Results represent mean ± SD. **p*<0.05 denotes significance. Main effects are denoted by horizontal bar - γ*p*<0.05 WT vs D2.*mdx*-VEH; §*p*<0.05 D2.*mdx*-VEH vs D2.*mdx*-HD; †*p*<0.05 WT vs D2.*mdx*-HD. No differences were detected in the LV using either substrate protocol (pyruvate + malate or succinate). N=8-12. All p values are FDR-adjusted by Benjamini, Krieger, and Yekutieli *post-hoc* analyses.

5 INTRODUCTION

Coronary artery disease (CAD), which is defined as the reduction of oxygenated blood flow to the myocardium attributed to build-up of atherosclerotic plaque formation in one or more of the coronary arteries, is the most common cause of death globally [441]. While percutaneous coronary interventions (PCIs), which involve the placement of vascular stents to mechanically open the occluded artery, and anti-ischemic drugs such as beta-blockers and calcium-channel inhibitors can halt the progression of atherosclerosis and prevent atherothrombotic events [442], on-pump coronary artery bypass grafting (CABG) surgeries are considered the gold standard intervention for treatment of complex multi-vessel CAD [443]. On-pump CABG surgeries are intended to re-route blood flow around major occluded coronary arteries with a grafted artery or vein (typically the mammary artery or saphenous vein) while minimizing ischemic damage to the myocardium, ultimately preventing the development of more severe long-term cardiovascular complications. During on-pump CABG, the heart is arrested, however, artificial circulation is maintained throughout the body by the cardiopulmonary bypass (CPB) machine. The CPB circulation system enables ‘impure’ blood to be drained from the heart via specialized cannulas so that it can be purified and pumped back to the patient, ensuring that the body receives adequate blood supply to sustain physiological processes. While the heart is being connected to CPB, high-potassium-containing cardioplegic solution that is infused via the aortic cannula is responsible for arresting the heart so that the surgeon is able to anastomose the harvested grafts to the appropriate occluded coronary arteries. While cardioplegic solutions are meant to protect the heart against ischemic injury during CABG by reducing myocardial oxygen consumption, the disruptive combination of ischemia and rapid reperfusion (following successful anastomosis)

overwhelms cardiac mitochondria with oxygen, thus representing a major precipitator of damage in cardiac surgery through mechanisms that may implicate mitochondrial stress responses.

While cardiac ischemia - defined as decreased oxygenated blood flow to the myocardium – can result in complications if the restricted blood flow is 10% or less of normal resting perfusion [444], reperfusion – the restoration of oxygenated blood flow to previously ischemic regions – can paradoxically exacerbate cellular dysfunction and death despite being necessary to ensure survival of the tissue. Collectively, this phenomenon is known as cardiac ischemia-reperfusion injury (IRI), and it exists in a multitude of cardiomyopathies and revascularization procedures.

IRI, whether it is induced by CABG or by other cardiovascular complications such as myocardial infarction, can present severe metabolic consequences for the myocardium during both the ischemic and reperfusion phase. For example, periods of cardiac ischemia can lead to decreased mitochondrial ATP production due to a lack of oxygen required for oxidative phosphorylation [445], which in turn can impact the functionality of ATP-dependent enzymes that regulate ion balance. One of these enzymes is the sarcoendoplasmic reticulum Ca^{2+} ATPase (SERCA), which, if impaired, can cause intracellular Ca^{2+} accumulation and overload if their ability to extrude and reuptake Ca^{2+} from the sarcoendoplasmic reticulum (SR) L-type Ca^{2+} channels is compromised [446]. Impairments to Ca^{2+} homeostasis during ischemia can be detrimental given its contributions to cardiac contractility with Ca^{2+}-troponin C interactions and may also lead to impaired post-ischemic mechanical function recovery [447]. On the other hand, rapid reperfusion following periods of prolonged ischemia can lead to alterations in ion flux, rapid renormalization of pH which can exacerbate cytotoxicity [448,449], and most notably, a myriad of mitochondrial stress responses which can impact the bioenergetic capacity of the heart. Together, severe cardiac IRI can lead to collapses in mitochondrial membrane potential ($\Delta\Psi_m$)

[450], damage to the ETC that perpetuates ROS generation [451], alterations to endogenous antioxidant systems [452,453], mitochondrial swelling [454], cytochrome *c* release [455], and disruption of cardiolipin [455], which can precipitate apoptotic and necrotic programs [456,457]. Another important metabolic response to cardiac IRI is mitochondrial substrate utilization shifts whereby cardiac ischemia leads to increased reliance on glycolysis-derived ATP while IRI increases reliance on fatty acid β-oxidation-derived ATP production [447]. Despite declines to both glucose and fatty acid β-oxidation during periods of cardiac ischemic stress attributed to the lack of oxygen as the final electron acceptor in the ETC, the latter remains the predominant source of residual oxidative metabolism due to increased availability of circulating FFAs, while glucose oxidation remains depressed [458–460]. Presently, it is not fully known why cardiac IRI favours fatty acid-stimulated oxidation as the primary ATP-generating source, however, pioneering work from the Lopaschuk group suggests that inhibiting fatty acid-stimulated oxidation while enhancing carbohydrate (pyruvate)-stimulated oxidation may ameliorate cardiac IRI and its associated downstream pathology, at least in murine models of inducible IR [461]. An experimental design comparing mitochondrial substrate utilization in pre- and post-CABG human right atrial appendage (RAA) samples has never been assessed. This gap in knowledge presents an opportunity for exploring how CABG influences adaptations to mitochondrial substrate oxidation and ROS damage (index of mitochondrial stress). The purpose of this chapter was to investigate the mitochondrial alterations associated with on-pump CABG by comparing pre-CABG RAA samples to post-CABG samples. By understanding the molecular mechanisms underpinning CABG surgeries at different time-points, future therapy development could target mitochondrial stress responses, including substrate oxidation adaptations and oxidative stress-induced damage, to improve both peri-operative and post-operative patient recovery outcomes.

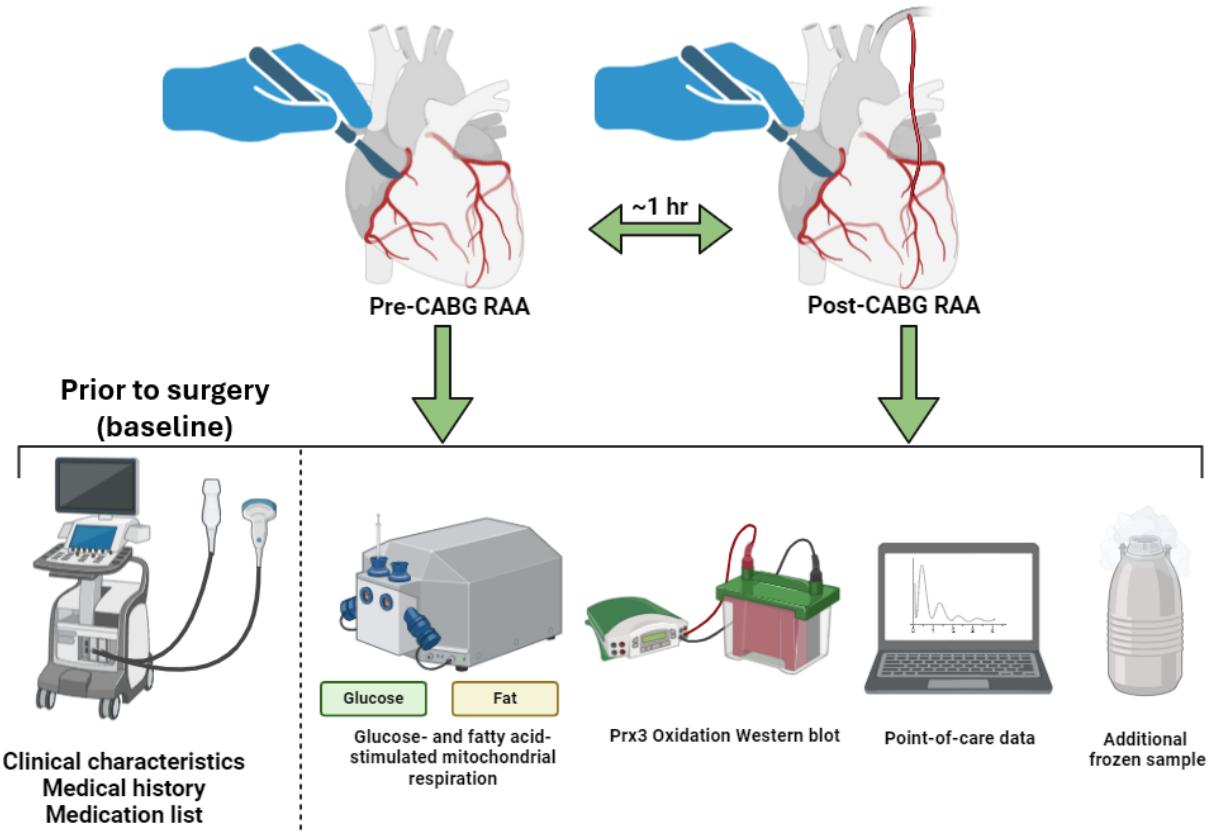

Figure 5-1. Novel repeated-measures study design for comparatively assessing pre- and post-CABG RAA samples in male patients. All samples were obtained from male patients aged 63-80 years undergoing elective CABG, who were monitored for up to three days post-operation. This study was characterized by implementation of a unique design in which clinical characteristics including circulating complete blood count, demographics information, previous medical history, and medication list were among the variables assessed alongside high resolution mitochondrial respirometry with glucose and fatty acid-stimulating substrates, prx3 oxidation, and 'additional planned measurements' at two distinct time-points. Figure created using www.BioRender.com.

6 LITERATURE REVIEW

6.1. Overview of CABG

Coronary artery disease (CAD) is the leading cause of death worldwide and coronary artery bypass grafting (CABG) surgeries are among the gold standard interventions for treatment of multi-vessel CAD [441]. CABG surgeries - sometimes referred to as heart bypass or revascularization procedures - are routinely performed when one or more of the major coronary arteries are narrowed or occluded (usually by atherosclerotic plaques), thus restricting blood supply to the heart. These invasive procedures are known to reduce mortality among medium- and high-risk patients and are generally preferred over non-surgical management options and percutaneous coronary interventions (PCIs) due to their ability to improve and extend lifespan [462–464]. CABG procedures are intended to re-route blood flow around major occluded coronary arteries while minimizing ischemic damage to the myocardium, ultimately preventing the development of more severe cardiovascular diseases.

There are two predominant coronary arteries that supply blood to the myocardium: the left main coronary artery (LMCA) and the right coronary artery (RCA). While the LMCA typically branches into the left anterior descending (LAD) artery and circumflex artery, the RCA branches into the posterior descending artery (PDA) and marginal branches. Without promptly restoring blood flow to the ischemic myocardium through one of the aforementioned major arteries during instances of coronary occlusion, patients may experience anginal symptoms and other precipitators of cardiac dysfunction leading to long-term complications like permanent infarct and even death.

The 2011 ACCF/AHA guidelines were developed to assess several indicators that would be indicative of a CABG recommendation. These indicators include LMCA disease >50%, three-

vessel CAD >70% without proximal LAD involvement (generally observed in diabetics), two-vessel disease impacting LAD and one other major artery, one or more significant stenoses >70% in patients with severe anginal symptoms, and/or one-vessel disease >70% in patient's surviving ischemia-related ventricular tachycardia [465]. In order to 'bypass' these atheromatous blockages, anastomosis of the artery with healthy harvested venous or arterial grafts/conduits is paramount. Typically, bypass grafts are harvested from the internal mammary artery (IMA; usually left origin – LIMA, but also on rare occasions right origin – RIMA) and/or the saphenous vein (SV) from the lower extremity. Other popular bypass graft options include the radial artery and gastroepiploic artery.

Grafts harvested from either the IMA or SV are associated with improvements to short- and long-term outcomes and patient survival following CABG due to their patency characteristics, which reflect their ability to remain unobstructed over time following CABG. While SV is among other common graft options, it is prone to early atherosclerotic changes, trauma from the harvesting procedure, and elevated arterial pressure exposure on the venous endothelium that perpetuates intimal hyperplasia, thus making it more susceptible to re-occlusion following CABG [465,466]. Interestingly, compared to IMA grafts, SV have reduced patency characteristics, whereby ~10-to-25% of grafts will occlude 1-year post-CABG, and only ~50-60% are patent 10-years post-CABG [465]. On the other hand, IMA grafts have the best long-term efficacy, with >90% patency 10-years post-CABG [467]. A study conducted by Loop *et al*., examined the 10-year survival of patients with an IMA graft to the LAD either exclusively or in the presence of additional vein grafts versus patients who only received SV grafts [468]. The group concluded that rates of survival for patients with an IMA graft (93.4%) were higher than rates of survival for patients with SV grafts (88.0%) in a one-vessel disease, two-vessel disease

(90.0% and 79.5%, respectively), and three-vessel disease as well (82.6% and 71.0%, respectively), thus solidifying IMA grafts as the superior option over SV grafts [468]. Additionally, unlike SV grafts, IMA grafts contain physiological, anatomical, and hemodynamic characteristics that insulate them against atherosclerotic changes [466]. It is thought that the non-fenestrated elastic lamina of the IMA protects it against susceptibility to intimal hyperplasia, whose development precedes atherosclerosis [466,468–470]. Determining the correct grafting conduit based on the individual patient's angiogram is essential for a successful CABG procedure.

6.1.1. Surgical Procedure

The CABG procedure serves to bypass atherosclerotic occlusions by connecting upstream blood flow from the ascending aorta or subclavian artery to a target distal to the blockage using a healthy grafted vein/artery **(Figure 6-1)**. Before bypass grafts of LIMA origin (as an example) can be harvested for revascularization, standard median sternotomy must be performed by the surgeon. Following median sternotomy, the LIMA can be harvested for grafting while another member of the surgical team will typically remove segments of the SV, which can alternatively be harvested for grafting if the LIMA is deemed unsuitable. Following harvest of a suitable graft, the patient is put on cardiopulmonary bypass (CPB), also referred to as the heart-lung machine, if the procedure to be performed is considered 'on-pump' CABG.

During on-pump CABG, the heart is arrested, however, artificial circulation is maintained throughout the body by the CPB machine. The CPB circulatory system enables 'impure' blood to be drained from the heart via specialized cannulas so that it can be purified and pumped back to the patient, essentially substituting the role of the pulmonary system. Alternative to this traditional technique is off-pump CABG, where the procedure is performed while the heart is

still beating independent of CPB. While some data proposes that the off-pump CABG method is associated with lesser post-operative complications compared to on-pump CABG for several reasons including due to the elimination of 1) artificial circulation, 2) excessive manipulation of the aorta, and 3) CPB-related cannulation, it is a complex technique that requires the surgeon to attach grafts to an actively beating heart, which can be accompanied with its own share of logistical intricacies [471].

The heart can be connected to CPB by cannulating the aorta and right atrium. Once the aorta is cannulated, it is connected to the arterial pump tubing, while the venous cannula is inserted into the right atrial appendage (RAA). High-potassium-containing cardioplegic solution that is infused via the aortic cannula is responsible for arresting the heart so that the surgeon is able to anastomose the harvested grafts to the appropriate coronary arteries affected by blockages.

Oftentimes, excess RAA sample can be collected prior to cross-clamping the aorta and exposing the heart to cardioplegic solution once the double purse-string suture has been inserted [472]. When the venous cannula is being inserted, the superior suture holds the venous cannula in place, while the inferior purse-string suture remains loose such that this portion of the atrium is still exposed to cardioplegic solution and CPB after removal of the aortic cross-clamp [472]. A second RAA sample can be obtained following CPB from the area in between the purse-string sutures while the venous cannula is being removed. The first RAA sample would be considered pre-ischemic (given that it is explanted prior to cardioplegia solution exposure), while the second sample would be exposed to reperfusion stress.

After the distal portions of the coronary arteries are anastomosed, and the grafts are attached to new ostia (openings) created in the proximal aorta, the cardioplegic solution can be washed out to allow the heart to once again contract. Upon the surgeon's discretion, if the CABG procedure is deemed successful, the chest can be closed, and the patient is sent to the cardiovascular ICU for monitoring.

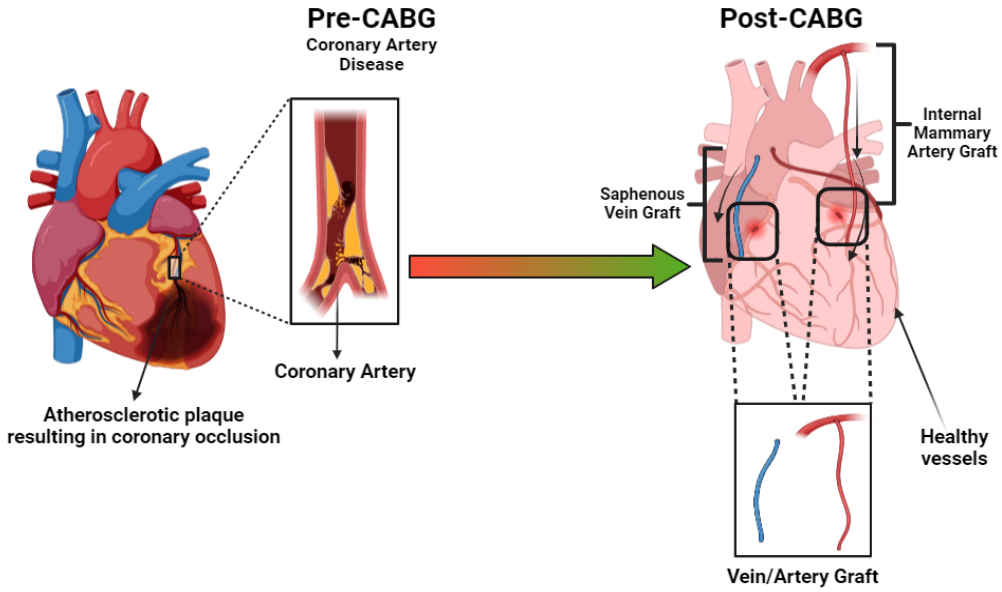

Figure 6-1. Schematic representation of coronary artery bypass grafting (CABG) surgical procedure. Left side of the image (pre-CABG) depicts one or more coronary arteries that are occluded by atherosclerotic plaque formation during coronary artery disease. Right side of the image (post-CABG) depicts two sample vessels that can be harvested as a graft (saphenous vein graft and internal mammary artery graft) to allow blood flow to be re-routed around the occluded coronary artery (denoted by glowing red 'boxed' occlusion), ultimately re-establishing coronary blood flow. Figure created using www.BioRender.com.

6.2. Possible Mechanisms of CABG-induced Ischemia-Reperfusion Injury (IRI)

While cardioplegic solutions that arrest the heart are meant to protect against ischemic injury during CABG by reducing cardiac mitochondrial oxygen demand, the disruptive combination of ischemia and subsequent reperfusion, which overwhelms cardiac mitochondria with oxygen, remains a major contributor to post-operative complications.

Cardiac ischemia - which is defined as reduced oxygenated blood flow to heart muscles – can result in a plethora of complications if the restricted blood flow is 10% or less of normal resting perfusion [444]. Severe damage that ensues following cardiac ischemia can lead to the onset of cell death starting in the endocardium as early as 20 minutes after blood flow cessation [444]. In addition to a decline in oxygen reaching the myocardium - which can result in severe metabolic consequences that impact mitochondrial oxidative phosphorylation (such as a sharp decline in aerobic ATP generation and simultaneous activation of anaerobic glycolysis), cardiac ischemia can also lead to tissue acidosis (reduction in pH) due to a disruption of intracellular ion kinetics implicating Na^+, H^+, K^+, and Ca^{2+} ions [473,474]. During CABG, total ischemia is induced by aortic cross-clamping and the use of cardioplegic solutions (in addition to the ischemia caused by atherosclerotic coronary occlusion). However, cardioplegia, which is achieved by hyperkalemic and hypothermic cardiac arrest with a solution that typically contains glucose, is intended to minimize myocardial metabolic activity and oxygen demand during this period of myocardial vulnerability [473]. Although much is known about the detriments associated with artificially inducing ischemia such that extra precautions are routinely taken during surgery to minimize the after-effects, the subsequent global, dramatic reperfusion is classically thought to overwhelm physiological capabilities of the heart, leading to arrhythmias, myocardial stunning, altered cardiac output, and even long-term consequences like post-operative myocardial infarction [473].

Cardiac reperfusion – which is the restoration or reintroduction of oxygenated blood flow to previously ischemic regions – can paradoxically exacerbate cellular dysfunction and death despite being necessary to ensure survival of the tissue. This is particularly intriguing given that timely reperfusion, which can be initiated ideally within 6 hours from onset of arterial thrombosis, can be critical for preserving left ventricular postinfarct contractile function to

improve patient survival [444]. Simultaneously, rapid reperfusion following periods of prolonged ischemia can lead to alterations in ion flux, rapid renormalization of pH which can exacerbate cytotoxicity [448,449], and most notably, a myriad of mitochondrial stress responses which can impact the bioenergetic capacity of the energetically demanding heart [444]. Aside from the aforementioned ischemic damage - which also includes damage to the electron transport chain (ETC) - damage to cardiac mitochondria that precedes aberrant mitochondrial metabolism during the early reperfusion period is a key contributor to the progression of cardiomyocyte death [444]. The mitochondrial stress responses associated with cardiac IRI will be discussed in detail in *Sections 6.3* and *6.4*.

CABG-induced ischemia-reperfusion injury (IRI) has been documented since at least the late 1970s, when Bulkely and Hutchins determined by histologic assessment that post-mortem autopsied patients who had undergone CABG exhibited contraction band necrosis and coagulation necrosis in regions of new graft-related coronary artery occlusions [475,476]. This data suggests that coronary artery reflow through harvested grafts (reperfusion), following periods of operative nonperfusion (ischemia), accounts for a large majority of CABG-related infarct developments [475,476]. Unsurprisingly, in one longitudinal study, it was determined that reperfusion injury was present in 25% of all myocardial infarction (MI)-related deaths 30 days following CABG procedures [477]. Accordingly, it is approximated that in experimental models of IR, 25-40% of cardiomyocyte death can be attributed to reperfusion injury [444].

Although ample evidence supports the claim that patient recovery outcomes following CABG procedures are highly influenced by IRI, the metabolic implications of these procedures in patients is still poorly understood. Furthermore, this gap in knowledge warrants further

exploration towards the metabolic consequences associated with this procedure and the potential therapeutic avenues that can be targeted to improve post-operative recovery outcomes.

6.3. Alterations Associated with Cardiac IRI and Implications for CABG: Mitochondrial Bioenergetics

6.3.1. Oxidative Phosphorylation and Substrate Utilization

Cardiac mitochondria are indispensable for continuously generating energy supply to maintain contraction-relaxation cycles, basal metabolism, and ionic homeostasis through a tightly regulated process known as oxidative phosphorylation, which is responsible for provisioning the energetic currency of the cell – ATP (See *Sections 2.7.* and *2.7.3.*). Unsurprisingly, the heart experiences a near complete turnover of the cardiac ATP pool every 10 seconds given that the ATP content in the myocardium is relatively low (~5 μmol/g wet wt) [478], and accordingly, cycles approximately 6 kg of ATP daily [447,479,480]. Specific enzymes, transporters, and proteins rely on the hydrolysis of ATP into its constituent products, ADP and an inorganic phosphate (Pi) molecule, which can be harnessed to maintain energetic demands of the cell.

While ADP and Pi can be viewed as metabolic substrates necessary for upholding physiological processes, they must be recombined back to ATP in a cycle that ensures constant provision of ATP to contracting muscles. Carbohydrates (such as glucose) and fatty acids are two essential energy substrates (among others, such as lactate and ketone bodies) required for re-synthesizing ATP through an organized system of enzymes that extract energy bound within hydrogen bonds tethered to the carbon backbones of both nutrient sources **(Figure 6-2)**. This process manipulates the structure of glucose and fatty acids such that transfer of energy can be permitted by directing the product of reducing equivalents (electrons and protons) towards the synthesis of ATP in the mitochondria by the reduced forms of nicotinamide adenine dinucleotide

(NADH) and flavin adenine dinucleotide ($FADH_2$). These reducing equivalents are generated through dehydrogenase reactions occurring within the tricarboxylic acid (TCA) cycle following the breakdown of pyruvate and also during fatty acid β-oxidation pathways. Glucose and fatty acid metabolism are tightly regulated in the healthy heart. Approximately 95% of ATP production can be attributed to oxidative phosphorylation of carbohydrate and fat, and moreover, fatty acid β-oxidation contributes 60-80% of ATP production while the remaining is accounted for by carbohydrate (glucose and lactate) and ketone body oxidation [478,480–482]. The remaining 5% is supplied by substrate-level phosphorylation in glycolysis [478]. The relationship between glucose oxidation and fatty acid β-oxidation, including their relative contributions to energy supply, is perturbed in hearts affected by cycles of cardiac IR [447].

Periods of cardiac ischemia can lead to decreased ATP production, which in turn, can impact the functionality of ATPase enzymes that regulate ion balance. For example, Na^+/K^+ antiporter ATPases, which exchange 3 Na^+ ions out of the cell for 2 K^+ ions into the cell to maintain ionic homeostasis, can lead to intracellular Na^+ accumulation and overload (and excessive K^+ efflux) if the Na^+/K^+ ATPase is impaired [483]. The accumulating intracellular Na^+ concentration could also be caused by intracellular proton accumulation-induced activation of Na^+/H^+ [484], perpetuating impairments to Ca^{2+} levels via the Na^+-Ca^{2+} exchanger (NCX) [485]. Furthermore, sarcoendoplasmic reticulum Ca^{2+} ATPases (SERCA), if impaired, can cause intracellular Ca^{2+} accumulation and overload if their ability to extrude and reuptake Ca^{2+} into the sarcoendoplasmic reticulum (SR) L-type Ca^{2+} channels is compromised [446]. Of note, impairments to Ca^{2+} homeostasis during ischemia can be detrimental given its contributions to cardiac contractility with Ca^{2+}-troponin C interactions and may also lead to impaired post-ischemic mechanical function recovery [447]. In addition to IR-induced ion dysregulation,

severe IRI can also lead to a collapse in mitochondrial membrane potential ($\Delta\Psi_m$), damage to the ETC that perpetuates reactive oxygen species (ROS) production, mitochondrial swelling, cytochrome *c* release, and disruption of cardiolipin, which collectively can precipitate apoptotic (mitochondrial outer membrane permeabilization (MOMP) and mitochondrial permeability transition pore (mPTP)) and necrotic programs [455–457]. Understanding the role of ATP in the context of mitochondrial function in physiological processes is paramount to exploring the differential contributions of substrate sources (carbohydrate and fatty acid) to ATP production, which will be discussed in the next section.

6.4. Carbohydrate (Glucose)- versus Fatty Acid-supported Respiration in the Heart

6.4.1. Carbohydrate (Glucose)-supported Respiration

Myocardial glucose utilization begins with the recruitment of the glucose transporters GLUT1 and GLUT4 to the sarcolemma (which are typically abundant), where, once glucose enters the cytosolic compartment, it is phosphorylated by hexokinase-II to generate glucose-6-phosphate (G-6-P) **(Figure 6-2)**. Depending on the energetic state of the heart, G-6-P is either stored in the form of glycogen (commonly recruited during cardiac ischemia) or catabolized during glycolysis. Glycolysis serves to breakdown glucose in the cytosol to either lactate (anaerobic conditions) or pyruvate (aerobic conditions) while producing 2 moles of ATP. Phosphofructo-1-kinase (PFK-1) is an important regulatory enzyme to consider in this process given that it is responsible for committing glucose to catabolism via glycolysis [486]. Of note, ATP, citrate, and protons serve as allosteric inhibitors of flux through PFK-1 to partly determine the fate of glucose [486]. Before glucose can be catabolized to either pyruvate or lactate, flux through glyceraldehyde-3-phosphate dehydrogenase (GAPDH) must occur, which enables the oxidation and phosphorylation of glyceraldehyde phosphate (GP) coupled to NADH production

[486]. NADH is re-oxidized to NAD^+ to ensure continuous flux through GAPDH either by lactate dehydrogenase (LDH) in the absence of oxygen, or by the malate/aspartate shuttle and ETC in the presence of oxygen.

At the end of glycolysis, the majority of pyruvate undergoes oxidative decarboxylation in the mitochondria by the pyruvate dehydrogenase complex (PDHc), which consists of PDH, PDH kinase (PDK), and PDH phosphatase (PDHp), to yield acetyl-CoA for the TCA cycle in the mitochondria [447,487,488] (**Figure 6-2)**. The proportion of PDH in its active versus inactive form can be influenced by an increase in glycolytic flux, increase in cardiac workload, or by catecholamine stimulation, with only approximately 20% of PDH in the active form prior to stimulation by one or more of these factors [447]. It is noteworthy that PDHc can be influenced by NADH:NAD^+ and/or acetyl-CoA:CoA and pyruvate. Furthermore, PDHp can dephosphorylate, and therefore activate PDHc, while PDK can phosphorylate and therefore deactivate PDHc in response to increasing acetyl-CoA:CoA and NADH:NAD^+ ratios, thus blocking the oxidation of carbon from glycolysis [489,490].

During periods of mild-to-moderate cardiac ischemia, which is defined by a transient absence of oxygen, glycolysis-derived ATP production (which is uncoupled from pyruvate oxidation) may be sufficient to maintain ionic homeostasis temporarily, however, it could lead to an accumulation of lactate and protons (intracellular metabolic acidosis) [447,491]. Moreover, myocardial glycogen stores are limited (albeit recruited during cardiac ischemia), meaning that glycolysis is generally viewed as a short-term solution [492]. Prolonged, complete ischemia can lead to impairments in glycolytic flux due to inhibition of the pathway by its own metabolic by-products including an accumulation of protons at PFK-1 and GAPDH [493,494]. It is interesting

to note that accelerated glycolysis during ischemic periods can be resolved following reperfusion but would still remain uncoupled from carbohydrate (pyruvate) oxidation [495,496].

6.4.2. Fatty Acid-supported Respiration

Fatty acids oxidized by cardiac muscle are largely derived from dietary fats following consumption of a lipid-rich meal (primarily long-chain fatty acids in the form of oleate and palmitate) [478], fats stored in white adipose tissue (WAT) delivered through circulation, and, to a lesser degree, from endogenous cardiac intracellular triglyceride (IMTG) pools [497]. Before free fatty acids (FFAs) can be metabolized in the mitochondria, they must be activated by esterification to CoA - a process that generates a fatty acyl-CoA moiety in the cytosol capable of being transported across mitochondrial membranes. This is an ATP-dependent process that is catalyzed by fatty acyl-CoA synthetase (ACS) enzymes. In the cytosolic compartment, acyl-CoA is bound to an acyl-CoA binding protein (ACBP), thus facilitating its transport for mitochondrial fatty acid β-oxidation. Mitochondrial membranes (specifically the inner mitochondrial membranes (IMM)) are impermeable to (long-chain) fatty acyl-CoA moieties but not those attached to a carnitine molecule, therefore, carnitine (CPT-I at the outer mitochondrial membrane (OMM)) is utilized as a shuttle mechanism by substituting the CoA for a carnitine **(Figure 6-2)**. To elaborate, at the OMM, carnitine palmitoyl-transferase I (CPT-I) is responsible for converting fatty acyl-CoA to fatty acylcarnitine moieties [498]. These fatty acylcarnitine moieties can then cross the IMM and are shuttled to the mitochondrial matrix via the carnitine-acylcarnitine translocase (which transports a free carnitine in the opposite direction). The fatty acylcarnitine moieties shuttled to the mitochondrial matrix are eventually reconverted back into a fatty acyl-CoA moiety by the actions of carnitine palmitoyl-transferase II (CPT-II) on the IMM for further processing towards β-oxidation [499]. Fatty acid β-oxidation occurs in the mitochondrial matrix

where fatty acyl-CoA molecules are broken down to process acetyl-CoA (further metabolized in the TCA cycle) as well as reducing equivalents (NADH and $FADH_2$) for the ETC.

There are three major factors that exert regulatory control over the rate of fatty acid β-oxidation: level of circulating FFAs (which are elevated following cardiac surgery) [500], the intracellular level of malonyl-CoA, and the enzymes involved in mitochondrial fatty acid β-oxidation. Circulating FFAs can become elevated as an outcome of catecholamine discharge (hormonal state) and norepinephrine (NE) levels that occurs during ischemic or surgical stress due to an increase in adipose tissue lipolysis and can also increase with fasting (prandial state) [447,501,502]. It is important to note that increased FFA delivery to the heart leads to increased rates of mitochondrial fatty acid β-oxidation [447]. The following section will primarily focus on the regulatory roles of malonyl-CoA on fatty acid β-oxidation.

Malonyl-CoA regulates fatty acid β-oxidation endogenous to the mitochondria. Malonyl-CoA is generated from the conversion of cytosolic acetyl-CoA by the regulatory control of an acetyl-CoA carboxylase (ACC) isozyme known as ACC_β, while it is broken back down to acetyl-CoA by malonyl-CoA decarboxylase (MCD) [503]. It is important to note that activity of ACC_β is under the phosphorylation control of AMPK, which is a critical energy-sensing enzyme that plays regulatory roles along several fatty acid and glucose metabolism pathways. Depending on the metabolic state of the heart, AMPK can phosphorylate (and thus inhibit) ACC_β to prevent chronic elevation of fatty acid levels, at least in skeletal muscle [504]. Malonyl-CoA is crucial for rates of β-oxidation given that it has the ability to inhibit the activity of CPT-I, therefore limiting mitochondrial fatty acid uptake at the OMM, as well as subsequent oxidation in the mitochondria [505,506]. Malonyl-CoA itself is regulated, in part, by the availability of acetyl-CoA, which can be transported into the cytosol from the mitochondria through the formation of

mitochondrial acetylcarnitine, which is reconverted to acetyl-CoA in the cytosol by cytosolic carnitine acetyl transferase [507]. Malonyl-CoA can also be regulated by citrate that escapes oxidation in the TCA cycle and translocates to the cytosol, where it can allosterically activate ACC or contribute to cytosolic acetyl-CoA levels by feeding into the ATP citrate lyase pathways [508–510].

6.4.3. Influence of Cardiac IR on Mitochondrial Substrate Selection

Glucose oxidation and fatty acid β-oxidation are inherently linked to each other, and the reciprocal relationship between shifts in glucose versus fatty acid oxidation has been known for over 60 years [511]. It is important to consider how these two energy substrate oxidation pathways regulate each other through a series of feedforward and feedback loops before exploring IR and its ability to influence shifts to their oxidation.

For example, fatty acid β-oxidation generates acetyl-CoA and NADH (similar to pyruvate oxidation) in the mitochondria which can activate PDH kinase and phosphorylation-inhibition of PDHc – a major regulatory complex involved in the conversion of pyruvate to acetyl-CoA through pyruvate decarboxylation during glucose oxidation. Moreover, as previously mentioned, β-oxidation-derived citrate – which contributes to the cytosolic acetyl-CoA pool, can inhibit PFK-1, thus inhibiting hexokinase (HK) via G-6-P during glycolysis and imparting an inhibitory effect on pyruvate (glucose) oxidation [512]. Since fatty acid β-oxidation uncouples glycolysis from glucose oxidation (e.g., during periods of ischemic stress where oxygen is limiting), the protons derived from ATP hydrolysis during glycolysis are not able to assist in the co-transport of pyruvate across the IMM, also leading to reductions in glucose oxidation [513].

On the other hand, glucose oxidation-derived acetyl-CoA generation can decrease fatty acid β-oxidation through feedback inhibition of 3-ketoacyl-CoA thiolase [447]. Glucose

oxidation-derived NADH can also decrease fatty acid β-oxidation through a feedback inhibition of acyl-CoA dehydrogenase and 3-hydroxyacyl-CoA dehydrogenase [447]. Cytosolic malonyl-CoA, a potent inhibitor of mitochondrial fatty acid uptake, can be increased by glucose oxidation-derived acetyl-CoA, which signals to carnitine acetyltransferase and ACC [447,514].

Despite declines to both glucose and fatty acid β-oxidation during periods of cardiac ischemic stress attributed to the lack of oxygen as the final electron acceptor in the ETC, the latter remains the predominant source of residual oxidative metabolism due to increased availability of circulating FFAs, while glucose oxidation remains depressed [458–460]. As glucose oxidation remains depressed during cardiac ischemia, pyruvate must be converted to lactate via LDH at the end of glycolysis to regenerate NAD^+ to maintain glycolytic flux through GAPDH as an alternate ATP-producing pathway [447]. Interestingly, in the post-ischemic, rapid reperfusion phase, rates of fatty acid β-oxidation can return to near pre-ischemic levels, thus leading to inhibition of PDH and elevated production of both lactate and protons [447,513,515]. While this is occurring, glucose oxidation, cardiac efficiency, and mechanical function all remain impaired [516,517]. This is significant because it leads to the hypothesis that cardiac function may still be perturbed in the post-IR heart despite recovery of fatty acid β-oxidation capacity to pre-ischemia levels, thus stipulating that inhibiting fatty acid β-oxidation, while increasing glucose oxidation, may represent a viable therapeutic intervention for not only maintaining ATP production, but also restoring cardiac function. Additionally, this is further supported by evidence demonstrating that fatty acid β-oxidation requires more oxygen consumption for a given amount of ATP synthesis compared to carbohydrate oxidation, thus linking with the well-established data that cardiac mechanical efficiency is impaired with elevated fatty acid oxidation [478,518]. To this end, there are several hypothetical ways in which substrate selection can be

influenced to optimize post-IR recovery, including: optimizing cellular uptake of specific substrate sources (glucose versus FFAs), upregulating transcription factors involved in substrate metabolism, modifying mitochondrial fatty acid uptake and/or regulators of mitochondrial fatty acid β-oxidation, and pharmacologically increasing glucose oxidation at the expense of fatty acid β-oxidation [447].

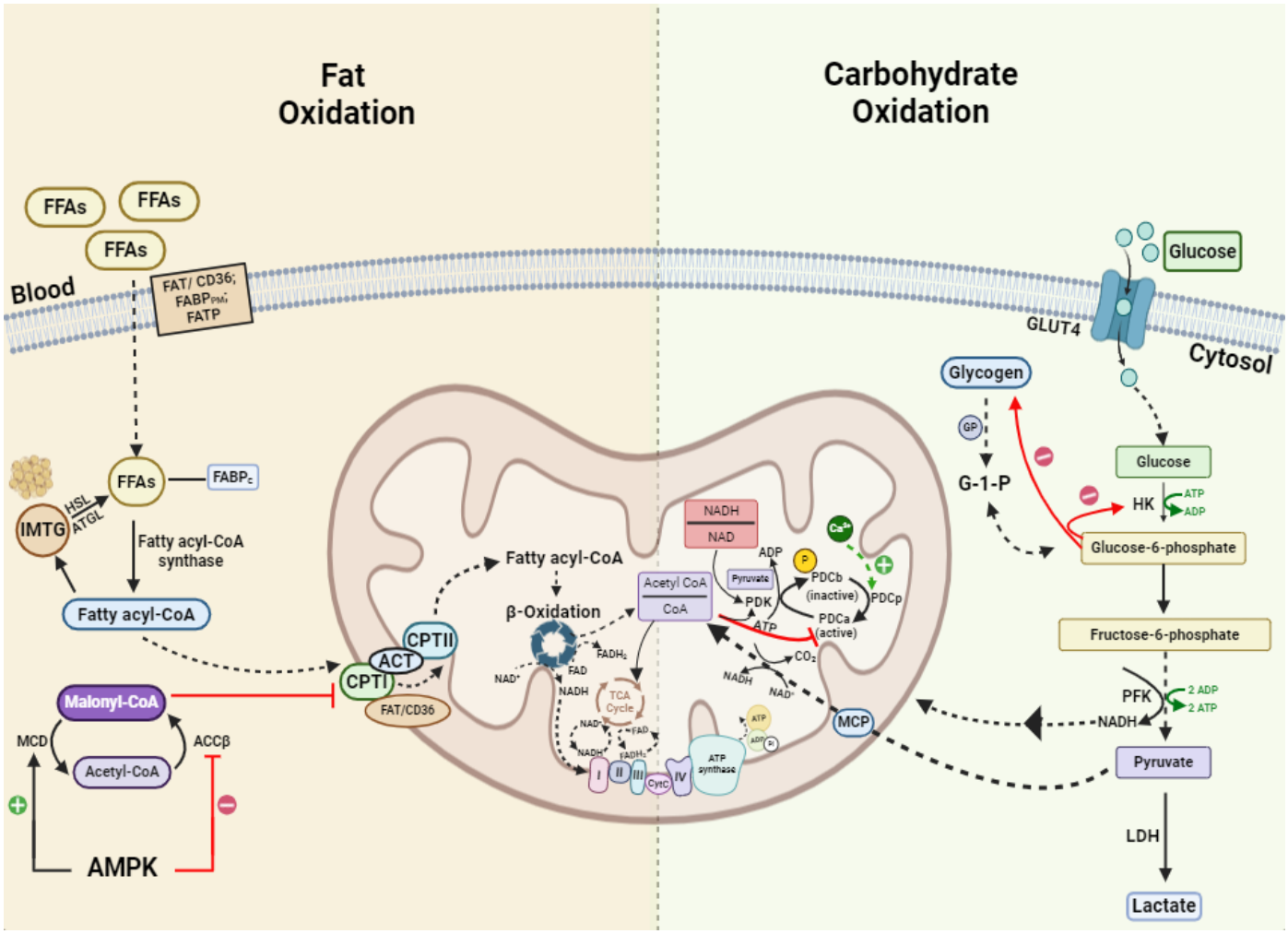

Figure 6-2. Schematic representation of integrated utilization of fat and carbohydrate oxidation in muscle, with key regulatory pathways, proteins, and enzymes. Differences in substrate catabolism are influenced by factors including metabolic demand, substrate availability, and diet. (Left side) Circulating free fatty acids (FFAs) are transported across the plasma membrane (PM) into the cytosol via fat-specific transporters, including fatty acid translocase/cluster of differentiation 36 (FAT/CD36), fatty acid binding protein ($FABP_{PM}$), and fatty acid transport protein (FATP). In the cytosol, FFAs interact with several key enzymes and proteins to be oxidized in the mitochondrion following sequential breakdown via β-oxidation and tricarboxylic acid (TCA) cycle, which both provide reducing equivalents to be used in the electron transport chain (ETC). Malonyl-CoA serves as a prominent regulator of fat oxidation given its inhibitory actions on the mitochondrial outer membrane enzyme carnitine palmitoyltransferase 1 (CPT-I), which regulates fat entry into the mitochondrion. (Right side) Circulating 6-carbon glucose is transported across the PM via glucose transporter type 4 (GLUT1/4), where it is sequentially broken down by various glycolytic enzymes. The product, known as 3-carbon pyruvate molecules, are either shuttled into the mitochondrion for further oxidation via TCA cycle enzymes which provide reducing equivalents for the electron transport chain (ETC), or transformed into lactate. FFA – free fatty acid; FAT/CD36 – fatty acid translocase/cluster of differentiation 36 (FAT/CD36); $FABP_{PM/c}$ – plasma membrane/cytosolic fatty acid binding protein; FATP – fatty acid transport protein; IMTG – intramuscular triglyceride; HSL – hormone sensitive lipase; ATGL – adipose triglyceride lipase; MCD – malonyl-CoA decarboxylase; ACCβ – acetyl-CoA carboxylase; AMPK – adenosine monophosphate kinase; CPT-I/II – carnitine palmitoyltransferase 1/2; ACT – acetyl-CoA transferase; NADH – nicotinamide adenine dinucleotide; $FADH_2$ – flavin adenine dinucleotide; TCA – tricarboxylic acid; I – IV – mitochondrial complexes I-IV; PDK – pyruvate dehydrogenase kinase; PDC – pyruvate dehydrogenase complex; MCP – monocarboxylate porter; GLUT – glucose transporter; GP – glycogen phosphorylase; G-1-P – glucose-1-phosphate; HK – hexokinase; PFK – phosphofructokinase; LDH – lactate dehydrogenase. Figure created using www.BioRender.com.

6.5. Mitochondrial Redox Stress

6.5.1. Cardiac IR-induced Oxidative Stress and Implications for CABG

While it has long been known that cardiomyocyte mitochondria can be damaged as a result of both prolonged normothermic and cold (organ preservation) IRI [444,519–523], the specific mitochondrial reactive oxygen species (ROS)-mediated oxidative stress mechanisms remain understudied. Furthermore, mitochondrial ROS data from CABG-induced IRI is limited, with no known studies available to date that compare mitochondrial ROS of pre- and post-CABG RAA samples. This gap in knowledge presents an opportunity for exploring how CABG influences mitochondrial ROS – specifically, the effects of blood flow occlusion (oxygen deprivation) and rapid restoration of oxygenated blood flow on ROS-mediated damage. Given the lack of CABG-specific data that is currently available, this section will focus on the role of mitochondrial ROS in other models of cardiac IRI, including myocardial infarction and inducible cardiac IR in small mammals (e.g., rabbit, canine, guinea pig, rat, etc.). It should be noted that there are several other sites of ROS generation during IR, including NADPH oxidases and xanthine oxidases to name a few, however, this section will focus on mitochondrial sources of ROS.

In physiological conditions, small amounts of ROS contribute to cellular signaling pathways and are in fact necessary to regulate several essential processes [524]. These molecules, which include the superoxide anion ($O_2^{\bullet -}$) and hydrogen peroxide (H_2O_2) (which is technically not a free radical but is still highly reactive) are generated as by-products of aerobic cellular metabolism from mitochondrial respiratory chain complexes embedded in the ETC (See *Section 2.7.4.*). Mitochondrial respiratory chain complexes I-IV are responsible for coupling the transfer of protons (H^+ ions) directed to the intermembrane space (IMS) to the transfer of

electrons (e^- ions) flowing through the complexes. During this process, attributable to the incomplete reduction of oxygen, superoxide radicals can form, primarily at complexes I and III, which can be quickly converted to H_2O_2 by mitochondrial manganese superoxide dismutase (MnSOD) [297,525] **(Figure 6-3)**. A well documented consequence of myocardial IR, and pre-eminent driver of IRI, is aberrant mitochondrial ROS production to levels that pathologically overwhelm the cell. IR-induced mitochondrial ROS bursts can be detrimental given that they often exceed the capability of endogenous antioxidant systems (e.g., mitochondrial catalase, glutathione peroxidase (GPx), MnSOD, peroxiredoxin/thioredoxin (Prx/Trx)) to scavenge these unstable molecules, leading to protein oxidation [526], lipid peroxidation [451,527], and opening of the mPTP [528] - collectively referred to as oxidative stress.

6.5.2. Ischemic Damage

ROS are primarily generated in mitochondria during ischemia [529,530]. It should be noted that cardiac ischemic damage independent of reperfusion can cause an increase in ROS generation from complex-I of isolated rat heart mitochondria, and it is hypothesized that complex-I activity decreases during ischemia due to this elevation in complex-I-derived ROS [531] **(Figure 6-3)**. Complex-I-derived ROS generation in response to ischemia can lead to a conformational change in complex-I which shifts complex-I from its active 'A' configuration to its dormant 'D' configuration [532]. This shift to the dormant configuration - which complex-I can be trapped in due to excessive oxidant stress - leads to persistent decreased activity of this complex [444]. Interestingly, the dormant configuration of complex-I is associated with lower reverse electron transfer (RET)-associated superoxide generation as well as inhibited ROS production from decreased forward electron transfer (FET), both attributed to lower complex-I activity [444,532,533]. In certain pathological conditions, the dormant configuration may be

favoured due to the lower generation of RET-associated ROS, however, it can become problematic over long periods due to the reductions in ATP production caused by blunted complex-I activity. It is noteworthy that administering Metformin in high doses partially inhibits complex-I, and if given 5 minutes at the onset of reperfusion, can decrease cardiac damage [534]. Collectively, this data suggests that temporary inhibition of complex-I can attenuate ROS generation, which could lead to favourable cardioprotective outcomes if the effects of ischemia and reperfusion do not compound. Similar to complex-I activity, complex-III activity is also decreased during ischemia [535]. When ischemic damage occurs to complex-III, residual electron flow to this complex (possibly due to its dimeric composition and/or because cytochrome *c* oxidase does not rapidly consume all residual oxygen) leads to ROS generation [444]. The idea of residual electron flow following ischemia contributing to ROS generation is important given that ROS production virtually ceases during periods of anoxia. For this reason, ROS generation is directly linked to period of ischemia. Despite the activity of complex-II being decreased in rat heart mitochondria following prolonged ischemia, and further decreased following reperfusion [536], it is thought that complex-II is relatively resistant to ischemic damage [537]. Following mild ischemia, RET-associated ROS generation can occur, and preventing this ROS has been correlated with decreases to cardiac injury during IR [533]. Together, data suggests that ischemic damage to mitochondria may be mediated by mitochondria themselves, which is why, paradoxically, inhibiting various complexes within the ETC with rotenone or amobarbital, as an example, often protects against ischemic damage [538].

6.5.3. Reperfusion Damage

While it is often assumed that the majority of damage associated with IRI occurs solely at the onset of reperfusion attributed to a rapid influx of oxygen that overwhelms mitochondrial

machinery and leads to aberrant ROS generation and oxidative stress, newer data suggests that mitochondria, when free of ischemic damage prior to onset of reperfusion, mostly avoid cardiac injury [539]. To elaborate, ROS generation at complex-I and -III is lower following reperfusion if the ROS are not compounding with ROS also generated during ischemia [539]. It has been well established that many of the defects to the ETC as well as loss of cardiolipin and cytochrome *c* that occur as a result of ischemic damage persist and can even aggravate during reperfusion [540–542] **(Figure 6-3)**. In this light, protecting cardiac mitochondria prior to reperfusion may carry forward into the early reperfusion period to minimize subsequent damage that ensues.

Despite this unique perspective, considerable research has been conducted on the effects of reperfusion and its contributions to mitochondrial ROS generation. Much of the detrimental effects of reperfusion are linked to ETC damage from a variety of sources, including during ischemia and due to both ischemia-derived and reperfusion-derived ROS-induced ROS release (RIRR). In some cases, reperfusion injury may seem like the major precipitator of cardiac injury due to its effects being enhanced by ischemia. For example, isolated rat heart mitochondria exposed to periods of ischemia and reperfusion exhibit a more pronounced burst of ROS at the onset of reperfusion and the days following, compared to after onset of ischemia [540]. It is possible that ischemic damage leads to elevated rates of superoxide formation as a result of ETC damage or low ATP demand, which can both cause a buildup of NADH [451]. The reduction of ETC complexes that can occur as a consequence of this NADH buildup can further increase the likelihood of premature electron slip from the ETC to generate more superoxide, thus perpetuating a cycle of persistent ETC-related ROS generation at the onset of reperfusion [451]. While the exact source of ETC-related ROS generation during reperfusion is still largely

unknown, pharmacological inhibition of complex-I has demonstrated ROS-mediated reperfusion injury [538].

Newer evidence suggests that succinate dehydrogenase (SDH) may be partly responsible for the mitochondrial ROS generated during early onset reperfusion. During ischemia, SDH may be playing a role in RET, which sees the conversion of fumarate to succinate, thereby driving succinate accumulation [533]. At the onset of reperfusion, SDH transitions back to FET, which leads to the rapid oxidation of the accumulated succinate to fumarate. This can ultimately lead to reduction of the CoQ pool on complex-II and cause electrons to transfer back towards the flavin mononucleotide site of complex-I, thus perpetuating RET-derived superoxide generation [451,533] **(Figure 6-3)**. Since RET requires sufficient $\Delta\Psi_m$, the severity of mitochondrial damage can be a strong predictor of RET-derived ROS generation, with moderate damage a stronger predictor of RET than severe damage, which could depolarize the mitochondria, during IR [451,533].

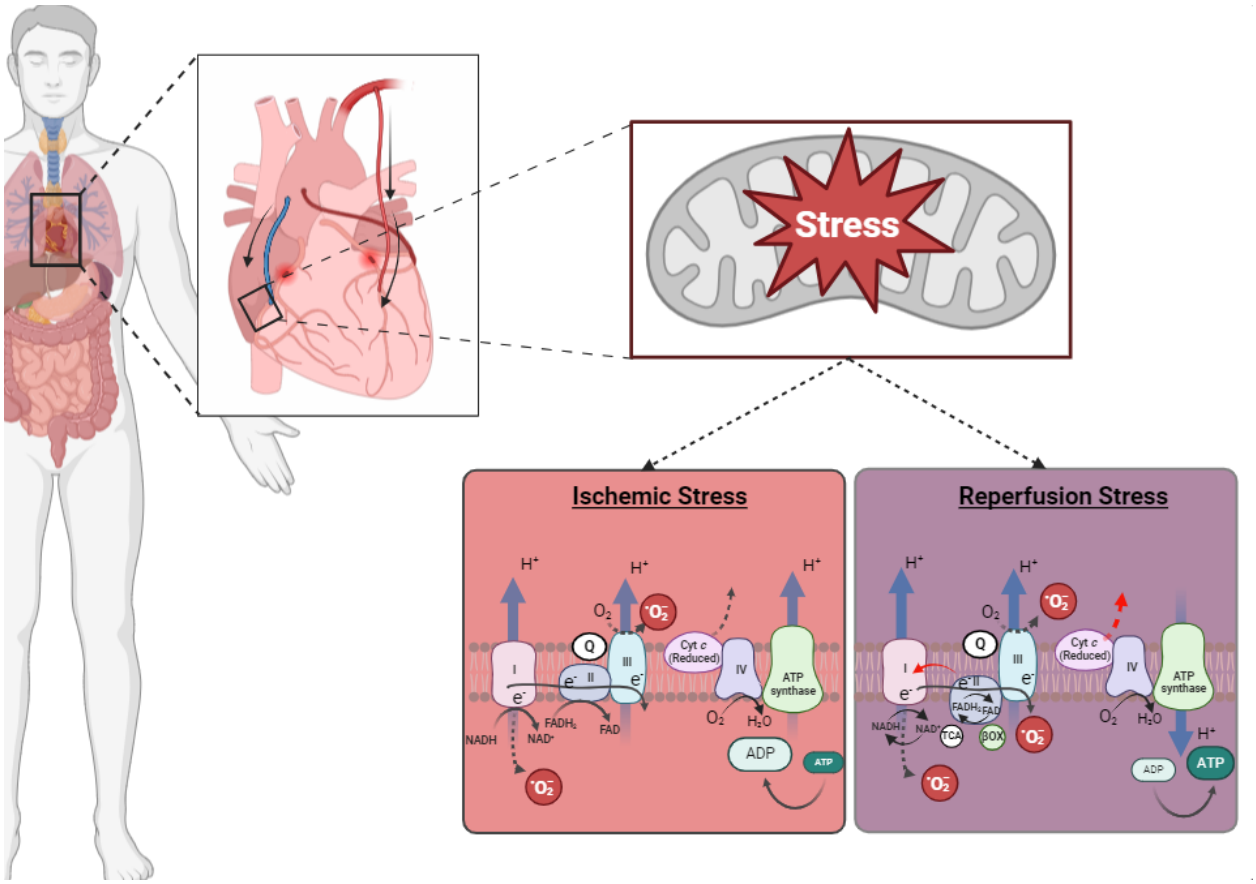

Figure 6-3. Cardiomyocyte mitochondria are differentially impacted during periods of cardiac ischemia and subsequent periods of reperfusion. (Left side) Ischemic stress is primarily characterized by complex I and III-derived superoxide ($O_2^{\bullet-}$) generation which rapidly dismutates into mitochondrial H_2O_2. During periods of ischemia, which is defined as reduced oxygenated blood flow to tissues, the [ATP]:[ADP] ratio is lower due to various impairments in the ETC, most of which are perpetuated by a lack of oxygen as the terminal electron accepter at complex IV. Loss of cytochrome *c* is another outcome of cardiac ischemic stress. (Right side) Reperfusion stress following ischemia reflects the compounding effect of both loss of oxygen and a rapid surge in oxygen. Complex I and III-derived ROS and loss of cytochrome *c* that occur during ischemia are further aggravated during reperfusion. Furthermore, reverse electron transfer (RET)-derived ROS at complex II may be responsible for some of the deleterious effects of reperfusion injury. Figure created using www.BioRender.com.

6.5.4. Peroxiredoxin 3 as a Potential Therapeutic Marker of Cardiac Damage

Superoxide, which is primarily generated at complex-I and complex-III in the ETC, and to a lesser extent, by RET at complex-II, is detoxified to mitochondrial H_2O_2 by MnSOD. Thereafter, through the actions of various endogenous antioxidant systems including catalase, GPx, and Prx/Trx, H_2O_2 can be converted to the more stable H_2O. The Prx antioxidant system (of which there are 6 isoforms in mammalian cells – Prx 1-6) is particularly interesting to consider in various cardiac diseases given that they are highly active in the elimination of intracellular ROS moieties such as H_2O_2 [543] **(Figure 6-4)**. The Trx antioxidant system is commonly implicated alongside Prx given that thioredoxin reductase (TrxR) activity is required to return the reaction back to the reduced Prx after it has been oxidized by ROS [451] **(Figure 6-4)**.

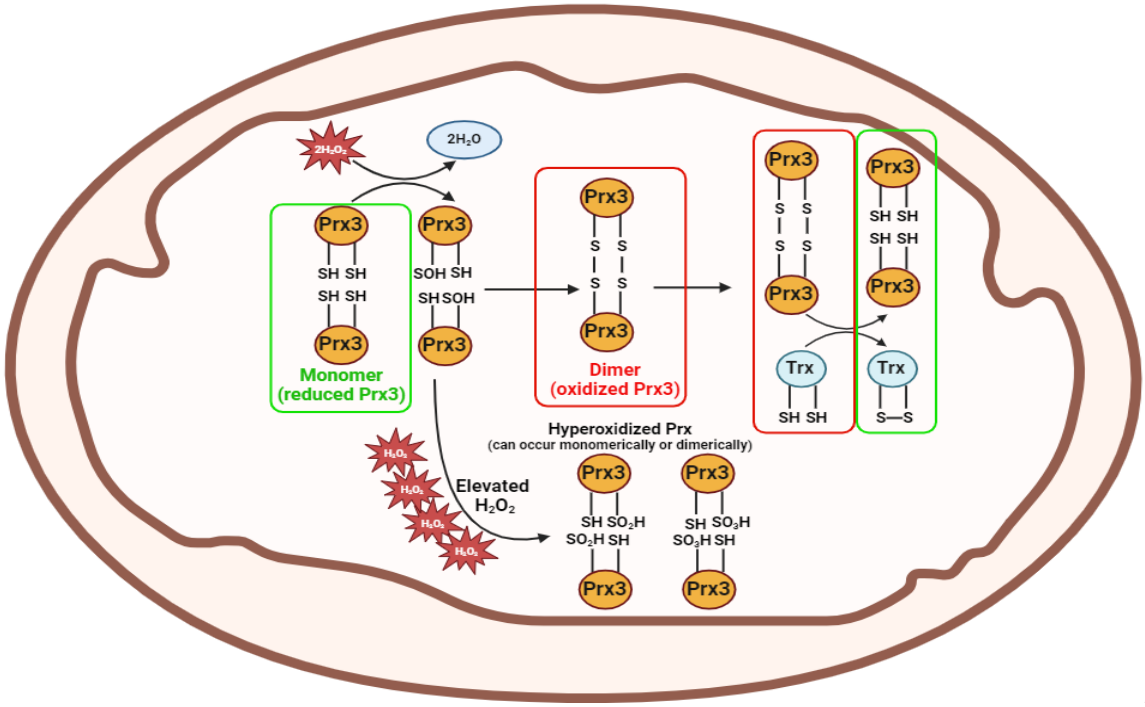

Figure 6-4. Mitochondrial peroxiredoxin 3 (Prx3) is an endogenous antioxidant involved in cardiac remodeling processes and may represent a 'snapshot' of oxidative stress occurring after cardiac ischemia and/or reperfusion during CABG. Prx3 is oxidized by H_2O_2 and resultantly converted into its dimeric moiety during periods of stress, while the thioredoxin (Trx) system is responsible for converting oxidized Prx3 back to its monomeric reduced form. SH – cysteine free thiol; SOH – sulphenic acid; SO_3H – sulphonic acid; SO_2H – Sulphinic acid. Figure created using www.BioRender.com.

In mouse hearts subjected to IR, it has been observed that the mitochondrial isoform Prx3 is oxidized during ischemia, however, interestingly, this oxidation was largely reversed during reperfusion [452]. Furthermore, overexpression of Prx3 can lead to changes in cardiac remodeling, including attenuated apoptosis of the non-infarcted myocardium, as well as reduced interstitial fibrosis and myocyte hypertrophy of the mouse LV following myocardial infarction [453]. While more research is certainly needed to define the complex, multifactorial role of mitochondrial Prx3 in IR, the limited data available suggests that Prx3 is protective against cardiac IRI through redox-related mechanisms that require further mechanistic insight.

7 OBJECTIVES AND HYPOTHESES

7.1. Overview of Study 2 (Chapter 8)

The major overview of this chapter was to understand how coronary artery bypass grafting surgery (an alternate model of cardiac stress) influences mitochondrial substrate selection adaptations and redox damage responses in human right atrial appendage samples obtained pre- and post-CABG.

7.2. Objectives and Hypotheses for Study 2 (Chapter 8) (CABG)

Coronary artery disease (CAD) is the leading cause of death worldwide, and accordingly, on-pump coronary artery bypass grafting (CABG) surgeries are the gold standard intervention for treatment of multi-vessel CAD. These surgeries are routinely performed when one or more of the major coronary arteries are narrowed or blocked, thus restricting blood supply to the heart. While cardioplegic solutions that arrest the heart during on-pump CABG are meant to protect the heart against ischemic injury by reducing cardiac oxygen consumption, the disruptive combination of ischemia and subsequent reperfusion, which overwhelms the myocardium with oxygen, remain a major precipitator of morbidity and mortality following cardiac surgery. While it has long been known that a cascade of metabolic stress responses drive cardiac ischemia-reperfusion injury (IRI) during ischemic heart disease, the specific mitochondrial alterations during CABG surgery have never been explored. Therefore, the objective of this chapter was to compare pre-CABG right atrial appendage (RAA) biopsy samples to post-CABG samples to determine if this short (~1 hr) period of on-pump CABG influences alterations to mitochondrial stress responses.

Hypotheses for Study 2 (Chapter 8)

1) Compared to pre-CABG RAA samples, post-CABG samples will demonstrate 'adaptations' in substrate-specific mitochondrial respiration consistent with previously published literature suggesting that fatty acid-supported oxidation dominates over glucose oxidation after bouts of ischemia and reperfusion.
2) Enhanced fatty acid-supported oxidation during on-pump CABG will be related to elevated mitochondrial stress responses (peroxiredoxin 3 redox state) as well as elevations to various serum immune cells, markers of the complete blood count, metabolites, and electrolytes.

8 Increased circulating leukocytes may predict elevations to mitochondrial fatty acid-supported respiration in the human myocardium during coronary artery bypass graft surgery.

This chapter is currently in preparation for submission to an academic journal.

Author Contributions: Logistics for establishing and overseeing a fully functional mitochondrial bioenergetics satellite laboratory at York PCI (Interventional cardiology) (641 Davis Drive, Newmarket, ON) were principally carried out by Shivam Gandhi from April 2023 to January 2024. Shivam Gandhi: conceptualization, methodology, validation, formal analysis, investigation, writing - original draft, writing – review & editing, visualization, project administration; Aditya N. Brahmbhatt: methodology; Ihtisham A. Rana: validation (prx3 Western blot), formal analysis; Madison C. Garibotti: methodology; Amireza N. Goli: methodology; Steven Miner: conceptualization, methodology; Charles Peniston: conceptualization, methodology (surgical sample retrieval); Christopher G.R. Perry: conceptualization, methodology, validation, formal analysis, investigation, writing -original draft, writing – review & editing, visualization, project administration. All persons designated as authors qualify for authorship, and all those who qualify for authorship are listed.

Increased circulating leukocytes may predict elevations to mitochondrial fatty acid-supported respiration in the human myocardium during coronary artery bypass graft surgery.

Authors: Shivam Gandhi[1], Aditya N. Brahmbhatt[1], Ihtisham A. Rana[1], Madison C. Garibotti[1], Amireza N. Goli[1], Steven Miner[2], Charles Peniston[2], and Christopher G.R. Perry[1]†.

Affiliations:

[1]School of Kinesiology & Health Science, Muscle Health Research Centre, York University, Toronto, ON, Canada

[2]York Percutaneous Coronary Intervention (PCI) Group, Southlake Regional Health Centre, Newmarket, ON, Canada

Key words: coronary artery bypass graft, mitochondria, human, atria, fatty acid, inflammation

†Address for Correspondence:

Christopher Perry, PhD

School of Kinesiology and Health Science Muscle Health Research Centre

344 Norman Bethune College

York University

4700 Keele Street

Toronto, Ontario M3J 1P3

(P) 416 736 2100 ext. 33232

cperry@yorku.ca

Conflict of Interest: The authors have declared that no conflict of interest exists.

Abstract

Introduction: According to global health estimates by the World Health Organization, coronary artery diseases (CAD) are, as of 2024, among the leading causes of death worldwide. In CAD, accumulating atherosclerotic plaques can narrow or block coronary arteries, thus restricting oxygen and nutrient supply to cardiac muscles and precipitating hypoxia-induced cardiomyopathic damage if left untreated. In severe cases of CAD where lifestyle changes are insufficient to minimize blockages, on-pump coronary artery bypass graft (CABG) surgery is performed to redirect blood flow with harvested veins or arteries. A combination of ischemia and reperfusion during cardiopulmonary bypass is hypothesized to exacerbate injury to the myocardium, primarily owing to metabolic stress, thus impacting patient recovery.

Purpose and methods: The purpose of this study was to employ a novel, repeated-measures clinically insightful design where viable pre- and post-CABG right atrial appendage (RAA) samples explanted from male patients undergoing elective CABG were compared for differences in mitochondrial stress responses and their correlation to indices of circulating immune cells, complete blood count, metabolites, and electrolytes at various time-points.

Results: Findings from this study suggest that post-CABG RAA demonstrate enhanced fatty acid-supported mitochondrial respiration compared to pre-CABG samples, while carbohydrate-supported respiration is unchanged between time-points. Furthermore, this ‘adaptation’ in substrate oxidation is related to reductions in post-CABG RAA peroxiredoxin 3 monomer abundance, an index of mitochondrial-mediated oxidative stress. While these mitochondrial stress responses were not statistically significant when correlated with patient discharge, a strong negative correlation was determined between these stress responses and circulating lymphocytes

and platelet count the day following surgery. Point-of-care data revealed that total leukocytes and neutrophils in circulation were significantly elevated immediately after the surgery.

Future directions: Planned experiments will determine if this enhanced fatty acid-supported respiration in the post-CABG RAA is a protective mechanism, or instead, reflects an adaptive mitochondrial reprogramming response to stress.

Conclusion: By understanding the complex relationship between human atrial appendage-specific mitochondrial reprogramming (adaptations to substrate selection and oxidative stress), systemic immune cell count, and recovery outcomes during and after CABG, this study will guide therapy development that targets an underlying mitochondrial-inflammation axis.

Introduction

Coronary artery diseases (CAD) are among the leading causes of death worldwide and on-pump coronary artery bypass grafting (CABG) surgeries are considered the gold standard intervention for treatment of multi-vessel CAD [441]. CABG surgeries are routinely performed when major coronary arteries are narrowed or occluded (usually by atherosclerotic plaques), thus restricting oxygenated blood supply to the myocardium. CABG procedures re-route blood flow around major occluded coronary arteries with a grafted artery or vein to minimize hypoxic damage to the myocardium, ultimately preventing the development of more severe long-term cardiovascular complications.

Despite the benefits of CABG, there are various peri- and post-operative (post-op) complications that can arise during and following the surgical period, including pulmonary hypertension, strokes, and post-op atrial fibrillation (POAF), the majority of which can be attributed to patient lifestyle, medical history, or extenuating post-op complications [544]. Beyond these factors, it is hypothesized that cardiac ischemia (which occurs when cardioplegic buffers arrest the heart for cardiopulmonary bypass (CPB)), and subsequent rapid reperfusion of blood flow, may play a pivotal role in precipitating cardiac damage [545–549]. While cardiac ischemia - defined as inadequate oxygenated blood supply to the myocardium – can result in complications if the restricted blood flow is 10% or less of normal resting perfusion [444], reperfusion – the abrupt restoration of oxygenated blood flow to previously ischemic regions – can paradoxically exacerbate cellular dysfunction and death despite being necessary to ensure survival of the tissue. Collectively, this phenomenon is known as cardiac ischemia-reperfusion injury (IRI), and it is thought to represent a major detrimental consequence of CABG.

Cardiac mitochondria are ‘stressed’ as a result of both prolonged normothermic and cold (organ preservation) cardiac IRI, at least in pre-clinical models [444,473,519,521–523]. This is evidenced by elevated post-reperfusion mitochondrial-derived reactive oxygen species (ROS) emissions [533] and over-reliance on fatty acid oxidation (which has been associated with detriments to functional mechanical recovery of ischemic hearts) in murine models subjected to cardiac IR [461,550]. However, to date, a comparative analysis of mitochondrial substrate-specific respiration and its relationship to oxidative stress remains vastly understudied in clinical settings, and more specifically, during CABG surgery. Repeated-measures mitochondrial respiratory and oxidative stress data (i.e. acquired from the same patient throughout the CABG procedure) is sparse, with no known studies that compare indices of mitochondrial stress in viable pre- and post-CABG atrial appendage samples. In the context of this study, pre-CABG is defined as right atrial appendage (RAA) samples explanted prior to CPB, while post-CABG is defined as RAA explanted following anastomosis and reperfusion of blood supply.

This gap in knowledge presents an opportunity for exploring how CABG influences adaptations to mitochondrial substrate oxidation and ROS-induced oxidative stress at two distinct time-points that have never been comparatively assessed in humans before. The study also presents opportunities for examining how adaptations to mitochondrial substrate oxidation (carbohydrate- and fatty acid-supported respiration as fuel sources for ATP) may predict post-op recovery outcomes, thus representing an avenue for exploration into therapeutic interventions to improve life after the procedure. With this unique study design, any adaptations to mitochondrial stress responses between pre- and post-CABG RAA can also be correlated to systemic inflammatory and metabolite markers (point-of-care data) that are monitored throughout various

peri- and post-op time-points. This could represent a potential CABG-induced mitochondrial-inflammation axis that lends insight to multimodal factors governing patient recovery.

The primary purpose of this study was to investigate mitochondrial stress responses associated with on-pump CABG in a novel and innovative study design that compares pre- and post-CABG RAA samples from the same patient. By understanding the molecular mechanisms underpinning CABG and its influence on repeated-measures mitochondrial stress responses before and after CPB, future therapy development could target mitochondrial adaptations, including respiratory substrate selection and oxidative stress-induced damage, to improve both peri- and post-op patient recovery outcomes.

Results

On-pump CABG is associated with enhanced mitochondrial fatty acid-supported respiration in post-CABG human RAA, while carbohydrate-supported respiration is unchanged

By implementing a repeated-measures study design, mitochondrial oxygen consumption of PmFBs prepared from pre- and post-CABG RAA sample was comparatively assessed using the NADH-generating substrates pyruvate (5 mM) and malate (2 mM). These substrates for carbohydrate-supported respiration were titrated in the presence and absence of saturating (20 mM) creatine. Respiration was assessed across a spectrum of metabolic demands (modeled by increasing ADP from 100 μM (physiological) to 7000 μM (supraphysiological)) in samples explanted from the same patient. No differences were detected between pre- and post-CABG PmFBs with this protocol with and without creatine (**Figure 8-1A**).

On separate PmFBs prepared from the same pre- and post-CABG RAA sample, 10 μM L-carnitine, 20 μM palmitoyl CoA, and 500 μM malate was titrated to represent an index of fatty acid-supported mitochondrial respiration across a similar spectrum of metabolic demand (100 μM to 7000 μM ADP) in the presence and absence of saturating creatine. Interestingly, fatty acid-supported respiration was significantly elevated in the post-CABG RAA sample compared to pre-CABG at maximal [ADP] (5000 μM (1.7-fold increase) and 7000 μM (1.7-fold increase)) in the presence of creatine, while results from the creatine-independent condition could not be conclusively interpreted due to low repeated-measures sample size (**Figure 8-1B**).

A separate protocol that also assesses mitochondrial oxidation of fatty acids, albeit bypassing carnitine transporters required for fatty acid entry into the mitochondria, was also investigated by titrating 75 μM palmitoyl-carnitine and 500 μM malate in the presence of creatine. Despite no differences, this measure was underpowered and could not be conducted in creatine-independent conditions due to logistical limitations (**Figure 8-1C**).

Significant differences were observed when comparing carbohydrate (PM-supported) respiration to fatty acid (LPM-supported) respiration in pre-CABG RAA (**Figure 8-1D**). Surprisingly, these differences were no longer detectable when comparing the same protocols in post-CABG RAA, thus suggesting that reliance on fatty acid respiration is enhanced after CPB (**Figure 8-1E**). Comparisons were made with repeated-measures data from the same patient.

State II respiration (prior to the addition of ADP) was assessed using carbohydrate oxidation-supporting substrates (pyruvate + malate) in the presence and absence of creatine. No significant differences were detected between pre- and post-CABG RAA samples in either condition (**Figure 8-2A**). Respiratory coupling ratio was assessed between State III PM (7 mM ADP) and State II PM to determine if complex I was uncoupled in the presence and/or absence of creatine, however, no significant differences were observed (**Figure 8-2B**). State III respiration (after the addition of ADP) was assessed using 10 mM glutamate (further NADH generation; complex I stimulation) and 10 mM succinate ($FADH_2$ generation; complex II stimulation), however, no differences were detected in both the presence and absence of creatine (**Figure 8-2C, D**). State II respiration was also assessed using fatty acid oxidation-supporting substrates (L-carnitine + palmitoyl CoA + malate) with and without creatine, however, no differences were detected (**Figure 8-2E**). Creatine sensitivity was assessed across a spectrum of metabolic demands (100 μM – 7 mM ADP) with carbohydrate- and fatty acid-supported mitochondrial respiration as an index of high-energy phosphocreatine shuttling for ATP export, however, no differences were detected with either protocol (**SFigure 8-1**). All measures were conducted and analyzed using a repeated-measures design.

Table 1.

Patient #	Age	Biological Sex	Race	Weight (kg)	Height (cm)	BMI (kg/m^2)	Days until discharge from CVICU	Days until discharge from hospital	Formerly smoked/used tobacco	Currently smokes/uses tobacco
1	67	M	C	113	191	31	1	5	Y	N
2	74	M	C	85	172	28.7	5	9	Y	N
3	63	M	C	94	177	30	2	5	Y	N
5	75	M	C	72	170	24.9	2	9	Y	N
6	75	M	C	87	179	27.2	2	6	N	Y
7	79	M	C	70	157	28.4	2	7	Y	N
8	80	M	C	65	176	21	6	8	N	N
9	65	M	C	72.5	173	24.2	3	5	N	N
10	69	M	C	104	178	32.8	1	5	N	Y
11	66	M	A	55	178	17.4	3	9	N	Y
12	67	M	C	97	191	26.6	4	5	N	N
Average	70.9	/	/	83.1	176.5	26.6	2.8	6.6		

Table 8-1. Baseline clinical characteristics and demographic information obtained from all enrolled patients prior to surgery. A total of 12 male patients, aged 63-80, consented to participating in this study. Patient 4 was dropped from analysis due to peri-operative complications. All morphometric data was collected by the interventional cardiology team prior to surgery. C = Caucasian; A = Asian; Y = Yes; N = No.

Table 2.

Patient #	CAD	Prior MI	Prior coronary revascularization	PCI with stent	Hypertension	Hypercholesterolemia	Diabetes Mellitus (Type II)	Previous Hepatitis C	Arthritis	COPD
1	Y	Y	Y	Y	Y	Y	Y	Y	N	N
2	Y	Y	N	N	Y	Y	Y	N	Y	Y
3	Y	N	N	N	Y	Y	N	N	N	N
5	N	N	N	N	N	N	N	N	N	N
6	Y	N	N	N	Y	Y	N	N	N	N
7	Y	Y	N	N	Y	Y	Y	N	N	N
8	N	N	N	N	N	N	N	N	N	N
9	N	N	N	N	Y	N	N	N	N	N
10	Y	Y	N	Y	Y	Y	N	N	N	N
11	N	N	N	N	N	N	N	N	N	N
12	N	N	N	N	Y	Y	N	N	N	N

Table 8-2. Patient medical history, including existence of various co-morbidities prior to surgery. All 12 participants were screened for comorbidities prior to surgery. Only confounding co-morbidities that may interfere with or influence the CABG surgical procedure (including use of certain drugs/condition-specific medications) were screened for. CAD = coronary artery disease; MI = myocardial infarction; PCI = percutaneous coronary intervention; COPD = chronic obstructive pulmonary disease; Y = Yes; N = No.

Table 3.

Patient #	Beta blocker	ACE/ARB	Anticoagulant	Low-to-moderate intensity statin	High intensity statin	Ezetimibe	Metformin	Ozempic	Aspirin	CCB	PCSK9 inhibitor	P2Y12 Inhibitor
1	Y	Y	Y	Y	N	Y	Y	Y	N	N	N	N
2	Y	Y	N	Y	N	N	N	N	Y	N	N	N
3	Y	N	N	Y	N	N	N	N	N	N	N	N
5	Y	N	N	N	N	N	N	N	Y	Y	N	N
6	Y	Y	N	Y	N	N	N	N	Y	N	Y	N
7	Y	Y	N	Y	N	N	Y	N	N	N	N	N
8	N	N	N	N	Y	N	N	N	Y	N	N	N
9	N	Y	N	Y	N	N	N	N	Y	N	N	N
10	Y	N	N	N	Y	N	N	N	Y	N	N	N
11	N	N	N	Y	N	N	N	N	Y	N	N	Y
12	Y	Y	N	Y	N	N	N	N	Y	N	N	N

Table 8-3. Medications taken by, or prescribed to, each patient reported prior to surgery. All 12 participants completed a questionnaire regarding history of medication use. Dosage information was not collected, except for intensity of statins (low-to-moderate versus high intensity). ACE = angiotensin-converting enzyme; ARB = angiotensin-receptor blocker; CCB = calcium channel blocker; Y = Yes; N = No.

Figure 1.

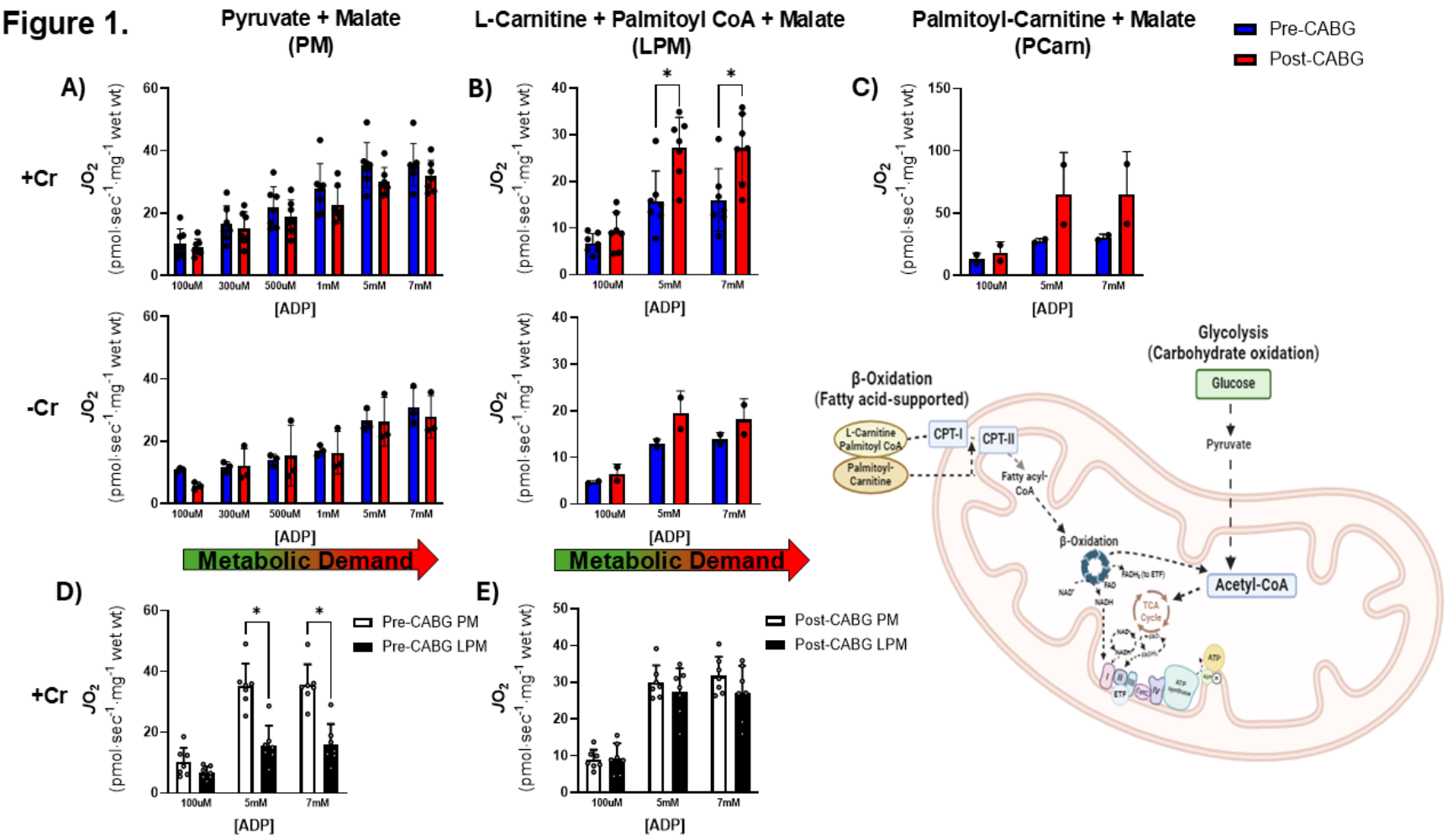
Pyruvate + Malate
(PM)
L-Carnitine + Palmitoyl CoA + Malate
(LPM)
Palmitoyl-Carnitine + Malate
(PCarn)
Pre-CABG
Post-CABG
A)
B)
C)
+Cr
-Cr
JO_2 (pmol·sec^{-1}·mg^{-1} wet wt)
[ADP]
100uM
300uM
500uM
1mM
5mM
7mM
Metabolic Demand
D)
E)
Pre-CABG PM
Pre-CABG LPM
Post-CABG PM
Post-CABG LPM
β-Oxidation
(Fatty acid-supported)
L-Carnitine
Palmitoyl CoA
Palmitoyl-
Carnitine
CPT-I
CPT-II
Fatty acyl-
CoA
β-Oxidation
Glycolysis
(Carbohydrate oxidation)
Glucose
Pyruvate
Acetyl-CoA
TCA
Cycle
ETF
ATP

Figure 8-1. Substrate-specific stimulation of mitochondrial respiration in permeabilized pre- and post-CABG RAA samples over a spectrum of metabolic demands. This novel study design was strengthened by repeated-measures analysis of right atrial appendage (RAA) mitochondrial respiration data with carbohydrate- and fatty acid-supporting substrates collected from the same patient before (pre-CABG) and after (post-CABG) cardiopulmonary bypass. A) ADP-stimulated respiration was supported by pyruvate (5 mM) supplemented with malate (2 mM) (NADH, mitochondrial complex-I stimulation) as an index of carbohydrate oxidation, in the presence (+Cr) and absence (-Cr) of saturating creatine across a spectrum of metabolic demands (100 μM to 7 mM ADP). B) 20 μM Palmitoyl CoA (supplemented with 10 μM L-Carnitine and 500 μM Malate (NADH and $FADH_2$ generating substrates) and 100 μM - 7 mM ADP) was added to a separate RAA PmFB as an index of fatty acid oxidation, also in +/- Cr conditions. $FADH_2$ from the TCA cycle transfers its electrons at complex-II while $FADH_2$ from beta oxidation provides electrons for ETF. C) On a separate PmFB also assessing fatty acid oxidation, 75 μM palmitoyl-carnitine and 500 μM malate (along with 100 μM - 7 mM ADP) were titrated and intended to bypass carnitine transporters across the mitochondrial membranes, thus providing reducing equivalents for ETF via beta oxidation. D-E) PM-supported respiration was compared to LPM-supported respiration from the same patient (pre- and post-CABG) over a spectrum of metabolic demands in +Cr conditions. NADH = Nicotinamide adenine dinucleotide; $FADH_2$ = Flavin adenine dinucleotide; ETF = Electron transport flavoprotein; CPT = carnitine palmitoyltransferase; CoA = Coenzyme A; I-IV = mitochondrial complexes; TCA = tricarboxylic acid. Results represent mean ± SD, n=7 repeated-measures data points in +Cr conditions; n=2 repeated-measures data points in –Cr conditions. A repeated-measures 2-way ANOVA was used to determine the difference between pre- and post-CABG RAA across [ADP]. All *p* values are FDR-adjusted by Benjamini, Krieger, and Yekutieli *post-hoc* analyses. *$p<0.05$ denotes significance.

Figure 2.

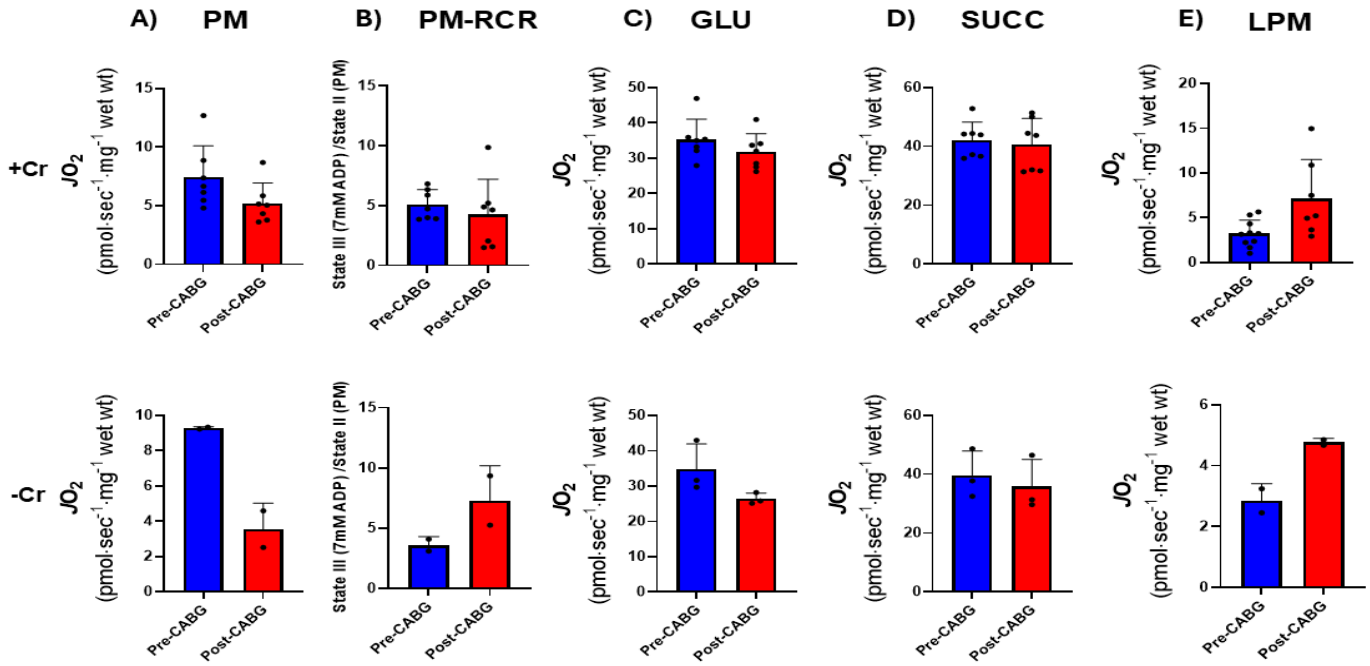

Figure 8-2. Complex I- and II-stimulated mitochondrial respiration in pre- and post-CABG RAA samples. A) To assess complex-I (carbohydrate)-supported respiration, repeated-measures pre- and post-CABG permeabilized RAA bundles were stimulated with 5 mM pyruvate and 2 mM malate, which are NADH-generating substrates used in tandem as a measure of state II respiration (absence of ADP), in +/- Cr conditions. B) Respiratory control ratio (RCR) was calculated by dividing maximal State III (ADP-supported) PM respiration by State II PM respiration (no ADP) to determine if mitochondria elicited uncoupled respiration. C) Following ADP (100 µM – 7 mM) titrations, 10 mM glutamate was titrated to further saturate complex-I with NADH generation (only PM protocol). D) Similarly, following ADP titrations, 10 mM succinate ($FADH_2$-stimulating) was added to further support complex-II respiration (only PM protocol). E) Fatty acid-supported respiration was assessed by titrating 10 µM L-carnitine, 20 µM palmitoyl CoA, and 500 µM malate to shuttle electrons through mitochondrial beta-oxidation pathways. This protocol is complex-I stimulating as it generates NADH, and ETF- and complex II-stimulating attributed to $FADH_2$ generation from beta-oxidation. NADH = Nicotinamide adenine dinucleotide; $FADH_2$ = Flavin adenine dinucleotide; ETF = Electron transport flavoprotein; PM = pyruvate + malate; GLU = glutamate; SUCC = succinate; LPM = L-Carnitine + palmitoyl CoA + malate. Results represent mean ± SD, n=7 repeated-measures data points in + Cr conditions; n=2-3 repeated-measures data points in – Cr conditions.

Enhanced mitochondrial fatty acid-supported respiration is accompanied by prx3 oxidation

When assessing pre- and post-CABG RAA samples expressed as the percentage of the total prx3 signal in the dimerized (oxidized) form relative to total protein content (monomer + dimer content), no significant differences were detected at a modest sample size of 5 repeated-measures data points (**Figure 8-3A**). While assessment of prx3 dimer density also did not reveal significant differences, prx3 monomer density demonstrated a significant decrease in post-CABG RAA samples (1.7-fold decrease) compared to pre-CABG, thus suggesting that the protein content of 'reduced' prx3 is lower following CABG compared to pre-CABG RAA sample (**Figure 8-3A**). The redox state of mitochondrial prx3 was assessed and compared between pre- and post-CABG RAA samples to determine if the surgical procedure influenced elevations to mitochondrial-mediated oxidative stress which would be consistent with reperfusion injury (**Figure 8-3B**). This measure was implemented to broadly determine if the observed enhanced fatty acid-supported respiration was associated with elevations to oxidative stress post-CABG, thus expanding future research to investigate components of fatty acid-supported respiration that regulate redox signaling.

Figure 3A.

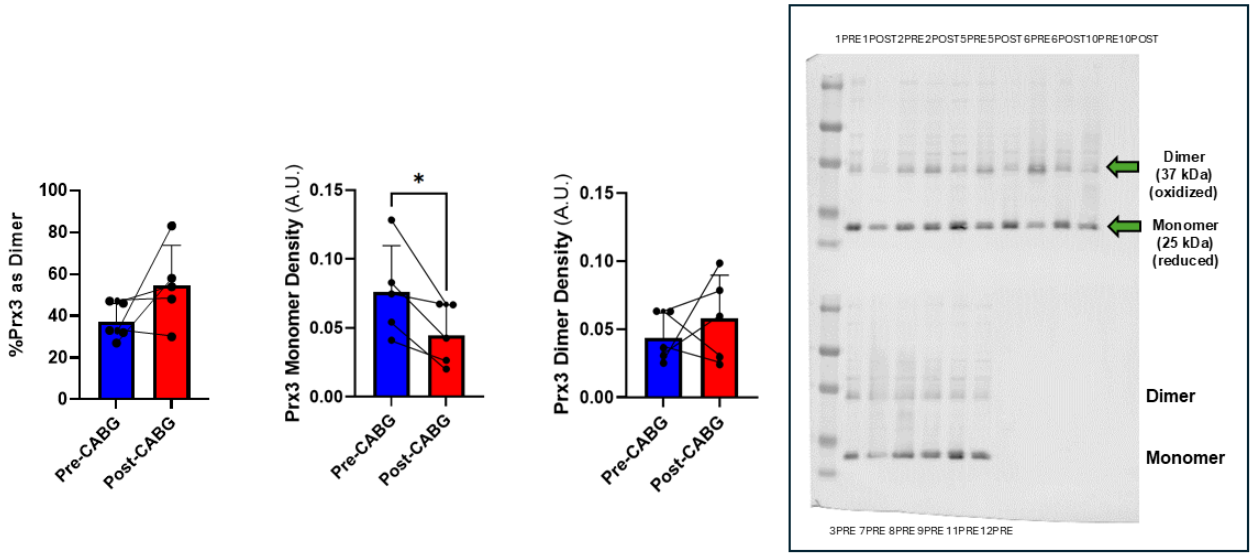

Figure 3B.

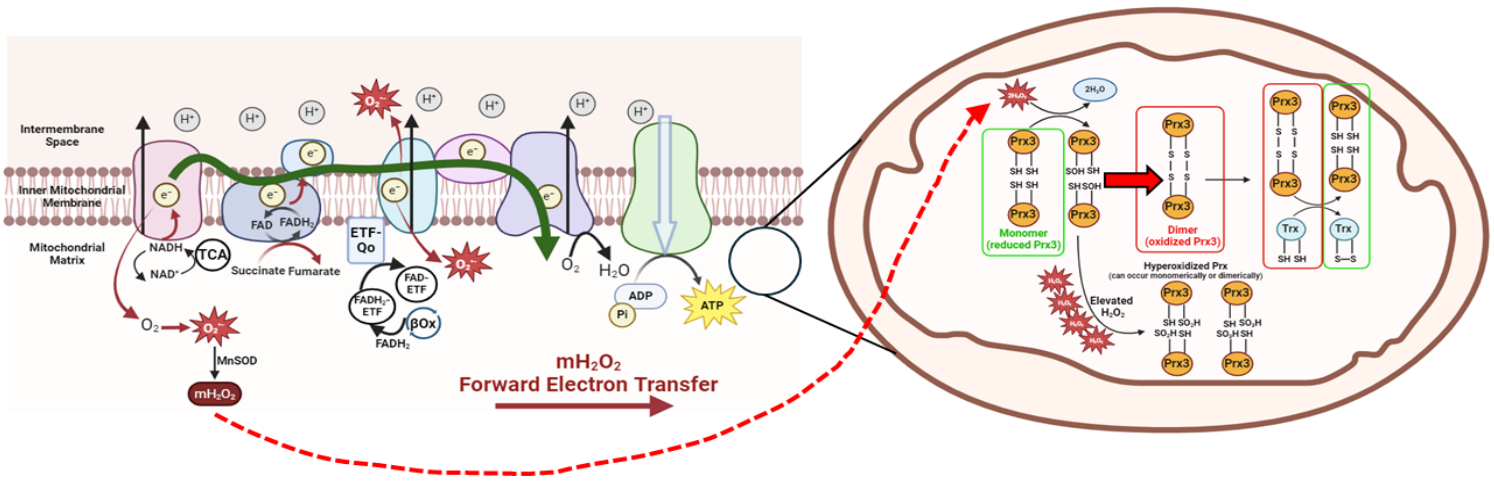

Figure 8-3A. Mitochondrial peroxiredoxin 3 dimerization percentage, monomer density content, and dimer density content in pre- and post-CABG RAA samples, with representative Western blot. A modified Western blot was utilized to determine if CABG influences oxidative stress to RAA samples obtained before and after cardiopulmonary bypass. Prx3 = peroxiredoxin 3. Results represent mean ± SD, n=5 patients. A repeated-measures paired t-test was used to determine statistical differences between pre- and post-CABG RAA. *$p<0.05$ denotes significance.

Figure 8-3B. Sources of mH_2O_2 during CABG that can oxidize mitochondrial peroxiredoxin 3. Mitochondrial superoxide ($O_2^{\bullet-}$) generated from premature electron slip at complex-I or III that is dismutated to mH_2O_2 by manganese superoxide dismutase (MnSOD) may be responsible for oxidizing mitochondrial prx3 in the mitochondrial matrix. Dimerized prx3 moieties are representative of oxidized prx3, whereas prx3 monomers represent its reduced state. Oxidized prx3 can be recycled back to its reduced state by the thioredoxin (Trx) antioxidant system. Oxidized prx3 represents a 'historical snapshot' that oxidative stress occurred. Figure created using www.BioRender.com.

Immune cells, complete blood count, metabolites, and electrolytes are differentially affected during and after surgery, and may be related to fatty acid-supported respiration

Systemic immune cell counts for total leukocytes, absolute neutrophils, and absolute lymphocytes were assessed at various time points throughout the surgical period, including pre-surgery, post-op surgery day, and up to three days following CABG (where applicable). These circulating cell counts were investigated at different stages of the surgical and post-op period to determine if enhanced fatty acid-supported respiration on the post-CABG RAA occurred in association with shifts to inflammatory state. Both total leukocytes and neutrophils were significantly elevated post-op surgery day compared to pre-surgery levels and remained elevated up to three days following the surgery, which was the duration that these markers were tracked for following the procedure (**Figure 8-4A, B**). Absolute lymphocytes did not change post-op surgery day, however, they were significantly decreased next day post-op and remained decreased two days after the surgery (**Figure 8-4C**). No significant differences were observed at any time point in absolute eosinophils and monocytes, while basophils were not detectable in the majority of patients (**Figure 8-4D-F**).

A complete blood count (CBC) panel was also assessed at the abovementioned time points. Erythrocytes, hemoglobin, and hematocrit were all significantly decreased post-op surgery day and remained significantly lower than the pre-surgery levels at the final measured time (three days post-op) (**Figure 8-5A-C**). For all three markers, two days post-op reflected the lowest cell count compared to pre-surgery (**Figure 8-5A-C**). Mean cell volume (**Figure 8-5D**), mean cell hemoglobin (**Figure 8-5E**), mean cell hemoglobin concentration (**Figure 8-5F**), and red blood cell distribution width (**Figure 8-5G**) were largely unaltered between time points. Platelet count was significantly lower compared to pre-surgery next day post-op but returned to pre-surgery levels three days post-op, with two days post-op being the lowest absolute cell count

throughout the duration of the measurement period (**Figure 8-5H**). Mean platelet volume was significantly elevated two days post-op and remained elevated until the final measured time point (**Figure 8-5I**).

Metabolites and electrolytes were assessed pre-biopsy, during CABG, immediately post-CABG, post-op surgery day, and up to two days post-op for patients requiring closer monitoring (**Figure 8-6**). First, it was observed that compared to pre-biopsy levels, glucose levels were significantly elevated during CABG, immediately post-CABG, post-op surgery day, and next day post-op, thus suggesting that circulating glucose is elevated at the onset of CABG and remains elevated until at least the day after surgery for most patients (**Figure 8-6A**). Circulating levels of sodium surprisingly remained unaltered throughout the measured surgical period (**Figure 8-6B**). Chloride, on the other hand, was only significantly elevated post-op surgery day and remained elevated until the day after surgery (next day post-op), compared to pre-biopsy (**Figure 8-6C**). Potassium levels were consistently elevated, with significant increases during CABG, immediately post-CABG, post-op surgery day, and even the day after surgery (next day post-op), suggesting that similar to glucose, CABG increases circulating potassium levels compared to pre-biopsy (**Figure 8-6D**). O_2 levels remained unchanged during CABG and also immediately post-CABG, however, these levels dramatically lowered post-op surgery day and remained significantly lower than pre-biopsy until the day after surgery (next day post-op) for most patients (**Figure 8-6E**). Arterial O_2 saturation % significantly decreased two days following CABG and remained decreased for at least two days post-op (**Figure 8-6F**). pCO_2 levels were significantly lower during CABG, immediately post-CABG, post-op surgery day, and even the day after surgery (next day post-op), thus suggesting that compared to pre-biopsy levels, CABG causes a continuous downward trend of pCO_2 (**Figure 8-6G**). Bicarbonate was significantly

decreased during CABG, immediately post-CABG and stayed significantly lower than pre-biopsy until the day after CABG (next day post-op) (**Figure 8-6H**). Interestingly, decreases to calcium began during CABG, and continued to remain significantly lower than pre-biopsy levels until the day after the surgery, akin to PCO_2 levels (**Figure 8-6I**). pH levels were relatively transient, with modest, albeit significant elevations during CABG which remarkably returned to pre-biopsy levels immediately post-CABG (**Figure 8-6J**). Circulating levels of lactate remained unaltered throughout the measured surgical period (**Figure 8-6K**).

Figure 4.

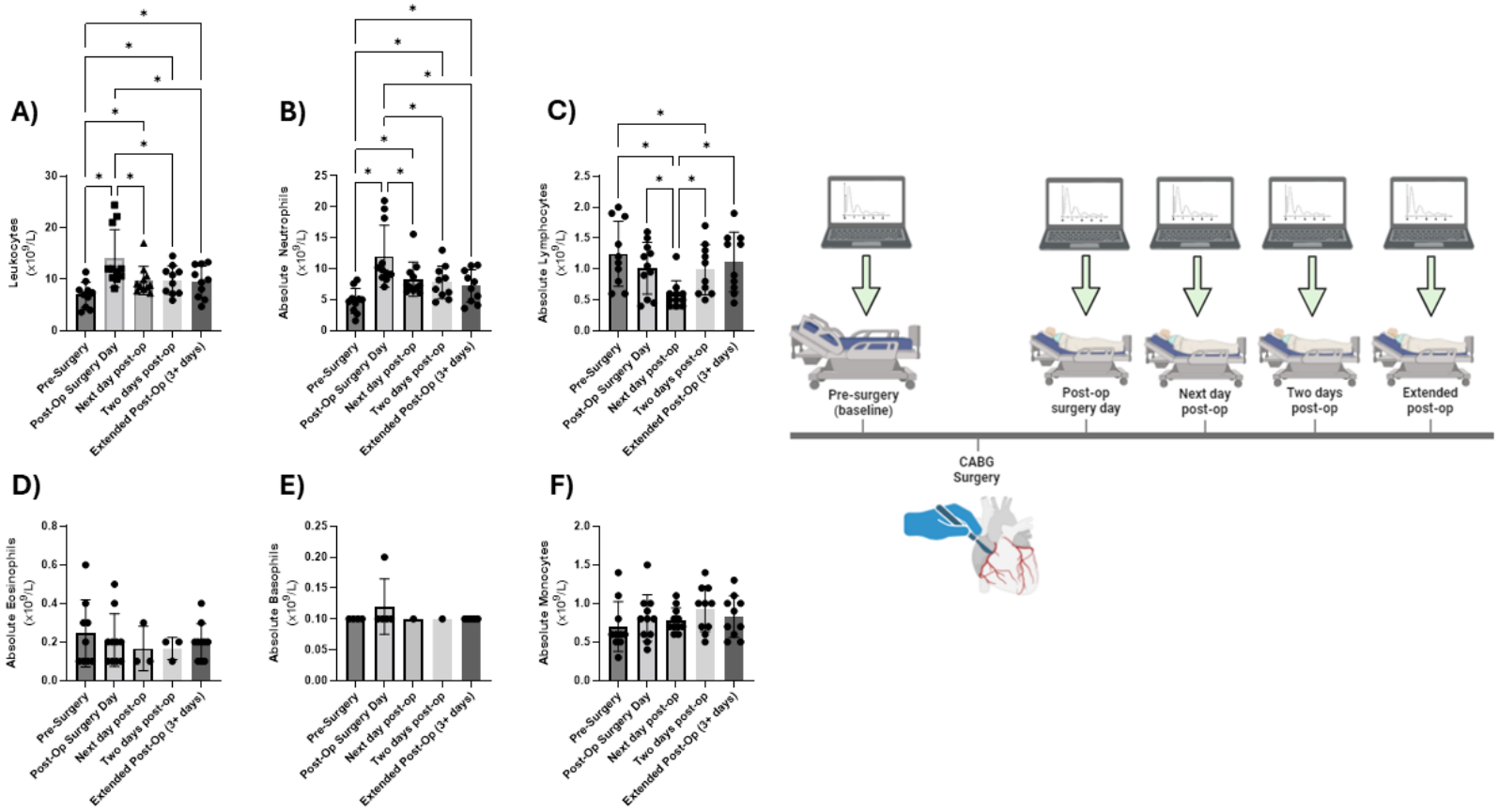

Figure 8-4. Circulating immune cell count obtained at various stages of the surgical procedure, including pre-surgery, post-op surgery day, next day post-op, two days post-op, and extended post-op (3+ days; where applicable). Point-of-care data was tracked in all patients undergoing CABG by the interventional cardiology team. Results represent mean ± SD, n=9-10 (with the exception of absolute eosinophils and basophils which were only detected in a smaller sub-set of patients). A 1-way ANOVA was used to determine if there was a difference in systemic immune cell count between various time-points throughout the surgery. All *p* values are FDR-adjusted by Benjamini, Krieger, and Yekutieli *post-hoc* analyses. *$p<0.05$ denotes significance. Figure created using www.BioRender.com.

Figure 5.

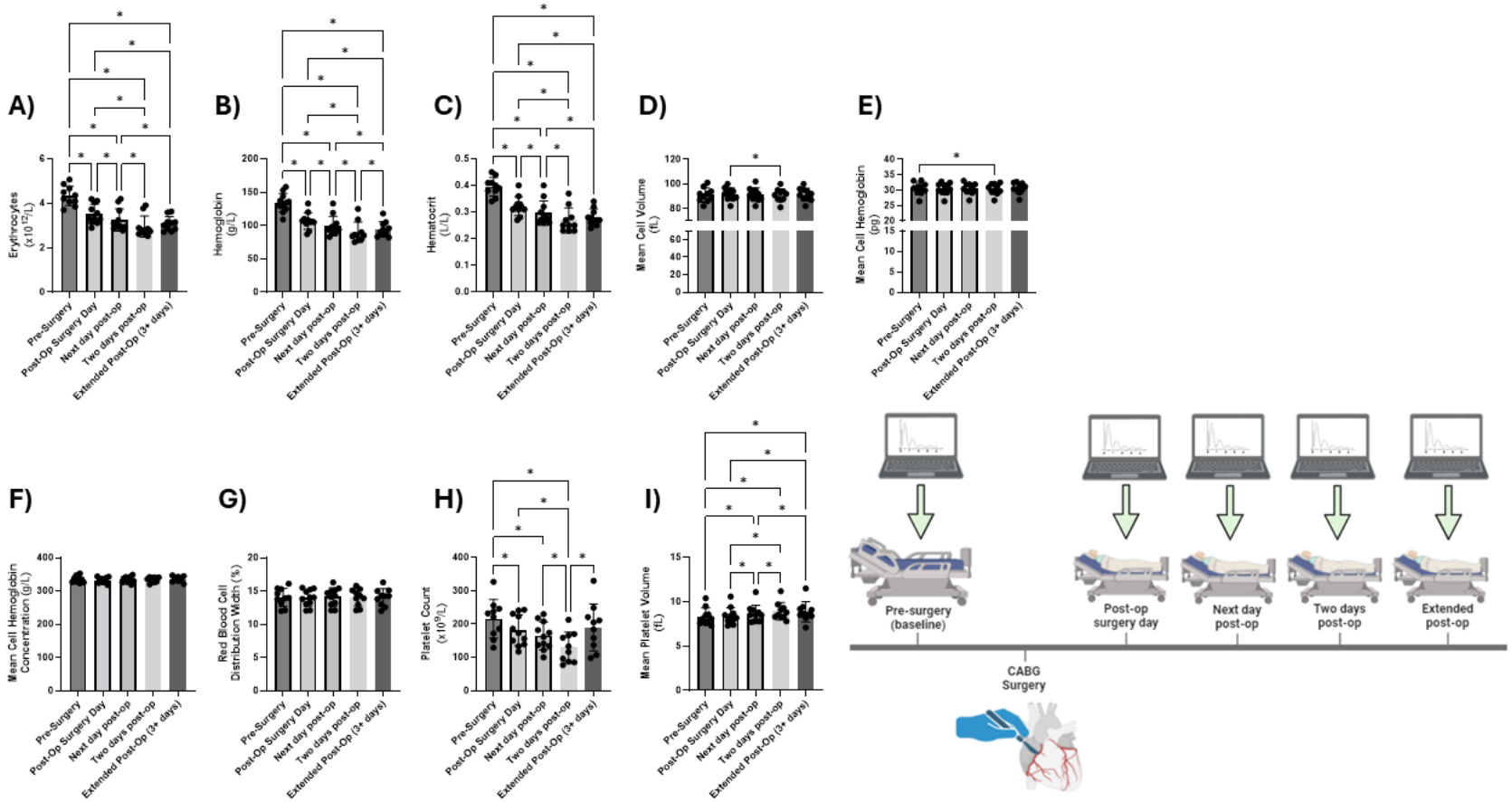

Figure 8-5. Circulating complete blood cell count obtained at various stages of the surgical procedure, including pre-surgery, post-op surgery day, next day post-op, two days post-op, and extended post-op (3+ days; where applicable). Point-of-care data was tracked in all patients undergoing CABG by the interventional cardiology team. Results represent mean ± SD, n=9-10. A 1-way ANOVA was used to determine if there was a difference in systemic complete blood cell count between various time-points throughout the surgery. All p values are FDR-adjusted by Benjamini, Krieger, and Yekutieli *post-hoc* analyses. *p<0.05 denotes significance. Figure created using www.BioRender.com.

Figure 6.

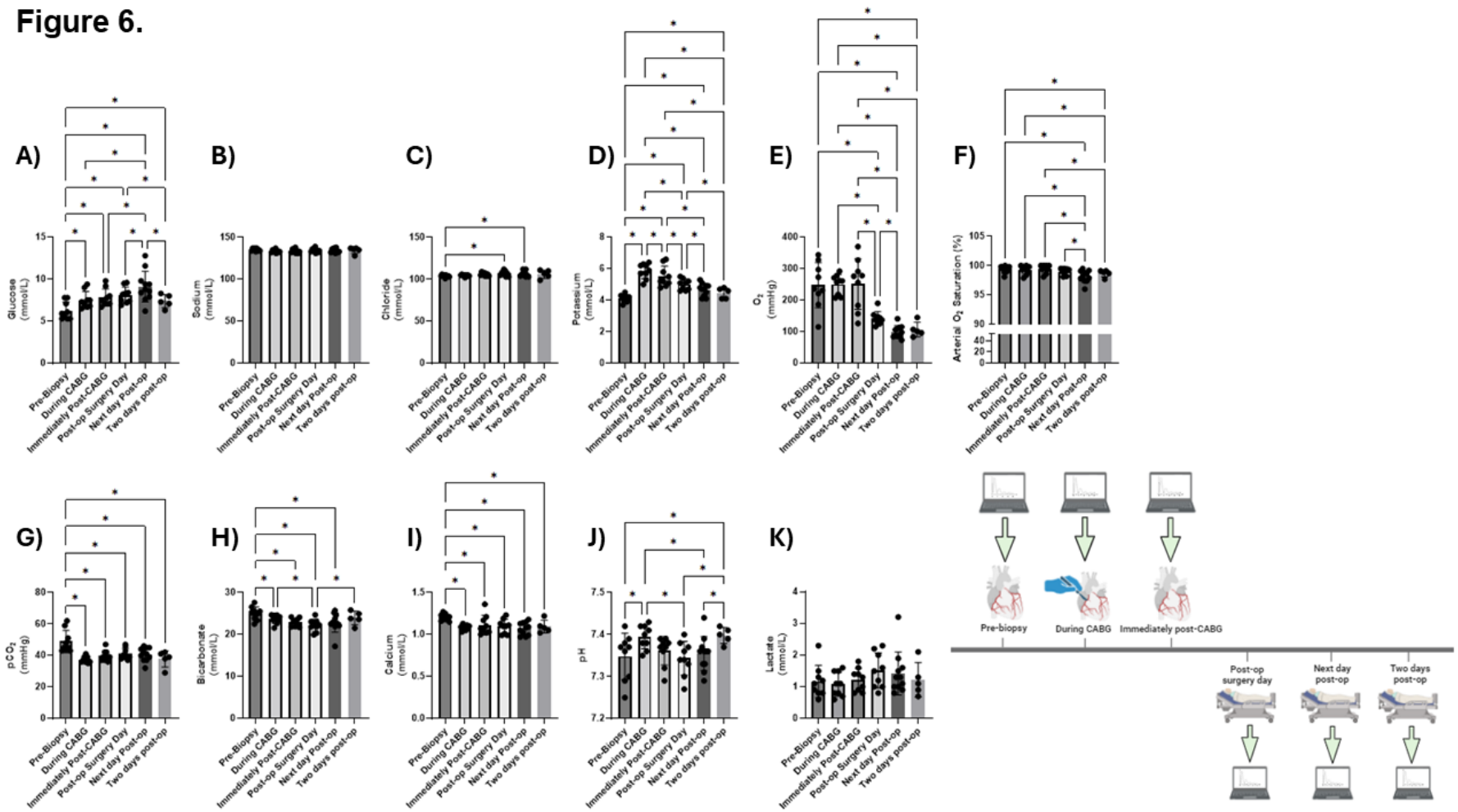

Figure 8-6. Circulating metabolites and electrolytes obtained at various stages of the surgical procedure, including pre-biopsy, during CABG, immediately post-CABG, post-op surgery day, next day post-op, and two days post-op (where applicable). Point-of-care data was tracked in all patients undergoing CABG by the interventional cardiology and CVICU perfusion team. Results represent mean ± SD, n=9-10. A 1-way ANOVA was used to determine if there was a difference in systemic metabolite and electrolyte cell count between various time-points throughout the surgery. All *p* values are FDR-adjusted by Benjamini, Krieger, and Yekutieli *post-hoc* analyses. **p*<0.05 denotes significance. Figure created using www.BioRender.com.

Elevations to fatty acid-supported respiration are statistically correlated with systemic lymphocyte and platelet count levels next day post-operation

A Pearson's correlation analysis was conducted to determine if statistically significant correlative relationships existed between RAA-specific mitochondrial data (fatty acid-supported respiration and prx3 monomer density expressed as delta % between pre-CABG and post-CABG) and patient discharge parameters such as days until discharge from the CVICU and days until discharge to home. No significant differences were observed when correlating mitochondrial fatty acid-supported respiration to days until discharge from CVICU or to home, nor when correlating mitochondrial prx3 monomer density to the same parameters (**Figure 8-7A**). This suggests that substrate selection adaptations that enhance fatty acid-supported respiration and lead to reduced prx3 monomer density (index of oxidative stress) post-CABG do not impact patient discharge times (**Figure 8-7A**). When correlating fatty acid-supported respiration (again expressed as delta % between pre- and post-CABG) to lymphocyte count next day post-op (expressed as delta % between next day post-op and pre-surgery values), it was observed that a significant negative correlation ($r = -0.9331$; $p<0.006$) persisted (**Figure 8-7B; SFigure 8-2**). This significant negative correlation also persisted between fatty acid-supported respiration (delta % between pre- and post-CABG) and platelet count next day post-op delta % ($r = -0.8853$; $p<0.019$) (**Figure 8-7B; SFigure 8-3**). Significant relationships between mitochondrial fatty acid-supported respiration delta and lymphocyte count next day post-op delta as well as platelet count next day post-op delta were detected using a correlation matrix, while no other statistically significant relationships between mitochondrial stress responses and point-of-care data were detected (**SFigure 8-3, 8-4**).

Figure 7.

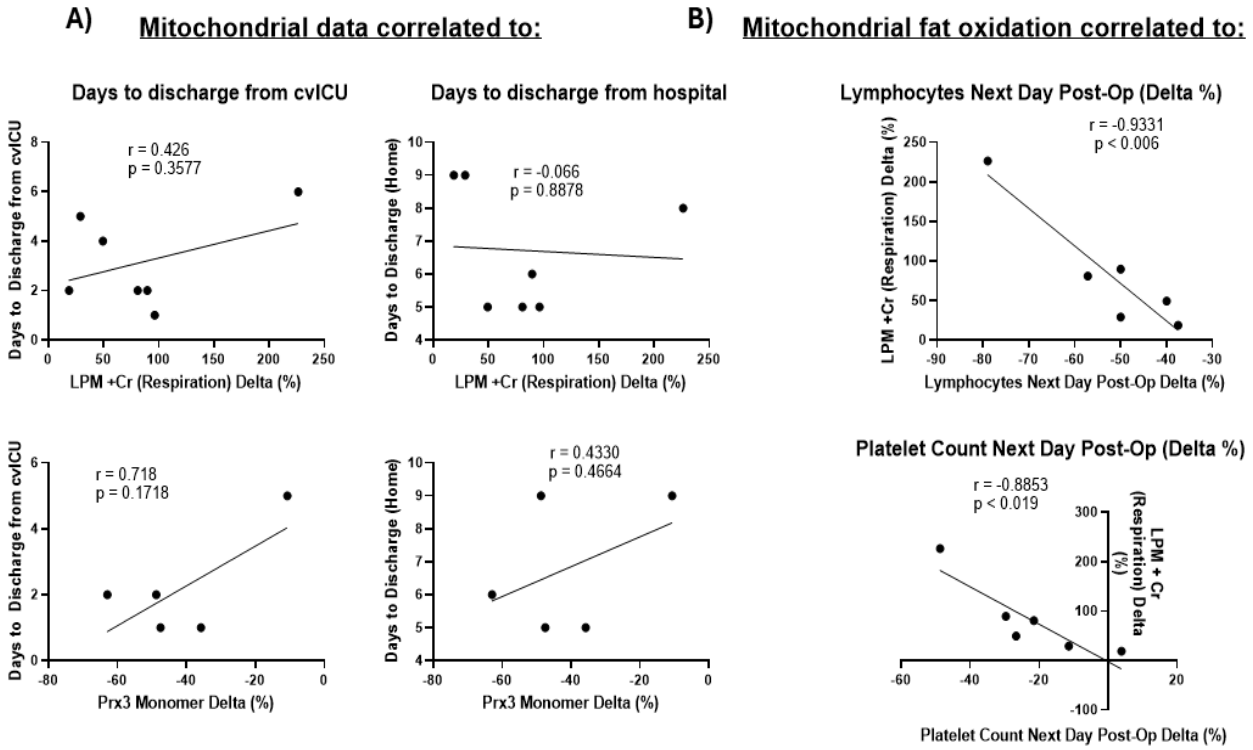

Figure 8-7. Analysis of RAA-specific mitochondrial respiratory and oxidative stress data correlated to patient recovery metrics, and RAA-specific mitochondrial fatty acid-supported respiration correlated to systemic lymphocyte and platelet count data. A) Correlation plot between days to discharge from cvICU, hospital and mitochondrial data (including fat-supported respiration and prx3 monomer density (expressed as delta % pre- and post-CABG RAA)). B) Correlation plot between fat-supported mitochondrial respiration and systemic lymphocyte and platelet count data (expressed as delta % pre-surgery and next day post-op). Results represent mean ± SD, n=5-7 repeated-measures data points. For significant correlations, Sig. (2-tailed) is defined as $p<0.05$, however, the Pearson correlation coefficient (r) is also reported.

Discussion

The present study employed a first-of-its-kind repeated-measures design in which RAA samples explanted from male hospital patients undergoing elective on-pump CABG were compared before (pre-CABG) and after (post-CABG) CPB for indices of mitochondrial stress. This study provides novel insight towards a relationship between CABG-induced mitochondrial stress responses and systemic inflammation that may guide clinical therapy development. First, we establish that mitochondrial respiration with fatty acid oxidation-supporting substrates (L-carnitine, palmitoyl CoA, malate) is significantly enhanced on the post-CABG RAA compared to pre-CABG, while respiration with carbohydrate oxidation-supporting substrates (pyruvate and malate) is unchanged. Second, this 'adaptation' towards enhanced fatty acid-supported respiration is accompanied by a significantly lower prx3 monomer band density (modified Western blot) compared to pre-CABG, indicating that these samples are less 'reduced' – a broad index of oxidative stress. Lastly, it was observed that markers of systemic inflammation, including total leukocytes and neutrophils, were elevated post-op, suggesting that mitochondrial stress adaptations may be predicted by an inflammatory response that informs patient recovery.

The relationship between adaptations to substrate-specific mitochondrial respiration and oxidative stress in RAA during CABG

Mitochondrial oxidative phosphorylation with fatty acid- and carbohydrate-supporting substrates accounts for >95% ATP production required to drive cardiac contraction in the healthy adult heart [447]. Plasticity and metabolic flexibility between energy substrate utilization upholds homeostatic processes [447]. Cardiac stress can lead to irregularities in the balance between fatty acid- and carbohydrate-supported mitochondrial respiration. In the post-ischemic reperfusion period, rates of fatty acid-supported respiration recover to pre-ischemic levels, while carbohydrate oxidation remains unchanged (in pre-clinical cardiac IRI) [515], however, the clinical implications of these substrate utilization adaptations during CABG are unknown.

In the present study, we observed enhanced fatty acid-supported respiration on the post-CABG RAA compared to pre-CABG samples, while carbohydrate-supported respiration was unchanged. The novel finding that CABG influences mitochondrial substrate-specific respiration warranted an exploration into oxidative stress responses that accompany respiratory adaptations to stress. The observation that prx3 monomer band density was significantly lower post-CABG, suggesting that it was less 'reduced' compared to pre-CABG samples, implies that transient oxidative stress is present in samples explanted after CPB, alongside the adaptation to enhanced fatty acid-stimulated respiration. It is possible that this response is associated with reperfusion stress whereby mitochondria are 'overwhelmed' by the rapid reintroduction of oxygen, leading to enhanced ROS generation as an outcome of higher mitochondrial membrane potential ($\Delta\Psi_M$).

Systemic inflammation that persists after surgery may predict atrial appendage-specific mitochondrial stress responses during CABG

Circulating total leukocytes and neutrophils were elevated post-op surgery day (compared to pre-surgery levels) and remained elevated for at least 3 days post-op. Although these immune cells were not measured directly in RAA due to tissue limitations, this does not preclude the existence of a potential axis between tissue-specific mitochondrial stress and a systemic inflammatory response. It is possible that CABG-induced systemic inflammation may be associated with adaptations in RAA-specific substrate utilization towards fatty acid-supported respiration as a response to stress. Previous literature suggests that a transcription factor with mitochondrial localization in the heart (signal transducer and activator of transcription 3 (STAT3)) may underpin the link between systemic inflammation and enhanced atrial appendage-specific fatty acid-supported respiration. STAT3 phosphorylation is associated with the induction of carnitine palmitoyltransferase-I (CPT-I) gene expression in the heart, a potent endogenous regulator of fatty acid oxidation [551]. To elaborate, the pro-inflammatory cytokine interleukin

(IL-6) is known to induce phosphorylation of STAT3 on its tyrosine 705 residue, and STAT3 phosphorylation has been previously reported in a pre-clinical model of cardiac IR [552–555]. Therefore, it is possible that IL-6-mediated phosphorylation of STAT3 influences enhanced fatty acid-supported mitochondrial respiration through a pathway that also implicates CPT-I, which has been shown to underpin mitochondrial dysfunction and cardiac hypertrophy in mice [551]. In the same study, pharmacological inactivation of the STAT3/CPT-I pathway, which decreased mitochondrial fatty acid oxidation, rescued cardiac pathology [551]. At least one study examining on-pump CABG in humans determined that levels of myocardial IL-6 production (calculated as the difference between IL-6 levels in the CPB circuit and levels in coronary venous blood) were elevated post-reperfusion and may promote neutrophil-mediated reperfusion injury in the myocardium [556]. Experiments on myocytes obtained from these CABG patients revealed that elevated IL-6 levels during IR may be derived from hypoxic myocytes [556]. The group proposed that ischemia-induced upregulation of systemic IL-6 may mediate and exacerbate reperfusion injury by enhancing neutrophil migration and infiltration to the affected myocardium (**SFigure 5**) [556]. This data is interesting given that we also observed elevated systemic neutrophils post-op. Future experiments can assess total and phosphorylated STAT3 protein content in pre- and post-CABG RAA to determine if concurrent with elevated circulating neutrophils, phosphorylated STAT3 is responsible for enhancing fatty acid-supported mitochondrial respiration (**SFigure 8-5**).

Future directions: Can assessment of malonyl-CoA or biosynthetic (non-ATP generating) fates of glycolytic enzymes explain the adaptive substrate utilization response?

Data positions the pharmacological upregulation of carbohydrate-supported respiration following cardiac reperfusion as a protective mechanism against oxidative stress in pre-clinical IR models. For example, in a seminal study conducted by Dyck *et al.*, it was demonstrated in rats

that malonyl-CoA decarboxylase (MCD) inhibition protected hearts affected by global IRI by significantly increasing myocardial malonyl-CoA levels, decreasing fatty acid-supported mitochondrial respiration, and subsequently enhancing glucose-supported respiration [557]. This work underscores the significance of adaptations to energy substrate utilization as an underlying mechanism for improving cardiac function during and after ischemia [557]. Kudo *et al.*, also from the Lopaschuk group, demonstrated that enhanced fatty acid oxidation during cardiac reperfusion was associated with decreased malonyl-CoA levels linked to increased AMPK-mediated inhibition of acetyl-CoA carboxylase (ACC) [550]. Malonyl-CoA in pre- and post-CABG RAA should be assessed to determine if adaptations to substrate utilization can be explained by differences in this potent regulator of fatty acid-supported mitochondrial respiration (**SFigure 8-5**).

Conversely, fatty acid-supported respiration may be enhanced because glycolytic enzymes are being redirected towards biosynthetic fates that prioritize defence against oxidative stress post-reperfusion. It is possible that CABG induces metabolic adaptations such that biosynthetic fates of glycolytic enzymes 'uncouple' glycolysis from glucose (pyruvate) oxidation. Pentose phosphate pathway (PPP), which is recognized as a prominent endogenous source of nicotinamide adenine dinucleotide phosphate (NADPH) (oxidative PPP), which is essential for the regulation of redox-dependent signaling in the heart, may be implicated (**SFigure 8-6**) [558,559]. It has been observed in a mouse model of cardiac IR that shifting glucose flux towards the PPP preserves cardiac function and ameliorates oxidative damage induced by IR while enhancing the cellular reducing potential via NADPH upregulation [560]. Glucose-6-phosphate dehydrogenase (G6PD), a key rate-limiting enzyme responsible for the regulation of glucose flux to the PPP, is known to increase in response to oxidative stress

stimulation in the heart [561], and accordingly, its enzyme activity can be investigated in pre- and post-CABG RAA. The elevated systemic glucose observed during and immediately post-CABG in the present study has been previously reported [562]. mRNA expression of GLUT1/4 can be investigated via qRT-PCR and compared between time-points to determine if the procedure influences expression of these transporters to explain the reliance on carbohydrate oxidation pre-CABG (**SFigure 8-6**).

Clinical relevance of the present study and ideas for therapy development

In the present study, human RAA exhibits metabolic flexibility to CABG, including adaptations towards enhanced fatty acid-supported mitochondrial respiration. The finding that fatty acid-supported respiration is upregulated between time points in CABG has never been reported in human heart. Given that oxidative stress (reduction to prx3 monomer band density) was also exhibited on the post-CABG RAA, and circulating immune cells (total leukocytes and neutrophils) were elevated post-op, the data suggests that RAA-specific mitochondrial stress may be informed by a systemic inflammatory response. Additional data is required to confirm if the observed metabolic flexibility is a pathological consequence of CABG or an intentional adaptation to limit damage. Understanding biosynthetic fates of glycolytic enzymes during CABG may lend insight towards these questions, particularly given that carbohydrate-supported respiration was unchanged during CABG. Additionally, investigation towards the proposed mitochondrial-inflammation axis that links the previously published ischemia-induced IL-6 upregulation and neutrophil-mediated reperfusion damage [556] to STAT3/CPT-I-mediated fatty acid oxidation may inform therapy development towards attenuating inflammation following CABG. Despite limited availability of human atrial appendage sample, this study highlighted key mitochondrial stress responses that occur during and after CABG, and proposes several signaling pathways that might be associated with these metabolic adaptations. This unique insight

positions both an enhanced tissue-specific fatty acid-supported mitochondrial respiration and a systemic inflammatory response as potential determinants of patient recovery.

Methods

Baseline patient morphometrics and clinical characteristics

Approval for this study was granted by the Southlake Regional Health Centre (SRHC) Research Ethics Board (*REB #059-1819*) in collaboration with the *Human Participants Review Committee* at York University, Toronto, Canada.

A total of 12 patients undergoing non-emergent on-pump coronary artery bypass graft (CABG) surgery using cardiopulmonary bypass (CPB) and hypothermic cardioplegic arrest between April 2023 and January 2024 were enrolled. Informed consent was obtained by the interventional cardiology research coordinator prior to each surgery. 1 patient was dropped from the surgery due to operative complications. A comprehensive assessment of baseline patient clinical characteristics and demographics information (**Table 8-1**), baseline patient medical history (**Table 8-2**), and medications taken prior to the CABG procedure for each patient was obtained by the interventional cardiology department (**Table 8-3**).

Human right atrial appendage (RAA) biopsy and tissue processing

Before grafts of healthy mammary artery or saphenous vein origin can be harvested for bypass anastomosis, standard median sternotomy must be performed by the surgeon. Following harvest of a suitable graft, the patient is put on cardiopulmonary bypass (CPB). Excess RAA sample can be explanted prior to cross-clamping the aorta and exposing the heart to cardioplegic solution once the double purse-string suture (directly inferior to the RAA) has been inserted (this sample is henceforth referred to as the pre-CABG RAA) [472,563,564]. When the venous cannula is being inserted, the superior suture holds it in place, while the inferior purse-string suture remains loose such that remaining portions of the atrium are exposed to cardioplegic solution and CPB after removal of the aortic cross-clamp [472]. A second RAA sample can be

explanted from the same patient following CPB and reperfusion of blood flow from the area in between the purse-string sutures while the venous cannula is being removed (henceforth referred to as the post-CABG RAA).

Following explanation of RAA samples (both pre- and post-CABG), a portion was promptly incubated in PBS containing 75 mM MMTS (methyl methanethiosulfonate; MMTS), for 10 mins at room temperature with constant rotating, and thereafter flash frozen in a previously empty 1.5 mL conical tube for further processing. MMTS is an alkylating agent used to prevent artefactual oxidation of peroxiredoxin 3 (prx3) during lysis and sample preparation [565]. A modified Western blot assay was conducted on these samples to assess for the presence of CABG-induced mitochondria-mediated stress via evaluation of prx3 redox status, which was reported as a percentage of total dimerized protein, band density of prx3 monomer, and band density of prx3 dimer, which all reflect a broad index of oxidative stress. This method was validated prior to commencement of the study (**SFigure 8-2**). Concurrently, a separate piece of RAA was incubated in pre-chilled BIOPS (extracellular preservation buffer) to be processed for mitochondrial bioenergetics analysis with high resolution respirometry. The BIOPS used consisted of (in mM): 50 MES Hydrate, 7.23 K_2EGTA, 2.77 CaK_2EGTA, 20 imidazole, 0.5 dithiothreitol (DTT), 20 taurine, 5.77 ATP, 15 PCr, and 6.56 $MgCl_2 \cdot 6H_2O$ (pH 7.1). Remaining tissue was promptly flash frozen in liquid N_2 for additional experiments (**SFigure 8-5, 8-6**).

Preparation of permeabilized muscle fibre bundles

Prior to conducting high-resolution mitochondrial respirometry, permeabilized muscle fibre bundles (PmFBs) were prepared from RAA that was carefully trimmed of excess connective tissue and fat to ensure that only viable tissue was assessed. The preparation of PmFBs is a technique previously performed in our lab [31,432,435,566–568]. Following harvest

of RAA during both the pre- and post-CABG stages of surgery, muscle samples were immediately submerged in ice-cold ATP-containing media (BIOPS buffer) supplemented with 3 mg/mL collagenase Type I (Sigma Aldrich) while rotating on a nutator for 30 mins at 4°C. Following this 30 mins incubation to enzymatically digest excessive collagen, whole RAA was transferred to a separate conical tube containing BIOPS without collagenase. PmFBs were prepared by carefully separating tissue with precision forceps into small (~2.0-4.5 mg wet weight) bundles that were dried on a Kimwipe and weighed in 1.5 mL tared ice-cold BIOPS. Precaution was taken to avoid permeabilizing regions containing residual connective tissue, collagen, and/or fat. Bundles were permeabilized in BIOPS supplemented with 40 μg/ml saponin for 30 mins at 4°C on a rotator to ensure that the cell membrane was adequately digested, and the cytosol was washed out while other intracellular organelles were left intact.

Mitochondrial respiration

Mitochondrial oxygen consumption was measured in PmFBs prepared from pre- and post-CABG RAA samples by performing high-resolution respirometry using the Oroboros Oxygraph-2k (OROBOROS Instruments, Corp., Innsbruck, Austria). Briefly, PmFBs were placed in respirometer chambers containing 2 mL Buffer Z consisting of (in mM): 105 K-MES, 30 KCl, 10 KH_2PO_4, 5 $MgCl_2 \bullet 6H_2O$, 1 EGTA, and 5 mg/mL bovine serum albumin (BSA). Chambers also contained 5 μM blebbistatin to prevent spontaneous contractions of PmFBs by rigor in response to ADP. PmFBs were exposed to constant stirring at 750 RPM and 37°C in the chamber [435]. Prior to stimulating PmFBs with various substrates, chambers were manually oxygenated with 100% O_2 to a starting concentration of ~350 μM, and all experiments were completed prior to chamber [O_2] dropping below 150 uM to prevent [O_2] being a limiting factor for respiration.

Mitochondrial respirometry was measured in either Buffer Z without creatine (-Cr) to prevent activation of mitochondrial creatine kinase (mtCK), or in Buffer Z supplemented with 20 mM Cr (+Cr) to saturate mtCK and promote high-energy phosphate shuttling through this complex, as previously performed [569].

To assess complex-I (carbohydrate)-supported respiration, PmFBs were stimulated with 5 mM pyruvate and 2 mM malate, which are NADH-generating substrates used in tandem as a measure of state II respiration. This was followed by titrations of basal (100 μM), sub-maximal (300 and 500 μM), and saturating ADP (1000, 5000, 7000, and 9000 μM) to assess mitochondrial responsiveness to ADP across a spectrum of metabolic demand (State III coupled respiration). 10 mM glutamate was then titrated to further saturate complex-I with NADH generation. As a quality control check, cytochrome *c* was titrated to test mitochondrial outer membrane integrity. Anomalous responses (over 15%), where ADP-stimulated respiration was correspondingly low, were selectively removed. Lastly, for this carbohydrate-supported protocol, 10 mM succinate ($FADH_2$-stimulating) was added to further support complex-II respiration.

In separate PmFBs, two fatty acid-supported oxidation protocols were implemented. The first fatty acid-supported protocol contained 10 μM L-carnitine, 20 μM palmitoyl-CoA, and 500 μM malate to shuttle electrons through beta-oxidation pathways via the outer mitochondrial membrane fat transporter, carnitine palmitoyltransferase-I (CPT-I) (**depicted in Figure 8-1**) [438]. This protocol is complex-I stimulating as it generates NADH and is ETF- and complex II-stimulating attributed to $FADH_2$ generation from beta-oxidation. The second protocol contained 75 μM palmitoyl-carnitine and 500 μM malate and was intended to bypass carnitine transporters on the outer mitochondrial membrane (**depicted in Figure 8-1**). For both protocols, a similar

ADP titration was performed as described above. Cytochrome *c* was the final substrate added to test for membrane integrity.

Western blotting

Pre- and post-CABG RAA samples were allocated for prx3 oxidation modified Western blot processing, while a separate portion was allocated for regular non-oxidizing Western blots.

Prx3 Oxidation Assay:

Explanted RAA samples were promptly incubated in PBS containing 75 mM MMTS (methyl methanethiosulfonate; MMTS) (Sigma Aldrich) for 10 mins at room temperature with constant rotating [565]. Following this incubation, samples were carefully removed from MMTS, transferred into an empty 1.5 mL conical tube and flash frozen in liquid N_2. A modified Western blot using standard SDS-PAGE procedures was performed for this assay. Briefly, a frozen section of each RAA sample was homogenized using a polytron homogenizer in 75 mM MMTS-RIPA buffer (Sigma Aldrich) supplemented with protease and phosphatase inhibitors (Sigma Aldrich). Protein concentrations were determined using a Bradford protein assay. Due to the presence of MMTS in the sample and homogenization buffer, a standard bicinchoninic acid (BCA) assay cannot be performed. Proteins were subjected to SDS-PAGE on 10% agarose gels followed by transfer onto 0.2 μM low-fluorescence polyvinylidene difluoride (PVDF) membrane (Bio-Rad) and blocked with Li-COR Intercept PBS Blocking Buffer (Li-COR) for 1 hour at room temperature. Membranes were then immunoblotted overnight (4°C) on a rotator with the following antibody:

Anti-Peroxiredoxin 3/PRDX3 antibody (ab73349; Abcam); 1:1,000 primary, 1:20,000 secondary (Goat anti-rabbit; IRDye 675LT).

Following an overnight primary antibody incubation, membranes were washed in TBS-T for 3x5 mins and incubated with the abovementioned infrared fluorescent secondary antibody for 1 hour

at room temperature with constant rotating. Immunoreactive proteins were detected using an infrared imager (Li-COR) and quantified with densitometry on ImageJ. All images were normalized to total protein from the same membrane using Amido Black total protein stain (Sigma Aldrich).

Statistics

All results are expressed as mean ± SD. Outliers were excluded in accordance with ROUT testing (Q=0.5%). Subsequently, the D'Agostino-Pearson Omnibus normality parameters were performed to determine if data resembled a Gaussian (normal) or lognormal distribution (GraphPad Prism 9.3.0 Software, La Jolla, CA, USA). A repeated-measures 2-way analysis of variance (ANOVA) was used for ADP-stimulated mitochondrial respiration, followed by Benjamini, Krieger, and Yekutieli's *post hoc* analysis to correct for false discovery rate when a significant interaction was observed. A paired t-test with repeated-measures was conducted for the prx3 oxidation modified Western blot assay. A mixed-model 1-way ANOVA was conducted to analyze point-of-care data given that systemic markers were not consistently detected in all patients through each of the specified time-points. Correlations were tested via Pearson's correlation coefficient, described by Pearson's *r*. Where deltas (Δ) are utilized to obtain percentage of change/difference between various CABG time-points, values were calculated as ((final value – initial value)/initial value) *100. Significance was established at $p<0.05$ for all statistics. While corrected *p*-values are typically reported as q-values with the Benjamini, Krieger, and Yekutieli's *post-hoc* analysis, we herein report them as *p*-values.

Supplementary Data – To be included in publication

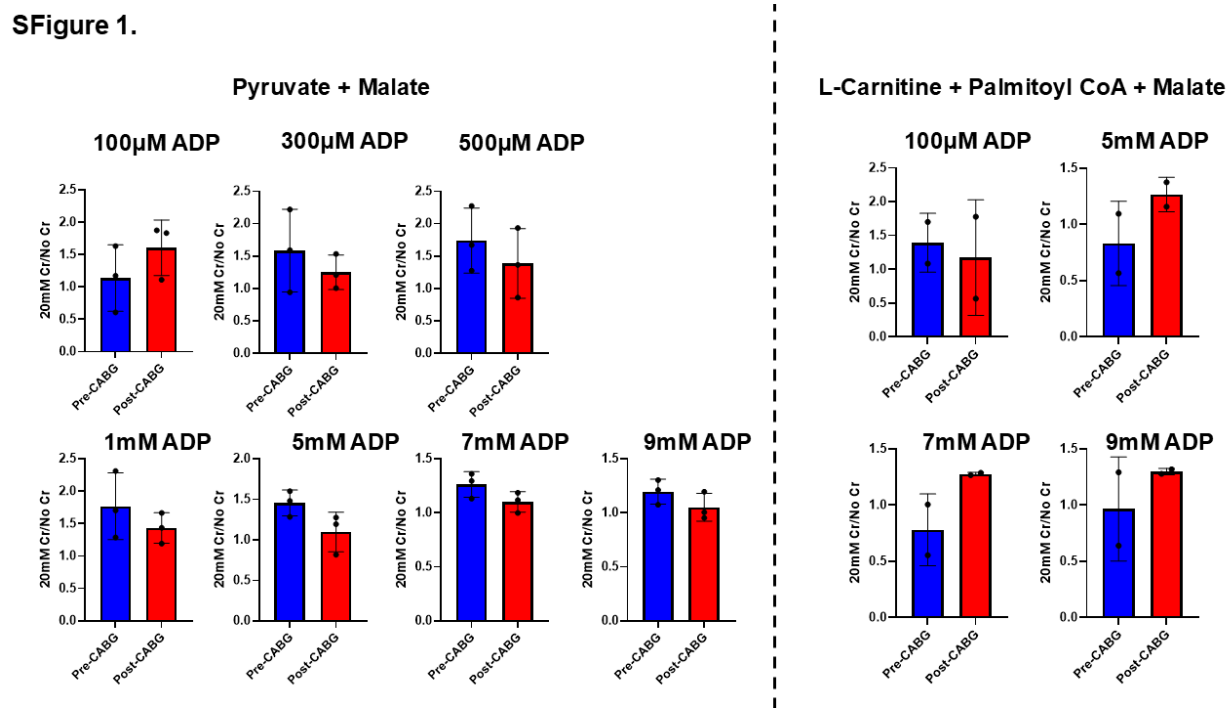

SFigure 8-1. Creatine sensitivity of PM and LPM protocol from pre- and post-CABG RAA over various metabolic demands with repeated measures analysis. Creatine sensitivity was assessed to determine if alterations to high-energy phosphate shuttling (the preferred/more efficient method of ATP export to the cytosol) was affected with either substrate protocols. Results represent mean ± SD, n=2-3 repeated-measures data points.

SFigure 2.

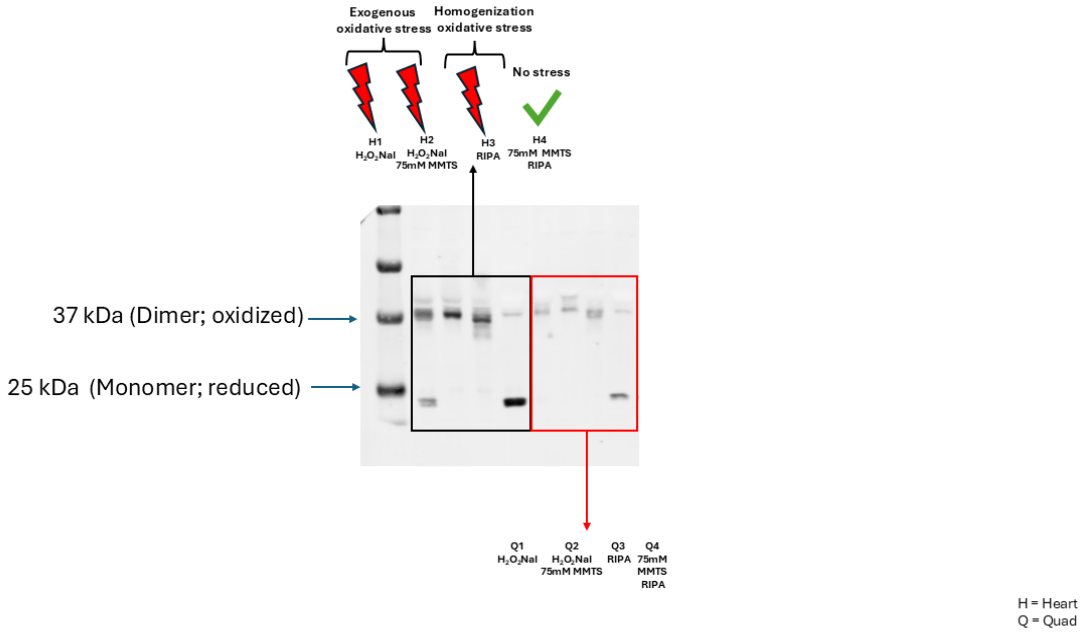

SFigure 8-2. Peroxiredoxin 3 modified Western blot validation experiment. Heart and quadricep tissue from control CD2F1 mice was incubated in various oxidizing and non-oxidizing conditions to validate efficacy of the modified Western blot assay. Samples were either incubated in H_2O_2+NaI to exogenously induce oxidative stress, H_2O_2+NaI and 75 mM MMTS to induce oxidative stress and then 'lock' the oxidation state via incubation in a chelating agent, regular RIPA homogenization buffer (mechanical homogenization-induced oxidative stress without a chelating agent to 'lock' oxidation state), or 75 mM MMTS + RIPA (no oxidative stress). H1 and H2 demonstrated the highest dimer density (index of oxidation), while H4 demonstrated the highest monomer density (index of reduction or, conversely, non-oxidation), as expected. Quadricep muscle demonstrated similar results, albeit lower overall band density due to lower abundance of prx3 compared to heart.

SFigure 3.

	Age	BMI	Days Until Discharge from cvICU	Days Until Discharge from Hospital	Mito +Cr LPM delta	Prx3 Pre Monomer delta	Leukocytes post-op surgery day delta	Neutrophils post-op surgery day delta	Lymphocytes post-op surgery day delta	Leukocytes next day post-op delta	Neutrophils next day post-op delta	Lymphocytes next day post-op delta
Age												
BMI	-0.117											
Days Until Discharge from cvICU	0.348	-0.528										
Days Until Discharge from Hospital	0.533	-0.581	0.460									
Mito +Cr LPM delta	0.421	-0.467	0.413	-0.066								
Prx3 Pre Monomer delta	-0.040	0.284	0.718	0.433	-0.399							
Leukocytes post-op surgery day delta	0.147	0.004	0.622	-0.027	-0.116	0.643						
Neutrophils post-op surgery day delta	0.020	-0.067	0.559	-0.108	-0.113	0.657	0.959					
Lymphocytes post-op surgery day delta	0.092	0.088	0.245	0.289	-0.335	0.750	0.552	0.595				
Leukocytes next day post-op delta	0.377	0.060	0.206	0.341	-0.415	0.510	0.628	0.643	0.897			
Neutrophils next day post-op delta	0.184	-0.035	0.240	0.203	-0.375	0.581	0.651	0.743	0.908	0.948		
Lymphocytes next day post-op delta	-0.187	0.682	-0.636	-0.480	-0.933	-0.208	-0.126	-0.089	0.075	0.105	0.067	

SFigure 8-3. Correlation matrix comparing statistically significant mitochondrial data (pre- and post-CABG delta %) with immune cell count (expressed as pre-surgery and next day post-op delta %). Yellow boxes denote that correlation is significant at the $p<0.05$ level (2-tailed). Green boxes denote that correlation is significant at the $p<0.01$ level (2-tailed).

SFigure 4.

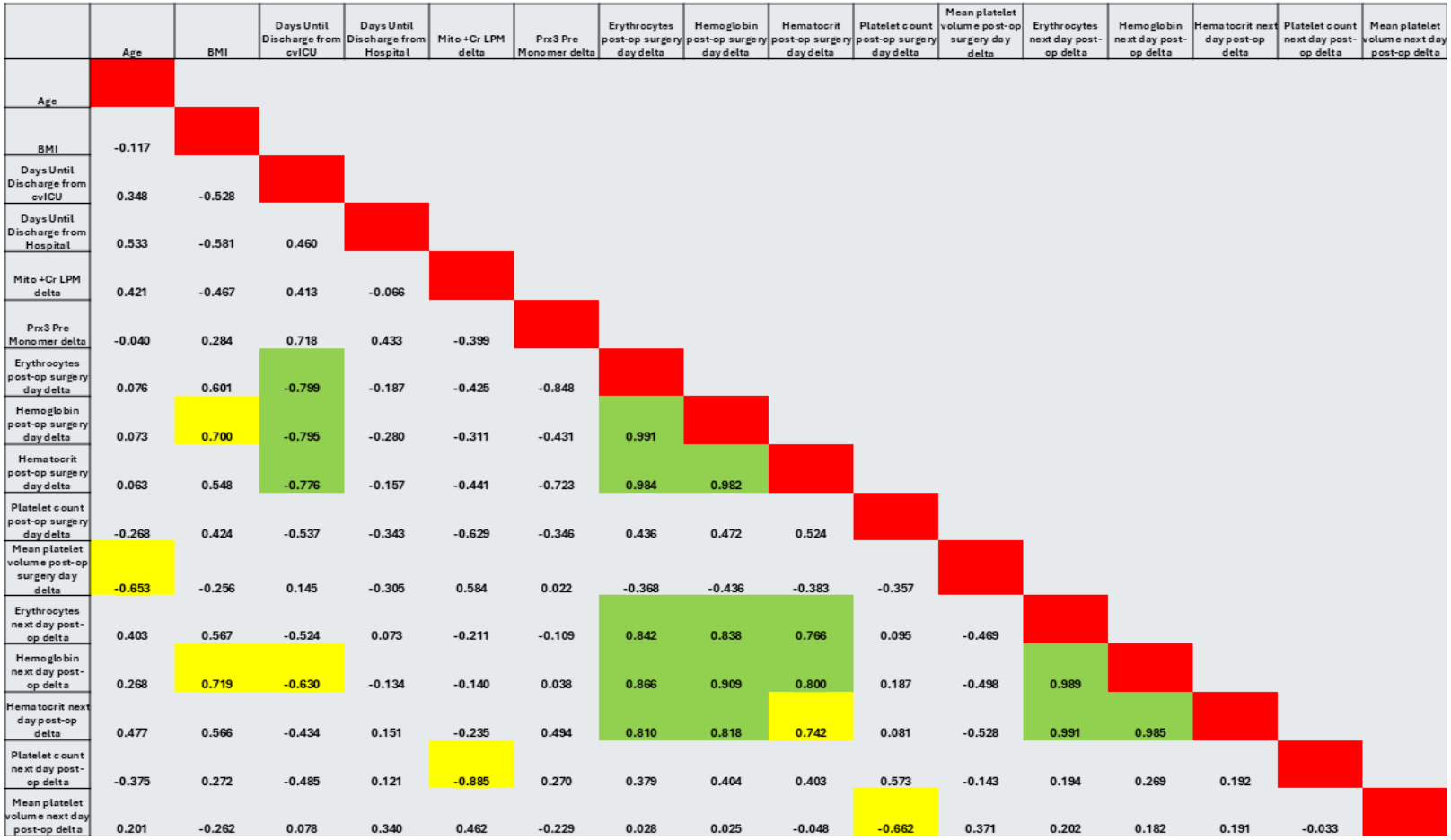

	Age	BMI	Days Until Discharge from cvICU	Days Until Discharge from Hospital	Mito +Cr LPM delta	Prx3 Pre Monomer delta	Erythrocytes post-op surgery day delta	Hemoglobin post-op surgery day delta	Hematocrit post-op surgery day delta	Platelet count post-op surgery day delta	Mean platelet volume post-op surgery day delta	Erythrocytes next day post-op delta	Hemoglobin next day post-op delta	Hematocrit next day post-op delta	Platelet count next day post-op delta	Mean platelet volume next day post-op delta
Age																
BMI	-0.117															
Days Until Discharge from cvICU	0.348	-0.528														
Days Until Discharge from Hospital	0.533	-0.581	0.460													
Mito +Cr LPM delta	0.421	-0.467	0.413	-0.066												
Prx3 Pre Monomer delta	-0.040	0.284	0.718	0.433	-0.399											
Erythrocytes post-op surgery day delta	0.076	0.601	-0.799	-0.187	-0.425	-0.848										
Hemoglobin post-op surgery day delta	0.073	0.700	-0.795	-0.280	-0.311	-0.431	0.991									
Hematocrit post-op surgery day delta	0.063	0.548	-0.776	-0.157	-0.441	-0.723	0.984	0.982								
Platelet count post-op surgery day delta	-0.268	0.424	-0.537	-0.343	-0.629	-0.346	0.436	0.472	0.524							
Mean platelet volume post-op surgery day delta	-0.653	-0.256	0.145	-0.305	0.584	0.022	-0.368	-0.436	-0.383	-0.357						
Erythrocytes next day post-op delta	0.403	0.567	-0.524	0.073	-0.211	-0.109	0.842	0.838	0.766	0.095	-0.469					
Hemoglobin next day post-op delta	0.268	0.719	-0.630	-0.134	-0.140	0.038	0.866	0.909	0.800	0.187	-0.498	0.989				
Hematocrit next day post-op delta	0.477	0.566	-0.434	0.151	-0.235	0.494	0.810	0.818	0.742	0.081	-0.528	0.991	0.985			
Platelet count next day post-op delta	-0.375	0.272	-0.485	0.121	-0.885	0.270	0.379	0.404	0.403	0.573	-0.143	0.194	0.269	0.192		
Mean platelet volume next day post-op delta	0.201	-0.262	0.078	0.340	0.462	-0.229	0.028	0.025	-0.048	-0.662	0.371	0.202	0.182	0.191	-0.033	

SFigure 8-4. Correlation matrix comparing statistically significant mitochondrial data (pre- and post-CABG delta %) with complete blood count (expressed as pre-surgery and post-op surgery day or next day post-op delta %). Yellow boxes denote that correlation is significant at the $p<0.05$ level (2-tailed). Green boxes denote that correlation is significant at the $p<0.01$ level (2-tailed).

SFigure 5.

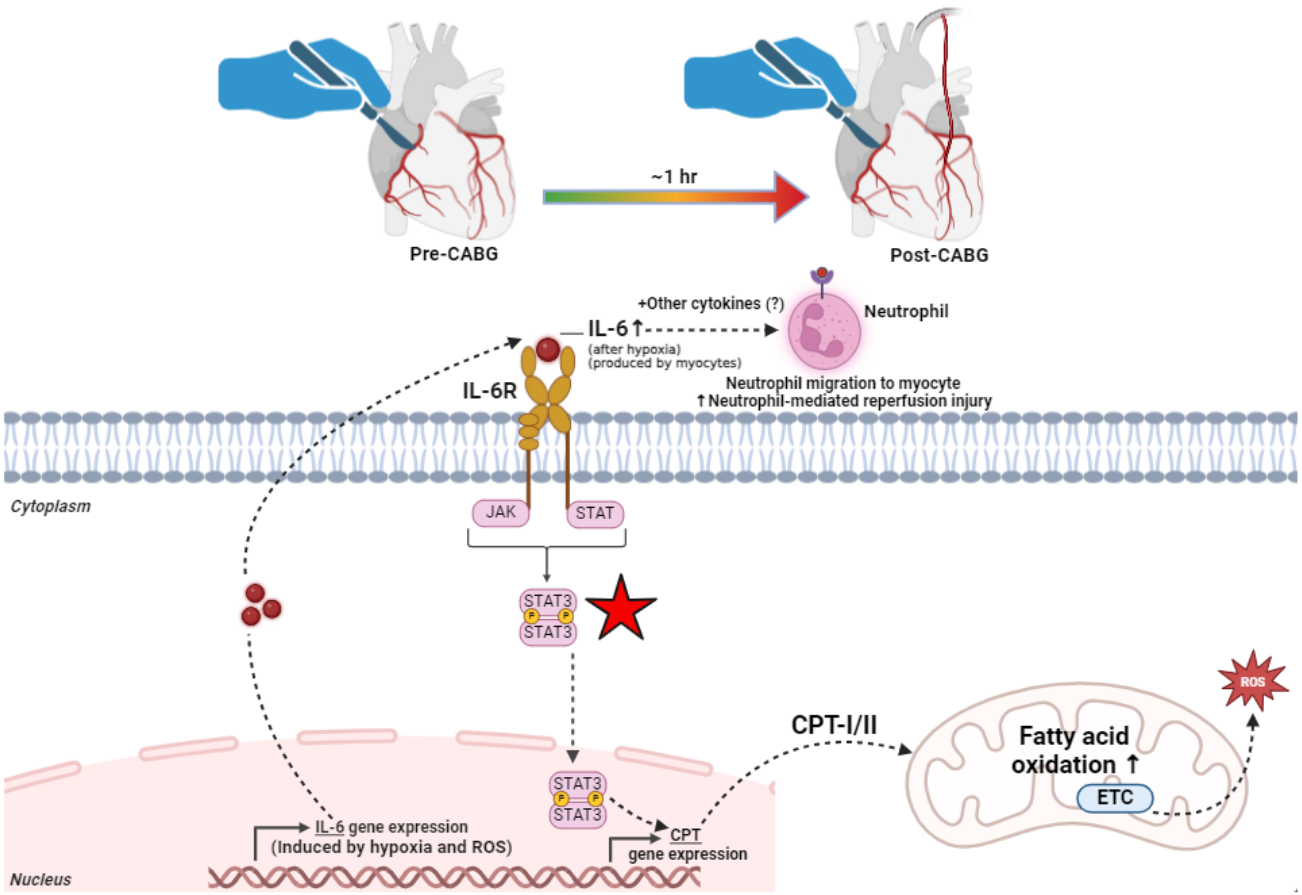

SFigure 8-5. IL-6-mediated phosphorylation of STAT3, which is related to systemic neutrophil migration, might be responsible for enhanced fatty acid-supported mitochondrial respiration through a STAT3/CPT-I axis. Red star denotes prospective pathway that can be investigated using frozen pre- and post-RAA CABG samples. Figure created using www.BioRender.com.

SFigure 6.

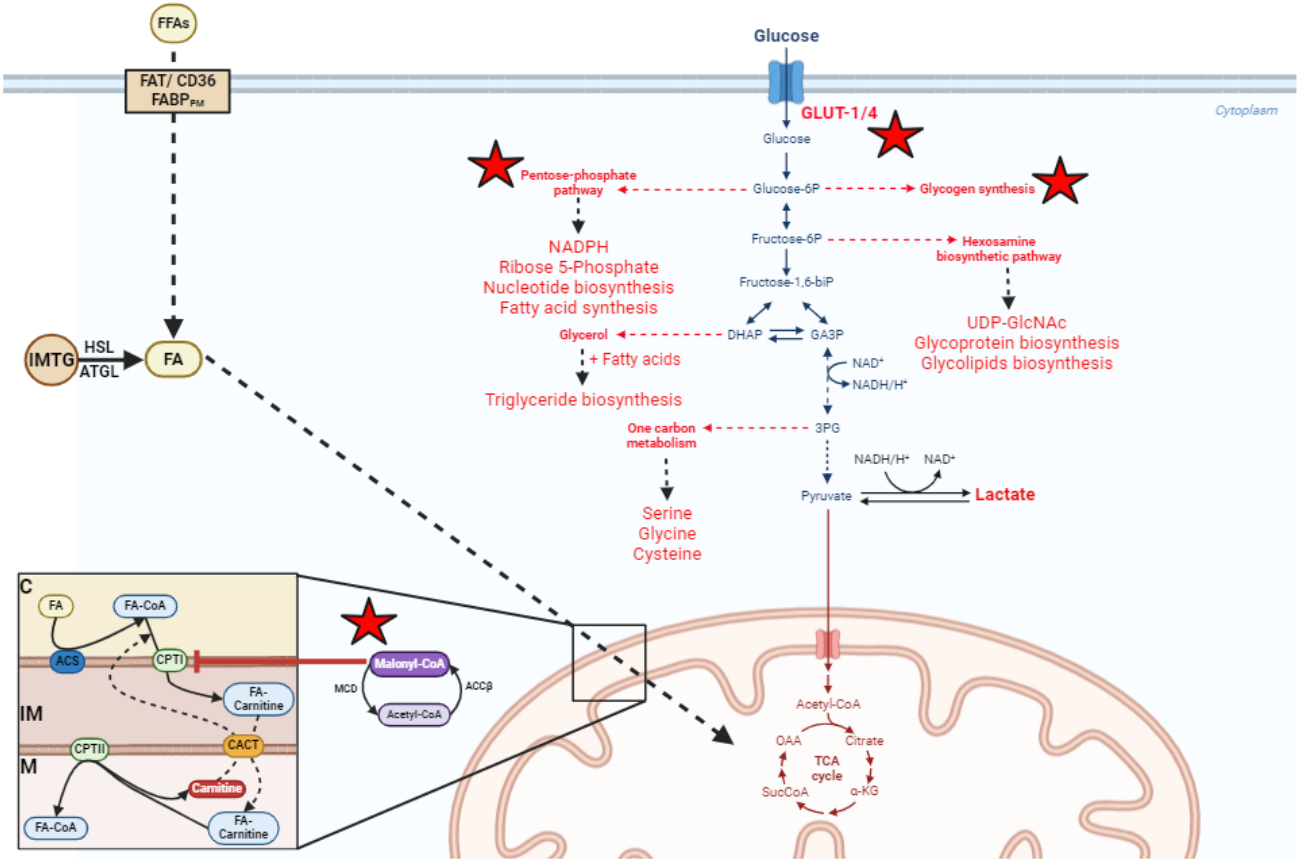

SFigure 8-6. Biosynthetic (non-ATP generating) fates of glucose/glycolytic enzymes, as well as potential blunted inhibitory effect of malonyl-CoA on CPT-I as mechanisms to be investigated that support increased fatty acid-supported respiration with no change to carbohydrate-supported respiration. Red stars denote prospective pathways that can be investigated using frozen pre- and post-RAA CABG samples. Figure created using www.BioRender.com.

9 SUMMARY OF FINDINGS

9.1 General Discussion and Future Directions

The heart is the most metabolically active organ in the body and possesses the highest mitochondrial content per muscle cell of any tissue [570]. Mitochondria are indispensable for a myriad of cellular processes - including ATP provision in the ETC through oxidative phosphorylation, regulating ROS emissions to govern homeostatic and pathological programs, shifting metabolic substrate utilization to reflect dynamic workloads, and mediating ion homeostasis to meet demands of the cell. Given that the heart is constitutively active and accounts for approximately 8% of total ATP consumption in mammals, it is unsurprising that aberrations to mitochondrial metabolism in cardiac tissue plays a pivotal role in the pathophysiological manifestations associated with stress-induced remodeling. We aptly refer to these aberrations as ‘mitochondrial stress responses’ when they begin to influence structure and/or function of a cell or tissue. The phrase ‘mitochondrial dysfunction’ is strategically avoided in this thesis as these responses are not always causal of myopathy or remodeling. In concert (and sometimes direct association) with mitochondrial stress responses, inflammation is also centrally involved in histopathological cardiac remodeling following damage. There are several diseases and ‘stress paradigms’ in which cardiac mitochondria and inflammation have been purported to be involved. However, the nature of why mitochondrial reprogramming and inflammation occur across diverse conditions with unrelated underlying causes of disease remains unclear. In this regard, the present thesis examined myofiber mitochondrial relationships to tissue-specific inflammation in distinct models of cardiomyopathy including dystrophin deficient mice (Duchenne muscular dystrophy, DMD) [26,82,276,571,572] and on-pump coronary artery bypass graft (CABG) surgery in humans [475,476,573].

DMD is an X-linked recessive muscle-wasting disease caused by mutations to the *DMD* gene [574]. The current standards of care for DMD, which includes immunosuppression via glucocorticoid administration and gene-editing therapies, provide some promise for patients, however, these interventions are often accompanied by unwanted side effects and are not always translatable to the full spectrum of mutations that cause DMD [24]. Both of these interventions have yielded variable results for dystrophin deficiency-induced cardiomyopathy, which represents a major gap in clinical therapy advancement for a disease that currently has no cure.

While pioneering work investigating the dystrophic LV has identified mitochondrial stress responses in a model of early onset DMD (4-week-old D2.*mdx* mice) in the absence of cardiac remodeling and dysfunction [571], data on the remaining chambers of the heart is scarce. The lack of comparative data between ventricles, and specifically pertaining to the RV, is of particular interest given that previous work by our group demonstrated fibrosis in the diaphragm of 4-week-old D2.*mdx* mice [392], while work by another group proposed diaphragm degeneration of aged *mdx* mice as a major contributor and precipitator to RV dystrophic pathology [575].

This thesis first attempted to comprehensively assess chamber-specific heterogeneity in dystrophin deficiency-induced cardiac remodeling in 4-week-old D2.*mdx* mice by comparing the histopathological, mitochondrial, and inflammatory profile across atria and ventricles where tissue availability was not a limiting factor. By understanding how the heart heterogeneously remodels in response to dystrophin deficiency at this early time point, the second objective was to determine if daily administration of a novel adiponectin peptidomimetic (ALY688) could prevent some of these remodeling signatures. The decision to investigate an adiponectin receptor-targeted intervention was supported by studies indicating that circulating levels of this cardioprotective hormone are lower in *mdx* [385] and humans with DMD [384].

The findings from this thesis first established that the RV and LA of 4-week-old D2.*mdx* mice demonstrated a previously undiscovered robust fibrosis that was not detectable in the LV, RA, or interventricular septum. Other histopathological remodeling signatures such as myocardial disorganization and cardiomyocyte hypertrophy were surprisingly identified in both ventricles, despite the absence of fibrosis in the LV. These signatures of histopathological remodeling were associated with several indices of mitochondrial stress responses in the RV, including lower mitochondrial respiration with carbohydrate (pyruvate) and fatty acid-supporting substrates, elevated caspase 9/3 activity, elevated mitochondrial ROS (H_2O_2) emissions, and lower calcium retention capacity, alongside elevations to circulating pro-inflammatory macrophage sub-populations. Importantly, the second contribution of this thesis established that ALY688 prevented remodeling signatures in the RV, thus positioning adiponectin receptors as a promising therapeutic target for right-sided histopathological cardiac remodeling.

9.1.1. Chambers of the D2.*mdx* heart should be investigated as four distinct organs, each with their own unique molecular and histopathological responses to stress

Although visually the heart is a single organ, the presence of different embryological origins, patterns of gene expression, and functional and structural capacities suggest that the heart can be analogized to four distinct organs, each with their own unique responses to stimuli.

The decision to examine chamber-specific histopathological and molecular remodeling signatures followed the novel and somewhat accidental observation that 4-week-old D2.*mdx* mice exhibit a unique RV and LA fibrosis that was nonexistent in the LV and RA. While several studies have investigated cardiac fibrosis in D2.*mdx* mice, including [397] which observed elevations to non-specified regions of the heart in mice as young as 10-weeks-old, and [86] which established RV-specific fibrosis at 18-weeks, no study has investigated chamber-specific

histopathological remodeling at 4-weeks, a time point representative of early phenotypic manifestation of dystrophin deficiency. Disparity in the development of fibrosis may be attributed to structural differences. For example, the RV is thinner than the LV due to the difference in type and amount of muscle fibres (it is estimated to be one-third of the LV's thickness) [576].

Other indices of remodeling such as myocardial disorganization were also elevated in the RV and LA, although this was exhibited in the LV as well. Ventricle-specific cardiomyocyte diameter was assessed to determine if dystrophin deficiency affected cell size (which can be interpreted as a broad index of cardiomyocyte hypertrophy). This hypertrophic response was observed in both ventricles of D2.*mdx* mice. While it was unexpected that these remodeling signatures persisted in both ventricles despite the absence of fibrosis in the LV, one explanation is that the fibrotic diaphragm of 4-week-old D2.*mdx* mice exerts a hemodynamic pulmonary artery-mediated back-pressure on the RV, thus precipitating pulmonary artery hypertension [575] that exacerbates respiratory dysfunction, leading to additional morphological changes to the RV and LA not observed in the LV. At least one study has demonstrated that at 16-17 weeks, D2.*mdx* mice present with pulmonary vascular resistance thought to be caused by a fibrotic diaphragm and RV [166].

There are anatomical and physiological differences between the ventricles that might explain the disparate responses observed. It is thought that the RV may be subjected to a 5-fold increase in afterload, compared to only <50% increase in the LV, in systemic hypertension, suggesting that the adaptation to higher pressures is more extreme/sensitive in the RV and may rely on enhanced fibrotic strengthening compared to the LV [577]. In aged *mdx* mice, there is histological evidence of pulmonary hypertension concomitant with RV fibrosis and elevated RV

wall thickness [575], thus supporting the proposed mechanism linking diaphragm fibrosis to fibrosis in the RV.

Alongside elevated RV fibrosis, mitochondrial stress responses also dominated this ventricle. This is a peculiar finding given that previous work in these mice demonstrated impairments to LV bioenergetics which were not observed this time [571]. Although this observation was difficult to explain, we believe it reflects the heterogeneity of disease severity between D2.*mdx* breeding colonies - a concern of the model that has been acknowledged by several groups. In contrast, the observation that PmFBs prepared from non-fibrotic regions of the RV exhibited decreased mitochondrial respiration with both carbohydrate- and fatty acid oxidation-supporting substrates suggested that cardiac remodeling may be associated with mitochondrial stress. This was an important observation given that mitochondrial stress responses have been previously characterized in fibrotic diseases [310]. In addition to mitochondrial respiration, ROS (mH_2O_2) was also investigated using complex-I supporting substrates that stimulate forward electron transfer. While it was not surprising that RV mH_2O_2 was elevated (given the presence of fibrosis), the finding of elevated LV mH_2O_2 was supported by previous literature [571]. Activity levels of caspases 9/3, which are uniquely involved in intrinsic mitochondrial-mediated apoptosis pathways [578], were unchanged in the LV, which was paralleled by no difference to mitochondrial CRC - aligning with previous literature [571]. Caspase activity and CRC are important measures to assess with regards to remodeling processes given that excess mitochondrial calcium uptake can lead to swelling-induced rupture and the release of cytochrome *c* from the OMM (a process termed mPT), which can activate downstream caspases 9/3 to initiate mitochondrial-mediated intrinsic apoptosis as part of regulated cell death processes [243]. It was unsurprising that activity levels of caspases 9/3 were elevated in the RV,

which was paired with decreased mitochondrial CRC when pooling PmFBs with and without mPT. Given that D2.*mdx* do not demonstrate differences to CRC in RV when only assessing PmFBs with mPT, this highlights the importance of interpreting data multiple ways (pooled with and without mPT versus only with mPT), which yielded disparate conclusions. Nevertheless, the elevated caspase 9/3 activity in the RV and no change to caspase 8 in both ventricles suggested that mitochondrial-mediated apoptosis, rather than extrinsic apoptotic pathways, may be contributing to cardiomyocyte loss that necessitates cardiac fibrosis.

Systemic inflammation is a well-known secondary contributor to DMD-induced pathology - therefore, assessing chamber-specific inflammatory signatures was paramount. Much of what is known about cardiac inflammation in *mdx* is limited to the LV, and the sparse data available is primarily retrieved from aged mice, as best exemplified in a study by Van Erp *et al.*, in 6-month-old *mdx* mice [25]. This group detected F4/80^{+} infiltration in the LV of aged *mdx* mice, suggesting that macrophages may be involved with LV cardiac fibrosis that was also observed [25]. To our knowledge, the only study assessing cardiac inflammation in 4-week-old *mdx* mice was conducted by Morroni *et al.*, who assessed cell counts of myeloid and T cell populations [579]. In this study, it was determined that 4-week-old *mdx* mice exhibited elevations to both myeloid (CD45^{+}CD11b^{+}) and T cells (CD45^{+}CD3^{+}) in the LV, which was interesting given that fibrosis was not detected [579]. This suggests that inflammatory infiltrate in the heart may precede development of overt cardiac fibrosis.

In the present study, immunofluorescent staining revealed that TGF-β1 and α-SMA were both elevated in the RV, consistent with the detection of cardiac fibrosis. This finding was supported by a plethora of research [580]. It was surprising, however, that only α-SMA was elevated in the fibrotic LA, while TGF-β was not. Although this was peculiar, we believe it

represents a unique response to damage elicited by each chamber. Inflammatory cytokines were also assessed by immunofluorescence, including the anti-inflammatory interleukin (IL-10) and pro-inflammatory IL-6. We noted that IL-10 was elevated in all chambers of D2.*mdx* mice, which was a strange observation given that IL-10 is generally associated with the resolution of inflammation and fibrosis [415]. This finding demonstrates a limitation of tissue-based immunofluorescent detection of transient cytokines (which should instead be detected with cell sorting or RT-qPCR), and secondarily also supports the complex pleomorphic and pleotropic nature of IL-10 in health and disease [415]. Differences were not detected between chambers when assessing IL-6, however, it is acknowledged that more sensitive techniques would have been superior for detecting a cytokine that is as transient as IL-6.

Due to limitations of immunofluorescence, ventricle-specific spectral flow cytometry was implemented in a subsequent phase to detect inflammatory macrophage sub-populations, particularly to examine shifts in bone marrow hematopoietic stem cell-derived recruited versus tissue-resident embryological and/or fetal yolk sac-derived macrophages. The novel finding that pro-inflammatory 'recruited' macrophages, defined by the validated serotype $CD11b^{+}CD45^{+}CD64^{+}F4/80^{+}CCR2^{+}$ [413,581], were elevated in the RV but not LV suggested that chamber-specific fibrosis might be mediated by systemic recruitment of inflammatory bone marrow-derived macrophages that exacerbate fibrosis. Furthermore, the parallel finding that anti-inflammatory 'tissue-resident' macrophages, defined by the serotype $CD11b^{+}CD45^{+}CD64^{+}F4/80^{+}CCR2^{-}$, were unchanged between groups in either ventricle contributes to the well-established literature associating the $F4/80^{+}CCR2^{-}$ population with homeostatic function [582]. Given that recruited macrophages ($F4/80^{+}CCR2^{+}$) are thought to mediate histological remodeling by stimulating cardiac fibroblast-to-myofibroblast

phenoconversion in response to damage [582], their upregulation observed in the RV (along with α-SMA) represents a mechanism integrating dystrophin deficiency-induced inflammation to aberrant cardiac fibrosis through potential myofibroblast activation.

9.1.2. Adiponectin receptor agonism attenuates histopathological and molecular signatures of RV remodeling, but is this a protective response?

A follow-up secondary objective of this study was to determine if daily administration of ALY688 could attenuate histopathological remodeling signatures through mitochondrial- and/or inflammatory-mediated pathways.

First, it was observed that 3 weeks of daily subcutaneous administration of ALY688 starting at 7-days significantly attenuated RV and LA fibrosis. This was a key finding given that both chambers affected by fibrosis were prevented by the drug, akin to a previous finding from our lab where ALY688 also prevented diaphragmatic fibrosis [392]. Given that respiratory impairments are a hallmark manifestation of disease progression, this finding suggests that early RV fibrosis may be linked to pulmonary vasoconstriction through an axis also implicating a fibrotic diaphragm and pulmonary vascular resistance in *mdx* mice [166,184]. It was also observed that ALY688 prevented RV cardiomyocyte hypertrophy, but did not prevent cardiomyocytes hypertrophied in the LV. The finding that LV cardiomyocyte hypertrophy is not prevented by the drug suggests that the fibrotic diaphragm and RV in D2.*mdx* mice may be more interconnected than previously appreciated.

Adiponectin receptor agonists play an important role in anti-fibrotic [583] and anti-inflammatory cascades [584], and also signal to 5' adenosine monophosphate-activated protein kinase (AMPK) [583] – a potent regulator of mitochondrial metabolism. To determine if mitochondrial stress underpins the attenuation of fibrosis, ventricle-specific high resolution

respirometry was assessed in mice treated with ALY688. Attenuation of RV fibrosis was paralleled by improvements to mitochondrial respiration using both carbohydrate (pyruvate)- and fatty acid-oxidation supporting substrates. Given that these findings were observed in the non-fibrotic regions of the RV, and were not revealed in the LV, this suggests that fibrosis may impact the metabolic capacity of neighbouring unaffected ventricular tissue. In addition to mitochondrial respiration, it was also observed that ALY688 attenuated caspase 9/3 activity in the RV, without affecting the LV. Caspase 8 activity was unchanged in both ventricles. This data suggests that ALY688 may play a role in downregulating intrinsic mitochondrial-mediated apoptosis. This is a significant finding given that cardiomyocyte apoptosis could be responsible for excessive cell loss in the RV of D2.*mdx* mice, which is prevented by ALY688. This finding also supports mitochondrial CRC data examining pooled RV PmFBs with and without clear mPT, whereby lower mitochondrial CRC in D2.*mdx* was prevented in ALY688-treated mice, suggesting that calcium dysregulation may be involved in chamber-specific dystrophin deficiency-induced pathology. Continuing with the role of ALY688 in chamber-specific mitochondrial bioenergetics, a surprising finding was the ability of ALY688 to prevent LV complex I-supported forward mH_2O_2 across a spectrum of metabolic demands, but not against mH_2O_2 in the RV. While this data was unexpected, it may be attributed to the lower mH_2O_2 (expressed as % of state II) in the LV of D2.*mdx* compared to the RV, which contained a relatively higher percentage.

Low circulating adiponectin concentrations have been detected in hypertrophic cardiomyopathy, while high adiponectin concentrations are cardioprotective and associated with a lower risk of myocardial infarction [585]. Evidence suggests that adiponectin exerts protection against inflammation, with reductions in circulating adiponectin shown to be associated with elevated inflammatory markers in different metabolic diseases (extensively reviewed in [372]).

Although literature in this area is still growing, pioneering work by Yokota *et al.*, and Ohashi *et al.*, has demonstrated a role of adiponectin as an anti-inflammatory hormone by regulating M1-like and M2-like macrophage proliferation, plasticity, and polarization [367,369,372]. The specific receptor-mediated mechanisms linking adiponectin to macrophage polarization remain to be elucidated [372]. At least one study has demonstrated that adiponectin incubation in primary human monocytes resulted in a 4-fold reduction of CCR2 surface abundance, suggesting that this adipokine might influence inflammatory state through an immunoregulatory role [586].

Mechanisms directly linking adiponectin to $CCR2^{+/-}$ macrophages have not yet been extensively mapped or investigated. Macrophage polarization shifts remain a hallmark characteristic of the inflammatory response to damage and represent a major potential contributor to the histopathological remodeling processes that are associated with dystrophin deficiency. Given the robust RV fibrosis that was exhibited in D2.*mdx* mice, there was value in assessing chamber-specific inflammatory macrophage sub-populations to determine if ALY688 shifted the macrophage polarization state towards an anti-inflammatory phenotype. Spectral flow cytometry of whole enzymatically digested ventricles revealed that ALY688-treated mice had reduced $F4/80^{+}CCR2^{+}$ cells in the RV compared to the significant elevated cells detected in D2.*mdx* mice. This finding demonstrated for the first time that adiponectin may attenuate RV fibrosis by decreasing the amount of 'circulating', or bone marrow hematopoietic stem cell (HSC)-derived, macrophages that are recruited to sites of damage. While $F4/80^{+}CCR2^{-}$ cells are responsible for homeostatic cardiac tissue repair (a concept more recently popularized by Dr. Slava Epelman), the systemic recruitment of bone marrow HSC-derived macrophages implies that embryologic- and/or fetal yolk sac-derived macrophages cannot sustain the excessive damage experienced by the RV in D2.*mdx* mice, and therefore signals for additional

'reinforcement'. Future work should investigate if pharmacological or genetic ablation of tissue-specific $CCR2^{+}$ recruitment attenuates the histopathological remodeling signatures exhibited in D2.*mdx* mice. Future work should also investigate if the elevated $F4/80^{+}CCR2^{+}$ cells in D2.*mdx* mice are associated with concomitant elevated pro-inflammatory cytokines such as IL-6. Additionally, combining $F4/80^{+}CCR2^{-}$ cells with additional discriminatory markers representative of specific embryologic and/or fetal yolk sac-derived resident macrophages may also be beneficial for determining with more confidence if these cells are impacted by dystrophin deficiency. These markers, which include a combination of $F4/80^{+}$ with Lyve1 + Timd4, and/or Folr2, would allow for the identification of specific 'resident' macrophage sub-populations [413]. While targeting the inflammatory response with an adiponectin receptor agonist represents a logical axis for addressing fibrosis, future work should assess myofibroblast activity in untreated and ALY688-treated mice to assess differences in collagen-producing ability.

Much of this study has focused on fibrosis as a detrimental consequence of histopathological cardiac remodeling. Despite this, fibrosis is a necessary stage of the inflammatory response and is intended to uphold structural and functional integrity of the failing heart by replacing apoptotic and/or necrotic areas with collagenous scar tissue. Therefore, as a future direction, there is value in treating D2.*mdx* mice for longer than 3 weeks, until the animals reach a size that improves the feasibility of obtaining reliable cardiac functional data, so that the effects of attenuating fibrosis can be investigated comprehensively. To elaborate, understanding if preventing fibrosis predisposes the heart to more functional impairments in the long run by disrupting a programmed reparative response is important. This can also be determined by conducting a longitudinal time-course design in which animals with and without RV fibrosis are compared for lifespan. Although this study could not answer the original question that was posed

(is attenuating cardiac fibrosis protective?), the study provides invaluable insight towards chamber-specific heterogenous remodeling programs in D2.*mdx* mice and also proposes critical questions for the next steps of this study design which can guide therapy development.

9.1.3. Right-sided adaptations in D2.*mdx* mice persist in other cardiac stress paradigms as well, including in human atrial appendage samples from CABG surgery

D2.*mdx* mice proved to be invaluable for gaining insight towards the right-sided metabolic and inflammatory stress responses underpinning dystrophin deficiency-induced damage. Still, it remained to be seen if other cardiac paradigms also elicited similar right-sided adaptive responses to stress. To test this hypothesis, pre- and post-CABG right atrial appendage (RAA) samples explanted from patients undergoing elective on-pump revascularization surgery were subjected to mitochondrial stress response experiments and assessed alongside markers of systemic inflammation. In this study, pre-CABG was defined as RAA samples explanted prior to cardiopulmonary bypass (CPB), while post-CABG was defined as RAA samples explanted following CPB. The primary objective of this study was to determine if the procedure, which is characterized by ischemia and reperfusion during CPB, influenced mitochondrial and inflammatory-mediated adaptations to the RAA and systemic circulation, respectively. This work was strengthened by repeated-measures analyses assessing mitochondrial respiration from RAA samples of the same patient at two unique time-points. By examining indices of mitochondrial stress and concurrently investigating how these responses manifested in concert with alterations to circulating immune cell count at various time-points, the study shed light on the mitochondrion-inflammation axis that underpins CABG surgery.

On-pump CABG surgery is performed worldwide to mitigate the consequences of coronary artery disease. It is well known that the healthy human heart relies on fatty acids as its

primary fuel source, while carbohydrates (glucose) remains a reliable secondary contributor to ATP. It is unknown if the relative contributions of fat and carbohydrates to ATP provision in the healthy human heart is perturbed in ischemic and reperfused hearts. Additionally, there is contention among researchers regarding the clinical importance and relevance of differential mitochondrial substrate selection and usage during cardiac stress.

It has been accepted that the heart's metabolic reserves (cardiac glycogen stores) are relatively limited [492], albeit recruited during ischemia along with glucose transporters at the sarcolemma. Additionally, circulating free fatty acids (FFAs) are upregulated during cardiac IRI. Despite this, it is unknown whether the adaptation to enhanced fatty acid-supported oxidation observed in pre-clinical rodent models during cardiac IRI is an intentional protective mechanism required for long-term survival of cardiac tissue, or a detrimental metabolic response to stress. Given that stimulation of carbohydrate (pyruvate)-supported oxidation, either directly or indirectly by inhibiting fatty acid-supported oxidation, significantly improves cardiac function and efficiency in pre-clinical rodent models, current theories posit that the adaptation to enhanced fatty acid-supported oxidation is a pathological consequence of IRI [587–589]. Collectively, this gap in knowledge regarding mitochondrial substrate selection in clinical settings presented an opportunity for first understanding how RAA samples metabolically respond to CABG surgery. Subsequently, this was followed up by characterization of the effects of CABG on RAA-specific mitochondrial oxidative stress and circulating immune, blood, metabolite, and electrolyte cell count during various stages of surgery.

The present study was the first (to our knowledge) to demonstrate an adaptation towards enhanced fatty acid-supported respiration in human atrial appendage samples explanted during CABG. There are several possible hypothetical explanations for this adaptive enhanced fatty

acid-supported respiration that represent rich-in-potential avenues for future experiments. Some of these prospective experiments will be discussed below.

First, it is possible that periods of hypoxia that affect pre-CABG RAA samples (attributed to the initial coronary artery disease-induced atherosclerotic blockage) metabolically reprogram the heart to prioritize the catabolism of glucose and cardiac glycogen stores towards pyruvate oxidation to uphold essential ATP-dependent processes (such as ion channel-specific ATPases) in the absence of adequate oxygen. Theoretically, this would allow pyruvate-supported oxidation to be reinforced by an enhanced reliance on fatty acid-supported respiration during the reperfusion phase of CABG (post-CABG RAA), when oxygen is no longer limiting. This theory could be tested by investigating RAA-specific GLUT-1/4 and glycogen content, as well as glycogen phosphorylase activity between time-points to determine if glucose uptake into cardiac muscle, and subsequent storage or further passage to pyruvate is perturbed on the post-CABG RAA sample. Research in this area is surprisingly sparse, even in pre-clinical models of ischemic heart disease. Lower GLUT-1/4 and/or glycogen content on the post-CABG sample could reflect lower substrate (glucose) availability for metabolism through oxidative phosphorylation pathways (via pyruvate), compared to high circulating FFAs that are available for β-oxidation post-reperfusion (at least in pre-clinical models of ischemic heart disease) [447,460,502]. In this regard, enzyme activities of pyruvate dehydrogenase (PDH) and its endogenous inhibitor pyruvate dehydrogenase kinase (PDK) can also be investigated to determine if pyruvate-supported carbohydrate oxidation is upregulated in pre-CABG RAA when oxygen is limiting (given that carbohydrate oxidation is more metabolically efficient than fat oxidation), while contributions to ATP supply are subsequently supported by fatty acids when oxygen is adequate during reperfusion (post-CABG RAA).

Additionally, there is value in investigating malonyl-CoA, which elicits potent endogenous regulatory control over fatty acid-supported respiration by inhibiting CPT-I on the OMM to limit oxidation of fatty acids in the mitochondria. Of note, malonyl CoA exists in flux with acetyl CoA, with acetyl CoA carboxylase (ACC) responsible for the conversion of acetyl CoA to malonyl CoA, while malonyl CoA decarboxylase (MCD) is responsible for the opposite conversion. A seminal study conducted by Kudo *et al.*, determined that high rates of fatty acid-supported oxidation during reperfusion were associated with decreases to malonyl-CoA content in isolated working rat hearts subjected to 30 mins of global ischemia, followed by 60 mins of aerobic reperfusion [550]. While it is conceivable that targeting the malonyl-CoA axis represents a therapeutic modality for limiting the consequences of enhanced fatty acid-supported oxidation in the post-reperfusion phase, human data is surprisingly limited. Mass spectrometry of RAA samples would be a gold-standard method for assessing malonyl-CoA content levels.

Other critical regulators of mitochondrial substrate selection for ATP synthesis are the various 'biosynthetic' fates of glycolytic enzymes that 'uncouple' glycolysis from glucose (pyruvate) oxidation. Glucose can also be prioritized for biosynthetic pathways that branch off of glycolysis, which include the pentose phosphate pathway (PPP), hexosamine biosynthetic pathway (HBP), or one-carbon metabolism for the generation of critical substrates that favour survival of the cell [558,590,591]. For the current study, only the PPP will be considered for future experiments given the plethora of data linking this pathway to cardiac IRI. The PPP, which is recognized as the predominant endogenous source of nicotinamide adenine dinucleotide phosphate (NADPH) (oxidative PPP), is important to investigate in the current model given that this intermediate is essential for the regulation of cardiac redox-dependent signaling [558,559].

Notably, the NADPH and NADP cycle provides reducing equivalents for glutathione peroxidase (GPx), glutathione reductase (GRx), and the thioredoxin (Trx) system in order to return oxidized glutathione back to its reduced forms, a process critically necessary against cardiac reperfusion injury [560]. The PPP and glycolysis share flux through glucose-6-phosphate (G-6-P), thus, downstream glycolytic inhibition could promote glucose flux towards the generation of PPP-mediated NADPH rather than towards pyruvate for ATP provision during periods of reperfusion stress where protection against highly reactive oxidants is paramount [560]. Interestingly, a study by He e*t al*., investigated the effects of genetically shifting glucose flux from glycolysis towards the PPP via L-2-hydroxyglutarate (L2HG) accumulation in mice (a mechanism that was originally validated in cell culture) to determine if this shift protected against cardiac IRI [560]. It was observed that shifting glucose flux towards PPP preserved cardiac function and ameliorated oxidative damage induced by reperfusion, while also enhancing cellular reducing potential via NADPH upregulation, suggesting that fatty acid-supported respiration may be enhanced over glucose-/pyruvate-supported respiration on post-CABG RAA to enable glucose-mediated biosynthetic processes to address the IR-induced oxidative damage [560]. Accordingly, glucose-6-phosphate dehydrogenase (G6PD), which is a key rate-limiting enzyme that regulates glucose flux to the PPP, is known to increase in response to oxidative stress stimulation in the heart [561] and this enzyme is also required to maintain reduced glutathione levels to prevent excessive IRI in mice with oxidative stress-induced cardiac dysfunction [592]. Collectively, this data suggests that enhanced fatty acid-supported respiration in response to IR is likely not entirely a pathological mechanism, but rather a ‘substrate-sparring’ response that prioritizes glucose catabolism for the generation of anti-oxidative intermediates (i.e. reduced glutathione) that are indispensable during reperfusion. The PPP can be assessed in

the current study by comparing pre- and post-CABG G6PD enzyme activity given that this enzyme (alongside 6-phosphogluconate dehydrogenase) is at the nexus of flux through the PPP.

Another hallmark characteristic associated with cardiac IR is oxidative stress. While the present study could not measure mitochondrial H_2O_2 emissions on live cardiac samples as previously performed in D2.*mdx* mice, a surrogate method recently adapted by our group that assesses oxidative stress as a 'historical snapshot' was utilized to determine if CABG samples were oxidized by ROS at different time-points. Data from the peroxiredoxin 3 (prx3) modified Western blot revealed post-CABG RAA had a significantly lower Prx3 monomer (reduced) protein density compared to pre-CABG, suggesting that the protein content of reduced Prx3 is lower post-CABG. Although dimer density and percentage of Prx3 as a dimer (oxidized) were not statistically different, this is likely attributed to the low repeated measures sample size and does not preclude post-CABG RAA samples from being oxidized.

A right-sided mitochondrial-inflammation axis as a coordinated adaptive response represents a commonality between two otherwise distinct models of cardiac stress: D2.*mdx* mice and human atrial samples from CABG surgery. Systemic immune cell data that was analyzed through 5 unique time-points before, throughout, and after the surgical period suggested that elevated fatty acid-supported oxidation post-CABG may be related to circulating total leukocytes and neutrophils post-operation surgery day. This data was intriguing because it suggests that a substrate selection adaptation towards enhanced fatty acid-supported oxidation post-CABG, although potentially protective, may also be associated with a systemic inflammatory response. While additional causal data is required to link mitochondrial stress to inflammation, findings from both D2.*mdx* mice and human atrial samples from CABG surgery suggest that cardiac stress may elicit these adaptive responses in an interdependent manner.

To mechanistically link inflammation to enhanced fatty acid-supported mitochondrial respiration as an underlying adaptive response in CABG, it is worth investigating changes to mitochondrial signal transducer and activator of transcription 3 (STAT3) in RAA from CABG, which is responsible for inducing the gene expression of the mitochondrial fatty acid transporter, CPT-I. This mitochondrial protein and transcription factor, which is known for its signal transduction capabilities from the plasma membrane to the nucleus, has multifaceted roles in the progression of myocardial hypertrophy, and notably, *in vivo* rodent models of cardiac IRI. STAT3 is activated through the phosphorylation of its tyrosine 705 residue, which can occur in response to stimulation by pro-inflammatory cytokines including IL-6, and has been reported to be phosphorylated on this residue during both cardiac ischemia and reperfusion *in vivo* [552–555].

There are several important regulatory roles of mitochondrial STAT3 in rodent cardiomyocytes. Recent work by Zheng *et al*., investigating lipid overload-induced mitochondrial dysfunction determined that inactivation of the STAT3/CPT-I pathway by Atorvastatin ameliorated myocardial hypertrophy by decreasing fatty acid-supported oxidation [551]. This work suggests that attenuating fatty acid-supported respiration may be protective against damage, possibly due to the upregulation of pyruvate oxidation, however, additional work is required to verify this theory. It would be interesting to assess protein content of phosphorylated and total STAT3 in pre-/post-CABG RAA to determine if inflammation-induced upregulation of phosphorylated STAT3 on the post-CABG RAA persists, which may partly explain the elevated fatty acid-supported oxidation that was observed (through a STAT3/CPT-I axis). This theoretical increase in phosphorylated STAT3 on post-CABG RAA as a result of enhanced systemic inflammation would position STAT3 as a therapeutic target for addressing mitochondrial substrate selection towards enhanced fatty acid oxidation after reperfusion.

9.2 Limitations and Perspectives (DMD)

Chapter 4 addressed several questions that were posed as future directions by [34], who demonstrated that impairments in LV mitochondrial bioenergetics preceded overt cardiac remodeling and dysfunction in 4-week-old D2.*mdx* mice. Despite our best efforts to ensure careful consideration of study design and execution, there were limitations that may influence interpretation of the findings. While many of the limitations revolved around insufficient tissue availability - which is a recurrent theme in this thesis - this study design was novel in that unique signatures of cardiac remodeling were comprehensively assessed at a time point previously thought to be logistically unfeasible to characterize. This limitation was overcome by conducting over four rounds of animal breeding and daily injections.

The first limitation of Chapter 4 was the absence of cardiac functional assessments which would allow for more clinically relevant interpretations of the data. Although LV echocardiography was not conducted given that this data has previously been published in this model [34], obtaining RV functional data presented difficulties despite our best attempts given the extremely small ventricular size and geospatial location beneath the septum/ribcage at this time-point in D2.*mdx* mice. Obtaining RV echocardiographic data was attempted in these mice aged 4-weeks, however, unreliability of readings due to morphological characteristics of the heart made interpreting the data difficult. While RV functional data (biventricular recording) has been previously demonstrated in C57BL/10.*mdx* mice, these mice were aged to 3-4 months prior to assessment, meaning both non-invasive (echocardiographic) and invasive catheterization techniques were more reliable [184]. Pilot experiments that attempted to assess invasive hemodynamics in the RV of 4-week-old mice resulted in several mice dying prematurely during the procedure. It should be noted that RV functional assessments have never been published at

this time point in D2.*mdx*¸while some data is available in older mice and other dystrophic models [171]. In one study assessing C57BL/10.*mdx* at 4-weeks-old with *in vivo* characterization techniques (LG-enhanced MRI) and dobutamine stress, cardiac abnormalities in the RV demonstrated by elevated end systolic volume compared to control were observed [185] in the absence of fibrosis. Given that robust RV fibrosis has been characterized in older (16-25 weeks) D2.*mdx* mice, correlating RV functional data (at a time point where it is logistically feasible) to cardiac fibrosis would provide invaluable insight towards the role of this remodeling program in the dystrophic heart [166].

Next, it is acknowledged that a comprehensive assessment of mitochondrial stress responses, frozen assays, or spectral flow cytometry could not be assessed in the atria as conducted in the ventricles. While the atria were assessed with histopathological techniques, tissue size limitations restricted the ability to assess these chambers with assays requiring PmFB preparation, frozen assay homogenization such as during Western blot, or cell digestion as with spectral flow cytometry. Future work should seek to pool atria to overcome these limitations.

Although a comprehensive inflammatory profile was conducted on both ventricles, which consisted of examining pro- and anti-inflammatory cytokines via immunofluorescence in addition to spectral flow cytometry, RT-qPCR may have strengthened the interpretation of some of these findings. While it is acknowledged that RT-qPCR is among the gold standard techniques for assessing gene expression of inflammatory cytokines, tissue size limitations would have necessitated a 5^{th} round of animal breeding to obtain sufficient tissue, which was not feasible.

Another limitation is that animals were sacrificed 24 hours following the final drug injection. This is a limitation of the study design given that adiponectin's signaling effects may have been washed out by the time tissue was harvested. Animals were not sacrificed earlier

because limb muscle functional tests for a separate study were conducted the morning prior to sacrifice, therefore, avoiding injection stress was paramount. Future studies may consider employing a time course design that investigates how many hours adiponectin elicits its signaling effects for prior to wash out.

Chapter 4 was also limited by sample size with regards to the mitochondrial calcium retention capacity assay. While this assay provides invaluable insight towards the contribution of mitochondrial calcium uptake to intrinsic apoptosis pathways, the sample size was underpowered when removing PmFBs without clear mPT (primarily evident in D2.*mdx*-HD). Although previous work from the lab has pooled mPT and no clear mPT PmFBs together, the current work acknowledges that this does not accurately represent the ability of mitochondria to uptake calcium prior to swelling-induced opening.

9.3 Conclusion (DMD)

The findings from Chapter 4 demonstrate that dystrophin deficiency in 4-week-old D2.*mdx* mice heterogeneously influences histopathological, inflammatory, and mitochondrial stress-related remodeling signatures across chambers of the heart. Robust fibrosis uniquely impacts the RV and LA in young D2.*mdx* mice, which is accompanied by RV-specific cardiomyocyte hypertrophy and myocardial disorganization. Daily subcutaneous administration of ALY688 for 3 weeks is sufficient to attenuate RV fibrosis and cardiomyocyte hypertrophy, in part by promoting anti-inflammatory macrophage sub-populations and by improving mitochondrial stress responses. Collectively, the data demonstrates that adiponectin receptor agonism may represent a therapeutic candidate for dystrophin deficiency-induced cardiac remodeling and should at least be considered among other compounds as part of a combinatorial therapy for addressing contributors to DMD pathology.

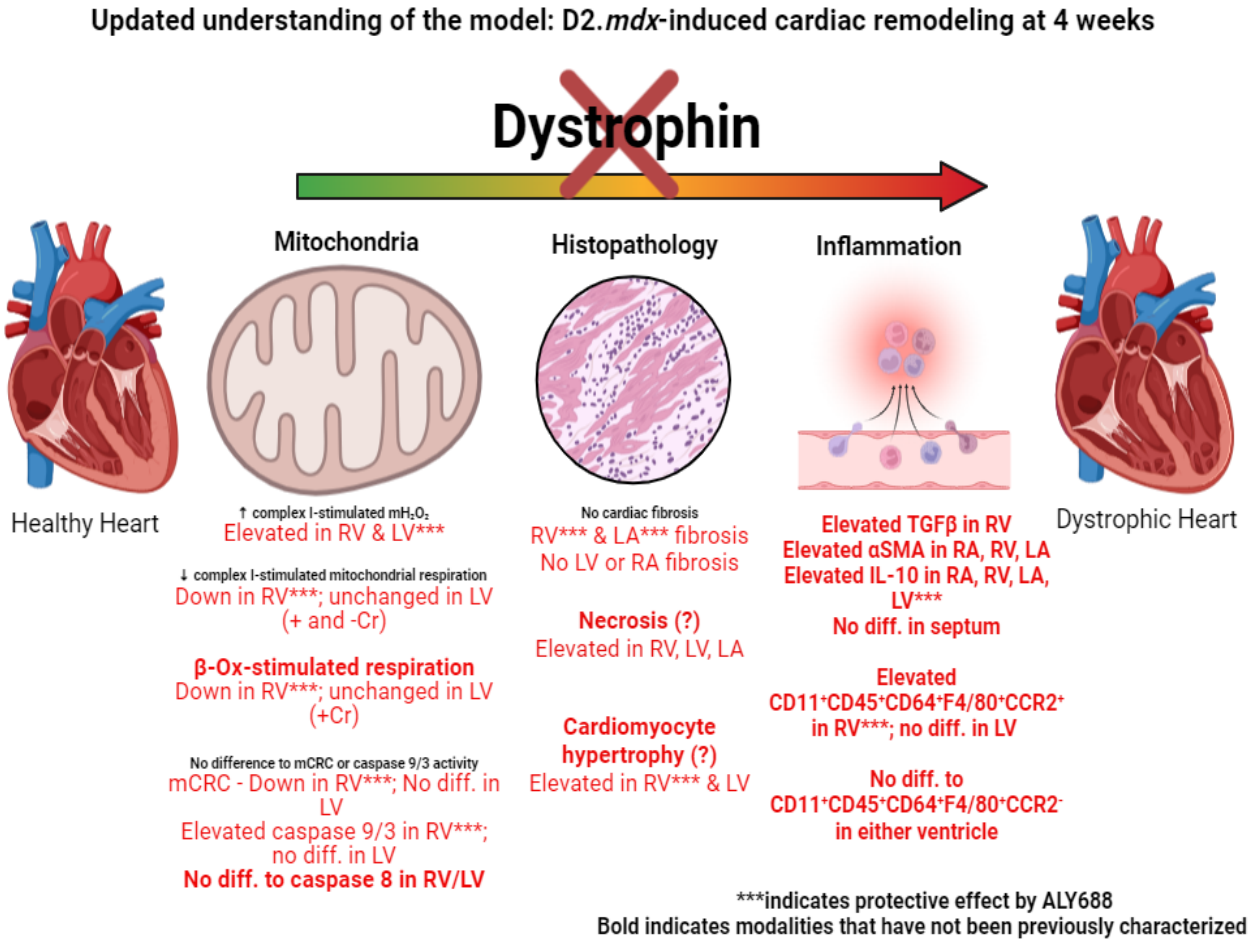

Figure 9-1. Updated understanding of newly discovered chamber-specific mitochondrial, histopathological, and inflammatory remodeling signatures in 4-week-old D2.mdx mice. Contributions of this thesis include a comprehensive characterization of chamber-specific histopathological remodeling, including robust RV and LA fibrosis, which may be related to metabolic and inflammatory perturbations in response to dystrophin deficiency-induced stress. Figure created using www.BioRender.com.

9.4 Limitations and Perspectives (CABG)

Similar to Chapter 4, careful measures were implemented to ensure strict adherence to study design and execution for Chapter 8, however, limitations are inevitable and still to be acknowledged. For this study to be conducted, a satellite lab was established at a York PCI facility associated with Southlake Regional Health Centre in Newmarket, Ontario. Here, respirometers were assembled to allow live tissue assessments of RAA samples freshly explanted from patients undergoing CABG surgeries. The satellite lab was set up after trialing a pilot experiment whereby transporting samples to York University reduced viability of the sample.

Firstly, given that we had limited control during the surgical procedure and could not confirm the stage of surgery at which RAA samples were explanted, we acknowledge that samples cannot be described as 'pre-ischemia' and 'post-reperfusion' given that the appropriate validation experiments were not conducted to verify these descriptors. Instead, the terms 'pre-' and 'post-CABG' were conservatively used throughout this study to define the two time-points at which RAA samples were obtained (before and after cardiopulmonary bypass).

Next, while extra caution was taken in handling the samples with time and temperature considered, there were several limitations that restricted additional data from being collected. Aside from high resolution respirometry, live tissue assessments of mitochondrial ROS (i.e. mH_2O_2 emissions) and mitochondrial CRC as an index of mitochondrial swelling-induced apoptosis could not be conducted on-site. This is because of logistical complications associated with transporting and setting up complex spectrofluorometry equipment outside of a conventional laboratory environment. Although this data could not be collected on live tissue, samples that were frozen in liquid N_2 were utilized for a Peroxiredoxin 3 (Prx3) assay that was adapted for this specific study design in order to assess Prx3 oxidation state.

Furthermore, the study had a relatively low sample size for a multitude of reasons. Firstly, to ensure consistency between samples, the same surgeon performed all RAA explants. While this prevented inter-surgeon variability, it also ensured that all samples were removed during the same point in surgery and with the same surgical technique. While this was a limitation because samples could only be obtained when the assigned surgeon was on site, it also presented other complications. On numerous occasions, patients required alternative surgeries (e.g. valve replacements or transcatheter aortic valve implantation) that disqualified them from consideration for the study. In addition, not all patients scheduled for a CABG procedure for the surgeon consented to donate their samples, thus reducing overall sample size.

Lastly, it should be noted that pre- versus post-CABG comparisons could not always be performed due to peri-operative complications. On numerous occasions, a post-CABG sample could not be obtained given that success of the surgery was always rightfully prioritized. Due to the possibility of peri-operative complications, samples were often on the smaller side (size-wise) given that the surgical procedures did not require excessive sample to be explanted.

9.5 Conclusion (CABG)

The novel and clinically insightful findings from Chapter 8 demonstrate that elective on-pump CABG surgery in male hospital patients influences adaptive mitochondrial stress responses to the RAA that are distinctive between pre- and post-CABG time-points. Notably, a unique observation in the post-CABG RAA suggests that the procedure, which is characterized by cycles of ischemia-reperfusion during and after CPB, enhances fatty acid-supported mitochondrial respiration in the absence of differences to carbohydrate (pyruvate)-supported respiration. While the contributions of IR as an underlying cause of this adaptation in substrate selection could not be verified with the current study design, this data agrees with rodent models

of myocardial ischemic heart disease whereby the reliance on fatty acid-supported substrates for ATP provision is elevated post-reperfusion. Additionally, this study suggests that elevated fatty acid-supported respiration on the post-CABG RAA is related to reduced prx3 monomer density, which reflects an index of oxidative stress potentially attributed to reperfusion injury. Comprehensive assessment of systemic immune cells, complete blood count, metabolites, and electrolytes at various time-points throughout the surgical period reveals that elevated total leukocytes and neutrophils following surgery occur in concert with the observed adaptation in mitochondrial RAA-specific substrate selection. Future experiments will elucidate if the enhanced fatty acid-supported respiration on the post-CABG RAA reflects an adaptive regulatory control over glucose metabolism that responds to local oxygen availability, reactive oxidant stress, and malonyl CoA activity. In this regard, rather than being passaged toward pyruvate for further oxidation, glucose in the post-CABG RAA may be instead sparred for biosynthetic fates that protect the heart against oxidative damage while fatty acids, the preferred substrate for ATP provision in the heart, dominate in a milieu where oxygen is once again abundant.

10 REFERENCES

1. Nigro, G.; Comi, L.I.; Limongelli, F.M.; Giugliano, M.A.M.; Politano, L.; Petretta, V.; Passamano, L.; Stefanelli, S. Prospective Study of X-linked Progressive Muscular Dystrophy in Campania. *Muscle Nerve* **1983**, *6*, 253–262, doi:10.1002/mus.880060403.

2. Jacobs, P.A.; Hunt, P.A.; Mayer, M.; Bart, R.D. Duchenne Muscular Dystrophy (DMD) in a Female with an X/Autosome Translocation: Further Evidence That the DMD Locus Is at Xp21. *Am. J. Hum. Genet.* **1981**, *33*, 513–518.

3. Crisafulli, S.; Sultana, J.; Fontana, A.; Salvo, F.; Messina, S.; Trifirò, G. Global Epidemiology of Duchenne Muscular Dystrophy: An Updated Systematic Review and Meta-Analysis. *Orphanet J. Rare Dis.* **2020**, *15*, 141, doi:10.1186/s13023-020-01430-8.

4. Ryder, S.; Leadley, R.M.; Armstrong, N.; Westwood, M.; de Kock, S.; Butt, T.; Jain, M.; Kleijnen, J. The Burden, Epidemiology, Costs and Treatment for Duchenne Muscular Dystrophy: An Evidence Review. *Orphanet J. Rare Dis.* **2017**, *12*, 79, doi:10.1186/s13023-017-0631-3.

5. Mah, J.K.; Korngut, L.; Dykeman, J.; Day, L.; Pringsheim, T.; Jette, N. A Systematic Review and Meta-Analysis on the Epidemiology of Duchenne and Becker Muscular Dystrophy. *Neuromuscul. Disord.* **2014**, *24*, 482–491, doi:10.1016/j.nmd.2014.03.008.

6. Bladen, C.L.; Rafferty, K.; Straub, V.; Monges, S.; Moresco, A.; Dawkins, H.; Roy, A.; Chamova, T.; Guergueltcheva, V.; Korngut, L.; et al. The TREAT-NMD Duchenne Muscular Dystrophy Registries: Conception, Design, and Utilization by Industry and Academia. *Hum. Mutat.* **2013**, *34*, 1449–1457, doi:10.1002/humu.22390.

7. Petrof, B.J.; Shrager, J.B.; Stedman, H.H.; Kelly, A.M.; Sweeney, H.L. Dystrophin Protects the Sarcolemma from Stresses Developed during Muscle Contraction. *Proc. Natl. Acad. Sci. U. S. A.* **1993**, *90*, 3710–3714, doi:10.1073/pnas.90.8.3710.

8. Wallace, G.Q.; McNally, E.M. Mechanisms of Muscle Degeneration, Regeneration, and Repair in the Muscular Dystrophies. *Annu. Rev. Physiol.* **2009**, *71*, 37–57, doi:10.1146/annurev.physiol.010908.163216.

9. McNally, E.M.; Kaltman, J.R.; Woodrow Benson, D.; Canter, C.E.; Cripe, L.H.; Duan, D.; Finder, J.D.; Hoffman, E.P.; Judge, D.P.; Kertesz, N.; et al. Contemporary Cardiac Issues in Duchenne Muscular Dystrophy. *Circulation* **2015**, *131*, 1590–1598, doi:10.1161/CIRCULATIONAHA.114.015151.

10. Bach, J.R.; O'Brien, J.; Krotenberg, R.; Alba, A.S. Management of End Stage Respiratory Failure in Duchenne Muscular Dystrophy. *Muscle Nerve* **1987**, *10*, 177–182, doi:10.1002/mus.880100212.

11. Zambon, A.A.; Ayyar Gupta, V.; Ridout, D.; Manzur, A.Y.; Baranello, G.; Trucco, F.; Muntoni, F. Peak Functional Ability and Age at Loss of Ambulation in Duchenne Muscular Dystrophy. *Dev. Med. Child Neurol.* **2022**, *64*, 979–988, doi:10.1111/dmcn.15176.

12. Schultz, T.I.; Raucci, F.J.; Salloum, F.N. Cardiovascular Disease in Duchenne Muscular Dystrophy: Overview and Insight Into Novel Therapeutic Targets. *JACC Basic to Transl. Sci.* **2022**, *7*, 608–625, doi:10.1016/j.jacbts.2021.11.004.

13. Nigro, G.; Comi, L.I.; Politano, L.; Bain, R.J.I. The Incidence and Evolution of Cardiomyopathy in Duchenne Muscular Dystrophy. *Int. J. Cardiol.* **1990**, *26*, 271–277, doi:10.1016/0167-5273(90)90082-G.

14. de Kermadec, J.M.; Bécane, H.M.; Chénard, A.; Tertrain, F.; Weiss, Y. Prevalence of Left Ventricular Systolic Dysfunction in Duchenne Muscular Dystrophy: An Echocardiographic Study. *Am. Heart J.* **1994**, *127*, 618–623, doi:10.1016/0002-8703(94)90672-6.

15. Szabo, S.M.; Salhany, R.M.; Deighton, A.; Harwood, M.; Mah, J.; Gooch, K.L. The Clinical Course of Duchenne Muscular Dystrophy in the Corticosteroid Treatment Era: A Systematic Literature Review. *Orphanet J. Rare Dis.* **2021**, *16*, 237, doi:10.1186/s13023-021-01862-w.

16. Bushby, K.; Connor, E. Clinical Outcome Measures for Trials in Duchenne Muscular Dystrophy: Report from International Working Group Meetings. *Clin. Investig. (Lond).* **2011**, *1*, 1217–1235, doi:10.4155/cli.11.113.

17. Passamano, L.; Taglia, A.; Palladino, A.; Viggiano, E.; D'Ambrosio, P.; Scutifero, M.; Cecio, M.R.; Torre, V.; De Luca, F.; Picillo, E.; et al. Improvement of Survival in Duchenne Muscular Dystrophy: Retrospective Analysis of 835 Patients. *Acta Myol.* 2012, *31*, 121–125.

18. Chey, Y.C.J.; Arudkumar, J.; Aartsma-Rus, A.; Adikusuma, F.; Thomas, P.Q. CRISPR Applications for Duchenne Muscular Dystrophy: From Animal Models to Potential Therapies. *WIREs Mech. Dis.* **2023**, doi:10.1002/wsbm.1580.

19. Fatehi, S.; Marks, R.M.; Rok, M.J.; Perillat, L.; Ivakine, E.A.; Cohn, R.D. Advances in CRISPR/Cas9 Genome Editing for the Treatment of Muscular Dystrophies. *Hum. Gene Ther.* **2023**, doi:10.1089/hum.2023.059.

20. Wilton-Clark, H.; Yokota, T. Biological and Genetic Therapies for the Treatment of Duchenne Muscular Dystrophy. *Expert Opin. Biol. Ther.* 2023.

21. Escolar, D.M.; Hache, L.P.; Clemens, P.R.; Cnaan, A.; McDonald, C.M.; Viswanathan, V.; Kornberg, A.J.; Bertorini, T.E.; Nevo, Y.; Lotze, T.; et al. Randomized, Blinded Trial of Weekend vs Daily Prednisone in Duchenne Muscular Dystrophy. *Neurology* **2011**, doi:10.1212/WNL.0b013e318227b164.

22. Connolly, A.M.; Zaidman, C.M.; Golumbek, P.T.; Cradock, M.M.; Flanigan, K.M.; Kuntz, N.L.; Finkel, R.S.; McDonald, C.M.; Iannaccone, S.T.; Anand, P.; et al. Twice-Weekly Glucocorticosteroids in Infants and Young Boys with Duchenne Muscular Dystrophy. *Muscle and Nerve* **2019**, doi:10.1002/mus.26441.

23. Quattrocelli, M.; Zelikovich, A.S.; Jiang, Z.; Peek, C.B.; Demonbreun, A.R.; Kuntz, N.L.; Barish, G.D.; Haldar, S.M.; Bass, J.; McNally, E.M. Pulsed Glucocorticoids Enhance Dystrophic Muscle Performance through Epigenetic-Metabolic Reprogramming. *JCI Insight* **2019**, doi:10.1172/jci.insight.132402.

24. Matthews, E.; Brassington, R.; Kuntzer, T.; Jichi, F.; Manzur, A.Y. Corticosteroids for the Treatment of Duchenne Muscular Dystrophy. *Cochrane Database Syst. Rev.* **2016**, *2016*, doi:10.1002/14651858.CD003725.pub4.

25. Van Erp, C.; Loch, D.; Laws, N.; Trebbin, A.; Hoey, A.J. Timeline of Cardiac Dystrophy in 3–18-month-old MDX Mice. *Muscle Nerve* **2010**, *42*, 504–513, doi:10.1002/mus.21716.

26. Mavrogeni, S.; Papavasiliou, A.; Spargias, K.; Constandoulakis, P.; Papadopoulos, G.; Karanasios, E.; Georgakopoulos, D.; Kolovou, G.; Demerouti, E.; Polymeros, S.; et al. Myocardial Inflammation in Duchenne Muscular Dystrophy as a Precipitating Factor for Heart Failure: A Prospective Study. *BMC Neurol.* **2010**, doi:10.1186/1471-2377-10-33.

27. Shirokova, N.; Niggli, E. Cardiac Phenotype of Duchenne Muscular Dystrophy: Insights from Cellular Studies. *J. Mol. Cell. Cardiol.* 2013.

28. Williams, I.A.; Allen, D.G. Intracellular Calcium Handling in Ventricular Myocytes from Mdx Mice. *Am. J. Physiol. Circ. Physiol.* **2007**, *292*, H846–H855, doi:10.1152/ajpheart.00688.2006.

29. Vallejo-Illarramendi, A.; Toral-Ojeda, I.; Aldanondo, G.; López de Munain, A. Dysregulation of Calcium Homeostasis in Muscular Dystrophies. *Expert Rev. Mol. Med.* **2014**, *16*, e16, doi:10.1017/erm.2014.17.

30. Bellissimo, C.A.; Garibotti, M.C.; Perry, C.G.R. Mitochondrial Stress Responses in Duchenne Muscular Dystrophy: Metabolic Dysfunction or Adaptive Reprogramming? *Am. J. Physiol. Physiol.* **2022**, *323*, C718–C730, doi:10.1152/ajpcell.00249.2022.

31. Hughes, M.C.; Ramos, S. V.; Turnbull, P.C.; Edgett, B.A.; Huber, J.S.; Polidovitch, N.; Schlattner, U.; Backx, P.H.; Simpson, J.A.; Perry, C.G.R. Impairments in Left Ventricular Mitochondrial Bioenergetics Precede Overt Cardiac Dysfunction and Remodelling in Duchenne Muscular Dystrophy. *J. Physiol.* **2020**, doi:10.1113/JP277306.

32. Wrogemann, K.; Pena, S.D.J. Mitochondrial Calcium Overload: A General Mechanism for Cell-Necrosis in Muscle Diseases. *Lancet* **1976**, *307*, 672–674, doi:10.1016/S0140-6736(76)92781-1.

33. Zulian, A.; Schiavone, M.; Giorgio, V.; Bernardi, P. Forty Years Later: Mitochondria as Therapeutic Targets in Muscle Diseases. *Pharmacol. Res.* **2016**, *113*, 563–573, doi:10.1016/j.phrs.2016.09.043.

34. Hughes, M.C.; Ramos, S. V.; Turnbull, P.C.; Edgett, B.A.; Huber, J.S.; Polidovitch, N.; Schlattner, U.; Backx, P.H.; Simpson, J.A.; Perry, C.G.R. Impairments in Left Ventricular Mitochondrial Bioenergetics Precede Overt Cardiac Dysfunction and Remodelling in Duchenne Muscular Dystrophy. *J. Physiol.* **2020**, *598*, 1377–1392, doi:10.1113/JP277306.

35. Cohn, J.N.; Ferrari, R.; Sharpe, N. Cardiac Remodeling—Concepts and Clinical Implications: A Consensus Paper from an International Forum on Cardiac Remodeling. *J. Am. Coll. Cardiol.* **2000**, *35*, 569–582, doi:10.1016/S0735-1097(99)00630-0.

36. Kamogawa, Y. Dystrophin-Deficient Myocardium Is Vulnerable to Pressure Overload in Vivo. *Cardiovasc. Res.* **2001**, *50*, 509–515, doi:10.1016/S0008-6363(01)00205-X.

37. Magrath, P.; Maforo, N.; Renella, P.; Nelson, S.F.; Halnon, N.; Ennis, D.B. Cardiac MRI Biomarkers for Duchenne Muscular Dystrophy. *Biomark. Med.* **2018**, *12*, 1271–1289, doi:10.2217/bmm-2018-0125.

38. Koenig, M.; Hoffman, E.P.; Bertelson, C.J.; Monaco, A.P.; Feener, C.; Kunkel, L.M. Complete Cloning of the Duchenne Muscular Dystrophy (DMD) CDNA and Preliminary Genomic Organization of the DMD Gene in Normal and Affected Individuals. *Cell* **1987**, *50*, 509–517, doi:10.1016/0092-8674(87)90504-6.

39. Hoffman, E.P. The Discovery of Dystrophin, the Protein Product of the Duchenne Muscular Dystrophy Gene. *FEBS J.* **2020**, *287*, 3879–3887, doi:10.1111/febs.15466.

40. Kamdar, F.; Garry, D.J. Dystrophin-Deficient Cardiomyopathy. *J. Am. Coll. Cardiol.* **2016**, *67*, 2533–2546, doi:10.1016/j.jacc.2016.02.081.

41. Bladen, C.L.; Salgado, D.; Monges, S.; Foncuberta, M.E.; Kekou, K.; Kosma, K.; Dawkins, H.; Lamont, L.; Roy, A.J.; Chamova, T.; et al. The TREAT-NMD DMD Global Database: Analysis of More than 7,000 Duchenne Muscular Dystrophy Mutations. *Hum. Mutat.* **2015**, *36*, 395–402, doi:10.1002/humu.22758.

42. Flanigan, K.M. Duchenne and Becker Muscular Dystrophies. *Neurol. Clin.* **2014**, *32*, 671–688, doi:10.1016/j.ncl.2014.05.002.

43. Aartsma-Rus, A.; Van Deutekom, J.C.T.; Fokkema, I.F.; Van Ommen, G.B.; Den Dunnen, J.T. Entries in the Leiden Duchenne Muscular Dystrophy Mutation Database: An Overview of Mutation Types and Paradoxical Cases That Confirm the Reading-frame Rule. *Muscle Nerve* **2006**, *34*, 135–144, doi:10.1002/mus.20586.

44. Magri, F.; Govoni, A.; D'Angelo, M.G.; Del Bo, R.; Ghezzi, S.; Sandra, G.; Turconi, A.C.; Sciacco, M.; Ciscato, P.; Bordoni, A.; et al. Genotype and Phenotype Characterization in a Large Dystrophinopathic Cohort with Extended Follow-Up. *J. Neurol.* **2011**, *258*, 1610–1623, doi:10.1007/s00415-011-5979-z.

45. Nakamura, A.; Fueki, N.; Shiba, N.; Motoki, H.; Miyazaki, D.; Nishizawa, H.; Echigoya, Y.; Yokota, T.; Aoki, Y.; Takeda, S. Deletion of Exons 3-9 Encompassing a Mutational Hot Spot in the DMD Gene Presents an Asymptomatic Phenotype, Indicating a Target Region for Multiexon Skipping Therapy. *J. Hum. Genet.* **2016**, *61*, 663–667, doi:10.1038/jhg.2016.28.

46. Aartsma-Rus, A.; Dunnen, J.T. Phenotype Predictions for Exon Deletions/Duplications: A User Guide for Professionals and Clinicians Using Becker and Duchenne Muscular Dystrophy as Examples. *Hum. Mutat.* **2019**, *40*, 1630–1633, doi:10.1002/humu.23850.

47. Jefferies, J.L.; Eidem, B.W.; Belmont, J.W.; Craigen, W.J.; Ware, S.M.; Fernbach, S.D.; Neish, S.R.; Smith, E.O.B.; Towbin, J.A. Genetic Predictors and Remodeling of Dilated Cardiomyopathy in Muscular Dystrophy. *Circulation* **2005**, *112*, 2799–2804, doi:10.1161/CIRCULATIONAHA.104.528281.

48. Yamamoto, T.; Awano, H.; Zhang, Z.; Sakuma, M.; Kitaaki, S.; Matsumoto, M.; Nagai, M.; Sato, I.;

Imanishi, T.; Hayashi, N.; et al. Cardiac Dysfunction in Duchenne Muscular Dystrophy Is Less Frequent in Patients With Mutations in the Dystrophin Dp116 Coding Region Than in Other Regions. *Circ. Genomic Precis. Med.* **2018**, *11*, E001782, doi:10.1161/CIRCGEN.117.001782.

49. Le, S.; Yu, M.; Hovan, L.; Zhao, Z.; Ervasti, J.; Yan, J. Dystrophin As a Molecular Shock Absorber. *ACS Nano* **2018**, *12*, 12140–12148, doi:10.1021/acsnano.8b05721.

50. Kaspar, R.W.; Allen, H.D.; Montanaro, F. Current Understanding and Management of Dilated Cardiomyopathy in Duchenne and Becker Muscular Dystrophy. *J. Am. Acad. Nurse Pract.* **2009**, *21*, 241–249, doi:10.1111/j.1745-7599.2009.00404.x.

51. Ervasti, J.M.; Campbell, K.P. A Role for the Dystrophin-Glycoprotein Complex as a Transmembrane Linker between Laminin and Actin. *J. Cell Biol.* **1993**, *122*, 809–823, doi:10.1083/jcb.122.4.809.

52. Allen, D.G.; Gervasio, O.L.; Yeung, E.W.; Whitehead, N.P. Calcium and the Damage Pathways in Muscular DystrophyThis Article Is One of a Selection of Papers Published in This Special Issue on Calcium Signaling. *Can. J. Physiol. Pharmacol.* **2010**, *88*, 83–91, doi:10.1139/Y09-058.

53. Masubuchi, N.; Shidoh, Y.; Kondo, S.; Takatoh, J.; Hanaoka, K. Subcellular Localization of Dystrophin Isoforms in Cardiomyocytes and Phenotypic Analysis of Dystrophin-Deficient Mice Reveal Cardiac Myopathy Is Predominantly Caused by a Deficiency in Full-Length Dystrophin. *Exp. Anim.* **2013**, *62*, 211–217, doi:10.1538/expanim.62.211.

54. Ramos, S. V.; Hughes, M.C.; Delfinis, L.J.; Bellissimo, C.A.; Perry, C.G.R. Mitochondrial Bioenergetic Dysfunction in the D2.Mdx Model of Duchenne Muscular Dystrophy Is Associated with Microtubule Disorganization in Skeletal Muscle. *PLoS One* **2020**, *15*, doi:10.1371/journal.pone.0237138.

55. Prins, K.W.; Humston, J.L.; Mehta, A.; Tate, V.; Ralston, E.; Ervasti, J.M. Dystrophin Is a Microtubule-Associated Protein. *J. Cell Biol.* **2009**, *186*, 363–369, doi:10.1083/jcb.200905048.

56. Belanto, J.J.; Olthoff, J.T.; Mader, T.L.; Chamberlain, C.M.; Nelson, D.M.; McCourt, P.M.; Talsness, D.M.; Gundersen, G.G.; Lowe, D.A.; Ervasti, J.M. Independent Variability of Microtubule Perturbations Associated with Dystrophinopathy. *Hum. Mol. Genet.* **2016**, *25*, 4951–4961, doi:10.1093/hmg/ddw318.

57. Nelson, D.M.; Lindsay, A.; Judge, L.M.; Duan, D.; Chamberlain, J.S.; Lowe, D.A.; Ervasti, J.M. Variable Rescue of Microtubule and Physiological Phenotypes in Mdx Muscle Expressing Different Miniaturized Dystrophins. *Hum. Mol. Genet.* **2018**, *27*, 2090–2100, doi:10.1093/hmg/ddy113.

58. Belanto, J.J.; Mader, T.L.; Eckhoff, M.D.; Strandjord, D.M.; Banks, G.B.; Gardner, M.K.; Lowe, D.A.; Ervasti, J.M. Microtubule Binding Distinguishes Dystrophin from Utrophin. *Proc. Natl. Acad. Sci. U. S. A.* **2014**, *111*, 5723–5728, doi:10.1073/pnas.1323842111.

59. Olthoff, J.T.; Lindsay, A.; Abo-Zahrah, R.; Baltgalvis, K.A.; Patrinostro, X.; Belanto, J.J.; Yu, D.Y.; Perrin, B.J.; Garry, D.J.; Rodney, G.G.; et al. Loss of Peroxiredoxin-2 Exacerbates Eccentric Contraction-Induced Force Loss in Dystrophin-Deficient Muscle. *Nat. Commun.* **2018**, *9*, doi:10.1038/s41467-018-07639-3.

60. Finsterer, J.; Cripe, L. Treatment of Dystrophin Cardiomyopathies. *Nat. Rev. Cardiol.* **2014**, *11*, 168–179, doi:10.1038/nrcardio.2013.213.

61. Van Westering, T.; Betts, C.; Wood, M. Current Understanding of Molecular Pathology and Treatment of Cardiomyopathy in Duchenne Muscular Dystrophy. *Molecules* **2015**, *20*, 8823–8855, doi:10.3390/molecules20058823.

62. Judge, D.P.; Kass, D.A.; Thompson, W.R.; Wagner, K.R. Pathophysiology and Therapy of Cardiac Dysfunction in Duchenne Muscular Dystrophy. *Am. J. Cardiovasc. Drugs* **2011**, *11*, 287–294, doi:10.2165/11594070-000000000-00000.

63. Verhaert, D.; Richards, K.; Rafael-Fortney, J.A.; Raman, S. V. Cardiac Involvement in Patients With Muscular Dystrophies. *Circ. Cardiovasc. Imaging* **2011**, *4*, 67–76, doi:10.1161/CIRCIMAGING.110.960740.

64. Bostick, B.; Yue, Y.; Duan, D. Gender Influences Cardiac Function in the Mdx Model of Duchenne Cardiomyopathy. *Muscle and Nerve* **2010**, *42*, 600–603, doi:10.1002/mus.21763.

65. Chamberlain, J.S.; Metzger, J.; Reyes, M.; Townsend, D.; Faulkner, J.A. Dystrophin-deficient Mdx Mice Display a Reduced Life Span and Are Susceptible to Spontaneous Rhabdomyosarcoma . *FASEB J.* **2007**, *21*, 2195–2204, doi:10.1096/fj.06-7353com.

66. van Putten, M.; Putker, K.; Overzier, M.; Adamzek, W.A.; Pasteuning-Vuhman, S.; Plomp, J.J.; Aartsma-Rus, A. Natural Disease History of the D2-Mdx Mouse Model for Duchenne Muscular Dystrophy. *FASEB J.* **2019**, *33*, 8110–8124, doi:10.1096/fj.201802488R.

67. Florian, A.; Rösch, S.; Bietenbeck, M.; Engelen, M.; Stypmann, J.; Waltenberger, J.; Sechtem, U.; Yilmaz, A. Cardiac Involvement in Female Duchenne and Becker Muscular Dystrophy Carriers in Comparison to Their First-Degree Male Relatives: A Comparative Cardiovascular Magnetic Resonance Study. *Eur. Heart J. Cardiovasc. Imaging* **2016**, *17*, 326–333, doi:10.1093/ehjci/jev161.

68. Birnkrant, D.J.; Bushby, K.; Bann, C.M.; Apkon, S.D.; Blackwell, A.; Brumbaugh, D.; Case, L.E.; Clemens, P.R.; Hadjiyannakis, S.; Pandya, S.; et al. Diagnosis and Management of Duchenne Muscular Dystrophy, Part 1: Diagnosis, and Neuromuscular, Rehabilitation, Endocrine, and Gastrointestinal and Nutritional Management. *Lancet Neurol.* **2018**, *17*, 251–267, doi:10.1016/S1474-4422(18)30024-3.

69. Gardner-Medwin, D. Clinical Features and Classification of the Muscular Dystrophies. *Br. Med. Bull.* **1980**, *36*, 109–116, doi:10.1093/oxfordjournals.bmb.a071623.

70. Emery, A.E.H. Muscular Dystrophy into the New Millennium. *Neuromuscul. Disord.* **2002**, *12*, 343–349, doi:10.1016/S0960-8966(01)00303-0.

71. Torriani, M.; Townsend, E.; Thomas, B.J.; Bredella, M.A.; Ghomi, R.H.; Tseng, B.S. Lower Leg Muscle Involvement in Duchenne Muscular Dystrophy: An MR Imaging and Spectroscopy Study. *Skeletal Radiol.* **2012**, *41*, 437–445, doi:10.1007/s00256-011-1240-1.

72. Florczyk-Soluch, U.; Polak, K.; Dulak, J. The Multifaceted View of Heart Problem in Duchenne Muscular Dystrophy. *Cell. Mol. Life Sci.* **2021**, *78*, 5447–5468, doi:10.1007/s00018-021-03862-2.

73. Archer, J.E.; Gardner, A.C.; Roper, H.P.; Chikermane, A.A.; Tatman, A.J. Duchenne Muscular Dystrophy: The Management of Scoliosis. *J. Spine Surg.* **2016**, *2*, 185–194, doi:10.21037/jss.2016.08.05.

74. Mercuri, E.; Bönnemann, C.G.; Muntoni, F. Muscular Dystrophies. *Lancet* **2019**, *394*, 2025–2038, doi:10.1016/S0140-6736(19)32910-1.

75. Banihani, R.; Smile, S.; Yoon, G.; Dupuis, A.; Mosleh, M.; Snider, A.; McAdam, L. Cognitive and Neurobehavioral Profile in Boys with Duchenne Muscular Dystrophy. *J. Child Neurol.* **2015**, *30*, 1472–1482, doi:10.1177/0883073815570154.

76. Mendell, J.R.; Shilling, C.; Leslie, N.D.; Flanigan, K.M.; Al-Dahhak, R.; Gastier-Foster, J.; Kneile, K.; Dunn, D.M.; Duval, B.; Aoyagi, A.; et al. Evidence-Based Path to Newborn Screening for Duchenne Muscular Dystrophy. *Ann. Neurol.* **2012**, *71*, 304–313, doi:10.1002/ana.23528.

77. Wagner, K.R.; Lechtzin, N.; Judge, D.P. Current Treatment of Adult Duchenne Muscular Dystrophy. *Biochim. Biophys. Acta - Mol. Basis Dis.* **2007**, *1772*, 229–237, doi:10.1016/j.bbadis.2006.06.009.

78. Coley, W.D.; Bogdanik, L.; Vila, M.C.; Yu, Q.; Van Der Meulen, J.H.; Rayavarapu, S.; Novak, J.S.; Nearing, M.; Quinn, J.L.; Saunders, A.; et al. Effect of Genetic Background on the Dystrophic Phenotype in Mdx Mice. *Hum. Mol. Genet.* **2016**, *25*, 130–145, doi:10.1093/hmg/ddv460.

79. Howard, Z.M.; Dorn, L.E.; Lowe, J.; Gertzen, M.D.; Ciccone, P.; Rastogi, N.; Odom, G.L.; Accornero, F.; Chamberlain, J.S.; Rafael-Fortney, J.A. Micro-Dystrophin Gene Therapy Prevents Heart Failure in an Improved Duchenne Muscular Dystrophy Cardiomyopathy Mouse Model. *JCI Insight* **2021**, *6*, doi:10.1172/jci.insight.146511.

80. Bulfield, G.; Siller, W.G.; Wight, P.A.L.; Moore, K.J. X Chromosome-Linked Muscular Dystrophy (Mdx)

in the Mouse. *Proc. Natl. Acad. Sci. U. S. A.* **1984**, *81*, 1189–1192, doi:10.1073/pnas.81.4.1189.

81. Burelle, Y.; Khairallah, M.; Ascah, A.; Allen, B.G.; Deschepper, C.F.; Petrof, B.J.; Des Rosiers, C. Alterations in Mitochondrial Function as a Harbinger of Cardiomyopathy: Lessons from the Dystrophic Heart. *J. Mol. Cell. Cardiol.* **2010**, *48*, 310–321, doi:10.1016/j.yjmcc.2009.09.004.

82. Ascah, A.; Khairallah, M.; Daussin, F.; Bourcier-Lucas, C.; Godin, R.; Allen, B.G.; Petrof, B.J.; Des Rosiers, C.; Burelle, Y. Stress-Induced Opening of the Permeability Transition Pore in the Dystrophin-Deficient Heart Is Attenuated by Acute Treatment with Sildenafil. *Am. J. Physiol. Circ. Physiol.* **2011**, *300*, H144–H153, doi:10.1152/ajpheart.00522.2010.

83. Shirokova, N.; Niggli, E. Cardiac Phenotype of Duchenne Muscular Dystrophy: Insights from Cellular Studies. *J. Mol. Cell. Cardiol.* **2013**, *58*, 217–224, doi:10.1016/j.yjmcc.2012.12.009.

84. Swiderski, K.; Lynch, G.S. Murine Models of Duchenne Muscular Dystrophy: Is There a Best Model? *Am. J. Physiol. Physiol.* **2021**, *321*, C409–C412, doi:10.1152/ajpcell.00212.2021.

85. Wong, T.W.Y.; Ahmed, A.; Yang, G.; Maino, E.; Steiman, S.; Hyatt, E.; Chan, P.; Lindsay, K.; Wong, N.; Golebiowski, D.; et al. A Novel Mouse Model of Duchenne Muscular Dystrophy Carrying a Multi-Exonic Dmd Deletion Exhibits Progressive Muscular Dystrophy and Early-Onset Cardiomyopathy. *Dis. Model. Mech.* **2020**, *13*, doi:10.1242/dmm.045369.

86. Hayes, H.M.; Angerosa, J.; Piers, A.T.; White, J.D.; Koleff, J.; Thurgood, M.; Moody, J.; Cheung, M.M.; Pepe, S. Preserved Left Ventricular Function despite Myocardial Fibrosis and Myopathy in the Dystrophin-Deficient D2.B10-Dmd Mdx/J Mouse. *Oxid. Med. Cell. Longev.* **2022**, *2022*, doi:10.1155/2022/5362115.

87. Taglietti, V.; Kefi, K.; Bronisz-Budzyńska, I.; Mirciloglu, B.; Rodrigues, M.; Cardone, N.; Coulpier, F.; Periou, B.; Gentil, C.; Goddard, M.; et al. Duchenne Muscular Dystrophy Trajectory in R-DMDdel52 Preclinical Rat Model Identifies COMP as Biomarker of Fibrosis. *Acta Neuropathol. Commun.* **2022**, *10*, 60, doi:10.1186/s40478-022-01355-2.

88. Nakamura, K.; Fujii, W.; Tsuboi, M.; Tanihata, J.; Teramoto, N.; Takeuchi, S.; Naito, K.; Yamanouchi, K.; Nishihara, M. Generation of Muscular Dystrophy Model Rats with a CRISPR/Cas System. *Sci. Rep.* **2015**, *4*, doi:10.1038/srep05635.

89. Larcher, T.; Lafoux, A.; Tesson, L.; Remy, S.V.; Thepenier, V.; François, V.; Guiner, C. Le; Goubin, H.; Dutilleul, M.V.; Guigand, L.; et al. Characterization of Dystrophin Deficient Rats: A New Model for Duchenne Muscular Dystrophy. *PLoS One* **2014**, *9*, doi:10.1371/journal.pone.0110371.

90. Howell, J.M.C.; Fletcher, S.; Kakulas, B.A.; O'Hara, M.; Lochmuller, H.; Karpati, G. Use of the Dog Model for Duchenne Muscular Dystrophy in Gene Therapy Trials. *Neuromuscul. Disord.* **1997**, *7*, 325–328, doi:10.1016/S0960-8966(97)00057-6.

91. Le Guiner, C.; Servais, L.; Montus, M.; Larcher, T.; Fraysse, B.; Moullec, S.; Allais, M.; François, V.; Dutilleul, M.; Malerba, A.; et al. Long-Term Microdystrophin Gene Therapy Is Effective in a Canine Model of Duchenne Muscular Dystrophy. *Nat. Commun.* **2017**, *8*, 16105, doi:10.1038/ncomms16105.

92. Felsburg, P.J. Overview of Immune System Development in the Dog: Comparison with Humans. *Hum. Exp. Toxicol.* **2002**, *21*, 487–492, doi:10.1191/0960327102ht286oa.

93. Sui, T.; Lau, Y.S.; Liu, D.; Liu, T.; Xu, L.; Gao, Y.; Lai, L.; Li, Z.; Han, R. A Novel Rabbit Model of Duchenne Muscular Dystrophy Generated by CRISPR/Cas9. *DMM Dis. Model. Mech.* **2018**, *11*, doi:10.1242/dmm.032201.

94. Klymiuk, N.; Blutke, A.; Graf, A.; Krause, S.; Burkhardt, K.; Wuensch, A.; Krebs, S.; Kessler, B.; Zakhartchenko, V.; Kurome, M.; et al. Dystrophin-Deficient Pigs Provide New Insights into the Hierarchy of Physiological Derangements of Dystrophic Muscle. *Hum. Mol. Genet.* **2013**, *22*, 4368–4382, doi:10.1093/hmg/ddt287.

95. Tamiyakul, H.; Kemter, E.; Kösters, M.; Ebner, S.; Blutke, A.; Klymiuk, N.; Flenkenthaler, F.; Wolf, E.;

Arnold, G.J.; Fröhlich, T. Progressive Proteome Changes in the Myocardium of a Pig Model for Duchenne Muscular Dystrophy. *iScience* **2020**, *23*, 101516, doi:10.1016/j.isci.2020.101516.

96. Chamberlain, J.S.; Benian, G.M. Muscular Dystrophy: The Worm Turns to Genetic Disease. *Curr. Biol.* **2000**, *10*, R795–R797, doi:10.1016/S0960-9822(00)00768-5.

97. Gieseler, K.; Grisoni, K.; Ségalat, L. Genetic Suppression of Phenotypes Arising from Mutations in Dystrophin-Related Genes in Caenorhabditis Elegans. *Curr. Biol.* **2000**, *10*, 1092–1097, doi:10.1016/S0960-9822(00)00691-6.

98. Lin, B.; Li, Y.; Han, L.; Kaplan, A.D.; Ao, Y.; Kalra, S.; Bett, G.C.L.; Rasmusson, R.L.; Denning, C.; Yang, L. Modeling and Study of the Mechanism of Dilated Cardiomyopathy Using Induced Pluripotent Stem Cells Derived from Individuals with Duchenne Muscular Dystrophy. *DMM Dis. Model. Mech.* **2015**, *8*, 457–466, doi:10.1242/dmm.019505.

99. Law, M.L.; Cohen, H.; Martin, A.A.; Angulski, A.B.B.; Metzger, J.M. Dysregulation of Calcium Handling in Duchenne Muscular Dystrophy-Associated Dilated Cardiomyopathy: Mechanisms and Experimental Therapeutic Strategies. *J. Clin. Med.* **2020**, *9*, 520, doi:10.3390/jcm9020520.

100. Svobodova, B.; Jelinkova, S.; Pesl, M.; Beckerová, D.; Lacampagne, A.; Meli, A.C.; Rotrekl, V. Cellular Pathology of the Human Heart in Duchenne Muscular Dystrophy (DMD): Lessons Learned from in Vitro Modeling. *Pflügers Arch. - Eur. J. Physiol.* **2021**, *473*, 1099–1115, doi:10.1007/s00424-021-02589-0.

101. Connuck, D.M.; Sleeper, L.A.; Colan, S.D.; Cox, G.F.; Towbin, J.A.; Lowe, A.M.; Wilkinson, J.D.; Orav, E.J.; Cuniberti, L.; Salbert, B.A.; et al. Characteristics and Outcomes of Cardiomyopathy in Children with Duchenne or Becker Muscular Dystrophy: A Comparative Study from the Pediatric Cardiomyopathy Registry. *Am. Heart J.* **2008**, *155*, 998–1005, doi:10.1016/j.ahj.2008.01.018.

102. Rose, E.A.; Gelijns, Annetine C. Moskowitz, A.J.; Heitjan, Daniel F. Stevenson, Lynne W. Dembitsky, W.; Long, J.W.; Ascheim, D.; Tierney, A.; Levitan, R.; Meier, P.; Watson, J. Long-Term Use of a Left Ventricular Assist Device. *N. Engl. J. Med.* **2001**, *345*, 1435–1443.

103. Shah, M.N.A.; Yokota, T. Cardiac Therapies for Duchenne Muscular Dystrophy. *Ther. Adv. Neurol. Disord.* **2023**, *16*, doi:10.1177/17562864231182934.

104. Escolar, D.M.; Hache, L.P.; Clemens, P.R.; Cnaan, A.; McDonald, C.M.; Viswanathan, V.; Kornberg, A.J.; Bertorini, T.E.; Nevo, Y.; Lotze, T.; et al. Randomized, Blinded Trial of Weekend vs Daily Prednisone in Duchenne Muscular Dystrophy. *Neurology* **2011**, *77*, 444–452, doi:10.1212/WNL.0b013e318227b164.

105. Angelini, C.; Peterle, E. Old and New Therapeutic Developments in Steroid Treatment in Duchenne Muscular Dystrophy. *Acta Myol.* 2012, *31*, 9–15.

106. Barber, B.J.; Andrews, J.G.; Lu, Z.; West, N.A.; Meaney, F.J.; Price, E.T.; Gray, A.; Sheehan, D.W.; Pandya, S.; Yang, M.; et al. Oral Corticosteroids and Onset of Cardiomyopathy in Duchenne Muscular Dystrophy. *J. Pediatr.* **2013**, *163*, doi:10.1016/j.jpeds.2013.05.060.

107. Schram, G.; Fournier, A.; Leduc, H.; Dahdah, N.; Therien, J.; Vanasse, M.; Khairy, P. All-Cause Mortality and Cardiovascular Outcomes with Prophylactic Steroid Therapy in Duchenne Muscular Dystrophy. *J. Am. Coll. Cardiol.* **2013**, *61*, 948–954, doi:10.1016/j.jacc.2012.12.008.

108. Markham, L.W.; Michelfelder, E.C.; Border, W.L.; Khoury, P.R.; Spicer, R.L.; Wong, B.L.; Benson, D.W.; Cripe, L.H. Abnormalities of Diastolic Function Precede Dilated Cardiomyopathy Associated with Duchenne Muscular Dystrophy. *J. Am. Soc. Echocardiogr.* **2006**, *19*, 865–871, doi:10.1016/j.echo.2006.02.003.

109. Silversides, C.K.; Webb, G.D.; Harris, V.A.; Biggar, D.W. Effects of Deflazacort on Left Ventricular Function in Patients with Duchenne Muscular Dystrophy. *Am. J. Cardiol.* **2003**, *91*, 769–772, doi:10.1016/S0002-9149(02)03429-X.

110. Spurney, C.; Shimizu, R.; Morgenroth, L.P.; Kolski, H.; Gordish-Dressman, H.; Clemens, P.R. Cooperative

International Neuromuscular Research Group Duchenne Natural History Study Demonstrates Insufficient Diagnosis and Treatment of Cardiomyopathy in Duchenne Muscular Dystrophy. *Muscle Nerve* **2014**, *50*, 250–256, doi:10.1002/mus.24163.

111. Raman, S. V.; Cripe, L.H. Glucocorticoid Therapy for Duchenne Cardiomyopathy: A Hobson's Choice? *J. Am. Heart Assoc.* **2015**, *4*, doi:10.1161/JAHA.115.001896.

112. Markham, L.W.; Kinnett, K.; Wong, B.L.; Woodrow Benson, D.; Cripe, L.H. Corticosteroid Treatment Retards Development of Ventricular Dysfunction in Duchenne Muscular Dystrophy. *Neuromuscul. Disord.* **2008**, *18*, 365–370, doi:10.1016/j.nmd.2008.03.002.

113. Dubinin, M. V.; Talanov, E.Y.; Tenkov, K.S.; Starinets, V.S.; Belosludtseva, N. V.; Belosludtsev, K.N. The Effect of Deflazacort Treatment on the Functioning of Skeletal Muscle Mitochondria in Duchenne Muscular Dystrophy. *Int. J. Mol. Sci.* **2020**, *21*, 1–18, doi:10.3390/ijms21228763.

114. Connolly, A.M.; Zaidman, C.M.; Golumbek, P.T.; Cradock, M.M.; Flanigan, K.M.; Kuntz, N.L.; Finkel, R.S.; McDonald, C.M.; Iannaccone, S.T.; Anand, P.; et al. Twice-Weekly Glucocorticosteroids in Infants and Young Boys with Duchenne Muscular Dystrophy. *Muscle and Nerve* **2019**, *59*, 650–657, doi:10.1002/mus.26441.

115. Quattrocelli, M.; Zelikovich, A.S.; Jiang, Z.; Peek, C.B.; Demonbreun, A.R.; Kuntz, N.L.; Barish, G.D.; Haldar, S.M.; Bass, J.; McNally, E.M. Pulsed Glucocorticoids Enhance Dystrophic Muscle Performance through Epigenetic-Metabolic Reprogramming. *JCI Insight* **2019**, *4*, doi:10.1172/jci.insight.132402.

116. Janssen, P.M.L.; Murray, J.D.; Schill, K.E.; Rastogi, N.; Schultz, E.J.; Tran, T.; Raman, S. V.; Rafael-Fortney, J.A. Prednisolone Attenuates Improvement of Cardiac and Skeletal Contractile Function and Histopathology by Lisinopril and Spironolactone in the Mdx Mouse Model of Duchenne Muscular Dystrophy. *PLoS One* **2014**, *9*, doi:10.1371/journal.pone.0088360.

117. Guerron, A.D.; Rawat, R.; Sali, A.; Spurney, C.F.; Pistilli, E.; Cha, H.J.; Pandey, G.S.; Gernapudi, R.; Francia, D.; Farajian, V.; et al. Functional and Molecular Effects of Arginine Butyrate and Prednisone on Muscle and Heart in the Mdx Mouse Model of Duchenne Muscular Dystrophy. *PLoS One* **2010**, *5*, doi:10.1371/journal.pone.0011220.

118. Bauer, R.; Straub, V.; Blain, A.; Bushby, K.; MacGowan, G.A. Contrasting Effects of Steroids and Angiotensin-Converting-Enzyme Inhibitors in a Mouse Model of Dystrophin-Deficient Cardiomyopathy. *Eur. J. Heart Fail.* **2009**, *11*, 463–471, doi:10.1093/eurjhf/hfp028.

119. Hoffman, E.P.; Reeves, E.; Damsker, J.; Nagaraju, K.; McCall, J.M.; Connor, E.M.; Bushby, K. Novel Approaches to Corticosteroid Treatment in Duchenne Muscular Dystrophy. *Phys. Med. Rehabil. Clin. N. Am.* **2012**, *23*, 821–828, doi:10.1016/j.pmr.2012.08.003.

120. Bylo, M.; Farewell, R.; Coppenrath, V.A.; Yogaratnam, D. A Review of Deflazacort for Patients With Duchenne Muscular Dystrophy. *Ann. Pharmacother.* **2020**, *54*, 788–794, doi:10.1177/1060028019900500.

121. Liu, D.; Ahmet, A.; Ward, L.; Krishnamoorthy, P.; Mandelcorn, E.D.; Leigh, R.; Brown, J.P.; Cohen, A.; Kim, H. A Practical Guide to the Monitoring and Management of the Complications of Systemic Corticosteroid Therapy. *Allergy, Asthma Clin. Immunol.* **2013**, *9*, 30, doi:10.1186/1710-1492-9-30.

122. Dikalov, S.I.; Nazarewicz, R.R. Angiotensin II-Induced Production of Mitochondrial Reactive Oxygen Species: Potential Mechanisms and Relevance for Cardiovascular Disease. *Antioxid. Redox Signal.* **2013**, *19*, 1085–1094, doi:10.1089/ars.2012.4604.

123. Dasgupta, C.; Zhang, L. Angiotensin II Receptors and Drug Discovery in Cardiovascular Disease. *Drug Discov. Today* **2011**, *16*, 22–34, doi:10.1016/j.drudis.2010.11.016.

124. Kawai, T.; Forrester, S.J.; O'Brien, S.; Baggett, A.; Rizzo, V.; Eguchi, S. AT1 Receptor Signaling Pathways in the Cardiovascular System. *Pharmacol. Res.* **2017**, *125*, 4–13, doi:10.1016/j.phrs.2017.05.008.

125. Greenberg, B.H. Role of Angiotensin Receptor Blockers in Heart Failure Not yet RESOLVD. *Circulation*

1999, *100*, 1032–1034.

126. Wagner, S.; Maier, L.S.; Bers, D.M. Role of Sodium and Calcium Dysregulation in Tachyarrhythmias in Sudden Cardiac Death. *Circ. Res.* **2015**, *116*, 1956–1970, doi:10.1161/CIRCRESAHA.116.304678.

127. Viollet, L.; Thrush, P.T.; Flanigan, K.M.; Mendell, J.R.; Allen, H.D. Effects of Angiotensin-Converting Enzyme Inhibitors and/or Beta Blockers on the Cardiomyopathy in Duchenne Muscular Dystrophy. *Am. J. Cardiol.* **2012**, *110*, 98–102, doi:10.1016/j.amjcard.2012.02.064.

128. Spurney, C.F.; Ascheim, D.; Charnas, L.; Cripe, L.; Hor, K.; King, N.; Kinnett, K.; McNally, E.M.; Sauer, J.-M.; Sweeney, L.; et al. Current State of Cardiac Troponin Testing in Duchenne Muscular Dystrophy Cardiomyopathy: Review and Recommendations from the Parent Project Muscular Dystrophy Expert Panel. *Open Hear.* **2021**, *8*, e001592, doi:10.1136/openhrt-2021-001592.

129. Rittoo, D.; Jones, A.; Lecky, B.; Neithercut, D. Elevation of Cardiac Troponin T, but Not Cardiac Troponin I, in Patients with Neuromuscular Diseases: Implications for the Diagnosis of Myocardial Infarction. *J. Am. Coll. Cardiol.* **2014**, *63*, 2411–2420, doi:10.1016/j.jacc.2014.03.027.

130. Wens, S.C.A.; Schaaf, G.J.; Michels, M.; Kruijshaar, M.E.; Van Gestel, T.J.M.; In 'T Groen, S.; Pijnenburg, J.; Dekkers, D.H.W.; Demmers, J.A.A.; Verdijk, L.B.; et al. Elevated Plasma Cardiac Troponin T Levels Caused by Skeletal Muscle Damage in Pompe Disease. *Circ. Cardiovasc. Genet.* **2016**, *9*, 6–13, doi:10.1161/CIRCGENETICS.115.001322.

131. Schmid, J.; Liesinger, L.; Birner-Gruenberger, R.; Stojakovic, T.; Scharnagl, H.; Dieplinger, B.; Asslaber, M.; Radl, R.; Beer, M.; Polacin, M.; et al. Elevated Cardiac Troponin T in Patients With Skeletal Myopathies. *J. Am. Coll. Cardiol.* **2018**, *71*, 1540–1549, doi:10.1016/j.jacc.2018.01.070.

132. Bodor, G.S.; Porterfield, D.; Voss, E.M.; Smith, S.; Apple, F.S. Cardiac Troponin-I Is Not Expressed in Fetal and Healthy or Diseased Adult Human Skeletal Muscle Tissue. *Clin. Chem.* **1995**, *41*, 1710–1715, doi:10.1093/clinchem/41.12.1710.

133. Abutaleb, A.R.A.; McNally, E.M.; Khan, S.S.; Anderson, A.S.; Carr, J.C.; Wilcox, J.E. Myocarditis in Duchenne Muscular Dystrophy After Changing Steroids. *JAMA Cardiol.* **2018**, *3*, 1006, doi:10.1001/jamacardio.2018.2695.

134. Hor, K.N.; Mah, M.L.; Johnston, P.; Cripe, T.P.; Cripe, L.H. Advances in the Diagnosis and Management of Cardiomyopathy in Duchenne Muscular Dystrophy. *Neuromuscul. Disord.* **2018**, *28*, 711–716, doi:10.1016/j.nmd.2018.06.014.

135. Cinteza, E.; Stoicescu, C.; Butoianu, N.; Balgradean, M.; Nicolescu, A.; Angrés, M. Acute Myocardial Injury in a Child with Duchenne Muscular Dystrophy: Pulse Steroid Therapy? *Maedica (Buchar).* **2017**, *12*, 180–183.

136. Cuccia, C.; Benedini, G.; Leonzi, O.; Pagnoni, N.; Giubbini, R. Infarto Acuto Del Miocardio in Un Tredicenne Con Malattia Di Duchenne. *G. Ital. Cardiol.* **1984**, *14*, 817–820.

137. Politano, L.; Palladino, A.; Petretta, V.R.; Mansi, L.; Passamano, L.; Nigro, G.; Comi, L.I.; Nigro, G. ST-Segment Displacement in Duchenne Muscular Dystrophy: Myocardial Necrosis or Apoptosis? *Acta Myol.* **2003**, *22*, 5–10.

138. Schoeffler, M.; Wallet, F.; Robert, M.O.; Tramoni, G.; Workineh, S.; Viale, J.P.; Duperret, S. Increased Troponin I Level in a Duchenne Muscular Dystrophy Patient with Normal Coronarography. *Ann. Fr. Anesth. Reanim.* **2008**, *27*, 345–347, doi:10.1016/j.annfar.2008.01.006.

139. Voleti, S.; Olivieri, L.; Hamann, K.; Gordish-Dressman, H.; Spurney, C. Troponin I Levels Correlate with Cardiac MR LGE and Native T1 Values in Duchenne Muscular Dystrophy Cardiomyopathy and Identify Early Disease Progression. *Pediatr. Cardiol.* **2020**, *41*, 1173–1179, doi:10.1007/s00246-020-02372-5.

140. Townsend, D.W.; Turner, I.; Yasuda, S.; Martindale, J.; Davis, J.; Shillingford, M.; Kornegay, J.N.; Metzger, J.M. Chronic Administration of Membrane Sealant Prevents Severe Cardiac Injury and Ventricular

Dilatation in Dystrophic Dogs. *J. Clin. Invest.* **2010**, *120*, 1140–1150, doi:10.1172/JCI41329.

141. Dittrich, S.; Tuerk, M.; Haaker, G.; Greim, V.; Buchholz, A.; Burkhardt, B.; Fujak, A.; Trollmann, R.; Schmid, A.; Schroeder, R. Cardiomyopathy in Duchenne Muscular Dystrophy: Current Value of Clinical, Electrophysiological and Imaging Findings in Children and Teenagers. *Klin. Pädiatrie* **2015**, *227*, 225–231, doi:10.1055/s-0034-1398689.

142. Demachi, J.; Kagaya, Y.; Watanabe, J.; Sakuma, M.; Ikeda, J.; Kakuta, Y.; Motoyoshi, I.; Kohnosu, T.; Sakuma, H.; Shimazaki, S.; et al. Characteristics of the Increase in Plasma Brain Natriuretic Peptide Level in Left Ventricular Systolic Dysfunction, Associated with Muscular Dystrophy in Comparison with Idiopathic Dilated Cardiomyopathy. *Neuromuscul. Disord.* **2004**, *14*, 732–739, doi:10.1016/j.nmd.2004.08.002.

143. Mohyuddin, T.; Jacobs, I.B.; Bahler, R.C. B-Type Natriuretic Peptide and Cardiac Dysfunction in Duchenne Muscular Dystrophy. *Int. J. Cardiol.* **2007**, *119*, 389–391, doi:10.1016/j.ijcard.2006.07.163.

144. Van Bockel, E.A.P.; Lind, J.S.; Zijlstra, J.G.; Wijkstra, P.J.; Meijer, P.M.; Van Den Berg, M.P.; Slart, R.H.J.A.; Aarts, L.P.H.J.; Tulleken, J.E. Cardiac Assessment of Patients with Late Stage Duchenne Muscular Dystrophy. *Netherlands Hear. J.* **2009**, *17*, 232–237, doi:10.1007/BF03086253.

145. Yanagisawa, A.; Yokota, N.; Miyagawa, M.; Kawamura, J.; Ishihara, T.; Aoyagi, T.; Ishikawa, K. Plasma Levels of Atrial Natriuretic Peptide in Patients with Duchenne's Progressive Muscular Dystrophy. *Am. Heart J.* **1990**, *120*, 1154–1158, doi:10.1016/0002-8703(90)90130-P.

146. Wang, H.; Liu, S.; Xing, Y.L.; Chen, R.; Yu, X.Y. The Limitation of MB Isoenzyme of Creatine Kinase Mass in Assess Myocardial Injury with Muscular Disease. *Chinese Crit. Care Med.* **2011**, *23*, 723–726, doi:10.3760/cma.j.issn.1003-0603.2011.12.005.

147. Su, J.A.; Ramos-Platt, L.; Menteer, J. Left Ventricular Tonic Contraction as a Novel Biomarker of Cardiomyopathy in Duchenne Muscular Dystrophy. *Pediatr. Cardiol.* **2016**, *37*, 678–685, doi:10.1007/s00246-015-1331-1.

148. Greally, E.; Davison, B.J.; Blain, A.; Laval, S.; Blamire, A.; Straub, V.; MacGowan, G.A. Heterogeneous Abnormalities of In-Vivo Left Ventricular Calcium Influx and Function in Mouse Models of Muscular Dystrophy Cardiomyopathy. *J. Cardiovasc. Magn. Reson.* **2013**, *15*, doi:10.1186/1532-429X-15-4.

149. Townsend, D.; Yasuda, S.; McNally, E.; Metzger, J.M. Distinct Pathophysiological Mechanisms of Cardiomyopathy in Hearts Lacking Dystrophin or the Sarcoglycan Complex. *FASEB J.* **2011**, *25*, 3106–3114, doi:10.1096/fj.10-178913.

150. Wagner, S.; Knipp, S.; Weber, C.; Hein, S.; Schinkel, S.; Walther, A.; Bekeredjian, R.; Müller, O.J.; Friedrich, O. The Heart in Duchenne Muscular Dystrophy: Early Detection of Contractile Performance Alteration. *J. Cell. Mol. Med.* **2012**, *16*, 3028–3036, doi:10.1111/j.1582-4934.2012.01630.x.

151. Batra, A.; Barnard, A.M.; Lott, D.J.; Willcocks, R.J.; Forbes, S.C.; Chakraborty, S.; Daniels, M.J.; Arbogast, J.; Triplett, W.; Henricson, E.K.; et al. Longitudinal Changes in Cardiac Function in Duchenne Muscular Dystrophy Population as Measured by Magnetic Resonance Imaging. *BMC Cardiovasc. Disord.* **2022**, *22*, doi:10.1186/s12872-022-02688-5.

152. Amedro, P.; Vincenti, M.; De La Villeon, G.; Lavastre, K.; Barrea, C.; Guillaumont, S.; Bredy, C.; Gamon, L.; Meli, A.C.; Cazorla, O.; et al. Speckle-Tracking Echocardiography in Children With Duchenne Muscular Dystrophy: A Prospective Multicenter Controlled Cross-Sectional Study. *J. Am. Soc. Echocardiogr.* **2019**, *32*, 412–422, doi:10.1016/j.echo.2018.10.017.

153. Dual, S.A.; Maforo, N.G.; McElhinney, D.B.; Prosper, A.; Wu, H.H.; Maskatia, S.; Renella, P.; Halnon, N.; Ennis, D.B. Right Ventricular Function and T1 Mapping in Boys With Duchenne Muscular Dystrophy. *J. Magn. Reson. Imaging* **2021**, *54*, 1503–1513, doi:10.1002/jmri.27729.

154. Panovský, R.; Pešl, M.; Máchal, J.; Holeček, T.; Feitová, V.; Juříková, L.; Masárová, L.; Pešlová, E.; Opatřil, L.; Mojica-Pisciotti, M.L.; et al. Quantitative Assessment of Left Ventricular Longitudinal Function and Myocardial Deformation in Duchenne Muscular Dystrophy Patients. *Orphanet J. Rare Dis.* **2021**, *16*,

doi:10.1186/s13023-021-01704-9.

155. Wynn, T.A. Cellular and Molecular Mechanisms of Fibrosis. *J. Pathol.* 2008.

156. Travers, J.G.; Kamal, F.A.; Robbins, J.; Yutzey, K.E.; Blaxall, B.C. Cardiac Fibrosis: The Fibroblast Awakens. *Circ. Res.* 2016.

157. Finsterer, J.; Stöllberger, C. The Heart in Human Dystrophinopathies. *Cardiology* **2003**, *99*, 1–19, doi:10.1159/000068446.

158. Goodwin, F.C.; Muntoni, F. Cardiac Involvement in Muscular Dystrophies: Molecular Mechanisms. *Muscle Nerve* **2005**, *32*, 577–588, doi:10.1002/mus.20352.

159. Perloff, J.K.; Roberts, W.C.; de Leon, A.C.; O'Doherty, D. The Distinctive Electrocardiogram of Duchenne's Progressive Muscular Dystrophy. An Electrocardiographic-Pathologic Correlative Study. *Am. J. Med.* **1967**, *42*, 179–188, doi:10.1016/0002-9343(67)90017-4.

160. Schneider, S.M.; Sansom, G.T.; Guo, L.J.; Furuya, S.; Weeks, B.R.; Kornegay, J.N. Natural History of Histopathologic Changes in Cardiomyopathy of Golden Retriever Muscular Dystrophy. *Front. Vet. Sci.* **2022**, *8*, doi:10.3389/fvets.2021.759585.

161. Sanyal, S.K.; Johnson, W.W.; Dische, M.R.; Pitner, S.E.; Beard, C. Dystrophic Degeneration of Papillary Muscle and Ventricular Myocardium. A Basis for Mitral Valve Prolapse in Duchenne's Muscular Dystrophy. *Circulation* **1980**, *62*, 430–438, doi:10.1161/01.CIR.62.2.430.

162. Mertens, L.; Ganame, J.; Claus, P.; Goemans, N.; Thijs, D.; Eyskens, B.; Van Laere, D.; Bijnens, B.; D'hooge, J.; Sutherland, G.R.; et al. Early Regional Myocardial Dysfunction in Young Patients With Duchenne Muscular Dystrophy. *J. Am. Soc. Echocardiogr.* **2008**, *21*, 1049–1054, doi:10.1016/j.echo.2008.03.001.

163. Hor, K.N.; Taylor, M.D.; Al-Khalidi, H.R.; Cripe, L.H.; Raman, S. V.; Jefferies, J.L.; O'Donnell, R.; Benson, D.W.; Mazur, W. Prevalence and Distribution of Late Gadolinium Enhancement in a Large Population of Patients with Duchenne Muscular Dystrophy: Effect of Age and Left Ventricular Systolic Function. *J. Cardiovasc. Magn. Reson.* **2013**, *15*, 107, doi:10.1186/1532-429X-15-107.

164. Buddhe, S.; Lewin, M.; Olson, A.; Ferguson, M.; Soriano, B.D. Comparison of Left Ventricular Function Assessment between Echocardiography and MRI in Duchenne Muscular Dystrophy. *Pediatr. Radiol.* **2016**, *46*, 1399–1408, doi:10.1007/s00247-016-3622-y.

165. Magrath, P.; Maforo, N.; Renella, P.; Nelson, S.F.; Halnon, N.; Ennis, D.B. Cardiac MRI Biomarkers for Duchenne Muscular Dystrophy. *Biomark. Med.* **2018**, *12*, 1271–1289, doi:10.2217/bmm-2018-0125.

166. De Giorgio, D.; Novelli, D.; Motta, F.; Cerrato, M.; Olivari, D.; Salama, A.; Fumagalli, F.; Latini, R.; Staszewsky, L.; Crippa, L.; et al. Characterization of the Cardiac Structure and Function of Conscious D2.B10-Dmdmdx/J (D2-Mdx) Mice from 16-17 to 24-25 Weeks of Age. *Int. J. Mol. Sci.* **2023**, *24*, 11805, doi:10.3390/ijms241411805.

167. Li, Y.; Zhang, S.; Zhang, X.; Li, J.; Ai, X.; Zhang, L.; Yu, D.; Ge, S.; Peng, Y.; Chen, X. Blunted Cardiac Beta-Adrenergic Response as an Early Indication of Cardiac Dysfunction in Duchenne Muscular Dystrophy. *Cardiovasc. Res.* **2014**, doi:10.1093/cvr/cvu119.

168. Farini, A.; Gowran, A.; Bella, P.; Sitzia, C.; Scopece, A.; Castiglioni, E.; Rovina, D.; Nigro, P.; Villa, C.; Fortunato, F.; et al. Fibrosis Rescue Improves Cardiac Function in Dystrophin-Deficient Mice and Duchenne Patient–Specific Cardiomyocytes by Immunoproteasome Modulation. *Am. J. Pathol.* **2019**, doi:10.1016/j.ajpath.2018.10.010.

169. Wehling-Henricks, M.; Jordan, M.C.; Gotoh, T.; Grody, W.W.; Roos, K.P.; Tidball, J.G. Arginine Metabolism by Macrophages Promotes Cardiac and Muscle Fibrosis in Mdx Muscular Dystrophy. *PLoS One* **2010**, doi:10.1371/journal.pone.0010763.

170. Spurney, C.F.; Sali, A.; Guerron, A.D.; Iantorno, M.; Yu, Q.; Gordish-Dressman, H.; Rayavarapu, S.; Van

Der Meulen, J.; Hoffman, E.P.; Nagaraju, K. Losartan Decreases Cardiac Muscle Fibrosis and Improves Cardiac Function in Dystrophin-Deficient Mdx Mice. *J. Cardiovasc. Pharmacol. Ther.* **2011**, doi:10.1177/1074248410381757.

171. Mehmood, M.; Hor, K.N.; Al-Khalidi, H.R.; Benson, D.W.; Jefferies, J.L.; Taylor, M.D.; Egnaczyk, G.F.; Raman, S. V.; Basu, S.K.; Cripe, L.H.; et al. Comparison of Right and Left Ventricular Function and Size in Duchenne Muscular Dystrophy. *Eur. J. Radiol.* **2015**, *84*, 1938–1942, doi:10.1016/j.ejrad.2015.07.007.

172. Shih, J.A.; Folch, A.; Wong, B.L. Duchenne Muscular Dystrophy: The Heart of the Matter. *Curr. Heart Fail. Rep.* **2020**, *17*, 57–66, doi:10.1007/s11897-020-00456-0.

173. Koenig, X.; Ebner, J.; Hilber, K. Voltage-Dependent Sarcolemmal Ion Channel Abnormalities in the Dystrophin-Deficient Heart. *Int. J. Mol. Sci.* **2018**, *19*, 3296, doi:10.3390/ijms19113296.

174. Segawa, K.; Komaki, H.; Mori-Yoshimura, M.; Oya, Y.; Kimura, K.; Tachimori, H.; Kato, N.; Sasaki, M.; Takahashi, Y. Cardiac Conduction Disturbances and Aging in Patients with Duchenne Muscular Dystrophy. *Med. (United States)* **2017**, *96*, doi:10.1097/MD.0000000000008335.

175. Corrado, G.; Lissoni, A.; Beretta, S.; Terenghi, L.; Tadeo, G.; Foglia-Manzillo, G.; Tagliagambe, L.M.; Spata, M.; Santarone, M. Prognostic Value of Electrocardiograms, Ventricular Late Potentials, Ventricular Arrhythmias, and Left Ventricular Systolic Dysfunction in Patients with Duchenne Muscular Dystrophy. *Am. J. Cardiol.* **2002**, *89*, 838–841, doi:10.1016/S0002-9149(02)02195-1.

176. Chiang, D.Y.; Allen, H.D.; Kim, J.J.; Valdes, S.O.; Wang, Y.; Pignatelli, R.H.; Lotze, T.E.; Miyake, C.Y. Relation of Cardiac Dysfunction to Rhythm Abnormalities in Patients with Duchenne or Becker Muscular Dystrophies. *Am. J. Cardiol.* **2016**, *117*, 1349–1354, doi:10.1016/j.amjcard.2016.01.031.

177. Villa, C.R.; Czosek, R.J.; Ahmed, H.; Khoury, P.R.; Anderson, J.B.; Knilans, T.K.; Jefferies, J.L.; Wong, B.; Spar, D.S. Ambulatory Monitoring and Arrhythmic Outcomes in Pediatric and Adolescent Patients with Duchenne Muscular Dystrophy. *J. Am. Heart Assoc.* **2016**, *5*, doi:10.1161/JAHA.115.002620.

178. Groh, W.J. Arrhythmias in the Muscular Dystrophies. *Hear. Rhythm* **2012**, *9*, 1890–1895, doi:10.1016/j.hrthm.2012.06.038.

179. Santos, M.A.B.; Costa, F.D.A.; Travessa, A.F.; Bombig, M.T.N.; Fonseca, F.H.; Luna Filho, B.; Mussi, A.; Souza, D. De; Oliveira, A. De; Povoa, R. Distrofia Muscular de Duchenne: Análise Eletrocardiográfica de 131 Pacientes. *Arq. Bras. Cardiol.* **2010**, *94*, 620–624, doi:10.1590/S0066-782X2010005000024.

180. Shah, A.M.; Jefferies, J.L.; Rossano, J.W.; Decker, J.A.; Cannon, B.C.; Kim, J.J. Electrocardiographic Abnormalities and Arrhythmias Are Strongly Associated with the Development of Cardiomyopathy in Muscular Dystrophy. *Hear. Rhythm* **2010**, *7*, 1484–1488, doi:10.1016/j.hrthm.2010.06.022.

181. Thrush, P.T.; Allen, H.D.; Viollet, L.; Mendell, J.R. Re-Examination of the Electrocardiogram in Boys With Duchenne Muscular Dystrophy and Correlation With Its Dilated Cardiomyopathy. *Am. J. Cardiol.* **2009**, *103*, 262–265, doi:10.1016/j.amjcard.2008.08.064.

182. Bosser, G.; Lucron, H.; Lethor, J.P.; Burger, G.; Beltramo, F.; Marie, P.Y.; Marçon, F. Evidence of Early Impairments in Both Right and Left Ventricular Inotropic Reserves in Children with Duchenne's Muscular Dystrophy. *Am. J. Cardiol.* **2004**, *93*, 724–727, doi:10.1016/j.amjcard.2003.12.005.

183. Mehmood, M.; Ambach, S.A.; Taylor, M.D.; Jefferies, J.L.; Raman, S. V.; Taylor, R.J.; Sawnani, H.; Mathew, J.; Mazur, W.; Hor, K.N.; et al. Erratum to: Relationship of Right Ventricular Size and Function with Respiratory Status in Duchenne Muscular Dystrophy. *Pediatr. Cardiol.* **2016**, *37*, 989–989, doi:10.1007/s00246-016-1388-5.

184. Meyers, T.A.; Townsend, D. Early Right Ventricular Fibrosis and Reduction in Biventricular Cardiac Reserve in the Dystrophin-Deficient Mdx Heart. *Am. J. Physiol. - Hear. Circ. Physiol.* **2015**, *308*, H303–H315, doi:10.1152/ajpheart.00485.2014.

185. Stuckey, D.J.; Carr, C.A.; Camelliti, P.; Tyler, D.J.; Davies, K.E.; Clarke, K. In Vivo MRI Characterization

of Progressive Cardiac Dysfunction in the Mdx Mouse Model of Muscular Dystrophy. *PLoS One* **2012**, *7*, doi:10.1371/journal.pone.0028569.

186. Kanisicak, O.; Khalil, H.; Ivey, M.J.; Karch, J.; Maliken, B.D.; Correll, R.N.; Brody, M.J.; Lin, S.C.J.; Aronow, B.J.; Tallquist, M.D.; et al. Genetic Lineage Tracing Defines Myofibroblast Origin and Function in the Injured Heart. *Nat. Commun.* **2016**, *7*, doi:10.1038/ncomms12260.

187. Borthwick, L.A.; Wynn, T.A.; Fisher, A.J. Cytokine Mediated Tissue Fibrosis. *Biochim. Biophys. Acta - Mol. Basis Dis.* **2013**, *1832*, 1049–1060, doi:10.1016/j.bbadis.2012.09.014.

188. Bernasconi, P.; Torchiana, E.; Confalonieri, P.; Brugnoni, R.; Barresi, R.; Mora, M.; Cornelio, F.; Morandi, L.; Mantegazza, R. Expression of Transforming Growth Factor-B1 in Dystrophic Patient Muscles Correlates with Fibrosis: Pathogenetic Role of a Fibrogenic Cytokine. *J. Clin. Invest.* **1995**, *96*, 1137–1144, doi:10.1172/jci118101.

189. Spencer, M.J.; Walsh, C.M.; Dorshkind, K.A.; Rodriguez, E.M.; Tidball, J.G. Myonuclear Apoptosis in Dystrophic Mdx Muscle Occurs by Perforin-Mediated Cytotoxicity. *J. Clin. Invest.* **1997**, *99*, 2745–2751, doi:10.1172/JCI119464.

190. Evans, N.P.; Misyak, S.A.; Robertson, J.L.; Bassaganya-Riera, J.; Grange, R.W. Immune-Mediated Mechanisms Potentially Regulate the Disease Time-Course of Duchenne Muscular Dystrophy and Provide Targets for Therapeutic Intervention. *PM&R* **2009**, *1*, 755–768, doi:10.1016/j.pmrj.2009.04.010.

191. Spencer, M.J.; Montecino-Rodriguez, E.; Dorshkind, K.; Tidball, J.G. Helper (CD4+) and Cytotoxic (CD8+) T Cells Promote the Pathology of Dystrophin-Deficient Muscle. *Clin. Immunol.* **2001**, *98*, 235–243, doi:10.1006/clim.2000.4966.

192. Mojumdar, K.; Liang, F.; Giordano, C.; Lemaire, C.; Danialou, G.; Okazaki, T.; Bourdon, J.; Rafei, M.; Galipeau, J.; Divangahi, M.; et al. Inflammatory Monocytes Promote Progression of Duchenne Muscular Dystrophy and Can Be Therapeutically Targeted via CCR 2. *EMBO Mol. Med.* **2014**, *6*, 1476–1492, doi:10.15252/emmm.201403967.

193. Gorospe, J.R.M.; Tharp, M.; Demitsu, T.; Hoffman, E.P. Dystrophin-Deficient Myofibers Are Vulnerable to Mast Cell Granule-Induced Necrosis. *Neuromuscul. Disord.* **1994**, *4*, 325–333, doi:10.1016/0960-8966(94)90068-X.

194. Cai, B.; Spencer, M.J.; Nakamura, G.; Tseng-Ong, L.; Tidball, J.G. Eosinophilia of Dystrophin-Deficient Muscle Is Promoted by Perforin-Mediated Cytotoxicity by T Cell Effectors. *Am. J. Pathol.* **2000**, *156*, 1789–1796, doi:10.1016/S0002-9440(10)65050-X.

195. Kumar, A.; Boriek, A.M. Mechanical Stress Activates the Nuclear Factor-kappaB Pathway in Skeletal Muscle Fibers: A Possible Role in Duchenne Muscular Dystrophy. *FASEB J.* **2003**, *17*, 386–396, doi:10.1096/fj.02-0542com.

196. Wehling, M.; Spencer, M.J.; Tidball, J.G. A Nitric Oxide Synthase Transgene Ameliorates Muscular Dystrophy in Mdx Mice. *J. Cell Biol.* **2001**, *155*, 123–131, doi:10.1083/jcb.200105110.

197. Delfín, D.A.; Xu, Y.; Peterson, J.M.; Guttridge, D.C.; Rafael-Fortney, J.A.; Janssen, P.M.L. Improvement of Cardiac Contractile Function by Peptide-Based Inhibition of NF-KB in the Utrophin/Dystrophin-Deficient Murine Model of Muscular Dystrophy. *J. Transl. Med.* **2011**, *9*, doi:10.1186/1479-5876-9-68.

198. Pelosi, L.; Berardinelli, M.G.; Forcina, L.; Spelta, E.; Rizzuto, E.; Nicoletti, C.; Camilli, C.; Testa, E.; Catizone, A.; De Benedetti, F.; et al. Increased Levels of Interleukin-6 Exacerbate the Dystrophic Phenotype in Mdx Mice. *Hum. Mol. Genet.* **2015**, *24*, 6041–6053, doi:10.1093/hmg/ddv323.

199. Messina, S.; Vita, G.L.; Aguennouz, M.; Sframeli, M.; Romeo, S.; Rodolico, C.; Vita, G. Activation of NF-KB Pathway in Duchenne Muscular Dystrophy: Relation to Age. *Acta Myol.* **2011**, *30*, 16–23.

200. Rufo, A.; Del Fattore, A.; Capulli, M.; Carvello, F.; De Pasquale, L.; Ferrari, S.; Pierroz, D.; Morandi, L.; De Simone, M.; Rucci, N.; et al. Mechanisms Inducing Low Bone Density in Duchenne Muscular

Dystrophy in Mice and Humans. *J. Bone Miner. Res.* **2011**, *26*, 1891–1903, doi:10.1002/jbmr.410.

201. Doll, D.N.; Rellick, S.L.; Barr, T.L.; Ren, X.; Simpkins, J.W. Rapid Mitochondrial Dysfunction Mediates TNF-Alpha-Induced Neurotoxicity. *J. Neurochem.* **2015**, *132*, 443–451, doi:10.1111/jnc.13008.

202. Morgan, M.J.; Kim, Y.S.; Liu, Z.G. TNFα and Reactive Oxygen Species in Necrotic Cell Death. *Cell Res.* **2008**, *18*, 343–349, doi:10.1038/cr.2008.31.

203. Valle, M.L.; Dworshak, J.; Sharma, A.; Ibrahim, A.S.; Al-Shabrawey, M.; Sharma, S. Inhibition of Interleukin-6 Trans-Signaling Prevents Inflammation and Endothelial Barrier Disruption in Retinal Endothelial Cells. *Exp. Eye Res.* **2019**, *178*, 27–36, doi:10.1016/j.exer.2018.09.009.

204. Viola, H.M.; Adams, A.M.; Davies, S.M.K.; Fletcher, S.; Filipovska, A.; Hool, L.C. Impaired Functional Communication between the L-Type Calcium Channel and Mitochondria Contributes to Metabolic Inhibition in the Mdx Heart. *Proc. Natl. Acad. Sci. U. S. A.* **2014**, *111*, doi:10.1073/pnas.1402544111.

205. Yasuda, S.; Townsend, D.W.; Michele, D.E.; Favre, E.G.; Day, S.M.; Metzger, J.M. Dystrophic Heart Failure Blocked by Membrane Sealant Poloxamer. *Nature* **2005**, *436*, 1025–1029, doi:10.1038/nature03844.

206. Meyers, T.A.; Townsend, D. Cardiac Pathophysiology and the Future of Cardiac Therapies in Duchenne Muscular Dystrophy. *Int. J. Mol. Sci.* **2019**, *20*, 4098, doi:10.3390/ijms20174098.

207. Feng, J.; Schaus, B.J.; Fallavollita, J.A.; Lee, T.C.; Canty, J. Preload Induces Troponin I Degradation Independently of Myocardial Ischemia. *Circulation* **2001**, *103*, 2035–2037, doi:10.1161/01.CIR.103.16.2035.

208. Spencer, M.J.; Croall, D.E.; Tidball, J.G. Calpains Are Activated in Necrotic Fibers from Mdx Dystrophic Mice. *J. Biol. Chem.* **1995**, *270*, 10909–10914, doi:10.1074/jbc.270.18.10909.

209. Johnstone, V.P.A.; Viola, H.M.; Hool, L.C. Dystrophic Cardiomyopathy—Potential Role of Calcium in Pathogenesis, Treatment and Novel Therapies. *Genes (Basel).* **2017**, *8*, 108, doi:10.3390/genes8040108.

210. Allen, D.G.; Whitehead, N.P. Duchenne Muscular Dystrophy – What Causes the Increased Membrane Permeability in Skeletal Muscle? *Int. J. Biochem. Cell Biol.* **2011**, *43*, 290–294, doi:10.1016/j.biocel.2010.11.005.

211. Lorin, C.; Vögeli, I.; Niggli, E. Dystrophic Cardiomyopathy: Role of TRPV2 Channels in Stretch-Induced Cell Damage. *Cardiovasc. Res.* **2015**, *106*, 153–162, doi:10.1093/cvr/cvv021.

212. Allen, D.G.; Whitehead, N.P.; Yeung, E.W. Mechanisms of Stretch-induced Muscle Damage in Normal and Dystrophic Muscle: Role of Ionic Changes. *J. Physiol.* **2005**, *567*, 723–735, doi:10.1113/jphysiol.2005.091694.

213. Cserne Szappanos, H.; Muralidharan, P.; Ingley, E.; Petereit, J.; Millar, H.A.; Hool, L.C. Identification of a Novel CAMP Dependent Protein Kinase A Phosphorylation Site on the Human Cardiac Calcium Channel. *Sci. Rep.* **2017**, *7*, doi:10.1038/s41598-017-15087-0.

214. Muralidharan, P.; Cserne Szappanos, H.; Ingley, E.; Hool, L.C. The Cardiac L-Type Calcium Channel Alpha Subunit Is a Target for Direct Redox Modification during Oxidative Stress—the Role of Cysteine Residues in the Alpha Interacting Domain. *Clin. Exp. Pharmacol. Physiol.* **2017**, *44*, 46–54, doi:10.1111/1440-1681.12750.

215. Viola, H.M.; Arthur, P.G.; Hool, L.C. Evidence for Regulation of Mitochondrial Function by the L-Type Ca2+ Channel in Ventricular Myocytes. *J. Mol. Cell. Cardiol.* **2009**, *46*, 1016–1026, doi:10.1016/j.yjmcc.2008.12.015.

216. Koenig, X.; Rubi, L.; Obermair, G.J.; Cervenka, R.; Dang, X.B.; Lukacs, P.; Kummer, S.; Bittner, R.E.; Kubista, H.; Todt, H.; et al. Enhanced Currents through L-Type Calcium Channels in Cardiomyocytes Disturb the Electrophysiology of the Dystrophic Heart. *Am. J. Physiol. Circ. Physiol.* **2014**, *306*, H564–H573, doi:10.1152/ajpheart.00441.2013.

217. Andersson, D.C.; Marks, A.R. Fixing Ryanodine Receptor Ca2+ Leak – a Novel Therapeutic Strategy for Contractile Failure in Heart and Skeletal Muscle. *Drug Discov. Today Dis. Mech.* **2010**, *7*, e151–e157, doi:10.1016/j.ddmec.2010.09.009.

218. Fauconnier, J.; Thireau, J.; Reiken, S.; Cassan, C.; Richard, S.; Matecki, S.; Marks, A.R.; Lacampagne, A. Leaky RyR2 Trigger Ventricular Arrhythmias in Duchenne Muscular Dystrophy. *Proc. Natl. Acad. Sci. U. S. A.* **2010**, *107*, 1559–1564, doi:10.1073/pnas.0908540107.

219. Bellinger, A.M.; Reiken, S.; Carlson, C.; Mongillo, M.; Liu, X.; Rothman, L.; Matecki, S.; Lacampagne, A.; Marks, A.R. Hypernitrosylated Ryanodine Receptor Calcium Release Channels Are Leaky in Dystrophic Muscle. *Nat. Med.* **2009**, *15*, 325–330, doi:10.1038/nm.1916.

220. Rohman, M.S.; Emoto, N.; Takeshima, Y.; Yokoyama, M.; Matsuo, M. Decreased MAKAP, Ryanodine Receptor, and SERCA2a Gene Expression in Mdx Hearts. *Biochem. Biophys. Res. Commun.* **2003**, *310*, 228–235, doi:10.1016/j.bbrc.2003.09.005.

221. Voit, A.; Patel, V.; Pachon, R.; Shah, V.; Bakhutma, M.; Kohlbrenner, E.; McArdle, J.J.; Dell'Italia, L.J.; Mendell, J.R.; Xie, L.-H.; et al. Reducing Sarcolipin Expression Mitigates Duchenne Muscular Dystrophy and Associated Cardiomyopathy in Mice. *Nat. Commun.* **2017**, *8*, 1068, doi:10.1038/s41467-017-01146-7.

222. Kranias, E.G.; Hajjar, R.J. Modulation of Cardiac Contractility by the Phopholamban/SERCA2a Regulatome. *Circ. Res.* **2012**, *110*, 1646–1660, doi:10.1161/CIRCRESAHA.111.259754.

223. MacLennan, D.H.; Kranias, E.G. Phospholamban: A Crucial Regulator of Cardiac Contractility. *Nat. Rev. Mol. Cell Biol.* **2003**, *4*, 566–577, doi:10.1038/nrm1151.

224. Mijares, A.; Altamirano, F.; Kolster, J.; Adams, J.A.; López, J.R. Age-Dependent Changes in Diastolic Ca2+ and Na+ Concentrations in Dystrophic Cardiomyopathy: Role of Ca2+ Entry and IP3. *Biochem. Biophys. Res. Commun.* **2014**, *452*, 1054–1059, doi:10.1016/j.bbrc.2014.09.045.

225. Boittin, F.X.; Petermann, O.; Hirn, C.; Mittaud, P.; Dorchies, O.M.; Roulet, E.; Ruegg, U.T. Ca2+-Independent Phospholipase A2 Enhances Store-Operated Ca2+ Entry in Dystrophic Skeletal Muscle Fibers. *J. Cell Sci.* **2006**, *119*, 3733–3742, doi:10.1242/jcs.03184.

226. Lindahl, M.; Backman, E.; Henriksson, K.G.; Gorospe, J.R.; Hoffman, E.P. Phospholipase A2 Activity in Dystrophinopathies. *Neuromuscul. Disord.* **1995**, *5*, 193–199, doi:10.1016/0960-8966(94)00045-B.

227. Kyrychenko, V.; Poláková, E.; Janíček, R.; Shirokova, N. Mitochondrial Dysfunctions during Progression of Dystrophic Cardiomyopathy. *Cell Calcium* **2015**, *58*, 186–195, doi:10.1016/j.ceca.2015.04.006.

228. Dubinin, M. V.; Talanov, E.Y.; Tenkov, K.S.; Starinets, V.S.; Mikheeva, I.B.; Belosludtsev, K.N. Transport of Ca2+ and Ca2+-Dependent Permeability Transition in Heart Mitochondria in the Early Stages of Duchenne Muscular Dystrophy. *Biochim. Biophys. Acta - Bioenerg.* **2020**, *1861*, doi:10.1016/j.bbabio.2020.148250.

229. Porte-Thomé, F.; Nagaraju, K.; Yu, Q.; Tatem, K.; Bkaily, G.; Scholz, W.; Slade, A.; Bot, N.; Kant, C. Development of Rimeporide, a Sodium-Hydrogen Exchanger (NHE-1) Inhibitor, for Patients with Duchenne Muscular Dystrophy. *Neuromuscul. Disord.* **2015**, *25*, S259–S260, doi:10.1016/j.nmd.2015.06.269.

230. Previtali, S.C.; Gidaro, T.; Díaz-Manera, J.; Zambon, A.; Carnesecchi, S.; Roux-Lombard, P.; Spitali, P.; Signorelli, M.; Szigyarto, C.A.K.; Johansson, C.; et al. Rimeporide as a FIrst- in-Class NHE-1 Inhibitor: Results of a Phase Ib Trial in Young Patients with Duchenne Muscular Dystrophy. *Pharmacol. Res.* **2020**, *159*, doi:10.1016/j.phrs.2020.104999.

231. Dunn, J.F.; Burton, K.A.; Dauncey, M.J. Ouabain Sensitive Na+ K+-ATPase Content Is Elevated in Mdx Mice: Implications for the Regulation of Ions in Dystrophic Muscle. *J. Neurol. Sci.* **1995**, *133*, 11–15, doi:10.1016/0022-510X(95)00167-Z.

232. Dubinin, M. V.; Starinets, V.S.; Chelyadnikova, Y.A.; Belosludtseva, N. V.; Mikheeva, I.B.; Penkina, D.K.; Igoshkina, A.D.; Talanov, E.Y.; Kireev, I.I.; Zorov, D.B.; et al. Effect of Large-Conductance Calcium-

Dependent K+ Channel Activator NS1619 on Function of Mitochondria in the Heart of Dystrophin-Deficient Mice. *Biochem.* **2023**, *88*, 189–201, doi:10.1134/S0006297923020037.

233. Graciotti, L.; Becker, J.; Granata, A.L.; Procopio, A.D.; Tessarollo, L.; Fulgenzi, G. Dystrophin Is Required for the Normal Function of the Cardio-Protective K ATP Channel in Cardiomyocytes. *PLoS One* **2011**, *6*, doi:10.1371/journal.pone.0027034.

234. Dubinin, M. V.; Starinets, V.S.; Belosludtseva, N. V.; Mikheeva, I.B.; Chelyadnikova, Y.A.; Penkina, D.K.; Vedernikov, A.A.; Belosludtsev, K.N. The Effect of Uridine on the State of Skeletal Muscles and the Functioning of Mitochondria in Duchenne Dystrophy. *Int. J. Mol. Sci.* **2022**, *23*, doi:10.3390/ijms231810660.

235. Dubinin, M. V.; Belosludtseva, N. V.; Mikheeva, I.B.; Chelyadnikova, Y.A.; Penkina, D.K.; Vafina, A.B.; Starinets, V.S.; Kireev, I.I.; Belosludtsev, K.N. Uridine Administration Promotes Normalization of Heart Mitochondrial Function in Dystrophin-Deficient Mice and Decreases Tissue Fibrosis. *Bull. Exp. Biol. Med.* **2023**, *176*, 54–59, doi:10.1007/s10517-023-05966-0.

236. Boyman, L.; Chikando, A.C.; Williams, G.S.B.; Khairallah, R.J.; Kettlewell, S.; Ward, C.W.; Smith, G.L.; Kao, J.P.Y.; Lederer, W.J. Calcium Movement in Cardiac Mitochondria. *Biophys. J.* **2014**, *107*, 1289–1301, doi:10.1016/j.bpj.2014.07.045.

237. Williams, G.S.B.; Boyman, L.; Chikando, A.C.; Khairallah, R.J.; Lederer, W.J. Mitochondrial Calcium Uptake. *Proc. Natl. Acad. Sci.* **2013**, *110*, 10479–10486, doi:10.1073/pnas.1300410110.

238. Rossmann, M.P.; Dubois, S.M.; Agarwal, S.; Zon, L.I. Mitochondrial Function in Development and Disease. *DMM Dis. Model. Mech.* 2021.

239. Nicholls, D.G.; Ferguson, S. *Bioenergetics*; Elsevier, 2013; ISBN 9780123884251.

240. Mitchell, P. Coupling of Phosphorylation to Electron and Hydrogen Transfer by a Chemi-Osmotic Type of Mechanism. *Nature* **1961**, doi:10.1038/191144a0.

241. Bernardi, P.; Carraro, M.; Lippe, G. The Mitochondrial Permeability Transition: Recent Progress and Open Questions. *FEBS J.* **2022**, *289*, 7051–7074, doi:10.1111/febs.16254.

242. Giorgio, V.; Guo, L.; Bassot, C.; Petronilli, V.; Bernardi, P. Calcium and Regulation of the Mitochondrial Permeability Transition. *Cell Calcium* **2018**, *70*, 56–63, doi:10.1016/j.ceca.2017.05.004.

243. Budihardjo, I.; Oliver, H.; Lutter, M.; Luo, X.; Wang, X. Biochemical Pathways of Caspase Activation During Apoptosis. *Annu. Rev. Cell Dev. Biol.* **1999**, *15*, 269–290, doi:10.1146/annurev.cellbio.15.1.269.

244. Halestrap, A.P.; Clarke, S.J.; Javadov, S.A. Mitochondrial Permeability Transition Pore Opening during Myocardial Reperfusion - A Target for Cardioprotection. *Cardiovasc. Res.* 2004.

245. Bround, M.J.; Havens, J.R.; York, A.J.; Sargent, M.A.; Karch, J.; Molkentin, J.D. ANT-Dependent MPTP Underlies Necrotic Myofiber Death in Muscular Dystrophy. *Sci. Adv.* **2023**, *9*, doi:10.1126/sciadv.adi2767.

246. Robert, V.; Massimino, M.L.; Tosello, V.; Marsault, R.; Cantini, M.; Sorrentino, V.; Pozzan, T. Alteration in Calcium Handling at the Subcellular Level in Mdx Myotubes. *J. Biol. Chem.* **2001**, *276*, 4647–4651, doi:10.1074/jbc.M006337200.

247. Hughes, M.C.; Ramos, S. V.; Turnbull, P.C.; Edgett, B.A.; Huber, J.S.; Polidovitch, N.; Schlattner, U.; Backx, P.H.; Simpson, J.A.; Perry, C.G.R. Impairments in Left Ventricular Mitochondrial Bioenergetics Precede Overt Cardiac Dysfunction and Remodelling in Duchenne Muscular Dystrophy. *J. Physiol.* **2020**, *598*, 1377–1392, doi:10.1113/JP277306.

248. Hughes, M.C.; Ramos, S. V.; Turnbull, P.C.; Rebalka, I.A.; Cao, A.; Monaco, C.M.F.; Varah, N.E.; Edgett, B.A.; Huber, J.S.; Tadi, P.; et al. Early Myopathy in Duchenne Muscular Dystrophy Is Associated with Elevated Mitochondrial H2O2 Emission during Impaired Oxidative Phosphorylation. *J. Cachexia. Sarcopenia Muscle* **2019**, *10*, 643–661, doi:10.1002/jcsm.12405.

249. Stevens, J.A.; Dobratz, T.C.; Fischer, K.D.; Palmer, A.; Bourdage, K.; Wong, A.J.; Chapoy-Villanueva, H.; Garry, D.J.; Liu, J.C.; Kay, M.W.; et al. Mechanisms of Reduced Myocardial Energetics of the Dystrophic Heart. *Am. J. Physiol. Circ. Physiol.* **2024**, *326*, H396–H407, doi:10.1152/ajpheart.00636.2023.

250. Millay, D.P.; Sargent, M.A.; Osinska, H.; Baines, C.P.; Barton, E.R.; Vuagniaux, G.; Sweeney, H.L.; Robbins, J.; Molkentin, J.D. Genetic and Pharmacologic Inhibition of Mitochondrial-Dependent Necrosis Attenuates Muscular Dystrophy. *Nat. Med.* **2008**, *14*, 442–447, doi:10.1038/nm1736.

251. De Luca, A.; Nico, B.; Liantonio, A.; Didonna, M.P.; Fraysse, B.; Pierno, S.; Burdi, R.; Mangieri, D.; Rolland, J.F.; Camerino, C.; et al. A Multidisciplinary Evaluation of the Effectiveness of Cyclosporine A in Dystrophic Mdx Mice. *Am. J. Pathol.* **2005**, *166*, 477–489, doi:10.1016/S0002-9440(10)62270-5.

252. Reutenauer, J.; Dorchies, O.M.; Patthey-Vuadens, O.; Vuagniaux, G.; Ruegg, U.T. Investigation of Debio 025, a Cyclophilin Inhibitor, in the Dystrophic Mdx Mouse, a Model for Duchenne Muscular Dystrophy. *Br. J. Pharmacol.* **2008**, *155*, 574–584, doi:10.1038/bjp.2008.285.

253. Wissing, E.R.; Millay, D.P.; Vuagniaux, G.; Molkentin, J.D. Debio-025 Is More Effective than Prednisone in Reducing Muscular Pathology in Mdx Mice. *Neuromuscul. Disord.* **2010**, *20*, 753–760, doi:10.1016/j.nmd.2010.06.016.

254. Schiavone, M.; Zulian, A.; Menazza, S.; Petronilli, V.; Argenton, F.; Merlini, L.; Sabatelli, P.; Bernardi, P. Alisporivir Rescues Defective Mitochondrial Respiration in Duchenne Muscular Dystrophy. *Pharmacol. Res.* **2017**, *125*, 122–131, doi:10.1016/j.phrs.2017.09.001.

255. Stocco, A.; Smolina, N.; Sabatelli, P.; Šileikytė, J.; Artusi, E.; Mouly, V.; Cohen, M.; Forte, M.; Schiavone, M.; Bernardi, P. Treatment with a Triazole Inhibitor of the Mitochondrial Permeability Transition Pore Fully Corrects the Pathology of Sapje Zebrafish Lacking Dystrophin. *Pharmacol. Res.* **2021**, *165*, doi:10.1016/j.phrs.2021.105421.

256. Giovarelli, M.; Zecchini, S.; Catarinella, G.; Moscheni, C.; Sartori, P.; Barbieri, C.; Roux-Biejat, P.; Napoli, A.; Vantaggiato, C.; Cervia, D.; et al. Givinostat as Metabolic Enhancer Reverting Mitochondrial Biogenesis Deficit in Duchenne Muscular Dystrophy. *Pharmacol. Res.* **2021**, *170*, doi:10.1016/j.phrs.2021.105751.

257. Handschin, C.; Kobayashi, Y.M.; Chin, S.; Seale, P.; Campbell, K.P.; Spiegelman, B.M. PGC-1α Regulates the Neuromuscular Junction Program and Ameliorates Duchenne Muscular Dystrophy. *Genes Dev.* **2007**, *21*, 770–783, doi:10.1101/gad.1525107.

258. Selsby, J.T.; Morine, K.J.; Pendrak, K.; Barton, E.R.; Sweeney, H.L. Rescue of Dystrophic Skeletal Muscle by PGC-1α Involves a Fast to Slow Fiber Type Shift in the Mdx Mouse. *PLoS One* **2012**, *7*, doi:10.1371/journal.pone.0030063.

259. Godin, R.; Daussin, F.; Matecki, S.; Li, T.; Petrof, B.J.; Burelle, Y. Peroxisome Proliferator-Activated Receptor γ Coactivator 1-α Gene Transfer Restores Mitochondrial Biomass and Improves Mitochondrial Calcium Handling in Post-Necrotic Mdx Mouse Skeletal Muscle. *J. Physiol.* **2012**, *590*, 5487–5502, doi:10.1113/jphysiol.2012.240390.

260. Ljubicic, V.; Jasmin, B.J. Metformin Increases Peroxisome Proliferator-Activated Receptor γ Co-Activator-1α and Utrophin a Expression in Dystrophic Skeletal Muscle. *Muscle and Nerve* **2015**, *52*, 139–142, doi:10.1002/mus.24692.

261. Moore, T.M.; Lin, A.J.; Strumwasser, A.R.; Cory, K.; Whitney, K.; Ho, T.; Ho, T.; Lee, J.L.; Rucker, D.H.; Nguyen, C.Q.; et al. Mitochondrial Dysfunction Is an Early Consequence of Partial or Complete Dystrophin Loss in Mdx Mice. *Front. Physiol.* **2020**, *11*, doi:10.3389/fphys.2020.00690.

262. Dubinin, M. V.; Starinets, V.S.; Talanov, E.Y.; Mikheeva, I.B.; Belosludtseva, N. V.; Belosludtsev, K.N. Alisporivir Improves Mitochondrial Function in Skeletal Muscle of Mdx Mice but Suppresses Mitochondrial Dynamics and Biogenesis. *Int. J. Mol. Sci.* **2021**, *22*, doi:10.3390/ijms22189780.

263. Glancy, B.; Balaban, R.S. Role of Mitochondrial Ca 2+ in the Regulation of Cellular Energetics. *Biochemistry* **2012**, *51*, 2959–2973, doi:10.1021/bi2018909.

264. Ionăşescu, V.; Luca, N.; Vuia, O. Respiratory Control and Oxidative Phosphorylation in the Dystrophic Muscle. *Acta Neurol. Scand.* **1967**, *43*, 564–572, doi:10.1111/j.1600-0404.1967.tb05551.x.

265. Wrogemann, K.; Blanchaer, M.C. Respiration and Oxidative Phosphorylation by Muscle and Heart Mitochondria of Hamsters with Hereditary Myocardiopathy and Polymyopathy. *Can. J. Biochem.* **1968**, *46*, 323–329, doi:10.1139/o68-048.

266. Wrogemann, K.; Blanchaer, M.C.; Jacobson, B.E. A Calcium-Associated Magnesium-Responsive Defect of Respiration and Oxidative Phosphorylation by Skeletal Muscle Mitochondria of BIO 14.6 Dystrophic Hamsters. *Life Sci.* **1970**, *9*, 1167–1173, doi:10.1016/0024-3205(70)90035-4.

267. Wrogemann, K.; Jacobson, B.E.; Blanchaer, M.C. On the Mechanism of a Calcium-Associated Defect of Oxidative Phosphorylation in Progressive Muscular Dystrophy. *Arch. Biochem. Biophys.* **1973**, *159*, 267–278, doi:10.1016/0003-9861(73)90453-0.

268. Willi, L.; Abramovich, I.; Fernandez-Garcia, J.; Agranovich, B.; Shulman, M.; Milman, H.; Baskin, P.; Eisen, B.; Michele, D.E.; Arad, M.; et al. Bioenergetic and Metabolic Impairments in Induced Pluripotent Stem Cell-Derived Cardiomyocytes Generated from Duchenne Muscular Dystrophy Patients. *Int. J. Mol. Sci.* **2022**, *23*, 9808, doi:10.3390/ijms23179808.

269. Cui, W.; Jang, A.; Zhang, P.; Thompson, B.; Townsend, D.; Metzger, J.M.; Zhang, J. Early Detection of Myocardial Bioenergetic Deficits: A 9.4 Tesla Complete Non Invasive 31P MR Spectroscopy Study in Mice with Muscular Dystrophy. *PLoS One* **2015**, *10*, doi:10.1371/journal.pone.0135000.

270. Guzun, R.; Gonzalez-Granillo, M.; Karu-Varikmaa, M.; Grichine, A.; Usson, Y.; Kaambre, T.; Guerrero-Roesch, K.; Kuznetsov, A.; Schlattner, U.; Saks, V. Regulation of Respiration in Muscle Cells in Vivo by VDAC through Interaction with the Cytoskeleton and MtCK within Mitochondrial Interactosome. *Biochim. Biophys. Acta - Biomembr.* **2012**, *1818*, 1545–1554, doi:10.1016/j.bbamem.2011.12.034.

271. Schlattner, U.; Kay, L.; Tokarska-Schlattner, M. Mitochondrial Proteolipid Complexes of Creatine Kinase. In *Subcellular Biochemistry*; 2018; Vol. 87, pp. 365–408.

272. Wallimann, T.; Tokarska-Schlattner, M.; Schlattner, U. The Creatine Kinase System and Pleiotropic Effects of Creatine. *Amino Acids* **2011**, *40*, 1271–1296, doi:10.1007/s00726-011-0877-3.

273. Meyer, R.A.; Sweeney, H.L.; Kushmerick, M.J. A Simple Analysis of the "Phosphocreatine Shuttle." *Am. J. Physiol. - Cell Physiol.* **1984**, *15*, doi:10.1152/ajpcell.1984.246.5.c365.

274. Aliev, M.; Guzun, R.; Karu-Varikmaa, M.; Kaambre, T.; Wallimann, T.; Saks, V. Molecular System Bioenergics of the Heart: Experimental Studies of Metabolic Compartmentation and Energy Fluxes versus Computer Modeling. *Int. J. Mol. Sci.* 2011.

275. Bellissimo, C.A.; Delfinis, L.J.; Hughes, M.C.; Turnbull, P.C.; Gandhi, S.; DiBenedetto, S.N.; Rahman, F.A.; Tadi, P.; Amaral, C.A.; Dehghani, A.; et al. Mitochondrial Creatine Sensitivity Is Lost in the D2.Mdx Model of Duchenne Muscular Dystrophy and Rescued by the Mitochondrial-Enhancing Compound Olesoxime. *Am. J. Physiol. - Cell Physiol.* **2023**, *324*, C1141–C1157, doi:10.1152/ajpcell.00377.2022.

276. Khairallah, M.; Khairallah, R.; Young, M.E.; Dyck, J.R.B.; Petrof, B.J.; Des Rosiers, C. Metabolic and Signaling Alterations in Dystrophin-Deficient Hearts Precede Overt Cardiomyopathy. *J. Mol. Cell. Cardiol.* **2007**, *43*, 119–129, doi:10.1016/j.yjmcc.2007.05.015.

277. Momose, M.; Iguchi, N.; Imamura, K.; Usui, H.; Ueda, T.; Miyamoto, K.; Inaba, S. Depressed Myocardial Fatty Acid Metabolism in Patients with Muscular Dystrophy. *Neuromuscul. Disord.* **2001**, *11*, 464–469, doi:10.1016/S0960-8966(01)00191-2.

278. Krumenacker, J.S.; Hyder, S.M.; Murad, F. Estradiol Rapidly Inhibits Soluble Guanylyl Cyclase Expression in Rat Uterus. *Proc. Natl. Acad. Sci.* **2001**, *98*, 717–722, doi:10.1073/pnas.98.2.717.

279. Naruse, H.; Miyagi, J.; Arii, T.; Ohyanagi, M.; Iwasaki, T.; Jinnai, K. The Relationship between Clinical Stage, Prognosis and Myocardial Damage in Patients with Duchenne-Type Muscular Dystrophy: Five-Year

Follow-up Study. *Ann. Nucl. Med.* **2004**, *18*, 203–208, doi:10.1007/BF02985001.

280. Perloff, J.K.; Henze, E.; Schelbert, H.R. Alterations in Regional Myocardial Metabolism, Perfusion, and Wall Motion in Duchenne Muscular Dystrophy Studied by Radionuclide Imaging. *Circulation* **1984**, *69*, 33–42, doi:10.1161/01.CIR.69.1.33.

281. Zorzano, A.; Sevilla, L.; Tomàs, E.; Gumà, A.; Palacín, M.; Fischer, Y. GLUT4 Trafficking in Cardiac and Skeletal Muscle: Isolation and Characterization of Distinct Intracellular GLUT4-Containing Vesicle Populations. *Biochem. Soc. Trans.* **1997**, *25*, 968–974, doi:10.1042/bst0250968.

282. Fischer, Y.; Thomas, J.; Sevilla, L.; Muñoz, P.; Becker, C.; Holman, G.; Kozka, I.J.; Palacín, M.; Testar, X.; Kammermeier, H.; et al. Insulin-Induced Recruitment of Glucose Transporter 4 (GLUT4) and GLUT1 in Isolated Rat Cardiac Myocytes. Evidence of the Existence of Different Intracellular GLUT4 Vesicle Populations. *J. Biol. Chem.* **1997**, *272*, 7085–7092, doi:10.1074/jbc.272.11.7085.

283. Birnbaum, M.J. Identification of a Novel Gene Encoding an Insulin-Responsive Glucose Transporter Protein. *Cell* **1989**, *57*, 305–315, doi:10.1016/0092-8674(89)90968-9.

284. Schneider, S.M.; Sridhar, V.; Bettis, A.K.; Heath-Barnett, H.; Balog-Alvarez, C.J.; Guo, L.J.; Johnson, R.; Jaques, S.; Vitha, S.; Glowcwski, A.C.; et al. Glucose Metabolism as a Pre-Clinical Biomarker for the Golden Retriever Model of Duchenne Muscular Dystrophy. *Mol. Imaging Biol.* **2018**, *20*, 780–788, doi:10.1007/s11307-018-1174-2.

285. Nikolaidis, L.A.; Sturzu, A.; Stolarski, C.; Elahi, D.; Shen, Y.T.; Shannon, R.P. The Development of Myocardial Insulin Resistance in Conscious Dogs with Advanced Dilated Cardiomyopathy. *Cardiovasc. Res.* **2004**, *61*, 297–306, doi:10.1016/j.cardiores.2003.11.027.

286. Glatz, J.F.C.; Nabben, M.; Young, M.E.; Schulze, P.C.; Taegtmeyer, H.; Luiken, J.J.F.P. Re-Balancing Cellular Energy Substrate Metabolism to Mend the Failing Heart. *Biochim. Biophys. Acta - Mol. Basis Dis.* **2020**, *1866*, 165579, doi:10.1016/j.bbadis.2019.165579.

287. Danialou, G.; Comtois, A.S.; Dudley, R.; Karpati, G.; Vincent, G.; Des Rosiers, C.; Petrof, B.J. Dystrophin-deficient Cardiomyocytes Are Abnormally Vulnerable to Mechanical Stress-induced Contractile Failure and Injury. *FASEB J.* **2001**, *15*, 1655–1657, doi:10.1096/fj.01-0030fje.

288. Burkhoff, D.; Weiss, R.G.; Schulman, S.P.; Kalil-Filho, R.; Wannenburg, T.; Gerstenblith, G. Influence of Metabolic Substrate on Rat Heart Function and Metabolism at Different Coronary Flows. *Am. J. Physiol. - Hear. Circ. Physiol.* **1991**, *261*, doi:10.1152/ajpheart.1991.261.3.h741.

289. Stanley, W.C.; Recchia, F.A.; Lopaschuk, G.D. Myocardial Substrate Metabolism in the Normal and Failing Heart. *Physiol. Rev.* **2005**, *85*, 1093–1129, doi:10.1152/physrev.00006.2004.

290. Stine, Z.E.; Schug, Z.T.; Salvino, J.M.; Dang, C. V. Targeting Cancer Metabolism in the Era of Precision Oncology. *Nat. Rev. Drug Discov.* **2022**, *21*, 141–162, doi:10.1038/s41573-021-00339-6.

291. Capitanio, D.; Moriggi, M.; Torretta, E.; Barbacini, P.; De Palma, S.; Viganò, A.; Lochmüller, H.; Muntoni, F.; Ferlini, A.; Mora, M.; et al. Comparative Proteomic Analyses of Duchenne Muscular Dystrophy and Becker Muscular Dystrophy Muscles: Changes Contributing to Preserve Muscle Function in Becker Muscular Dystrophy Patients. *J. Cachexia. Sarcopenia Muscle* **2020**, *11*, 547–563, doi:10.1002/jcsm.12527.

292. Griffin, J.L.; Des Rosiers, C. Applications of Metabolomics and Proteomics to the Mdx Mouse Model of Duchenne Muscular Dystrophy: Lessons from Downstream of the Transcriptome. *Genome Med.* **2009**, *1*, 32, doi:10.1186/gm32.

293. Nisoli, E.; Falcone, S.; Tonello, C.; Cozzi, V.; Palomba, L.; Fiorani, M.; Pisconti, A.; Brunelli, S.; Cardile, A.; Francolini, M.; et al. Mitochondrial Biogenesis by NO Yields Functionally Active Mitochondria in Mammals. *Proc. Natl. Acad. Sci. U. S. A.* **2004**, *101*, 16507–16512, doi:10.1073/pnas.0405432101.

294. Krumenacker, J.S.; Hanafy, K.A.; Murad, F. Regulation of Nitric Oxide and Soluble Guanylyl Cyclase. *Brain Res. Bull.* **2004**, *62*, 505–515, doi:10.1016/S0361-9230(03)00102-3.

295. Timpani, C.A.; Trewin, A.J.; Stojanovska, V.; Robinson, A.; Goodman, C.A.; Nurgali, K.; Betik, A.C.; Stepto, N.; Hayes, A.; McConell, G.K.; et al. Attempting to Compensate for Reduced Neuronal Nitric Oxide Synthase Protein with Nitrate Supplementation Cannot Overcome Metabolic Dysfunction but Rather Has Detrimental Effects in Dystrophin-Deficient Mdx Muscle. *Neurotherapeutics* **2017**, *14*, 429–446, doi:10.1007/s13311-016-0494-7.

296. Lundberg, J.O.; Weitzberg, E. Nitric Oxide Signaling in Health and Disease. *Cell* **2022**, *185*, 2853–2878, doi:10.1016/j.cell.2022.06.010.

297. Murphy, M.P. How Mitochondria Produce Reactive Oxygen Species. *Biochem. J.* 2009.

298. Korshunov, S.S.; Skulachev, V.P.; Starkov, A.A. High Protonic Potential Actuates a Mechanism of Production of Reactive Oxygen Species in Mitochondria. *FEBS Lett.* **1997**, doi:10.1016/S0014-5793(97)01159-9.

299. Lambert, A.J.; Brand, M.D. Superoxide Production by NADH:Ubiquinone Oxidoreductase (Complex I) Depends on the PH Gradient across the Mitochondrial Inner Membrane. *Biochem. J.* **2004**, doi:10.1042/BJ20040485.

300. Meyer, L.E.; Machado, L.B.; Santiago, A.P.S.A.; Da-Silva, W.S.; De Felice, F.G.; Holub, O.; Oliveira, M.F.; Galina, A. Mitochondrial Creatine Kinase Activity Prevents Reactive Oxygen Species Generation. *J. Biol. Chem.* **2006**, *281*, 37361–37371, doi:10.1074/jbc.M604123200.

301. Gartz, M.; Haberman, M.; Prom, M.J.; Beatka, M.J.; Strande, J.L.; Lawlor, M.W. A Long-Term Study Evaluating the Effects of Nicorandil Treatment on Duchenne Muscular Dystrophy-Associated Cardiomyopathy in Mdx Mice. *J. Cardiovasc. Pharmacol. Ther.* **2022**, *27*, doi:10.1177/10742484221088655.

302. Prosser, B.L.; Ward, C.W.; Lederer, W.J. X-ROS Signaling: Rapid Mechano-Chemo Transduction in Heart. *Science (80-.).* **2011**, *333*, 1440–1445, doi:10.1126/science.1202768.

303. Gonzalez, D.R.; Treuer, A. V.; Lamirault, G.; Mayo, V.; Cao, Y.; Dulce, R.A.; Hare, J.M. NADPH Oxidase-2 Inhibition Restores Contractility and Intracellular Calcium Handling and Reduces Arrhythmogenicity in Dystrophic Cardiomyopathy. *Am. J. Physiol. - Hear. Circ. Physiol.* **2014**, *307*, doi:10.1152/ajpheart.00890.2013.

304. Khairallah, R.J.; Shi, G.; Sbrana, F.; Prosser, B.L.; Borroto, C.; Mazaitis, M.J.; Hoffman, E.P.; Mahurkar, A.; Sachs, F.; Sun, Y.; et al. Microtubules Underlie Dysfunction in Duchenne Muscular Dystrophy. *Sci. Signal.* **2012**, *5*, doi:10.1126/scisignal.2002829.

305. Prosser, B.L.; Khairallah, R.J.; Ziman, A.P.; Ward, C.W.; Lederer, W.J. X-ROS Signaling in the Heart and Skeletal Muscle: Stretch-Dependent Local ROS Regulates [Ca2+]I. *J. Mol. Cell. Cardiol.* **2013**, *58*, 172–181, doi:10.1016/j.yjmcc.2012.11.011.

306. Jung, C.; Martins, A.S.; Niggli, E.; Shirokova, N. Dystrophic Cardiomyopathy: Amplification of Cellular Damage by Ca 2+ Signalling and Reactive Oxygen Species-Generating Pathways. *Cardiovasc. Res.* **2008**, *77*, 766–773, doi:10.1093/cvr/cvm089.

307. Kyrychenko, S.; Poláková, E.; Kang, C.; Pocsai, K.; Ullrich, N.D.; Niggli, E.; Shirokova, N. Hierarchical Accumulation of RyR Post-Translational Modifications Drives Disease Progression in Dystrophic Cardiomyopathy. *Cardiovasc. Res.* **2013**, *97*, 666–675, doi:10.1093/cvr/cvs425.

308. Pinniger, G.J.; Terrill, J.R.; Assan, E.B.; Grounds, M.D.; Arthur, P.G. Pre-Clinical Evaluation of N-Acetylcysteine Reveals Side Effects in the Mdx Mouse Model of Duchenne Muscular Dystrophy. *J. Physiol.* **2017**, *595*, 7093–7107, doi:10.1113/JP274229.

309. Reid, A.L.; Alexander, M.S. The Interplay of Mitophagy and Inflammation in Duchenne Muscular Dystrophy. *Life* **2021**, *11*, doi:10.3390/life11070648.

310. Li, X.; Zhang, W.; Cao, Q.; Wang, Z.; Zhao, M.; Xu, L.; Zhuang, Q. Mitochondrial Dysfunction in Fibrotic

Diseases. *Cell Death Discov.* **2020**, *6*, 80, doi:10.1038/s41420-020-00316-9.

311. Eisner, D.A.; Caldwell, J.L.; Kistamás, K.; Trafford, A.W. Calcium and Excitation-Contraction Coupling in the Heart. *Circ. Res.* **2017**, *121*, 181–195, doi:10.1161/CIRCRESAHA.117.310230.

312. Kang, C.; Badr, M.A.; Kyrychenko, V.; Eskelinen, E.L.; Shirokova, N. Deficit in PINK1/PARKIN-Mediated Mitochondrial Autophagy at Late Stages of Dystrophic Cardiomyopathy. *Cardiovasc. Res.* **2018**, *114*, 90–102, doi:10.1093/cvr/cvx201.

313. Luan, P.; Amico, D.D.; Andreux, P.A.; Laurila, P.P.; Wohlwend, M.; Li, H.; Lima, T.I.; Place, N.; Rinsch, C.; Zanou, N.; et al. Urolithin A Improves Muscle Function by Inducing Mitophagy in Muscular Dystrophy. *Sci. Transl. Med.* **2021**, *13*, doi:10.1126/scitranslmed.abb0319.

314. Pauly, M.; Daussin, F.; Burelle, Y.; Li, T.; Godin, R.; Fauconnier, J.; Koechlin-Ramonatxo, C.; Hugon, G.; Lacampagne, A.; Coisy-Quivy, M.; et al. AMPK Activation Stimulates Autophagy and Ameliorates Muscular Dystrophy in the Mdx Mouse Diaphragm. *Am. J. Pathol.* **2012**, *181*, 583–592, doi:10.1016/j.ajpath.2012.04.004.

315. Kuno, A.; Hosoda, R.; Sebori, R.; Hayashi, T.; Sakuragi, H.; Tanabe, M.; Horio, Y. Resveratrol Ameliorates Mitophagy Disturbance and Improves Cardiac Pathophysiology of Dystrophin-Deficient Mdx Mice. *Sci. Rep.* **2018**, *8*, 15555, doi:10.1038/s41598-018-33930-w.

316. De Palma, C.; Morisi, F.; Cheli, S.; Pambianco, S.; Cappello, V.; Vezzoli, M.; Rovere-Querini, P.; Moggio, M.; Ripolone, M.; Francolini, M.; et al. Autophagy as a New Therapeutic Target in Duchenne Muscular Dystrophy. *Cell Death Dis.* **2012**, *3*, doi:10.1038/cddis.2012.159.

317. Sarma, S.; Li, N.; Van Oort, R.J.; Reynolds, C.; Skapura, D.G.; Wehrens, X.H.T. Genetic Inhibition of PKA Phosphorylation of RyR2 Prevents Dystrophic Cardiomyopathy. *Proc. Natl. Acad. Sci. U. S. A.* **2010**, *107*, 13165–13170, doi:10.1073/pnas.1004509107.

318. Iwata, Y.; Ohtake, H.; Suzuki, O.; Matsuda, J.; Komamura, K.; Wakabayashi, S. Blockade of Sarcolemmal TRPV2 Accumulation Inhibits Progression of Dilated Cardiomyopathy. *Cardiovasc. Res.* **2013**, *99*, 760–768, doi:10.1093/cvr/cvt163.

319. Matsumura, T.; Matsui, M.; Iwata, Y.; Asakura, M.; Saito, T.; Fujimura, H.; Sakoda, S. A Pilot Study of Tranilast for Cardiomyopathy of Muscular Dystrophy. *Intern. Med.* **2018**, *57*, 311–318, doi:10.2169/internalmedicine.8651-16.

320. Shin, J.H.; Bostick, B.; Yue, Y.; Hajjar, R.; Duan, D. SERCA2a Gene Transfer Improves Electrocardiographic Performance in Aged Mdx Mice. *J. Transl. Med.* **2011**, *9*, doi:10.1186/1479-5876-9-132.

321. Wasala, N.B.; Yue, Y.; Lostal, W.; Wasala, L.P.; Niranjan, N.; Hajjar, R.J.; Babu, G.J.; Duan, D. Single SERCA2a Therapy Ameliorated Dilated Cardiomyopathy for 18 Months in a Mouse Model of Duchenne Muscular Dystrophy. *Mol. Ther.* **2020**, *28*, 845–854, doi:10.1016/j.ymthe.2019.12.011.

322. Law, M.L.; Prins, K.W.; Olander, M.E.; Metzger, J.M. Exacerbation of Dystrophic Cardiomyopathy by Phospholamban Deficiency Mediated Chronically Increased Cardiac Ca2+ Cycling in Vivo. *Am. J. Physiol. - Hear. Circ. Physiol.* **2018**, *315*, H1544–H1552, doi:10.1152/ajpheart.00341.2018.

323. Murphy, M.P. Targeting Lipophilic Cations to Mitochondria. *Biochim. Biophys. Acta - Bioenerg.* **2008**, *1777*, 1028–1031, doi:10.1016/j.bbabio.2008.03.029.

324. Szeto, H.H.; Birk, A. V. Serendipity and the Discovery of Novel Compounds That Restore Mitochondrial Plasticity. *Clin. Pharmacol. Ther.* **2014**, *96*, 672–683, doi:10.1038/clpt.2014.174.

325. Zhao, K.; Luo, G.; Zhao, G.-M.; Schiller, P.W.; Szeto, H.H. Transcellular Transport of a Highly Polar 3+ Net Charge Opioid Tetrapeptide. *J. Pharmacol. Exp. Ther.* **2003**, *304*, 425–432, doi:10.1124/jpet.102.040147.

326. Birk, A. V.; Liu, S.; Soong, Y.; Mills, W.; Singh, P.; Warren, J.D.; Seshan, S. V.; Pardee, J.D.; Szeto, H.H.

The Mitochondrial-Targeted Compound SS-31 Re-Energizes Ischemic Mitochondria by Interacting with Cardiolipin. *J. Am. Soc. Nephrol.* **2013**, *24*, 1250–1261, doi:10.1681/ASN.2012121216.

327. Zhao, K.; Zhao, G.M.; Wu, D.; Soong, Y.; Birk, A. V.; Schiller, P.W.; Szeto, H.H. Cell-Permeable Peptide Antioxidants Targeted to Inner Mitochondrial Membrane Inhibit Mitochondrial Swelling, Oxidative Cell Death, and Reperfusion Injury. *J. Biol. Chem.* **2004**, *279*, 34682–34690, doi:10.1074/jbc.M402999200.

328. Koufen, P.; Rück, A.; Brdiczka, D.; Wendt, S.; Wallimann, T.; Stark, G. Free Radical-Induced Inactivation of Creatine Kinase: Influence on the Octameric and Dimeric States of the Mitochondrial Enzyme (Mi(b)-CK). *Biochem. J.* **1999**, *344*, 413–417, doi:10.1042/0264-6021:3440413.

329. Dolder, M.; Wendt, S.; Wallimann, T. Mitochondrial Creatine Kinase in Contact Sites: Interaction with Porin and Adenine Nucleotide Translocase, Role in Permeability Transition and Sensitivity to Oxidative Damage. *NeuroSignals* **2001**, *10*, 93–111, doi:10.1159/000046878.

330. Siegel, M.P.; Kruse, S.E.; Percival, J.M.; Goh, J.; White, C.C.; Hopkins, H.C.; Kavanagh, T.J.; Szeto, H.H.; Rabinovitch, P.S.; Marcinek, D.J. Mitochondrial-Targeted Peptide Rapidly Improves Mitochondrial Energetics and Skeletal Muscle Performance in Aged Mice. *Aging Cell* **2013**, *12*, 763–771, doi:10.1111/acel.12102.

331. Szeto, H.H.; Schiller, P.W. Novel Therapies Targeting Inner Mitochondrial Membrane—From Discovery to Clinical Development. *Pharm. Res.* **2011**, *28*, 2669–2679, doi:10.1007/s11095-011-0476-8.

332. Szeto, H.H. First-in-class Cardiolipin-protective Compound as a Therapeutic Agent to Restore Mitochondrial Bioenergetics. *Br. J. Pharmacol.* **2014**, *171*, 2029–2050, doi:10.1111/bph.12461.

333. Eirin, A.; Ebrahimi, B.; Zhang, X.; Zhu, X.Y.; Woollard, J.R.; He, Q.; Textor, S.C.; Lerman, A.; Lerman, L.O. Mitochondrial Protection Restores Renal Function in Swine Atherosclerotic Renovascular Disease. *Cardiovasc. Res.* **2014**, *103*, 461–472, doi:10.1093/cvr/cvu157.

334. Dai, D.F.; Chen, T.; Szeto, H.; Nieves-Cintrón, M.; Kutyavin, V.; Santana, L.F.; Rabinovitch, P.S. Mitochondrial Targeted Antioxidant Peptide Ameliorates Hypertensive Cardiomyopathy. *J. Am. Coll. Cardiol.* **2011**, *58*, 73–82, doi:10.1016/j.jacc.2010.12.044.

335. Gillis, J.C.; Benfield, P.; McTavish, D. Idebenone: A Review of Its Pharmacodynamic and Pharmacokinetic Properties, and Therapeutic Use in Age-Related Cognitive Disorders. *Drugs Aging* **1994**, *5*, 133–152, doi:10.2165/00002512-199405020-00007.

336. Zs.-Nagy, I. Chemistry, Toxicology, Pharmacology and Pharmacokinetics of Idebenone: A Review. *Arch. Gerontol. Geriatr.* **1990**, *11*, 177–186, doi:10.1016/0167-4943(90)90063-C.

337. Suno, M.; Nagaoka, A. Inhibition of Lipid Peroxidation by Idebenone in Brain Mitochondria in the Presence of Succinate. *Arch. Gerontol. Geriatr.* **1989**, *8*, 291–297, doi:10.1016/0167-4943(89)90010-1.

338. Suno, M.; Nagaoka, A. Inhibition of Lipid Peroxidation by a Novel Compound, Idebenone (CV-2619). *Jpn. J. Pharmacol.* **1984**, *35*, 196–198, doi:10.1254/jjp.35.196.

339. Buyse, G.M.; Van Der Mieren, G.; Erb, M.; D'hooge, J.; Herijgers, P.; Verbeken, E.; Jara, A.; Van Den Bergh, A.; Mertens, L.; Courdier-Fruh, I.; et al. Long-Term Blinded Placebo-Controlled Study of SNT-MC17/Idebenone in the Dystrophin Deficient Mdx Mouse: Cardiac Protection and Improved Exercise Performance. *Eur. Heart J.* **2009**, *30*, 116–124, doi:10.1093/eurheartj/ehn406.

340. Buyse, G.M.; Goemans, N.; van den Hauwe, M.; Thijs, D.; de Groot, I.J.M.; Schara, U.; Ceulemans, B.; Meier, T.; Mertens, L. Idebenone as a Novel, Therapeutic Approach for Duchenne Muscular Dystrophy: Results from a 12 Month, Double-Blind, Randomized Placebo-Controlled Trial. *Neuromuscul. Disord.* **2011**, *21*, 396–405, doi:10.1016/j.nmd.2011.02.016.

341. Buyse, G.M.; Voit, T.; Schara, U.; Straathof, C.S.M.; D'Angelo, M.G.; Bernert, G.; Cuisset, J.M.; Finkel, R.S.; Goemans, N.; Rummey, C.; et al. Treatment Effect of Idebenone on Inspiratory Function in Patients with Duchenne Muscular Dystrophy. *Pediatr. Pulmonol.* **2017**, *52*, 508–515, doi:10.1002/ppul.23547.

342. Buyse, G.M.; Voit, T.; Schara, U.; Straathof, C.S.M.; D'Angelo, M.G.; Bernert, G.; Cuisset, J.M.; Finkel, R.S.; Goemans, N.; McDonald, C.M.; et al. Efficacy of Idebenone on Respiratory Function in Patients with Duchenne Muscular Dystrophy Not Using Glucocorticoids (DELOS): A Double-Blind Randomised Placebo-Controlled Phase 3 Trial. *Lancet* **2015**, *385*, 1748–1757, doi:10.1016/S0140-6736(15)60025-3.

343. Gueven, N.; Ravishankar, P.; Eri, R.; Rybalka, E. Idebenone: When an Antioxidant Is Not an Antioxidant. *Redox Biol.* **2021**, *38*, 101812, doi:10.1016/j.redox.2020.101812.

344. Dubuisson, N.; Versele, R.; Davis-López de Carrizosa, M.A.; Selvais, C.M.; Noel, L.; Planchon, C.; Van den Bergh, P.Y.K.; Brichard, S.M.; Abou-Samra, M. The Adiponectin Receptor Agonist, ALY688: A Promising Therapeutic for Fibrosis in the Dystrophic Muscle. *Cells* **2023**, doi:10.3390/cells12162101.

345. Yamauchi, T.; Kadowaki, T. Physiological and Pathophysiological Roles of Adiponectin and Adiponectin Receptors in the Integrated Regulation of Metabolic and Cardiovascular Diseases. *Int. J. Obes.* 2008.

346. Yamauchi, T.; Nio, Y.; Maki, T.; Kobayashi, M.; Takazawa, T.; Iwabu, M.; Okada-Iwabu, M.; Kawamoto, S.; Kubota, N.; Kubota, T.; et al. Targeted Disruption of AdipoR1 and AdipoR2 Causes Abrogation of Adiponectin Binding and Metabolic Actions. *Nat. Med.* **2007**, doi:10.1038/nm1557.

347. Turer, A.T.; Scherer, P.E. Adiponectin: Mechanistic Insights and Clinical Implications. *Diabetologia* 2012.

348. Achari, A.E.; Jain, S.K. Adiponectin, a Therapeutic Target for Obesity, Diabetes, and Endothelial Dysfunction. *Int. J. Mol. Sci.* 2017.

349. Scherer, P.E.; Williams, S.; Fogliano, M.; Baldini, G.; Lodish, H.F. A Novel Serum Protein Similar to C1q, Produced Exclusively in Adipocytes. *J. Biol. Chem.* **1995**, doi:10.1074/jbc.270.45.26746.

350. Magkos, F.; Sidossis, L.S. Recent Advances in the Measurement of Adiponectin Isoform Distribution. *Curr. Opin. Clin. Nutr. Metab. Care* 2007.

351. Hui, X.; Lam, K.S.; Vanhoutte, P.M.; Xu, A. Adiponectin and Cardiovascular Health: An Update. *Br. J. Pharmacol.* 2012.

352. Tsao, T.S.; Tomas, E.; Murrey, H.E.; Hug, C.; Lee, D.H.; Ruderman, N.B.; Heuser, J.E.; Lodish, H.F. Role of Disulfide Bonds in Acrp30/Adiponectin Structure and Signaling Specificity: Different Oligomers Activate Different Signal Transduction Pathways. *J. Biol. Chem.* **2003**, doi:10.1074/jbc.M309469200.

353. Fiaschi, T.; Giannoni, E.; Taddei, M.L.; Chiarugi, P. Globular Adiponectin Activates Motility and Regenerative Traits of Muscle Satellite Cells. *PLoS One* **2012**, doi:10.1371/journal.pone.0034782.

354. Waki, H.; Yamauchi, T.; Kamon, J.; Kita, S.; Ito, Y.; Hada, Y.; Uchida, S.; Tsuchida, A.; Takekawa, S.; Kadowaki, T. Generation of Globular Fragment of Adiponectin by Leukocyte Elastase Secreted by Monocytic Cell Line THP-1. *Endocrinology* **2005**, doi:10.1210/en.2004-1096.

355. Yoda-Murakami, M.; Taniguchi, M.; Takahashi, K.; Kawamata, S.; Saito, K.; Choi-Miura, N.H.; Tomita, M. Change in Expression of GBP28/Adiponectin in Carbon Tetrachloride-Administrated Mouse Liver. *Biochem. Biophys. Res. Commun.* **2001**, doi:10.1006/bbrc.2001.5134.

356. Delaigle, A.M.; Jonas, J.C.; Bauche, I.B.; Cornu, O.; Brichard, S.M. Induction of Adiponectin in Skeletal Muscle by Inflammatory Cytokines: In Vivo and in Vitro Studies. *Endocrinology* **2004**, doi:10.1210/en.2004-0503.

357. Patel, J. V.; Abraheem, A.; Dotsenko, O.; Creamer, J.; Gunning, M.; Hughes, E.A.; Lip, G.Y.H. Circulating Serum Adiponectin Levels in Patients with Coronary Artery Disease: Relationship to Atherosclerotic Burden and Cardiac Function. *J. Intern. Med.* **2008**, doi:10.1111/j.1365-2796.2008.02007.x.

358. Procaccini, C.; De Rosa, V.; Galgani, M.; Carbone, F.; Rocca, C. La; Formisano, L.; Matarese, G. Role of Adipokines Signaling in the Modulation of T Cells Function. *Front. Immunol.* 2013.

359. Berner, H.S.; Lyngstadaas, S.P.; Spahr, A.; Monjo, M.; Thommesen, L.; Drevon, C.A.; Syversen, U.; Reseland, J.E. Adiponectin and Its Receptors Are Expressed in Bone-Forming Cells. *Bone* **2004**,

doi:10.1016/j.bone.2004.06.008.

360. Onodera, T.; Wang, M.Y.; Rutkowski, J.M.; Deja, S.; Chen, S.; Balzer, M.S.; Kim, D.S.; Sun, X.; An, Y.A.; Field, B.C.; et al. Endogenous Renal Adiponectin Drives Gluconeogenesis through Enhancing Pyruvate and Fatty Acid Utilization. *Nat. Commun.* **2023**, doi:10.1038/s41467-023-42188-4.

361. Maeda, K.; Okubo, K.; Shimomura, I.; Funahashi, T.; Matsuzawa, Y.; Matsubara, K. CDNA Cloning and Expression of a Novel Adipose Specific Collagen-like Factor, ApM1 (Adipose Most Abundant Gene Transcript 1). *Biochem. Biophys. Res. Commun.* **1996**, doi:10.1006/bbrc.1996.0587.

362. Zhu, W.; Cheng, K.K.Y.; Vanhoutte, P.M.; Lam, K.S.L.; Xu, A. Vascular Effects of Adiponectin: Molecular Mechanisms and Potential Therapeutic Intervention. *Clin. Sci.* 2008.

363. Arita, Y.; Kihara, S.; Ouchi, N.; Takahashi, M.; Maeda, K.; Miyagawa, J.I.; Hotta, K.; Shimomura, I.; Nakamura, T.; Miyaoka, K.; et al. Paradoxical Decrease of an Adipose-Specific Protein, Adiponectin, in Obesity. *Biochem. Biophys. Res. Commun.* **1999**, doi:10.1006/bbrc.1999.0255.

364. Halberg, N.; Schraw, T.D.; Wang, Z. V.; Kim, J.Y.; Yi, J.; Hamilton, M.P.; Luby-Phelps, K.; Scherer, P.E. Systemic Fate of the Adipocyte-Derived Factor Adiponectin. *Diabetes* **2009**, doi:10.2337/db08-1750.

365. Liu, Y.; Vu, V.; Sweeney, G. Examining the Potential of Developing and Implementing Use of Adiponectin-Targeted Therapeutics for Metabolic and Cardiovascular Diseases. *Front. Endocrinol. (Lausanne).* 2019.

366. Kamareddine, L.; Ghantous, C.M.; Allouch, S.; Al-Ashmar, S.A.; Anlar, G.; Kannan, S.; Djouhri, L.; Korashy, H.M.; Agouni, A.; Zeidan, A. Between Inflammation and Autophagy: The Role of Leptin-Adiponectin Axis in Cardiac Remodeling. *J. Inflamm. Res.* **2021**, doi:10.2147/JIR.S322231.

367. Ohashi, K.; Parker, J.L.; Ouchi, N.; Higuchi, A.; Vita, J.A.; Gokce, N.; Pedersen, A.A.; Kalthoff, C.; Tullin, S.; Sams, A.; et al. Adiponectin Promotes Macrophage Polarization toward an Anti-Inflammatory Phenotype. *J. Biol. Chem.* **2010**, doi:10.1074/jbc.M109.088708.

368. Wolf, A.M.; Wolf, D.; Rumpold, H.; Enrich, B.; Tilg, H. Adiponectin Induces the Anti-Inflammatory Cytokines IL-10 and IL-1RA in Human Leukocytes. *Biochem. Biophys. Res. Commun.* **2004**, doi:10.1016/j.bbrc.2004.08.145.

369. Yokota, T.; Oritani, K.; Takahashi, I.; Ishikawa, J.; Matsuyama, A.; Ouchi, N.; Kihara, S.; Funahashi, T.; Tenner, A.J.; Tomiyama, Y.; et al. Adiponectin, a New Member of the Family of Soluble Defense Collagens, Negatively Regulates the Growth of Myelomonocytic Progenitors and the Functions of Macrophages. *Blood* **2000**, doi:10.1182/blood.v96.5.1723.

370. Lovren, F.; Pan, Y.; Quan, A.; Szmitko, P.E.; Singh, K.K.; Shukla, P.C.; Gupta, M.; Chan, L.; Al-Omran, M.; Teoh, H.; et al. Adiponectin Primes Human Monocytes into Alternative Anti-Inflammatory M2 Macrophages. *Am. J. Physiol. - Hear. Circ. Physiol.* **2010**, doi:10.1152/ajpheart.00115.2010.

371. Ajuwon, K.M.; Spurlock, M.E. Adiponectin Inhibits LPS-Induced NF-KB Activation and IL-6 Production and Increases PPARγ2 Expression in Adipocytes. *Am. J. Physiol. - Regul. Integr. Comp. Physiol.* **2005**, doi:10.1152/ajpregu.00397.2004.

372. Luo, Y.; Liu, M. Adiponectin: A Versatile Player of Innate Immunity. *J. Mol. Cell Biol.* 2016.

373. Ramos-Ramírez, P.; Malmhäll, C.; Tliba, O.; Rådinger, M.; Bossios, A. Adiponectin/AdipoR1 Axis Promotes IL-10 Release by Human Regulatory T Cells. *Front. Immunol.* **2021**, doi:10.3389/fimmu.2021.677550.

374. Otvos, L.; Haspinger, E.; La Russa, F.; Maspero, F.; Graziano, P.; Kovalszky, I.; Lovas, S.; Nama, K.; Hoffmann, R.; Knappe, D.; et al. Design and Development of a Peptide-Based Adiponectin Receptor Agonist for Cancer Treatment. *BMC Biotechnol.* **2011**, doi:10.1186/1472-6750-11-90.

375. Zhang, Y.; Zhao, J.; Li, R.; Lau, W.B.; Yuan, Y.X.; Liang, B.; Li, R.; Gao, E.H.; Koch, W.J.; Ma, X.L.; et al. AdipoRon, the First Orally Active Adiponectin Receptor Activator, Attenuates Postischemic Myocardial Apoptosis through Both AMPK-Mediated and AMPK-Independent Signalings. *Am. J. Physiol. - Endocrinol.*

Metab. **2015**, doi:10.1152/ajpendo.00577.2014.

376. Okada-Iwabu, M.; Yamauchi, T.; Iwabu, M.; Honma, T.; Hamagami, K.I.; Matsuda, K.; Yamaguchi, M.; Tanabe, H.; Kimura-Someya, T.; Shirouzu, M.; et al. A Small-Molecule AdipoR Agonist for Type 2 Diabetes and Short Life in Obesity. *Nature* **2013**, doi:10.1038/nature12656.

377. Sapio, L.; Nigro, E.; Ragone, A.; Salzillo, A.; Illiano, M.; Spina, A.; Polito, R.; Daniele, A.; Naviglio, S. AdipoRon Affects Cell Cycle Progression and Inhibits Proliferation in Human Osteosarcoma Cells. *J. Oncol.* **2020**, doi:10.1155/2020/7262479.

378. Otvos, L. Potential Adiponectin Receptor Response Modifier Therapeutics. *Front. Endocrinol. (Lausanne).* **2019**, *10*, doi:10.3389/fendo.2019.00539.

379. Otvos, L.; Knappe, D.; Hoffmann, R.; Kovalszky, I.; Olah, J.; Hewitson, T.D.; Stawikowska, R.; Stawikowski, M.; Cudic, P.; Lin, F.; et al. Development of Second Generation Peptides Modulating Cellular Adiponectin Receptor Responses. *Front. Chem.* **2014**, doi:10.3389/fchem.2014.00093.

380. Kumar, P.; Smith, T.; Rahman, K.; Thorn, N.E.; Anania, F.A. Adiponectin Agonist ADP355 Attenuates CCL4-Induced Liver Fibrosis in Mice. *PLoS One* **2014**, doi:10.1371/journal.pone.0110405.

381. Wang, H.; Zhang, H.; Zhang, Z.; Huang, B.; Cheng, X.; Wang, D.; La Gahu, Z.; Xue, Z.; Da, Y.; Li, D.; et al. Adiponectin-Derived Active Peptide ADP355 Exerts Anti-Inflammatory and Anti-Fibrotic Activities in Thioacetamide-Induced Liver Injury. *Sci. Rep.* **2016**, doi:10.1038/srep19445.

382. Sung, H.K.; Mitchell, P.L.; Gross, S.; Marette, A.; Sweeney, G. ALY688 Elicits Adiponectin-Mimetic Signaling and Improves Insulin Action in Skeletal Muscle Cells. *Am. J. Physiol. - Cell Physiol.* **2022**, doi:10.1152/ajpcell.00603.2020.

383. Cho, S.; Dadson, K.; Sung, H.K.; Ayansola, O.; Mirzaesmaeili, A.; Noskovicova, N.; Zhao, Y.; Cheung, K.; Radisic, M.; Hinz, B.; et al. Cardioprotection by the Adiponectin Receptor Agonist ALY688 in a Preclinical Mouse Model of Heart Failure with Reduced Ejection Fraction (HFrEF). *Biomed. Pharmacother.* **2024**, doi:10.1016/j.biopha.2023.116119.

384. Hathout, Y.; Liang, C.; Ogundele, M.; Xu, G.; Tawalbeh, S.M.; Dang, U.J.; Hoffman, E.P.; Gordish-Dressman, H.; Conklin, L.S.; van den Anker, J.N.; et al. Disease-Specific and Glucocorticoid-Responsive Serum Biomarkers for Duchenne Muscular Dystrophy. *Sci. Rep.* **2019**, doi:10.1038/s41598-019-48548-9.

385. Zelikovich, A.S.; Quattrocelli, M.; Salamone, I.M.; Kuntz, N.L.; McNally, E.M. Moderate Exercise Improves Function and Increases Adiponectin in the Mdx Mouse Model of Muscular Dystrophy. *Sci. Rep.* **2019**, doi:10.1038/s41598-019-42203-z.

386. Abou-Samra, M.; Lecompte, S.; Schakman, O.; Noel, L.; Many, M.C.; Gailly, P.; Brichard, S.M. Involvement of Adiponectin in the Pathogenesis of Dystrophinopathy. *Skelet. Muscle* **2015**, doi:10.1186/s13395-015-0051-9.

387. Abou-Samra, M.; Selvais, C.M.; Boursereau, R.; Lecompte, S.; Noel, L.; Brichard, S.M. AdipoRon, a New Therapeutic Prospect for Duchenne Muscular Dystrophy. *J. Cachexia. Sarcopenia Muscle* **2020**, doi:10.1002/jcsm.12531.

388. Lecompte, S.; Abou-Samra, M.; Boursereau, R.; Noel, L.; Brichard, S.M. Skeletal Muscle Secretome in Duchenne Muscular Dystrophy: A Pivotal Anti-Inflammatory Role of Adiponectin. *Cell. Mol. Life Sci.* **2017**, doi:10.1007/s00018-017-2465-5.

389. Yamauchi, T.; Kamon, J.; Minokoshi, Y.; Ito, Y.; Waki, H.; Uchida, S.; Yamashita, S.; Noda, M.; Kita, S.; Ueki, K.; et al. Adiponectin Stimulates Glucose Utilization and Fatty-Acid Oxidation by Activating AMP-Activated Protein Kinase. *Nat. Med.* **2002**, doi:10.1038/nm788.

390. Iwabu, M.; Yamauchi, T.; Okada-Iwabu, M.; Sato, K.; Nakagawa, T.; Funata, M.; Yamaguchi, M.; Namiki, S.; Nakayama, R.; Tabata, M.; et al. Adiponectin and AdipoR1 Regulate PGC-1α and Mitochondria by Ca 2+ and AMPK/SIRT1. *Nature* **2010**, doi:10.1038/nature08991.

391. Juban, G.; Saclier, M.; Yacoub-Youssef, H.; Kernou, A.; Arnold, L.; Boisson, C.; Ben Larbi, S.; Magnan, M.; Cuvellier, S.; Théret, M.; et al. AMPK Activation Regulates LTBP4-Dependent TGF-B1 Secretion by Pro-Inflammatory Macrophages and Controls Fibrosis in Duchenne Muscular Dystrophy. *Cell Rep.* **2018**, doi:10.1016/j.celrep.2018.10.077.

392. Bellissimo, C.A.; Gandhi, S.; Castellani, L.N.; Murugathasan, M.; Delfinis, L.J.; Thuhan, A.; Garibotti, M.C.; Seo, Y.; Rebalka, I.A.; Hsu, H.H.; et al. The Slow-Release Adiponectin Analog ALY688-SR Modifies Early-Stage Disease Development in the D2. Mdx Mouse Model of Duchenne Muscular Dystrophy. *Am. J. Physiol. Physiol.* **2024**, *326*, C1011–C1026, doi:10.1152/ajpcell.00638.2023.

393. Bellissimo, C.A.; Castellani, L.N.; Finch, M.S.; Murugathasan, M.; Gandhi, S.; Sweeney, G.; Abdul-Sater, A.A.; MacPherson, R.E.K.; Perry, C.G.R. Memory Impairment in the D2.Mdx Mouse Model of Duchenne Muscular Dystrophy Is Prevented by the Adiponectin Receptor Agonist ALY688. *Exp. Physiol.* **2023**, doi:10.1113/EP091274.

394. Boursereau, R.; Abou-Samra, M.; Lecompte, S.; Noel, L.; Brichard, S.M. Downregulation of the NLRP3 Inflammasome by Adiponectin Rescues Duchenne Muscular Dystrophy. *BMC Biol.* **2018**, doi:10.1186/s12915-018-0501-z.

395. Crisafulli, S.; Sultana, J.; Fontana, A.; Salvo, F.; Messina, S.; Trifirò, G. Global Epidemiology of Duchenne Muscular Dystrophy: An Updated Systematic Review and Meta-Analysis. *Orphanet J. Rare Dis.* **2020**, *15*, 141, doi:10.1186/s13023-020-01430-8.

396. Coley, W.D.; Bogdanik, L.; Vila, M.C.; Yu, Q.; Van Der Meulen, J.H.; Rayavarapu, S.; Novak, J.S.; Nearing, M.; Quinn, J.L.; Saunders, A.; et al. Effect of Genetic Background on the Dystrophic Phenotype in Mdx Mice. *Hum. Mol. Genet.* **2016**, doi:10.1093/hmg/ddv460.

397. Putten, M.; Putker, K.; Overzier, M.; Adamzek, W.A.; Pasteuning-Vuhman, S.; Plomp, J.J.; Aartsma-Rus, A. Natural Disease History of the D2-mdx Mouse Model for Duchenne Muscular Dystrophy. *FASEB J.* **2019**, *33*, 8110–8124, doi:10.1096/fj.201802488R.

398. Cohn, R.D.; Campbell, K.P. Molecular Basis of Muscular Dystrophies. *Muscle Nerve* **2000**, *23*, 1456–1471, doi:10.1002/1097-4598(200010)23:10<1456::AID-MUS2>3.0.CO;2-T.

399. Tan, L.B.; Jalil, J.E.; Pick, R.; Janicki, J.S.; Weber, K.T. Cardiac Myocyte Necrosis Induced by Angiotensin II. *Circ. Res.* **1991**, *69*, 1185–1195, doi:10.1161/01.RES.69.5.1185.

400. Anderson, K.R.; Sutton, M.G.S.J.; Lie, J.T. Histopathological Types of Cardiac Fibrosis in Myocardial Disease. *J. Pathol.* **1979**, *128*, 79–85, doi:10.1002/path.1711280205.

401. Esfahani, M.; Movahedian, A.; Baranchi, M.; Goodarzi, M.T. Adiponectin: An Adipokine with Protective Features against Metabolic Syndrome. *Iran. J. Basic Med. Sci.* **2015**, *18*, 430–442.

402. Sung, H.K.; Mitchell, P.L.; Gross, S.; Marette, A.; Sweeney, G. ALY688 Elicits Adiponectin-Mimetic Signaling and Improves Insulin Action in Skeletal Muscle Cells. *Am. J. Physiol. Physiol.* **2022**, *322*, C151–C163, doi:10.1152/ajpcell.00603.2020.

403. Abou-Samra, M.; Selvais, C.M.; Boursereau, R.; Lecompte, S.; Noel, L.; Brichard, S.M. AdipoRon, a New Therapeutic Prospect for Duchenne Muscular Dystrophy. *J. Cachexia. Sarcopenia Muscle* **2020**, *11*, 518–533, doi:10.1002/jcsm.12531.

404. Boland, B.J.; Silbert, P.L.; Groover, R. V.; Wollan, P.C.; Silverstein, M.D. Skeletal, Cardiac, and Smooth Muscle Failure in Duchenne Muscular Dystrophy. *Pediatr. Neurol.* **1996**, *14*, 7–12, doi:10.1016/0887-8994(95)00251-0.

405. Steinberg, G.R.; Kemp, B.E. AMPK in Health and Disease. *Physiol. Rev.* **2009**, *89*, 1025–1078, doi:10.1152/physrev.00011.2008.

406. Kulisz, A.; Chen, N.; Chandel, N.S.; Shao, Z.; Schumacker, P.T. Mitochondrial ROS Initiate Phosphorylation of P38 MAP Kinase during Hypoxia in Cardiomyocytes. *Am. J. Physiol. Cell. Mol. Physiol.*

2002, *282*, L1324–L1329, doi:10.1152/ajplung.00326.2001.

407. Xin, X.; Zhou, L.; Reyes, C.M.; Liu, F.; Dong, L.Q. APPL1 Mediates Adiponectin-Stimulated P38 MAPK Activation by Scaffolding the TAK1-MKK3-P38 MAPK Pathway. *Am. J. Physiol. Metab.* **2011**, *300*, E103–E110, doi:10.1152/ajpendo.00427.2010.

408. de Alvaro, C.; Teruel, T.; Hernandez, R.; Lorenzo, M. Tumor Necrosis Factor α Produces Insulin Resistance in Skeletal Muscle by Activation of Inhibitor KB Kinase in a P38 MAPK-Dependent Manner. *J. Biol. Chem.* **2004**, *279*, 17070–17078, doi:10.1074/jbc.M312021200.

409. Akimoto, M.; Maruyama, R.; Kawabata, Y.; Tajima, Y.; Takenaga, K. Antidiabetic Adiponectin Receptor Agonist AdipoRon Suppresses Tumour Growth of Pancreatic Cancer by Inducing RIPK1/ERK-Dependent Necroptosis. *Cell Death Dis.* **2018**, *9*, 804, doi:10.1038/s41419-018-0851-z.

410. Wissing, E.R.; Boyer, J.G.; Kwong, J.Q.; Sargent, M.A.; Karch, J.; McNally, E.M.; Otsu, K.; Molkentin, J.D. P38α MAPK Underlies Muscular Dystrophy and Myofiber Death through a Bax-Dependent Mechanism. *Hum. Mol. Genet.* **2014**, *23*, 5452–5463, doi:10.1093/hmg/ddu270.

411. Tong, M.; Saito, T.; Zhai, P.; Oka, S.-I.; Mizushima, W.; Nakamura, M.; Ikeda, S.; Shirakabe, A.; Sadoshima, J. Mitophagy Is Essential for Maintaining Cardiac Function During High Fat Diet-Induced Diabetic Cardiomyopathy. *Circ. Res.* **2019**, *124*, 1360–1371, doi:10.1161/CIRCRESAHA.118.314607.

412. Tandon, A.; Villa, C.R.; Hor, K.N.; Jefferies, J.L.; Gao, Z.; Towbin, J.A.; Wong, B.L.; Mazur, W.; Fleck, R.J.; Sticka, J.J.; et al. Myocardial Fibrosis Burden Predicts Left Ventricular Ejection Fraction and Is Associated with Age and Steroid Treatment Duration in Duchenne Muscular Dystrophy. *J. Am. Heart Assoc.* **2015**, *4*, doi:10.1161/JAHA.114.001338.

413. Dick, S.A.; Macklin, J.A.; Nejat, S.; Momen, A.; Clemente-Casares, X.; Althagafi, M.G.; Chen, J.; Kantores, C.; Hosseinzadeh, S.; Aronoff, L.; et al. Self-Renewing Resident Cardiac Macrophages Limit Adverse Remodeling Following Myocardial Infarction. *Nat. Immunol.* **2019**, doi:10.1038/s41590-018-0272-2.

414. O'Garra, A.; Barrat, F.J.; Castro, A.G.; Vicari, A.; Hawrylowicz, C. Strategies for Use of IL-10 or Its Antagonists in Human Disease. *Immunol. Rev.* 2008.

415. Steen, E.H.; Wang, X.; Balaji, S.; Butte, M.J.; Bollyky, P.L.; Keswani, S.G. The Role of the Anti-Inflammatory Cytokine Interleukin-10 in Tissue Fibrosis. *Adv. Wound Care* 2020.

416. Nitahara-Kasahara, Y.; Hayashita-Kinoh, H.; Chiyo, T.; Nishiyama, A.; Okada, H.; Takeda, S.; Okada, T. Dystrophic Mdx Mice Develop Severe Cardiac and Respiratory Dysfunction Following Genetic Ablation of the Anti-Inflammatory Cytokine IL-10. *Hum. Mol. Genet.* **2014**, *23*, 3990–4000, doi:10.1093/hmg/ddu113.

417. Frangogiannis, N.G. Transforming Growth Factor–β in Tissue Fibrosis. *J. Exp. Med.* **2020**, *217*, doi:10.1084/jem.20190103.

418. Gabbiani, G. The Role of Contractile Proteins in Wound Healing and Fibrocontractive Diseases. *Methods Achiev. Exp. Pathol.* **1979**, *9*, 187–206.

419. Hinz, B. Myofibroblasts. *Exp. Eye Res.* **2016**, *142*, 56–70, doi:10.1016/j.exer.2015.07.009.

420. Tomasek, J.J.; Gabbiani, G.; Hinz, B.; Chaponnier, C.; Brown, R.A. Myofibroblasts and Mechano-Regulation of Connective Tissue Remodelling. *Nat. Rev. Mol. Cell Biol.* **2002**, *3*, 349–363, doi:10.1038/nrm809.

421. Shinde, A. V.; Humeres, C.; Frangogiannis, N.G. The Role of α-Smooth Muscle Actin in Fibroblast-Mediated Matrix Contraction and Remodeling. *Biochim. Biophys. Acta - Mol. Basis Dis.* **2017**, *1863*, 298–309, doi:10.1016/j.bbadis.2016.11.006.

422. Araya, L.E.; Soni, I. V.; Hardy, J.A.; Julien, O. Deorphanizing Caspase-3 and Caspase-9 Substrates In and Out of Apoptosis with Deep Substrate Profiling. *ACS Chem. Biol.* **2021**, *16*, 2280–2296, doi:10.1021/acschembio.1c00456.

423. Bernardi, P.; Gerle, C.; Halestrap, A.P.; Jonas, E.A.; Karch, J.; Mnatsakanyan, N.; Pavlov, E.; Sheu, S.-S.; Soukas, A.A. Identity, Structure, and Function of the Mitochondrial Permeability Transition Pore: Controversies, Consensus, Recent Advances, and Future Directions. *Cell Death Differ.* **2023**, *30*, 1869–1885, doi:10.1038/s41418-023-01187-0.

424. Peterzan, M.A.; Lygate, C.A.; Neubauer, S.; Rider, O.J. Metabolic Remodeling in Hypertrophied and Failing Myocardium: A Review. *Am. J. Physiol. - Hear. Circ. Physiol.* 2017.

425. Shen, W.; Spindler, M.; Higgins, M.A.; Jin, N.; Gill, R.M.; Bloem, L.J.; Ryan, T.P.; Ingwall, J.S. The Fall in Creatine Levels and Creatine Kinase Isozyme Changes in the Failing Heart Are Reversible: Complex Post-Transcriptional Regulation of the Components of the CK System. *J. Mol. Cell. Cardiol.* **2005**, doi:10.1016/j.yjmcc.2005.05.003.

426. Neubauer, S.; Frank, M.; Hu, K.; Remkes, H.; Laser, A.; Horn, M.; Ertl, G.; Lohse, M.J. Changes of Creatine Kinase Gene Expression in Rat Heart Post-Myocardial Infarction. *J. Mol. Cell. Cardiol.* **1998**, doi:10.1006/jmcc.1998.0645.

427. Yamauchi, T.; Kamon, J.; Ito, Y.; Tsuchida, A.; Yokomizo, T.; Kita, S.; Sugiyama, T.; Miyagishi, M.; Hara, K.; Tsunoda, M.; et al. Cloning of Adiponectin Receptors That Mediate Antidiabetic Metabolic Effects. *Nature* **2003**, *423*, 762–769, doi:10.1038/nature01705.

428. Qin, F.; Liang, M.C.; Liang, C.S. Progressive Left Ventricular Remodeling, Myocyte Apoptosis, and Protein Signaling Cascades after Myocardial Infarction in Rabbits. In Proceedings of the Biochimica et Biophysica Acta - Molecular Basis of Disease; 2005.

429. Heusch, P.; Canton, M.; Aker, S.; Van De Sand, A.; Konietzka, I.; Rassaf, T.; Menazza, S.; Brodde, O.E.; Di Lisa, F.; Heusch, G.; et al. The Contribution of Reactive Oxygen Species and P38 Mitogen-Activated Protein Kinase to Myofilament Oxidation and Progression of Heart Failure in Rabbits. *Br. J. Pharmacol.* **2010**, doi:10.1111/j.1476-5381.2010.00793.x.

430. Tenhunen, O.; Rysä, J.; Ilves, M.; Soini, Y.; Ruskoaho, H.; Leskinen, H. Identification of Cell Cycle Regulatory and Inflammatory Genes as Predominant Targets of P38 Mitogen-Activated Protein Kinase in the Heart. *Circ. Res.* **2006**, doi:10.1161/01.RES.0000238387.85144.92.

431. Junqueira, L.C.U.; Bignolas, G.; Brentani, R.R. Picrosirius Staining plus Polarization Microscopy, a Specific Method for Collagen Detection in Tissue Sections. *Histochem. J.* **1979**, *11*, 447–455, doi:10.1007/BF01002772.

432. Hughes, M.C.; Ramos, S. V.; Turnbull, P.C.; Rebalka, I.A.; Cao, A.; Monaco, C.M.F.; Varah, N.E.; Edgett, B.A.; Huber, J.S.; Tadi, P.; et al. Early Myopathy in Duchenne Muscular Dystrophy Is Associated with Elevated Mitochondrial H2O2 Emission during Impaired Oxidative Phosphorylation. *J. Cachexia. Sarcopenia Muscle* **2019**, doi:10.1002/jcsm.12405.

433. Houde, V.P.; Donzelli, S.; Sacconi, A.; Galic, S.; Hammill, J.A.; Bramson, J.L.; Foster, R.A.; Tsakiridis, T.; Kemp, B.E.; Grasso, G.; et al. <scp>AMPK</Scp> B1 Reduces Tumor Progression and Improves Survival in P53 Null Mice. *Mol. Oncol.* **2017**, *11*, 1143–1155, doi:10.1002/1878-0261.12079.

434. Delfinis, L.J.; Bellissimo, C.A.; Gandhi, S.; DiBenedetto, S.N.; Garibotti, M.C.; Thuhan, A.K.; Tsitkanou, S.; Rosa-Caldwell, M.E.; Rahman, F.A.; Cheng, A.J.; et al. Muscle Weakness Precedes Atrophy during Cancer Cachexia and Is Linked to Muscle-Specific Mitochondrial Stress. *JCI Insight* **2022**, *7*, doi:10.1172/jci.insight.155147.

435. Perry, C.G.R.; Kane, D.A.; Lin, C.-T.; Kozy, R.; Cathey, B.L.; Lark, D.S.; Kane, C.L.; Brophy, P.M.; Gavin, T.P.; Anderson, E.J.; et al. Inhibiting Myosin-ATPase Reveals a Dynamic Range of Mitochondrial Respiratory Control in Skeletal Muscle. *Biochem. J.* **2011**, *437*, 215–222, doi:10.1042/BJ20110366.

436. Bellissimo, C.A.; Delfinis, L.J.; Hughes, M.C.; Turnbull, P.C.; Gandhi, S.; DiBenedetto, S.N.; Rahman, F.A.; Tadi, P.; Amaral, C.A.; Dehghani, A.; et al. Mitochondrial Creatine Sensitivity Is Lost in the D2. Mdx Model of Duchenne Muscular Dystrophy and Rescued by the Mitochondrial-Enhancing Compound Olesoxime. *Am. J. Physiol. Physiol.* **2023**, *324*, C1141–C1157, doi:10.1152/ajpcell.00377.2022.

437. Perry, C.G.R.; Heigenhauser, G.J.F.; Bonen, A.; Spriet, L.L. High-Intensity Aerobic Interval Training Increases Fat and Carbohydrate Metabolic Capacities in Human Skeletal Muscle. *Appl. Physiol. Nutr. Metab.* **2008**, *33*, 1112–1123, doi:10.1139/H08-097.

438. Cooper, M.A.; McCoin, C.; Pei, D.; Thyfault, J.P.; Koestler, D.; Wright, D.E. Reduced Mitochondrial Reactive Oxygen Species Production in Peripheral Nerves of Mice Fed a Ketogenic Diet. *Exp. Physiol.* **2018**, *103*, 1206–1212, doi:10.1113/EP087083.

439. Rahman, F.A.; Hian-Cheong, D.J.; Boonstra, K.; Ma, A.; Thoms, J.P.; Zago, A.S.; Quadrilatero, J. Augmented Mitochondrial Apoptotic Signaling Impairs C2C12 Myoblast Differentiation Following Cellular Aging through Sequential Passaging. *J. Cell. Physiol.* **2024**, doi:10.1002/jcp.31155.

440. Glickman, M.E.; Rao, S.R.; Schultz, M.R. False Discovery Rate Control Is a Recommended Alternative to Bonferroni-Type Adjustments in Health Studies. *J. Clin. Epidemiol.* **2014**, *67*, 850–857, doi:10.1016/j.jclinepi.2014.03.012.

441. Dalen, J.E.; Alpert, J.S.; Goldberg, R.J.; Weinstein, R.S. The Epidemic of the 20th Century: Coronary Heart Disease. *Am. J. Med.* 2014.

442. Knuuti, J. 2019 ESC Guidelines for the Diagnosis and Management of Chronic Coronary Syndromes The Task Force for the Diagnosis and Management of Chronic Coronary Syndromes of the European Society of Cardiology (ESC). *Russ. J. Cardiol.* **2020**, doi:10.15829/1560-4071-2020-2-3757.

443. Doenst, T.; Thiele, H.; Haasenritter, J.; Wahlers, T.; Massberg, S.; Haverich, A. The Treatment of Coronary Artery Disease—Current Status Six Decades after the First Bypass Operation. *Dtsch. Arztebl. Int.* **2022**, doi:10.3238/arztebl.m2022.0277.

444. Lesnefsky, E.J.; Chen, Q.; Tandler, B.; Hoppel, C.L. Mitochondrial Dysfunction and Myocardial Ischemia-Reperfusion: Implications for Novel Therapies. *Annu. Rev. Pharmacol. Toxicol.* 2017.

445. Jennings, R.B.; Reimer, K.A. The Cell Biology of Acute Myocardial Ischemia. *Annu. Rev. Med.* 1991.

446. Hool, L.C. What Cardiologists Should Know About Calcium Ion Channels and Their Regulation by Reactive Oxygen Species. *Hear. Lung Circ.* 2007.

447. Jaswal, J.S.; Keung, W.; Wang, W.; Ussher, J.R.; Lopaschuk, G.D. Targeting Fatty Acid and Carbohydrate Oxidation - A Novel Therapeutic Intervention in the Ischemic and Failing Heart. *Biochim. Biophys. Acta - Mol. Cell Res.* 2011.

448. Bond, J.M.; Herman, B.; Lemasters, J.J. Protection by Acidotic PH against Anoxia/Reoxygenation Injury to Rat Neonatal Cardiac Myocytes. *Biochem. Biophys. Res. Commun.* **1991**, doi:10.1016/0006-291X(91)91887-I.

449. Lemasters, J.J.; Bond, J.M.; Chacon, E.; Harper, I.S.; Kaplan, S.H.; Ohata, H.; Trollinger, D.R.; Herman, B.; Cascio, W.E. The PH Paradox in Ischemia-Reperfusion Injury to Cardiac Myocytes. *EXS* 1996.

450. Ashok, D.; Papanicolaou, K.; Sidor, A.; Wang, M.; Solhjoo, S.; Liu, T.; O'Rourke, B. Mitochondrial Membrane Potential Instability on Reperfusion after Ischemia Does Not Depend on Mitochondrial Ca2+ Uptake. *J. Biol. Chem.* **2023**, doi:10.1016/j.jbc.2023.104708.

451. Bugger, H.; Pfeil, K. Mitochondrial ROS in Myocardial Ischemia Reperfusion and Remodeling. *Biochim. Biophys. Acta - Mol. Basis Dis.* 2020.

452. Kumar, V.; Kitaeff, N.; Hampton, M.B.; Cannell, M.B.; Winterbourn, C.C. Reversible Oxidation of Mitochondrial Peroxiredoxin 3 in Mouse Heart Subjected to Ischemia and Reperfusion. *FEBS Lett.* **2009**, doi:10.1016/j.febslet.2009.02.018.

453. Matsushima, S.; Ide, T.; Yamato, M.; Matsusaka, H.; Hattori, F.; Ikeuchi, M.; Kubota, T.; Sunagawa, K.; Hasegawa, Y.; Kurihara, T.; et al. Overexpression of Mitochondrial Peroxiredoxin-3 Prevents Left Ventricular Remodeling and Failure after Myocardial Infarction in Mice. *Circulation* **2006**, doi:10.1161/CIRCULATIONAHA.105.582239.

454. Griffiths, E.J.; Halestrap, A.P. Mitochondrial Non-Specific Pores Remain Closed during Cardiac Ischaemia, but Open upon Reperfusion. *Biochem. J.* **1995**, doi:10.1042/bj3070093.

455. Paradies, G.; Petrosillo, G.; Pistolese, M.; Di Venosa, N.; Serena, D.; Ruggiero, F.M. Lipid Peroxidation and Alterations to Oxidative Metabolism in Mitochondria Isolated from Rat Heart Subjected to Ischemia and Reperfusion. *Free Radic. Biol. Med.* **1999**, doi:10.1016/S0891-5849(99)00032-5.

456. Kuznetsov, A. V.; Javadov, S.; Margreiter, R.; Grimm, M.; Hagenbuchner, J.; Ausserlechner, M.J. The Role of Mitochondria in the Mechanisms of Cardiac Ischemia-Reperfusion Injury. *Antioxidants* 2019.

457. Leist, M.; Single, B.; Castoldi, A.F.; Kühnle, S.; Nicotera, P. Intracellular Adenosine Triphosphate (ATP) Concentration: A Switch in the Decision between Apoptosis and Necrosis. *J. Exp. Med.* **1997**, doi:10.1084/jem.185.8.1481.

458. Lloyd, S.G.; Wang, P.; Zeng, H.; Chatham, J.C. Impact of Low-Flow Ischemia on Substrate Oxidation and Glycolysis in the Isolated Perfused Rat Heart. *Am. J. Physiol. - Hear. Circ. Physiol.* **2004**, doi:10.1152/ajpheart.00983.2003.

459. Liedtke, A.J.; Nellis, S.H.; Mjos, O.D. Effects of Reducing Fatty Acid Metabolism on Mechanical Function in Regionally Ischemic Hearts. *Am. J. Physiol. - Hear. Circ. Physiol.* **1984**, doi:10.1152/ajpheart.1984.247.3.h387.

460. Whitmer, J.T.; Idell-Wenger, J.A.; Rovetto, M.J.; Neely, J.R. Control of Fatty Acid Metabolism in Ischemic and Hypoxic Hearts. *J. Biol. Chem.* **1978**, doi:10.1016/s0021-9258(17)34720-8.

461. Lopaschuk, G.D.; Spafford, M.A.; Davies, N.J.; Wall, S.R. Glucose and Palmitate Oxidation in Isolated Working Rat Hearts Reperfused after a Period of Transient Global Ischemia. *Circ. Res.* **1990**, doi:10.1161/01.RES.66.2.546.

462. Hoffman, S.N.; TenBrook, J.A.; Wolf, M.P.; Pauker, S.G.; Salem, D.N.; Wong, J.B. A Meta-Analysis of Randomized Controlled Trials Comparing Coronary Artery Bypass Graft with Percutaneous Transluminal Coronary Angioplasty: One- to Eight-Year Outcomes. *J. Am. Coll. Cardiol.* **2003**, doi:10.1016/S0735-1097(03)00157-8.

463. Yusuf, S.; Zucker, D.; Passamani, E.; Peduzzi, P.; Takaro, T.; Fisher, L.D.; Kennedy, J.W.; Davis, K.; Killip, T.; Norris, R.; et al. Effect of Coronary Artery Bypass Graft Surgery on Survival: Overview of 10-Year Results from Randomised Trials by the Coronary Artery Bypass Graft Surgery Trialists Collaboration. *Lancet* **1994**, doi:10.1016/S0140-6736(94)91963-1.

464. Rihal, C.S.; Raco, D.L.; Gersh, B.J.; Yusuf, S. Indications for Coronary Artery Bypass Surgery and Percutaneous Coronary Intervention in Chronic Stable Angina: Review of the Evidence and Methodological Considerations. *Circulation* 2003.

465. Hillis, L.D.; Smith, P.K.; Bittl, J.A.; Bridges, C.R.; Byrne, J.G.; Cigarroa, J.E.; DiSesa, V.J.; Hiratzka, L.F.; Hutter, A.M.; Jessen, M.E.; et al. 2011 ACCF/AHA Guideline for Coronary Artery Bypass Graft Surgery a Report of the American College of Cardiology Foundation/American Heart Association Task Force on Practice Guidelines. *Circulation* **2011**, doi:10.1161/CIR.0b013e31823c074e.

466. He, G.W. Arterial Grafts for Coronary Artery Bypass Grafting: Biological Characteristics, Functional Classification, and Clinical Choice. *Ann. Thorac. Surg.* 1999.

467. Berger, A.; MacCarthy, P.A.; Siebert, U.; Carlier, S.; Wijns, W.; Heyndrickx, G.; Bartunek, J.; Vanermen, H.; De Bruyne, B. Long-Term Patency of Internal Mammary Artery Bypass Grafts: Relationship with Preoperative Severity of the Native Coronary Artery Stenosis. *Circulation* **2004**, doi:10.1161/01.CIR.0000141256.05740.69.

468. Loop, F.D.; Lytle, B.W.; Cosgrove, D.M.; Stewart, R.W.; Goormastic, M.; Williams, G.W.; Golding, L.A.R.; Gill, C.C.; Taylor, P.C.; Sheldon, W.C.; et al. Influence of the Internal-Mammary-Artery Graft on 10-Year Survival and Other Cardiac Events. *N. Engl. J. Med.* **1986**, doi:10.1056/nejm198601023140101.

469. Dobrin, P.; Canfield, T.; Moran, J.; Sullivan, H.; Pifarré, R. Coronary Artery Bypass. The Physiological Basis for Differences in Flow with Internal Mammary Artery and Saphenous Vein Grafts. *J. Thorac. Cardiovasc. Surg.* **1977**, doi:10.1016/s0022-5223(19)41361-5.

470. Otsuka, F.; Yahagi, K.; Sakakura, K.; Virmani, R. Why Is the Mammary Artery so Special and What Protects It from Atherosclerosis? *Ann Cardiothorac Surg* **2013**, doi:10.3978/j.issn.2225-319X.2013.07.06.

471. Afilalo, J.; Rasti, M.; Ohayon, S.M.; Shimony, A.; Eisenberg, M.J. Off-Pump vs. on-Pump Coronary Artery Bypass Surgery: An Updated Meta-Analysis and Meta-Regression of Randomized Trials. *Eur. Heart J.* 2012.

472. Andres, A.M.; Tucker, K.C.; Thomas, A.; Taylor, D.J.R.; Sengstock, D.; Jahania, S.M.; Dabir, R.; Pourpirali, S.; Brown, J.A.; Westbrook, D.G.; et al. Mitophagy and Mitochondrial Biogenesis in Atrial Tissue of Patients Undergoing Heart Surgery with Cardiopulmonary Bypass. *JCI Insight* **2017**, doi:10.1172/jci.insight.89303.

473. Turer, A.T.; Hill, J.A. Pathogenesis of Myocardial Ischemia-Reperfusion Injury and Rationale for Therapy. *Am. J. Cardiol.* 2010.

474. Karmazyn, M. The Myocardial Sodium-Hydrogen Exchanger (NHE) and Its Role in Mediating Ischemic and Reperfusion Injury. *Keio J. Med.* 1998.

475. Hutchins, G.M.; Bulkley, B.H. Correlation of Myocardial Contraction Band. Necrosis and Vascular Patency. A Study of Coronary Artery Bypass Graft Anastomoses at Branch Points. *Lab. Investig.* **1977**.

476. Bulkley, B.H.; Hutchins, G.M. Myocardial Consequences of Coronary Artery Bypass Graft Surgery. The Paradox of Necrosis in Areas of Revascularization. *Circulation* **1977**, doi:10.1161/01.cir.56.6.906.

477. Weman, S.M.; Karhunen, P.J.; Penttilä, A.; Järvinen, A.A.; Salminen, U.S.; Karl, T.R. Reperfusion Injury Associated with One-Fourth of Deaths after Coronary Artery Bypass Grafting. *Ann. Thorac. Surg.* **2000**, doi:10.1016/S0003-4975(00)01638-6.

478. Stanley, W.C. Myocardial Energy Metabolism during Ischemia and the Mechanisms of Metabolic Therapies. *J. Cardiovasc. Pharmacol. Ther.* 2004.

479. Neubauer, S. The Failing Heart — An Engine Out of Fuel. *N. Engl. J. Med.* **2007**, doi:10.1056/nejmra063052.

480. Neely, J.R.; Morgan, H.E. Relationship between Carbohydrate and Lipid Metabolism and the Energy Balance of Heart Muscle. *Annu. Rev. Physiol.* 1974.

481. Bing, R.J.; Siegel, A.; Ungar, I.; Gilbert, M. Metabolism of the Human Heart. II. Studies on Fat, Ketone and Amino Acid Metabolism. *Am. J. Med.* **1954**, doi:10.1016/0002-9343(54)90365-4.

482. Opie, L.H. Metabolism of the Heart in Health and Disease. Part I. *Am. Heart J.* 1968.

483. Bers, D.M.; Barry, W.H.; Despa, S. Intracellular Na+ Regulation in Cardiac Myocytes. *Cardiovasc. Res.* 2003.

484. Xia, Z.; Li, H.; Irwin, M.G. Myocardial Ischaemia Reperfusion Injury: The Challenge of Translating Ischaemic and Anaesthetic Protection from Animal Models to Humans. *Br. J. Anaesth.* **2016**, doi:10.1093/bja/aew267.

485. Tani, M.; Neely, J.R. Role of Intracellular Na+ in Ca2+ Overload and Depressed Recovery of Ventricular Function of Reperfused Ischemic Rat Hearts: Possible Involvement of H+-Na+ and Na+-Ca2+ Exchange. *Circ. Res.* **1989**, doi:10.1161/01.RES.65.4.1045.

486. Depré, C.; Rider, M.H.; Hue, L. Mechanisms of Control of Heart Glycolysis. *Eur. J. Biochem.* 1998.

487. Panchal, A.R.; Comte, B.; Huang, H.; Dudar, B.; Roth, B.; Chandler, M.; Des Rosiers, C.; Brunengraber, H.; Stanley, W.C. Acute Hibernation Decreases Myocardial Pyruvate Carboxylation and Citrate Release. *Am. J.*

Physiol. - Hear. Circ. Physiol. **2001**, doi:10.1152/ajpheart.2001.281.4.h1613.

488. Panchal, A.R.; Comte, B.; Huang, H.; Kerwin, T.; Darvish, A.; Des Rosiers, C.; Brunengraber, H.; Stanley, W.C. Partitioning of Pyruvate between Oxidation and Anaplerosis in Swine Hearts. *Am. J. Physiol. - Hear. Circ. Physiol.* **2000**, doi:10.1152/ajpheart.2000.279.5.h2390.

489. Holness, M.J.; Sugden, M.C. Regulation of Pyruvate Dehydrogenase Complex Activity by Reversible Phosphorylation. In Proceedings of the Biochemical Society Transactions; 2003.

490. Sugden, M.C.; Holness, M.J. Recent Advances in Mechanisms Regulating Glucose Oxidation at the Level of the Pyruvate Dehydrogenase Complex by PDKs. *Am. J. Physiol. - Endocrinol. Metab.* 2003.

491. Robergs, R.A.; Ghiasvand, F.; Parker, D. Biochemistry of Exercise-Induced Metabolic Acidosis. *Am. J. Physiol. - Regul. Integr. Comp. Physiol.* 2004.

492. Opie, L.H. Effects of Regional Ischemia on Metabolism of Glucose and Fatty Acids. Relative Rates of Aerobic and Anaerobic Energy Production during Myocardial Infarction and Comparison with Effects of Anoxia. *Circ. Res.* **1976**.

493. King, L.M.; Opie, L.H. Glucose and Glycogen Utilisation in Myocardial Ischemia - Changes in Metabolism and Consequences for the Myocyte. *Mol. Cell. Biochem.* 1998.

494. Depre, C.; Veitch, K.; Hue, L. Role of Fructose 2,6-Bisphosphate in the Control of Glycolysis. Stimulation of Glycogen Synthesis by Lactate in the Isolated Working Rat Heart. In Proceedings of the Acta Cardiologica; 1993.

495. Finegan, B.A.; Lopaschuk, G.D.; Coulson, C.S.; Clanachan, A.S. Adenosine Alters Glucose Use during Ischemia and Reperfusion in Isolated Rat Hearts. *Circulation* **1993**, doi:10.1161/01.cir.87.3.900.

496. Finegan, B.A.; Lopaschuk, G.D.; Gandhi, M.; Clanachan, A.S. Inhibition of Glycolysis and Enhanced Mechanical Function of Working Rat Hearts as a Result of Adenosine A1 Receptor Stimulation during Reperfusion Following Ischaemia. *Br. J. Pharmacol.* **1996**, doi:10.1111/j.1476-5381.1996.tb15410.x.

497. Kerr, D.S.; DeBrosse, S.D.; Hoppel, C.L. Mitochondrial Disorders: Metabolic and Genetic Basis. In *Encyclopedia of the Neurological Sciences*; 2014 ISBN 9780123851574.

498. Murthy, M.S.R.; Pande, S. V. Mechanism of Carnitine Acylcarnitine Translocase-Catalyzed Import of Acylcarnitines into Mitochondria. *J. Biol. Chem.* **1984**, doi:10.1016/s0021-9258(17)47268-1.

499. McGarry, J.D.; Brown, N.F. The Mitochondrial Carnitine Palmitoyltransferase System. From Concept to Molecular Analysis. *Eur. J. Biochem.* 1997.

500. Lopaschuk, G.D.; Collins-Nakai, R.; Olley, P.M.; Montague, T.J.; McNeil, G.; Gayle, M.; Penkoske, P.; Finegan, B.A. Plasma Fatty Acid Levels in Infants and Adults after Myocardial Ischemia. *Am. Heart J.* **1994**, doi:10.1016/0002-8703(94)90010-8.

501. Kenyon, N.S.; Ranuncoli, A.; Masetti, M.; Chatzipetrou, M.; Ricordi, C. Islet Transplantation: Present and Future Perspectives. *Diabetes. Metab. Rev.* 1998.

502. Frayn, K.N.; Arner, P.; Yki-Järvinen, H. Fatty Acid Metabolism in Adipose Tissue, Muscle and Liver in Health and Disease. *Essays Biochem.* **2006**, doi:10.1042/bse0420089.

503. Ussher, J.R.; Lopaschuk, G.D. The Malonyl CoA Axis as a Potential Target for Treating Ischaemic Heart Disease. *Cardiovasc. Res.* 2008.

504. Dulloo, A.G.; Gubler, M.; Montani, J.P.; Seydoux, J.; Solinas, G. Substrate Cycling between de Novo Lipogenesis and Lipid Oxidation: A Thermogenic Mechanism against Skeletal Muscle Lipotoxicity and Glucolipotoxicity. *Int. J. Obes.* **2004**, doi:10.1038/sj.ijo.0802861.

505. Paulson, D.J.; Ward, K.M.; Shug, A.L. Malonyl CoA Inhibition of Carnitine Palmityltransferase in Rat Heart Mitochondria. *FEBS Lett.* **1984**, doi:10.1016/0014-5793(84)81201-6.

506. McGarry, J.D.; Leatherman, G.F.; Foster, D.W. Carnitine Palmitoyltransferase I. The Site of Inhibition of Hepatic Fatty Acid Oxidation by Malonyl-CoA. *J. Biol. Chem.* **1978**, doi:10.1016/s0021-9258(17)34693-8.

507. Reszko, A.E.; Kasumov, T.; David, F.; Thomas, K.R.; Jobbins, K.A.; Cheng, J.F.; Lopaschuk, G.D.; Dyck, J.R.B.; Diaz, M.; Des Rosiers, C.; et al. Regulation of Malonyl-CoA Concentration and Turnover in the Normal Heart. *J. Biol. Chem.* **2004**, doi:10.1074/jbc.M405488200.

508. Munday, M.R. Regulation of Mammalian Acetyl-CoA Carboxylase. In Proceedings of the Biochemical Society Transactions; 2002.

509. Comte, B.; Vincent, G.; Bouchard, B.; Jetté, M.; Cordeau, S.; Des Rosiers, C. A 13C Mass Isotopomer Study of Anaplerotic Pyruvate Carboxylation in Perfused Rat Hearts. *J. Biol. Chem.* **1997**, doi:10.1074/jbc.272.42.26125.

510. Poirier, M.; Vincent, G.; Reszko, A.E.; Bouchard, B.; Kelleher, J.K.; Brunengraber, H.; Des Rosiers, C. Probing the Link between Citrate and Malonyl-CoA in Perfused Rat Hearts. *Am. J. Physiol. - Hear. Circ. Physiol.* **2002**, doi:10.1152/ajpheart.00244.2002.

511. Randle, P.J.; Garland, P.B.; Hales, C.N.; Newsholme, E.A. THE GLUCOSE FATTY-ACID CYCLE ITS ROLE IN INSULIN SENSITIVITY AND THE METABOLIC DISTURBANCES OF DIABETES MELLITUS. *Lancet* **1963**, doi:10.1016/S0140-6736(63)91500-9.

512. Randle, P.J. Regulatory Interactions between Lipids and Carbohydrates: The Glucose Fatty Acid Cycle after 35 Years. *Diabetes. Metab. Rev.* 1998.

513. Dennis, S.C.; Gevers, W.; Opie, L.H. Protons in Ischemia: Where Do They Come from; Where Do They Go To? *J. Mol. Cell. Cardiol.* 1991.

514. Lysiak, W.; Toth, P.P.; Suelter, C.H.; Bieber, L.L. Quantitation of the Efflux of Acylcarnitines from Rat Heart, Brain, and Liver Mitochondria. *J. Biol. Chem.* **1986**, doi:10.1016/s0021-9258(18)67077-2.

515. Liu, Q.; Docherty, J.C.; Rendell, J.C.T.; Clanachan, A.S.; Lopaschuk, G.D. High Levels of Fatty Acids Delay the Recovery of Intracellular PH and Cardiac Efficiency in Post-Ischemic Hearts by Inhibiting Glucose Oxidation. *J. Am. Coll. Cardiol.* **2002**, doi:10.1016/S0735-1097(01)01803-4.

516. Taniguchi, M.; Wilson, C.; Hunter, C.A.; Pehowich, D.J.; Clanachan, A.S.; Lopaschuk, G.D. Dichloroacetate Improves Cardiac Efficiency after Ischemia Independent of Changes in Mitochondrial Proton Leak. *Am. J. Physiol. - Hear. Circ. Physiol.* **2001**, doi:10.1152/ajpheart.2001.280.4.h1762.

517. McVeigh, J.J.; Lopaschuk, G.D. Dichloroacetate Stimulation of Glucose Oxidation Improves Recovery of Ischemic Rat Hearts. *Am. J. Physiol. - Hear. Circ. Physiol.* **1990**, doi:10.1152/ajpheart.1990.259.4.h1079.

518. Stanley, W.C.; Chandler, M.P. Energy Metabolism in the Normal and Failing Heart: Potential for Therapeutic Interventions. *Heart Fail. Rev.* 2002.

519. Kuznetsov, A. V.; Schneeberger, S.; Seiler, R.; Brandacher, G.; Mark, W.; Steurer, W.; Saks, V.; Usson, Y.; Margreiter, R.; Gnaiger, E. Mitochondrial Defects and Heterogeneous Cytochrome c Release after Cardiac Cold Ischemia and Reperfusion. *Am. J. Physiol. - Hear. Circ. Physiol.* **2004**, doi:10.1152/ajpheart.00701.2003.

520. Lesnefsky, E.J.; Moghaddas, S.; Tandler, B.; Kerner, J.; Hoppel, C.L. Mitochondrial Dysfunction in Cardiac Disease: Ischemia - Reperfusion, Aging, and Heart Failure. *J. Mol. Cell. Cardiol.* 2001.

521. Di Lisa, F.; Menabò, R.; Canton, M.; Petronilli, V. The Role of Mitochondria in the Salvage and the Injury of the Ischemic Myocardium. *Biochim. Biophys. Acta - Bioenerg.* **1998**, doi:10.1016/S0005-2728(98)00121-2.

522. Bagur, R.; Tanguy, S.; Foriel, S.; Grichine, A.; Sanchez, C.; Pernet-Gallay, K.; Kaambre, T.; Kuznetsov, A. V.; Usson, Y.; Boucher, F.; et al. The Impact of Cardiac Ischemia/Reperfusion on the Mitochondria-Cytoskeleton Interactions. *Biochim. Biophys. Acta - Mol. Basis Dis.* **2016**, doi:10.1016/j.bbadis.2016.03.009.

523. Lucas, D.T.; Szweda, L.I. Cardiac Reperfusion Injury: Aging, Lipid Peroxidation, and Mitochondrial Dysfunction. *Proc. Natl. Acad. Sci. U. S. A.* **1998**, doi:10.1073/pnas.95.2.510.

524. Becker, L.B. New Concepts in Reactive Oxygen Species and Cardiovascular Reperfusion Physiology. *Cardiovasc. Res.* 2004.

525. Chen, Y.R.; Zweier, J.L. Cardiac Mitochondria and Reactive Oxygen Species Generation. *Circ. Res.* 2014.

526. Peoples, J.N.; Saraf, A.; Ghazal, N.; Pham, T.T.; Kwong, J.Q. Mitochondrial Dysfunction and Oxidative Stress in Heart Disease. *Exp. Mol. Med.* 2019, 1–13.

527. Bianchi, P.; Kunduzova, O.; Masini, E.; Cambon, C.; Bani, D.; Raimondi, L.; Seguelas, M.H.; Nistri, S.; Colucci, W.; Leducq, N.; et al. Oxidative Stress by Monoamine Oxidase Mediates Receptor-Independent Cardiomyocyte Apoptosis by Serotonin and Postischemic Myocardial Injury. *Circulation* **2005**, doi:10.1161/CIRCULATIONAHA.104.528133.

528. Hausenloy, D.J.; Yellon, D.M. Myocardial Ischemia-Reperfusion Injury: A Neglected Therapeutic Target. *J. Clin. Invest.* 2013.

529. Becker, L.B.; Vanden Hoek, T.L.; Shao, Z.H.; Li, C.Q.; Schumacker, P.T. Generation of Superoxide in Cardiomyocytes during Ischemia before Reperfusion. *Am. J. Physiol. - Hear. Circ. Physiol.* **1999**, doi:10.1152/ajpheart.1999.277.6.h2240.

530. Vanden Hoek, T.L.; Li, C.; Shao, Z.; Schumacker, P.T.; Becker, L.B. Significant Levels of Oxidants Are Generated by Isolated Cardiomyocytes during Ischemia Prior to Reperfusion. *J. Mol. Cell. Cardiol.* **1997**, doi:10.1006/jmcc.1997.0497.

531. Chen, Q.; Moghaddas, S.; Hoppel, C.L.; Lesnefsky, E.J. Ischemic Defects in the Electron Transport Chain Increase the Production of Reactive Oxygen Species from Isolated Rat Heart Mitochondria. *Am. J. Physiol. - Cell Physiol.* **2008**, doi:10.1152/ajpcell.00211.2007.

532. Galkin, A.; Abramov, A.Y.; Frakich, N.; Duchen, M.R.; Moncada, S. Lack of Oxygen Deactivates Mitochondrial Complex I: Implications for Ischemic Injury? *J. Biol. Chem.* **2009**, doi:10.1074/jbc.M109.054346.

533. Chouchani, E.T.; Pell, V.R.; Gaude, E.; Aksentijević, D.; Sundier, S.Y.; Robb, E.L.; Logan, A.; Nadtochiy, S.M.; Ord, E.N.J.; Smith, A.C.; et al. Ischaemic Accumulation of Succinate Controls Reperfusion Injury through Mitochondrial ROS. *Nature* **2014**, doi:10.1038/nature13909.

534. Mohsin, A.A.; Chen, Q.; Quan, N.; Rousselle, T.; Maceyka, M.W.; Samidurai, A.; Thompson, J.; Hu, Y.; Li, J.; Lesnefsky, E.J. Mitochondrial Complex I Inhibition by Metformin Limits Reperfusion Injury. *J. Pharmacol. Exp. Ther.* **2019**, doi:10.1124/jpet.118.254300.

535. Lesnefsky, E.J.; Gudz, T.I.; Migita, C.T.; Ikeda-Saito, M.; Hassan, M.O.; Turkaly, P.J.; Hoppel, C.L. Ischemic Injury to Mitochondrial Electron Transport in the Aging Heart: Damage to the Iron-Sulfur Protein Subunit of Electron Transport Complex III. *Arch. Biochem. Biophys.* **2001**, doi:10.1006/abbi.2000.2066.

536. Pasdois, P.; Beauvoit, B.; Tariosse, L.; Vinassa, B.; Bonoron-Adèle, S.; Dos Santos, P. MitoKATP - Dependent Changes in Mitochondrial Volume and in Complex II Activity during Ischemic and Pharmacological Preconditioning of Langendorff-Perfused Rat Heart. *J. Bioenerg. Biomembr.* **2006**, doi:10.1007/s10863-006-9016-3.

537. Lesnefsky, E.J.; Tandler, B.; Ye, J.; Slabe, T.J.; Turkaly, J.; Hoppel, C.L. Myocardial Ischemia Decreases Oxidative Phosphorylation through Cytochrome Oxidase in Subsarcolemmal Mitochondria. *Am. J. Physiol. - Hear. Circ. Physiol.* **1997**, doi:10.1152/ajpheart.1997.273.3.h1544.

538. Lesnefsky, E.J.; Chen, Q.; Moghaddas, S.; Hassan, M.O.; Tandler, B.; Hoppel, C.L. Blockade of Electron Transport during Ischemia Protects Cardiac Mitochondria. *J. Biol. Chem.* **2004**, doi:10.1074/jbc.M409720200.

539. Chen, Q.; Moghaddas, S.; Hoppel, C.L.; Lesnefsky, E.J. Reversible Blockade of Electron Transport during

Ischemia Protects Mitochondria and Decreases Myocardial Injury Following Reperfusion. *J. Pharmacol. Exp. Ther.* **2006**, doi:10.1124/jpet.106.110262.

540. Petrosillo, G.; Ruggiero, F.M.; Di Venosa, N.; Paradies, G. Decreased Complex III Activity in Mitochondria Isolated from Rat Heart Subjected to Ischemia and Reperfusion: Role of Reactive Oxygen Species and Cardiolipin. *FASEB J.* **2003**, doi:10.1096/fj.02-0729fje.

541. Gadicherla, A.K.; Stowe, D.F.; Antholine, W.E.; Yang, M.; Camara, A.K.S. Damage to Mitochondrial Complex i during Cardiac Ischemia Reperfusion Injury Is Reduced Indirectly by Anti-Anginal Drug Ranolazine. *Biochim. Biophys. Acta - Bioenerg.* **2012**, doi:10.1016/j.bbabio.2011.11.021.

542. Paradies, G.; Petrosillo, G.; Pistolese, M.; Di Venosa, N.; Federici, A.; Ruggiero, F.M. Decrease in Mitochondrial Complex I Activity in Ischemic/Reperfused Rat Heart: Involvement of Reactive Oxygen Species and Cardiolipin. *Circ. Res.* **2004**, doi:10.1161/01.RES.0000109416.56608.64.

543. Jeong, S.J.; Park, J.G.; Oh, G.T. Peroxiredoxins as Potential Targets for Cardiovascular Disease. *Antioxidants* 2021.

544. Montrief, T.; Koyfman, A.; Long, B. Coronary Artery Bypass Graft Surgery Complications: A Review for Emergency Clinicians. *Am. J. Emerg. Med.* 2018.

545. Ketema, E.B.; Ahsan, M.; Zhang, L.; Karwi, Q.G.; Lopaschuk, G.D. Protein Lysine Acetylation Does Not Contribute to the High Rates of Fatty Acid Oxidation Seen in the Post-Ischemic Heart. *Sci. Rep.* **2024**, doi:10.1038/s41598-024-51571-0.

546. Smit, M.; Coetzee, A.R.; Lochner, A. The Pathophysiology of Myocardial Ischemia and Perioperative Myocardial Infarction. *J. Cardiothorac. Vasc. Anesth.* 2020.

547. Folmes, C.D.L.; Sowah, D.; Clanachan, A.S.; Lopaschuk, G.D. High Rates of Residual Fatty Acid Oxidation during Mild Ischemia Decrease Cardiac Work and Efficiency. *J. Mol. Cell. Cardiol.* **2009**, doi:10.1016/j.yjmcc.2009.03.005.

548. Liedtke, A.J.; DeMaison, L.; Eggleston, A.M.; Cohen, L.M.; Nellis, S.H. Changes in Substrate Metabolism and Effects of Excess Fatty Acids in Reperfused Myocardium. *Circ. Res.* **1988**, doi:10.1161/01.RES.62.3.535.

549. Heusch, G. Regulation of Coronary Blood Flow in Normal and Ischemic States: Myocardial Ischemia: Lack of Coronary Blood Flow, Myocardial Oxygen Supply-Demand Imbalance, or What? *Am. J. Physiol. - Hear. Circ. Physiol.* **2019**.

550. Kudo, N.; Barr, A.J.; Barr, R.L.; Desai, S.; Lopaschuk, G.D. High Rates of Fatty Acid Oxidation during Reperfusion of Ischemic Hearts Are Associated with a Decrease in Malonyl-CoA Levels Due to an Increase in 5′-AMP-Activated Protein Kinase Inhibition of Acetyl-CoA Carboxylase. *J. Biol. Chem.* **1995**, doi:10.1074/jbc.270.29.17513.

551. Zheng, P.; Wu, H.; Gu, Y.; Li, L.; Hu, R.; Ma, W.; Bian, Z.; Liu, N.; Yang, D.; Chen, X. Atorvastatin Ameliorates Lipid Overload-Induced Mitochondrial Dysfunction and Myocardial Hypertrophy by Decreasing Fatty Acid Oxidation through Inactivation of the p-STAT3/CPT1 Pathway. *Biomed. Pharmacother.* **2023**, doi:10.1016/j.biopha.2022.114024.

552. Harhous, Z.; Booz, G.W.; Ovize, M.; Bidaux, G.; Kurdi, M. An Update on the Multifaceted Roles of STAT3 in the Heart. *Front. Cardiovasc. Med.* 2019.

553. Fuchs, M.; Hilfiker, A.; Kaminski, K.; Hilfiker-Kleiner, D.; Guener, Z.; Klein, G.; Podewski, E.; Schieffer, B.; Rose-John, S.; Drexler, H. Role of Interleukin-6 for LV Remodeling and Survival after Experimental Myocardial Infarction. *FASEB J.* **2003**.

554. Omura, T.; Yoshiyama, M.; Ishikura, F.; Kobayashi, H.; Takeuchi, K.; Beppu, S.; Yoshikawa, J. Myocardial Ischemia Activates the JAK-STAT Pathway through Angiotensin II Signaling in in Vivo Myocardium of Rats. *J. Mol. Cell. Cardiol.* **2001**, doi:10.1006/jmcc.2000.1303.

555. Hilfiker-Kleiner, D.; Hilfiker, A.; Fuchs, M.; Kaminski, K.; Schaefer, A.; Schieffer, B.; Hillmer, A.; Schmiedl, A.; Ding, Z.; Podewski, E.; et al. Signal Transducer and Activator of Transcription 3 Is Required for Myocardial Capillary Growth, Control of Interstitial Matrix Deposition, and Heart Protection from Ischemic Injury. *Circ. Res.* **2004**, doi:10.1161/01.RES.0000134921.50377.61.

556. Sawa, Y.; Ichikawa, H.; Kagisaki, K.; Ohata, T.; Matsuda, H. Interleukin-6 Derived from Hypoxic Myocytes Promotes Neutrophil-Mediated Reperfusion Injury in Myocardium. *J. Thorac. Cardiovasc. Surg.* **1998**, doi:10.1016/S0022-5223(98)70018-2.

557. Dyck, J.R.B.; Cheng, J.F.; Stanley, W.C.; Barr, R.; Chandler, M.P.; Brown, S.; Wallace, D.; Arrhenius, T.; Harmon, C.; Yang, G.; et al. Malonyl Coenzyme a Decarboxylase Inhibition Protects the Ischemic Heart by Inhibiting Fatty Acid Oxidation and Stimulating Glucose Oxidation. *Circ. Res.* **2004**, doi:10.1161/01.res.0000129255.19569.8f.

558. Tian, H.; Zhao, X.; Zhang, Y.; Xia, Z. Abnormalities of Glucose and Lipid Metabolism in Myocardial Ischemia-Reperfusion Injury. *Biomed. Pharmacother.* 2023.

559. Rawat, D.K.; Hecker, P.; Watanabe, M.; Chettimada, S.; Levy, R.J.; Okada, T.; Edwards, J.G.; Gupte, S.A. Glucose-6-Phosphate Dehydrogenase and NADPH Redox Regulates Cardiac Myocyte L-Type Calcium Channel Activity and Myocardial Contractile Function. *PLoS One* **2012**, doi:10.1371/journal.pone.0045365.

560. He, H.; Mulhern, R.M.; Oldham, W.M.; Xiao, W.; Lin, Y.D.; Liao, R.; Loscalzo, J. L-2-Hydroxyglutarate Protects Against Cardiac Injury via Metabolic Remodeling. *Circ. Res.* **2022**, doi:10.1161/CIRCRESAHA.122.321227.

561. Kato, T.; Niizuma, S.; Inuzuka, Y.; Kawashima, T.; Okuda, J.; Tamaki, Y.; Iwanaga, Y.; Narazaki, M.; Matsuda, T.; Soga, T.; et al. Analysis of Metabolic Remodeling in Compensated Left Ventricular Hypertrophy and Heart Failure. *Circ. Hear. Fail.* **2010**, doi:10.1161/CIRCHEARTFAILURE.109.888479.

562. Anderson, R.E.; Brismar, K.; Barr, G.; Ivert, T. Effects of Cardiopulmonary Bypass on Glucose Homeostasis after Coronary Artery Bypass Surgery. *Eur. J. Cardio-thoracic Surg.* **2005**, doi:10.1016/j.ejcts.2005.05.025.

563. Anderson, E.J.; Kypson, A.P.; Rodriguez, E.; Anderson, C.A.; Lehr, E.J.; Neufer, P.D. Substrate-Specific Derangements in Mitochondrial Metabolism and Redox Balance in the Atrium of the Type 2 Diabetic Human Heart. *J. Am. Coll. Cardiol.* **2009**, doi:10.1016/j.jacc.2009.07.031.

564. Anderson, E.J.; Efird, J.T.; Davies, S.W.; O'Neal, W.T.; Darden, T.M.; Thayne, K.A.; Katunga, L.A.; Kindell, L.C.; Ferguson, T.B.; Anderson, C.A.; et al. Monoamine Oxidase Is a Major Determinant of Redox Balance in Human Atrial Myocardium and Is Associated with Postoperative Atrial Fibrillation. *J. Am. Heart Assoc.* **2014**, doi:10.1161/JAHA.113.000713.

565. Stretton, C.; Pugh, J.N.; McDonagh, B.; McArdle, A.; Close, G.L.; Jackson, M.J. 2-Cys Peroxiredoxin Oxidation in Response to Hydrogen Peroxide and Contractile Activity in Skeletal Muscle: A Novel Insight into Exercise-Induced Redox Signalling? *Free Radic. Biol. Med.* **2020**, doi:10.1016/j.freeradbiomed.2020.06.020.

566. Pesta, D.; Gnaiger, E. High-Resolution Respirometry: OXPHOS Protocols for Human Cells and Permeabilized Fibers from Small Biopsies of Human Muscle. *Methods Mol. Biol.* **2012**, doi:10.1007/978-1-61779-382-0_3.

567. Perry, C.G.R.; Kane, D.A.; Lanza, I.R.; Neufer, P.D. Methods for Assessing Mitochondrial Function in Diabetes. *Diabetes* 2013, 1041–1053.

568. Hughes, M.C.; Ramos, S. V.; Turnbull, P.C.; Nejatbakhsh, A.; Baechler, B.L.; Tahmasebi, H.; Laham, R.; Gurd, B.J.; Quadrilatero, J.; Kane, D.A.; et al. Mitochondrial Bioenergetics and Fiber Type Assessments in Microbiopsy vs. Bergstrom Percutaneous Sampling of Human Skeletal Muscle. *Front. Physiol.* **2015**, doi:10.3389/fphys.2015.00360.

569. Bellissimo, C.A.; Delfinis, L.J.; Hughes, M.C.; Turnbull, P.C.; Gandhi, S.; DiBenedetto, S.N.; Rahman,

F.A.; Tadi, P.; Amaral, C.A.; Dehghani, A.; et al. Mitochondrial Creatine Sensitivity Is Lost in the D2.Mdx Model of Duchenne Muscular Dystrophy and Rescued by the Mitochondrial-Enhancing Compound Olesoxime. *Am. J. Physiol. - Cell Physiol.* **2023**, doi:10.1152/ajpcell.00377.2022.

570. Brown, D.A.; Perry, J.B.; Allen, M.E.; Sabbah, H.N.; Stauffer, B.L.; Shaikh, S.R.; Cleland, J.G.F.; Colucci, W.S.; Butler, J.; Voors, A.A.; et al. Expert Consensus Document: Mitochondrial Function as a Therapeutic Target in Heart Failure. *Nat. Rev. Cardiol.* **2017**, doi:10.1038/nrcardio.2016.203.

571. Hughes, M.C.; Ramos, S. V.; Turnbull, P.C.; Edgett, B.A.; Huber, J.S.; Polidovitch, N.; Schlattner, U.; Backx, P.H.; Simpson, J.A.; Perry, C.G.R. Impairments in Left Ventricular Mitochondrial Bioenergetics Precede Overt Cardiac Dysfunction and Remodelling in Duchenne Muscular Dystrophy. *J. Physiol.* **2020**, *598*, doi:10.1113/JP277306.

572. Burelle, Y.; Khairallah, M.; Ascah, A.; Allen, B.G.; Deschepper, C.F.; Petrof, B.J.; Des Rosiers, C. Alterations in Mitochondrial Function as a Harbinger of Cardiomyopathy: Lessons from the Dystrophic Heart. *J. Mol. Cell. Cardiol.* 2010.

573. Weman, S.M.; Karhunen, P.J.; Penttilä, A.; Järvinen, A.A.; Salminen, U.S.; Karl, T.R. Reperfusion Injury Associated with One-Fourth of Deaths after Coronary Artery Bypass Grafting. *Ann. Thorac. Surg.* **2000**, *70*, 807–812, doi:10.1016/S0003-4975(00)01638-6.

574. Nigro, G.; Comi, L.I.; Limongelli, F.M.; Giugliano, M.A.M.; Politano, L.; Petretta, V.; Passamano, L.; Stefanelli, S. Prospective Study of X-linked Progressive Muscular Dystrophy in Campania. *Muscle Nerve* **1983**, doi:10.1002/mus.880060403.

575. Barbin, I.C.C.; Pereira, J.A.; Bersan Rovere, M.; de Oliveira Moreira, D.; Marques, M.J.; Santo Neto, H. Diaphragm Degeneration and Cardiac Structure in Mdx Mouse: Potential Clinical Implications for Duchenne Muscular Dystrophy. *J. Anat.* **2016**, doi:10.1111/joa.12443.

576. Bernal-Ramirez, J.; Diaz-Vesga, M.C.; Talamilla, M.; Mendez, A.; Quiroga, C.; Garza-Cervantes, J.A.; Lazaro-Alfaro, A.; Jerjes-Sanchez, C.; Henriquez, M.; Garcia-Rivas, G.; et al. Exploring Functional Differences between the Right and Left Ventricles to Better Understand Right Ventricular Dysfunction. *Oxid. Med. Cell. Longev.* **2021**, doi:10.1155/2021/9993060.

577. Andersen, S.; Nielsen-Kudsk, J.E.; Vonk Noordegraaf, A.; De Man, F.S. Right Ventricular Fibrosis: A Pathophysiological Factor in Pulmonary Hypertension? *Circulation* **2019**, doi:10.1161/CIRCULATIONAHA.118.035326.

578. Brentnall, M.; Rodriguez-Menocal, L.; De Guevara, R.L.; Cepero, E.; Boise, L.H. Caspase-9, Caspase-3 and Caspase-7 Have Distinct Roles during Intrinsic Apoptosis. *BMC Cell Biol.* **2013**, doi:10.1186/1471-2121-14-32.

579. Morroni, J.; Schirone, L.; Vecchio, D.; Nicoletti, C.; D'ambrosio, L.; Valenti, V.; Sciarretta, S.; Lozanoska-Ochser, B.; Bouchè, M. Accelerating the Mdx Heart Histo-Pathology through Physical Exercise. *Life* **2021**, doi:10.3390/life11070706.

580. Bujak, M.; Frangogiannis, N.G. The Role of TGF-β Signaling in Myocardial Infarction and Cardiac Remodeling. *Cardiovasc. Res.* 2007.

581. Chen, B.; Brickshawana, A.; Frangogiannis, N.G. The Functional Heterogeneity of Resident Cardiac Macrophages in Myocardial Injury: CCR2+ Cells Promote Inflammation, Whereas CCR2- Cells Protect. *Circ. Res.* 2019.

582. Hu, S.; Yang, M.; Huang, S.; Zhong, S.; Zhang, Q.; Ding, H.; Xiong, X.; Hu, Z.; Yang, Y. Different Roles of Resident and Non-Resident Macrophages in Cardiac Fibrosis. *Front. Cardiovasc. Med.* 2022.

583. Lei, X.; Qiu, S.; Yang, G.; Wu, Q. Adiponectin and Metabolic Cardiovascular Diseases: Therapeutic Opportunities and Challenges. *Genes Dis.* 2023.

584. Ouchi, N.; Walsh, K. Adiponectin as an Anti-Inflammatory Factor. *Clin. Chim. Acta* 2007, 24–30.

585. Ouchi, N.; Shibata, R.; Walsh, K. Cardioprotection by Adiponectin. *Trends Cardiovasc. Med.* 2006.

586. Neumeier, M.; Bauer, S.; Brühl, H.; Eisinger, K.; Kopp, A.; Abke, S.; Walter, R.; Schäffler, A.; Buechler, C. Adiponectin Stimulates Release of CCL2, -3, -4 and -5 While the Surface Abundance of CCR2 and -5 Is Simultaneously Reduced in Primary Human Monocytes. *Cytokine* **2011**, doi:10.1016/j.cyto.2011.08.017.

587. Liu, B.; Alaoui-Talibi, Z.E.L.; Clanachan, A.S.; Schulz, R.; Lopaschuk, G.D. Uncoupling of Contractile Function from Mitochondrial TCA Cycle Activity and MV̇O2 during Reperfusion of Ischemic Hearts. *Am. J. Physiol. - Hear. Circ. Physiol.* **1996**, doi:10.1152/ajpheart.1996.270.1.h72.

588. Liu, B.; Clanachan, A.S.; Schulz, R.; Lopaschuk, G.D. Cardiac Efficiency Is Improved after Ischemia by Altering Both the Source and Fate of Protons. *Circ. Res.* **1996**, doi:10.1161/01.RES.79.5.940.

589. Lopaschuk, G.D.; Stanley, W.C. Glucose Metabolism in the Ischemic Heart. *Circulation* 1997.

590. Chen, S.; Zou, Y.; Song, C.; Cao, K.; Cai, K.; Wu, Y.; Zhang, Z.; Geng, D.; Sun, W.; Ouyang, N.; et al. The Role of Glycolytic Metabolic Pathways in Cardiovascular Disease and Potential Therapeutic Approaches. *Basic Res. Cardiol.* 2023.

591. Tran, D.H.; Wang, Z. V. Glucose Metabolism in Cardiac Hypertrophy and Heart Failure. *J. Am. Heart Assoc.* 2019.

592. Jain, M.; Cui, L.; Brenner, D.A.; Wang, B.; Handy, D.E.; Leopold, J.A.; Loscalzo, J.; Apstein, C.S.; Liao, R. Increased Myocardial Dysfunction after Ischemia-Reperfusion in Mice Lacking Glucose-6-Phosphate Dehydrogenase. *Circulation* **2004**, doi:10.1161/01.CIR.0000112605.43318.CA.

593. Voit, A.; Patel, V.; Pachon, R.; Shah, V.; Bakhutma, M.; Kohlbrenner, E.; McArdle, J.J.; Dell'Italia, L.J.; Mendell, J.R.; Xie, L.H.; et al. Reducing Sarcolipin Expression Mitigates Duchenne Muscular Dystrophy and Associated Cardiomyopathy in Mice. *Nat. Commun.* **2017**, doi:10.1038/s41467-017-01146-7.

594. Hughes, M.C.; Ramos, S. V.; Turnbull, P.C.; Edgett, B.A.; Huber, J.S.; Polidovitch, N.; Schlattner, U.; Backx, P.H.; Simpson, J.A.; Perry, C.G.R. Impairments in Left Ventricular Mitochondrial Bioenergetics Precede Overt Cardiac Dysfunction and Remodelling in Duchenne Muscular Dystrophy. *J. Physiol.* **2020**, *598*, 1377–1392, doi:10.1113/JP277306.

595. Wong, H.S.; Dighe, P.A.; Mezera, V.; Monternier, P.A.; Brand, M.D. Production of Superoxide and Hydrogen Peroxide from Specific Mitochondrial Sites under Different Bioenergetic Conditions. *J. Biol. Chem.* 2017.

Appendix A: Additional Contributions

The following first-author review articles were significant components of my PhD and were adapted for the literature review to *Chapter 4*. Sections (and relevant Figures) from these reviews can be found in *Chapter 2*. More comprehensive versions are available online (see below).

A.1 First Author: Published

1) **Gandhi, S**, Sweeney, G, and Perry, CGR (2024). Recent Advances in Pre-Clinical Development of Adiponectin Receptor Agonist Therapies for Duchenne Muscular Dystrophy. *Biomedicines.* **12**(7):1407. DOI: 10.3390/biomedicines12071407

2) **Gandhi, S**, Sweeney, HL, Hart, CC, Han, R, and Perry, CGR (2024). Cardiomyopathy in Duchenne Muscular Dystrophy and the Potential for Mitochondrial Therapeutics to Improve Treatment Response. *Cells.* **13**(14):1168. DOI: 10.3390/cells13141168

The following work encompasses the additional contributions made throughout my PhD that are not included in my dissertation.

A.2 Co-Author: Published

1) Bellissimo, CA, **Gandhi, S**, Castellani, LN, Murugathasan, M, Delfinis, LJ, Thuhan, A, Garibotti, MC, Seo, Y, Rebalka, IA, Sweeney, G, Hawke, TJ, Sater, AA, and Perry, CGR (2024). The slow-release adiponectin analog ALY688-SR modifies early-stage disease development in the D2.*mdx* mouse model of Duchenne muscular dystrophy. *Am J Physiol Cell Physiol*. **326**(4):C1011-C1026. DOI: 10.1152/ajpcell.00638.2023

2) Delfinis, LJ, Ogilvie, LM, Khajehzadehshoushtar, S, **Gandhi, S**, Garibotti, MC, Thuhan, AK, Matuszewska, K, Periera, M, Jones, RG, Cheng, AJ, Hawke, TJ, Greene, NP, Murach, KA, Simpson, JA, Petrik, J, and Perry, CGR (2024). Muscle weakness and mitochondrial stress occur before metastasis in a novel mouse model of ovarian cancer cachexia. *Molecular Metabolism.* **86**(5):101976. DOI: 10.1016/j.molmet.2024.101976

3) Ferguson, EJ, Bureau, J, Stokes, T, Nyman, D, Seigel, J, **Gandhi, S**, Delfinis, LJ, Gurd, BJ, Perry, CGR, and McGlory, C (2024). Quantifying Variability Associated with High-

resolution Respirometry in Human Permeabilized Skeletal Muscle Fibers (2024). *Advanced Exercise and Health Science*. https://doi.org/10.1016/j.aehs.2024.05.006

4) Ogilvie, LM, Delfinis, LJ, Coyle-Asbil, B, Vudatha, V, Alshamali, R, Garlisi, B, Pereira, M, Matuszewska, K, Garibotti, MC, **Gandhi, S**, Brunt, KR, Trevino, JG, Perry, CGR, Petrik, J, and Simpson, JA (2024). Cardiac atrophy, dysfunction, and metabolic impairments: a cancer-induced heart failure phenotype. *American Journal of Pathology*. DOI: 10.1016/j.ajpath.2024.06.008

5) Bellissimo, CA, Castellani, LN, Finch, MS, Murugathasan, M, **Gandhi, S**, Sweeney, G, Sater, AA, MacPherson, REK, and Perry, CGR (2023). Memory impairment in the D2.*mdx* mouse model of Duchenne muscular dystrophy is prevented by the adiponectin receptor agonist ALY688. *Exp Physiol*. **108**(9):1108-1117. DOI: 10.1113/EP091274

6) Bellissimo, CA, Delfinis, LJ, Hughes, MC, Turnbull, PC, **Gandhi, S**, DiBenedetto, SN, Rahman, FA, Tadi, P, Amaral, CA, Dehghani, A, Cobley, JN, Quadrilatero, J, Schlattner U, and Perry, CGR (2023). Mitochondrial creatine sensitivity is lost in the D2.*mdx* model of Duchenne muscular dystrophy and rescued by the mitochondrial-enhancing compound Olesoxime. *Am J Physiol Cell Physiol*. **324**(5):C1141-C1157. DOI: 10.1152/ajpcell.00377.2022

7) Fuller, NZK, McCoin, CS, Stierwalt, H, Allen, J, **Gandhi, S**, Perry, CGR, Jambal, P, Shankar, K, and Thyfault, JP (2022). Oral combined contraceptives induce liver mitochondrial reactive oxygen species and whole-body metabolic adaptations in female mice. *J Physiol.* **600**(24):5215-5245. DOI: 10.1113/JP283733

8) Delfinis, LJ, Bellissimo, CA, **Gandhi, S**, DiBenedetto, SN, Rosa-Caldwell, ME, Rahman, FA, Wiggs, MP, Schlattner U, Quadrilatero, J, Greene, NP, and Perry, CGR (2022). Muscle weakness precedes atrophy during cancer cachexia and is associated with muscle-specific mitochondrial stress. *JCI Insight*. **7**(24):e155147. DOI: 10.1172/jci.insight.155147

9) **Gandhi, S**, and Perry, CGR (2020). Mapping the role of mitochondrial DRP1 in skeletal muscle health: is too much and too little a bad thing? *J Physiol.* **598**(17) DOI: 10.1113/JP280316

A.3 Co-Author: In Submission

1) Delfinis, LJ, Khajehzadehshoushtar, S, Flewwelling, L, Andrews, N, Garibotti, MC, **Gandhi, S**, Brahmbhatt, AN, Morris, BA, Garlisi, B, Lauks, S, Aitken, C, Cheng, AJ, Petrik, J, and Perry, CGR. SkQ1 treatment in a mouse model of ovarian cancer prevents early- and late-stage skeletal muscle weakness while modulating skeletal muscle calcium release. *In submission*.

A.4 Textbook chapter: *In press*

1. **Gandhi, S**, Brahmbhatt, AN, and Perry, CGR. Open Textbook of Exercise Physiology; Chapter 6: Energy Supply for Muscle Contraction. *In press.*

A.5 Co-Author: In progress

1) Khajehzadehshoushtar, S, Delfinis, LJ, Rahman, F, Garibotti, MC, **Gandhi, S**, Brahmbhatt, AN, Morris, BA, Garlisi, B, Lauks, S, Aitken, C, Petrik, J, Quadrilatero, J, and Perry, CGR. Exploring the relationship between mitochondrial-linked cell death and muscle atrophy during ovarian cancer progression. *In progress*.

Appendix B: Detailed Experimental Methods

B.1 ALY688-SR Drug Preparation

The test article is provided as a lyophilized powder. Each vial of Lot# ALL.1188.BR.01 contains 46.14 mg ALY688-SR. By weight, the lyophilized powder is 60% ALY688 peptide.

Diluent: The diluent for this lot is 1:5 PBS (1X, pH 7.4):water (DIO water or water for injection). This can be prepared and stored in the refrigerator. If possible, it should be sterile.

To reconstitute the entire vial:

1. Add 3 ± 0.1 mL of PBS:water diluent to vial, resulting in a 15.4 mg/mL suspension.
2. Vortex/hand swirl for 30-60 seconds. Visually inspect the contents of the vial to confirm that the suspension is uniform (no large particles).
3. Immediately load all suspension into syringes (within 5-10 minutes), using an 18- or 20-gauge needle to draw it up. The suspension will thicken over time, making it more difficult to work with (will stick to the inside of the vial, making it more difficult to remove.
4. Loaded syringes can be used immediately (suggest dosing within 30 mins of resuspension), or syringes can be stored frozen for use on a different day.
5. To use frozen syringes: let thaw at room temperature. Attach another syringe using a syringe or luer-lock connector. Gently mix the suspension to resuspend any settled particles, by moving the suspension back and forth between the connected syringes several times.

To reconstitute a partial vial:
Lyophilized powder can be aliquoted into smaller amounts (i.e. the amount needed for each day of dosing. Accurately weigh (± 1 mg) the desired amount into an appropriate container (i.e. small conical Eppendorf tube). Reconstitute with the appropriate amount of diluent for the desired concentration. Note that the lyophilized powder is 60% ALY688-SR peptide by weight, thus 25.6 mg of powder contains 15.4 mg ALY688-SR. Thus, an aliquot of 25.6 mg of powder would be resuspended with 1 mL of diluent to achieve a concentration of 15.4 mg/mL ALY688-SR.

Stock suspension can be further diluted with PBS as diluent. For instance, to prepare 3 mg/mL suspension: dilute the stock 15 mg/mL suspension 1:4 with PBS.

Sample dosing schemes:

Dose (mg/kg)	Avg Weight (kg)*	Total mg	ALY688-SR Concentration (mg/mL)	Injection Vol (mL)	Dose volume (mL/kg)
3	0.005	0.02	3	0.005	1.000
15	0.005	0.08	15	0.005	1.000
	Pup weight: 3-5 g				

3	0.025	0.08	3	0.025	1.000
15	0.025	0.38	15	0.025	1.000
	* Full grown mouse weight: 25 g				

B.2 ALY688-ER Drug Preparation

Dose Formulation:

1. Testing material is supplied as a sterile stock solution of ALY688-ER 40 mg/mL solution (store refrigerated 2-8°C at all times when not in use).
2. The pH of the solution is approximately 4.7. When diluted with high pH buffer, a suspension forms which results in an extended-release profile.
3. To formulate the SC dose (ALY688-ER suspension), ALY688-ER at 40 mg/mL will be mixed with PBS pH 9 (adjust the pH of the PBS using 1N NaOH to 9 ± 0.2) to create the ALY688-ER suspension at a final concentration of 15 mg/mL

Recommended dosing scheme:

Dose (mg/kg)	Avg Weight (kg)	Total mg	Concentration (mg/mL)	Injection Vol (mL)	Dose volume (mL/kg)	Number of Animals	Number of Doses/day	Overage	Total Volume/day (mL)
15	0.007	0.105	5	0.021	3.0	20	1	2	0.9

Per the dosing scheme above, a daily volume of 1 mL should be sufficient to dose 15 µL/mouse x 20 mice The dilution should be prepared fresh for each set of daily injections. The total daily volume can be adjusted if needed, using the same mixing ratios as described below.

To make 1 mL of 15 mg/mL ALY688-ER for each dosing day, follow these instructions:

Materials:

- Tube (2 mL Eppendorf or equivalent)
- Pipette with tips that can aliquot up to 1 mL
- 40 mg/mL ALY688-ER concentrate solution
- Diluent (1X PBS adjusted to pH 9)
- Insulin syringes (u-100, 0.3cc, 30-gauge needle) or a glass Hamilton syringe (50 or 100 µL), with luer lock and removable 27-gauge needle.

Instructions

- Remove the stock solution of 40 mg/mL ALY688-ER from the refrigerator, inspect for particulates. If the solution is not clear, make notes in the study documents
- With a pipettor, aliquot 0.875 mL of diluent (PBS, pH 9) into the tube
- With a pipettor, aliquot 0.125 mL of ALY688 (40 mg/mL) into the tube with the PBS
- Gently pipette up and down 5-10 times to mix the solution. The solution may be slightly cloudy, which indicates that a suspension has formed. It should flow as a normal aqueous solution, but if it becomes more viscous, should still be able to inject easily.
- Draw up the desired volume (3 µL/g x body weight (g) x number of mice injected per syringe) into the injection syringe.
- Be careful not to shear the solution when drawing up the syringe (i.e., when loading the syringe, do not press the plunger hard to push the solution back into the tube. Shearing of the solution will increase viscosity)

Notes:

- The 40 mg/mL ALY688-ER stock solution is sterile and does not contain a preservative. Care should be taken to avoid contamination (suggest pipetting within a BSC). If necessary, it can be re-sterilized through a 0.22 µM syringe filter (PES or PVDF membrane recommended).
- Multiple aliquots of 0.125 mL of ALY688-ER 40 mg/mL can be prepared in advance (one for each study day) and stored at 2-8°C in Eppendorf tubes until needed for the daily dilution.
- If the mixed suspension becomes too thick and will not draw up through the 30-gauge needle fixed to the insulin syringe, we suggest using a syringe with a removable needle (such as a 50 µL glass/Hamilton syringe) and drawing up the suspension with a larger diameter needle (27-gauge should work better), or directly into the syringe. Because of the dead space in the needle hub, it may need to be primed by loading suspension using a different syringe.

B.3 Caspase 8/3/9 Activity Assay

Sample Preparation:

1. Homogenize 10-15 mg of sample tissue in 19X volumes of Muscle Lysis Buffer. Do NOT add protease inhibitor
   *** Remember: you will need enough homogenate for 3 caspase assays in duplicate (90 µL) and 1 protein assay (10 µL)
2. Only homogenize 3-4 samples at one time. For example, if you have 4 groups, homogenize 1 sample from each group and proceed to step #3. As first set of samples are incubating on ice, start homogenizing next set
3. Incubate on ice for 15 minutes, centrifuge at 1000 g for 10 mins at 4°C
4. Transfer supernatant to new Eppendorf tube, and store in -80°C freezer until needed

Caspase Assay:

1. Try to run all samples on one plate and run only 1 caspase type per plate. If all samples do not fit in one plate, split samples into even groups in two or more plates. If required, make sure a standard is in each plate so you can normalize values to the plate
2. Set fluorometer to the correct excitation and emission wavelengths for the substrates in question (excitation: 360 nm, emission: 440 nm)
3. Prepare all appropriate working solutions for the assay(s) to be performed
   a. Do everything in DUPLICATE
   b. Be sure to keep fluorogenic substrates, inhibitors, and positive controls in the dark and on ice until needed (i.e. in a drawer or a cupboard)
   c. Assay is performed at room temperature. Make sure the temperature is turned off on the plate reader!
4. Use the following table to work out volumes of each solution to be plated (total volume of each well is 100 µL):

	1X Assay Buffer	**Positive control**	**Unknown sample**	**Inhibitor**	**Substrate**
Blank (AB only)	100 µL	---	---	---	---
AB + substrate	90 µL	---	---	---	10 µL
AB + substrate + positive control	88 µL (cas-3, cas-8) 80 µL (new-cas-9)	2 µL (cas-3, cas-8) 10 µL (new-cas-9)	---	---	10 µL
AB + substrate + positive	86 µL	2 µL	---	2 µL	10 µL

control + inhibitor	(cas-3, cas-8) 78 µL (new-cas-9)	(cas-3, cas-8) 10 µL (new-cas-9)			
Unknown sample + Substrate	75 µL	---	15 µL*	---	10 µL
Unknown sample + inhibitor + substrate	73 µL	---	15 µL*	2 µL	10 µL

* If initial sample volume is low, you can use 10 µL here (adjust assay buffer accordingly)

5. Add the necessary amount of 1X Assay Buffer to each well of BLACK 96-well plate, as calculated from the table above
6. Add necessary inhibitors to appropriate wells
7. Place positive control or unknown samples into appropriate wells
8. Using repeater pipette, dispense 10 µL of substrate into appropriate wells
9. Place the plate in the spectrofluorometer and read at 15-minute intervals for 2-3 hours

Data Analysis

1. Pick a time point where all samples have positive activity (usually 1 or 2 hours into assay run time)
2. Calculate the Gross Fluorescence of each unknown sample (2 wells per sample) and subtract the associated zero time points. Next, calculate the Gross Fluorescence of the "Assay Buffer + Substrate" wells and subtract the associated zero time point. If this number is positive, subtract it from the unknown Gross Fluorescence; if it is negative, do not subtract. This gives the Mean Net Fluorescence

   Net Fluorescence = $D_{unknown} - D_{AB+substrate}$

   where

   $D_{unknown}$ = difference between unknown sample fluorescence at chosen time point and zero time point

   $D_{AB+substrate}$ = difference between Assay Buffer (AB) + Substrate fluorescence at chosen time point and zero time point
3. Calculate the Mean Net Fluorescence by taking the mean of the original and duplicate net fluorescence values.
4. Normalize the Mean Net Fluorescence obtained for each sample to that sample's protein concentration (see Western procedures for protein assay procedure)

Reagents

- Muscle Lysis Buffer
- 2X Caspase Assay Buffer

- Substrates
    - Caspase-3: Ac-DEVD-AMC [prod. # 260-031-M005, Alexis Biochemicals]
    - Caspase-8: Ac-IETD-AMC [prod. # A7457-1ML, Sigma]
    - Caspase-9: Ac-LEHD-AMC [prod. # 260-080-M001, Alexis Biochemicals]
- Inhibitors
    - Caspase-3: Ac-DEVD-CHO [prod. # 260-030-M001, Alexis Biochemicals]
    - Caspase-8: Ac-IETD-CHO [prod. # A6464-500UL, Sigma]
    - Caspase-9: Ac-LEHD-CHO [prod. # 260-079-M001, Alexis Biochemicals]
- Positive controls
    - Caspase-3 [prod. # SE-169, Biomol International]
    - Caspase-8 [prod. # C68498-5µg, Sigma]
    - Caspase-9 [prod. # SE-173, Biomol International]

Reagent preparation

Muscle Lysis Buffer (20 mM HEPES, 10 mM NaCl, 1.5 mM MgCl, 1 mM DTT, 20% glycerol, 0.1% Triton X-100), pH 7.4

2.383 g HEPES (FW 238.3)
0.2922 g NaCl (FW 58.44)
0.0714 g MgCl (FW 95.22)
0.077125 g DTT (FW 154.25)
100 mL 100% Glycerol
500 µL Triton X-100
Add all ingredients to 300 mL ddH_2O. Adjust pH to 7.4. Top up to a final volume of 500 mL with ddH_2O. Store at 4°C

2X Assay Buffer, pH 7.5 (stock solution) (40 mM HEPES, 20 % glycerol)

0.95324 g HEPES (FW 238.3)
20 mL 100% Glycerol
Add all ingredients to 70 mL ddH_2O. Adjust pH to 7.5. Top up to 100 mL with ddH_2O. Store at 4°C

1X Assay Buffer (working solution, made fresh every day)

Dilute stock solution down to appropriate dilution
**Add DTT fresh to 1X assay Buffer at a 10 mM concentration prior to use. Store on ice

Caspase-3 reagents:

Substrate [Ac-DEVD-AMC] (10 mM stock solution – 50X)

Add 740 µL of 0.2 µm filtered DMSO to 5 mg of Ac-DEVD-AMC. Vortex well and aliquot to 20 µL vials
Store at -20ºC

Substrate [Ac-DEVD-AMC] (200 µM working solution)

Prior to use, remove ONLY the required amount from one tube, add to new tube, and dilute 50X in 1X Assay Buffer. Place an "X" on the tube so you use this tube first the next time you run the assay

For example, remove 2 µL of 10 mM stock and add to 98 µL of 1X Assay Buffer and vortex well. This is a working solution of 200 µM and is sufficient for 10 wells (at 10 µL per well); the final concentration in each well is 20 µM. Always make a little bit more than needed (i.e. If 50 wells worth are needed, then make up enough for 55 wells)

Inhibitor [Ac-DEVD-CHO] (10 mM stock solution – 10X)

Add 199 µL of 0.2 µm filtered DMSO to 1 mg of Ac-DEVD-CHO, vortex well and aliquot entire contents to 5 µL vials
Store at -20ºC

Inhibitor [Ac-DEVD-CHO] (1 mM working solution)

Prior to use, add 45 µL of 1X Assay Buffer to one tube of 5 µL stock solution, making a 1 mM working solution
Add 2 µL of this solution to the appropriate wells; the final concentration is 20 µM/well. Mark tube containing remaining solution with an "X", and freeze at -20ºC for future use

Positive control (200 U/tube stock solution – 8X)
Aliquot directly to 2µL vials. Store at -80ºC
Prior to use, add 14 µL of 1X assay buffer to one 2 µL tube of stock solution. Add 2 µL of working solution to appropriate wells, giving a final concentration of 25 U/well

Caspase-8 reagents:
*****NEW** Substrate [Ac-IETD-AMC] (10 mM stock solution – 50X), rec'd Sept. 2009***
Add 740 µL of 0.2µm filtered DMSO to 5 mg of Ac-IETD-AMC, vortex well and aliquot to 20 µL vials. Store at -20˚C

*****NEW** Substrate [Ac-IETD-AMC] (200 µM working solution)***
Prior to use, remove ONLY the required amount from one tube, add to new tube, and dilute 50X in 1X Assay Buffer. Place an "X" on the tube so you use this tube first the next time you run the assay

For example, remove 2 µL of 10 mM stock and add to 98 µL of 1X Assay Buffer and vortex well. This is a working solution of 200 µM and is sufficient for 10 wells (at 10 µL per well); the final concentration in each well is 20 µM. Always make a little bit more than needed (i.e. If 50 wells worth are needed, then make up enough for 55 wells)

Inhibitor [Ac-IETD-CHO] (25 µM working solution – 40X)
Combine 2 µL of inhibitor stock (1.5 mM) and 78 µL of 1X Assay Buffer

Aliquot to 10 µL vials and store at -20ºC
Use required amount, which will give a final concentration of 0.5 µM/well, then re-label tube with an "X" and put back in freezer to use in next assay

Positive control (100 µg/mL stock solution – 10X)
Original shipped solution (100 µg/mL) is reconstituted in 50 µL of ddH_2O to a concentration of 10 µg/mL. Vortex solution and aliquot into 2.5 µL volumes
Store at -80ºC
Prior to use, add 22.5 µL ddH_2O to one tube. Add 2 µL of working solution to appropriate wells, giving a final concentration of 0.02 µg/well

Re-label tube and freeze working solution for future use at -80ºC

Caspase-9 reagents:
Substrate [Ac-LEHD-AMC] (10 mM stock solution – 50X), rec'd Jan 2009
Add 702.4 µL of 0.2µm filtered DMSO to 5mg of Ac-LEHD-AMC, vortex well and aliquot to 20 µL vials. Store at -20ºC

Substrate [Ac-LEHD-AMC] (200 µM working solution)
Prior to use, remove ONLY the required amount from one tube, add to new tube, and dilute 50X in 1X Assay Buffer. Place an "X" on the tube so you use this tube first the next time you run the assay

For example, remove 2 µL of 10 mM stock and add to 98 µL of 1X Assay Buffer and vortex well. This is a working solution of 200 µM and is sufficient for 10 wells (at 10 µL per well); the final concentration in each well is 20 µM. Always make a little bit more than needed (i.e. If 50 wells worth are needed, then make up enough for 55 wells)

Inhibitor [Ac-LEHD-CHO] (10 mM stock solution – 10X)
Add 185.67 µL of 0.2 µm filtered DMSO to 1 mg of Ac-LEHD-CHO
Aliquot entire contents to 5 µL vials and store at -20ºC

Inhibitor [Ac-LEHD-AMC] (1 mM working solution)
Prior to use, add 45 µL of 1X Assay Buffer to one 5 µL tube of stock solution, making a 1 mM working solution
Plate 2 µL of this solution to the appropriate wells; this gives a concentration of 20 µM/well. Mark tube containing remaining solution with an "X", and freeze at -20ºC for future use

Positive control (15X)
Aliquot directly to 2 µL vials. Store at -80ºC
Prior to use, add 28 µL of 1X assay buffer to one 2 µL tube of stock solution. Add 10 µL of working solution to appropriate wells

B.4 Mitochondrial Calcium Retention Capacity

Buffers:

1. **BIOPS**

Chemical	Stock Solution	Molecular Weight	Final Concentration	Addition to 2 L final volume
CaK_2EGTA	100 mM		2.77 mM	55.4 mL
K_2EGTA	100 mM		7.23 mM	144.6 mL
Na_2ATP		555.1	5.77 mM	6.28 g
$MgCl_2 \bullet 6H_2O$		203.3	6.56 mM	2.67 g
Taurine		125.1	20 mM	5.02 g
Na_2Phosphocreatine		327.14	15 mM	9.81 g
Imidazole		68.1	20 mM	2.72 g
Dithiothreitol (DTT)		154.2	0.5 mM	0.154 g
MES Hydrate		195.2	50 mM	19.52 g

2. **Buffer Y – pH 7.1**

Chemical	Final Concentration	Addition to 500 mL final volume
Sucrose	250 mM	42.78 g
Tris-HCl	10 mM	0.788 g
Tris Base	20 mM	1.21 g
KH_2PO_4	10 mM	0.68 g
BSA	0.5 mg/mL	0.25 g

- *store in fridge at 4°C quickly*
- *filter once total volume is made*
- *may require heat to dissolve everything*

Sucrose: Weak antioxidant
Tris-HCl: Acidic form
Tris Base: Basic form
KH_2PO_4: Potassium salt; buffers protons
BSA: Common in biological buffers; buffers protons and certain amino acids; weak antioxidant

3. **CRC Assay Buffer – with Creatine (NEW Composition)**

Chemical	Molecular Weight	Final Concentration	Addition to 120 mL final volume
Buffer Y (freshly made)			120 mL
Creatine	131.13	20 mM	0.315 g
EGTA		40 uM	9.6 uL of 0.5 M
BLEB		5 uM	60 uL of 10 mM
Calcium Green 5N*	1192.19	1 uM	400 uL of 0.3 mM
Thapsigargin**	650.76	2 uM	160 uL of 1.5 mM

* Dissolve 0.5 mg CG5N in 1.398 mL water

** 1mg vial, make 1mL, aliquot into 165 uL stocks and freeze

- **Aliquot in 900 uL aliquots**

4. **Create a stock of 5 mM & 50 mM $CaCl_2$ dissolved in water and store in 50 uL aliquots in freezer**

Procedure

*Place cuvettes on stir plate and fill with ddH_2O and 10 uL EGTA (0.5 M stock) (10 mins)

1. Harvest muscle and place in ice cold **BIOPS**
2. Separate fibres into bundles (SMALLER than those used for respiration & even more separated)
3. Permeabilize for 30 minutes in BIOPS with 30 ug/mL saponin
4. WASH 1: 10 minutes in 1.5 mL Buffer Y + 1 mM EGTA (3 uL of 0.5 M)
5. Turn on fluorometer to allow lamp to heat up
6. WASH 2: 10 minutes in 1.5 mL Buffer Y + 10 uM BLEB (1.5 uL of 10 mM BLEB) **be conscious of how long bundles are in fridge for- max viability 4 hours
7. Aspirate out water from cuvette but DO NOT RINSE (keep cuvette lined with EGTA) & add necessary ingredients according to table below and fibre
8. Select Calcium Uptake Assay Protocol on PTI Software. Make sure the following parameters are set:
    a. Excitation: 506
    b. Emission: 532
    c. Duration – 3000 seconds
    d. Slit Widths: Excitation 3 nM
       Emission 3 nM
    e. x-axis window: 2000 seconds
    f. y axis max and min: 200 000 and 500 000 – this can change depending on strength of the bulb (newer bulbs may be closer 500 000 as the min)

Substrate	**Stock Concentration**	**Addition to cuvette**	**Final Concentration in Cuvette**
CRC Assay Buffer		300 uL	
Glutamate	2 M	1.5 uL	10 mM
Malate	1 M	1.5 uL	5 mM
ADP	500 mM	3 uL	5 mM
Fibre ** make sure fibre is at the bottom of cuvette attached to stir bar**			
Collect 400 second background to establish "F-Min"			
$CaCl_2$	5 mM	2.5 uL	8 nmol
Wait 5 minutes or until steady state			
$CaCl_2$	5 mM	1.25 uL	12 nmol (4 nmol pulse)
Wait 5 minutes in between pulses and continue pulsing until pore opens			
$CaCl_2$	50 mM	3 uL	0.5 mM Pulse (F-Max)
Wait 3 minutes before final addition, this should establish F-Max but last addition is to make sure			
$CaCl_2$	50 mM	3 uL	0.5 mM Pulse (F-Max)

- For each addition remove cuvette from holder and ensure fibre has not been disrupted
- Make sure y axis is no more than 300 000 units or you will miss opening

9. Remove bundle and save for freeze drying (if applicable)

B.5 Mitochondrial H_2O_2 Emission (mH_2O_2)

BUFFER Z (Intracellular)

Chemical	Molecular Weight (g/mol)	Final Concentration	Addition to 500 mL Final Volume
K-MES	233.33	105 mM	12.26 g
KCl	74.55	30 mM	1.12 g
KH_2PO_4	136.08	10 mM	0.7 g
$MgCl_2 \cdot 6H_2O$	203.3	5 mM	0.51 g
EGTA	380.35	1 mM	0.19 g
BSA		5 mg/mL	2.5 g

*__ALWAYS__ double check molecular weights for supplier-specific chemicals (n=m/M.W.)

To make Buffer Z:

1. Add approximately 400 mL of ddH_2O to 1000 mL beaker
2. Weigh and add all powder chemicals
3. Adjust pH to 7.4 using KOH pellets
4. Using graduated cylinder, bring total volume to 500 mL
5. Filter and then aliquot into 50 mL falcon tubes
6. Freeze falcon tubes

Amplex Ultra Red (AUR) Preparation

Total volume per experiment: 1000 uL
Total volume per tube: 1050 uL

Stock A = No Creatine
Stock B = 20 mM Cr (saturating mtCK)
Stock C = 13.9 PCr + 9.1 Cr (modelling *in vivo* resting concentrations)

Ingredients required for all 3 Stocks:

Amplex Ultra-Red (Invitrogen A36006)
5000 IU/ml Cu/Zn Superoxide dismutase (SOD1; Sigma S9697)
10 mM Blebbistatin (BLEB; Cayman)
DMSO
Buffer Z (0.5 mg/mL BSA)
0.5 M EGTA (aliquots in freezer)

Final concentrations for **all stocks**:

10 uM AUR
5 uM BLEB
25 U/mL Cu/Zn SOD1
1 mM EGTA

Stock B additional ingredients:

20 mM Creatine hydrate

Stock C additional requirements:

13.9 mM Phosphocreatine and 9.1 mM Creatine

Preparation of Stock Ingredients
Step 1: Make Fresh Buffer Z (500 mL) – will only need approximately 320 mL, freeze the rest
Step 2: Prepare 5 mM AUR. Add 666.6 uL of DMSO to 1 mg AUR. Vortex gently. Place tube in drawer out of light (do not place on ice DMSO will freeze)
Step 3: Thaw 10 mM BLEB stocks – you will need a total of 165 uL so you likely need 8 tubes
Step 4: Thaw 5000 IU/mL SOD – you will need 2 Eppendorf's of stock (will need to add KOH pellet when making solution)
Step 5: Thaw 0.5 M EGTA – you will likely need 4 Eppendorf's of stock

Preparation of AUR Stock A (No Creatine): Multiply these values by 3
Prepare 10 uM AUR stock. Mix the following (have this stirring in a beaker covered in foil):

- 107 mL of Buffer Z – 321 mL
- 216.7 uL of 5 mM AUR – 650.1 uL
- 541.7 uL of 5000 IU/mL SOD1 – 1625.1 uL
- 53.5 uL of 10 mM BLEB – 160.5 uL
- 216.7 uL of 0.5 M EGTA – 650.1 uL

Aliquot 1050 uL into tubes and store in freezer labeled Ziplock bag (No Creatine Amplex Red – Date and Name)
Total volume (with x3 amount) = 321 mL + 3.0858 mL = 324.1 mL
324.1/3 = 108.03 mL per stock

Preparation of AUR Stock B (20 mM Creatine):

Prepare 10 uM AUR stock. Mix the following (have this stirring in a beaker covered in foil):

- 107 mL of Buffer Z
- 281 mg of creatine
- 216.7 uL of 5 mM AUR
- 541.7 uL of 5000 IU/mL SOD1
- 53.5 uL of 10 mM BLEB
- 216.7 uL of 0.5 M EGTA

Aliquot 1050 uL into tubes and store in freezer labeled Ziplock bag (20 mM Creatine Amplex Red – Date and Name)
Preparation of AUR Stock C (13.9 PCr and 9.1 Cr):
Prepare 10 uM AUR stock. Mix the following (have this stirring in a beaker covered in foil):

- 107 mL of Buffer Z
- 127.8 mg of creatine
- 354.8 mg of phosphocreatine
- 216.7 uL of 5 mM AUR
- 541.7 uL of 5000 IU/mL SOD1
- 53.5 uL of 10 mM BLEB
- 216.7 uL of 0.5 M EGTA

Aliquot 1050 uL into tubes and store in freezer labeled Ziplock bag (13.9 PCr and 9.1 Cr Amplex Red – Date and Name)

H_2O_2 Standard curve for Amplex Ultra Red

1. H_2O_2 dilution (serial dilution)
    - H_2O_2 is light sensitive. Keep in dark when possible.
    - Use H_2O_2 purchased within the last 6 months (stored in fridge, wrapped in foil).
    - One standard curve per batch is acceptable, but re-make curve if batch approaches 6 months of age. Discard if curve no longer consistent with original curve.
    - Good in -20°C freezer for up to 6 months or so.
    - Use stock 3% w/w H_2O_2: 3 g H_2O_2 / 100 mL solution (1 mol H_2O_2 / 34.01 g) = 0.0882 mol H_2O_2 / .100 L = .882 mol H_2O_2 / 1 L = 0.882 M H_2O_2
        (1) 4310 ul ddH_2O + 100ul 3% w/w H_2O_2 >>>> 20 mM H_2O_2. Use in dilution step 2.
        (2) 3980 ul ddH_2O + 20ul of 20mM H_2O_2 >>>>>> 100 uM H_2O_2. Use in dilution step 3 for 20uM.
        (3) 3200 ul ddH_2O + 800ul 100uM H_2O_2 >>>>> 20 uM H_2O_2. Use in table below.
        (4) 2000 ul ddH_2O + 2000ul 20uM H_2O_2 >>>>>> 10 uM H_2O_2. Use in table below.
        (5) 2000 ul ddH_2O + 2000ul 10uM H_2O_2 >>>>>> 5 uM H_2O_2. Use in table below.

    NOTE:

    - H_2O_2 is light sensitive. (KEEP H_2O_2 (in tin foil) ON ICE)
    - Prepare large volumes to minimize pipetting/dilution errors.
    - Do not vortex – H_2O_2 is unstable and dismutates spontaneously to H_2O_2 over time. Agitation may worsen. Flip tube in hand several times.
    - Make this right before you are about to start standard curve

2. Add your Amplex UltraRed (photosensitive and keep in oven under lid), HRP (photosensitive), (oligomycin) and other substrates (G/M/S/G-3-P……) into the cuvette as per your protocol.

Step 1: Clean out cuvette with 3 EtOH and 3 water washes

Step 2: Once all substrates are thawed and H_2O_2 has been prepared, begin background (add AUR, HRP, ADP (7.3 uL of 500 D), Substrate into cuvette, which goes in slot 1, and then hit start for a 3 min background)

Only hit Start and Pause, no stop until experiment is over

After 3 min background, begin first H_2O_2 titration (3.33 uL of 5 uM H_2O_2)

3. H_2O_2 titration. NOTE: [final H_2O_2] depends on the final volume in the cuvette, which will vary depending on your protocol

Make sure to clean the pipette tip by pipetting up and down in a beaker of ddH_2O after each addition, and wipe pipette tip with Kim wipe. This avoids excess additions of H_2O_2 as you progress.

If for 1000 ul Titrate very fast, 45-60 sec		**If for 600 ul** Titrate very fast, 45-60 sec	
[H_2O_2] (µM)	Add (µl)	[H_2O_2] (µM)	Add (µl)
5	3.33	5	2.0
5	3.33	5	2.0
10	3.33	10	2.0
10	5	10	3
20	5	20	3
20	5	20	3
20	10	20	6

4. Repeat 3 times. Average all 3 standard curves to make one equation for analyses in Excel if values are consistent. See next page for acceptable ranges of values and general considerations…

   NOTE: Prepare a standard curve for project- make sure you save some Amplex red buffer for any redos for standard curve you need to do.

General Considerations:

- In general, collect background of 3 mins and collect 45s-60s for each H_2O_2 titration.
- During analyses, it can be common to drop points if the standard curve begins to form a curvilinear response. Check curve closely following analyses. Aim for at least 4 data points in the final curve.
- Finally, the accuracy of dilutions has an enormous effect on the lowest H_2O_2 points of the standard curve. It is not uncommon for new trainees to see scattered points at the low end. The stocks must be re-made with new curves prepared if this is the case.

RANGES:

A. SLOPE: LOW 1 million- LOW 2 million (**newer bulbs will give you closer to low 2 million)

- Bulb should be changed if slopes are seeing less than 1 million- always check bulb usage hours if you are getting lower slope maximum bulb usage time is 400 hours. Always check bulb usage hours before you start a study
- If you get a very high slope (i.e. 2.5 million) it might be a new bulb but re-run the standard curve to be sure it was not an H_2O_2 dilution error

B. Y-INTERCEPT: do not go above 5000 if slope is around 1 million, 8000 if slope is closer to 2 million

- You need positive value- needs to be as close to 0 as possible
- If all y-intercepts are positive, then go to the values as closest to 0 (and are below cutoffs listed above) and average these intercepts
- If all y-intercepts are negative, then redo standard curves. But negatives that are close to 0 might be acceptable as well

B.6 Mitochondrial High Resolution Respirometry

Pre-surgery

1. For every fibre bundle you are going to make you will need one 0.5 mL tube for wet weights one 1.5 mL Eppendorf tube for permeabilization and one 1.5 mL tube for wash

* Keep all tubes and buffers on ice

2. In a 5 mL tube, make 10 mg/mL Saponin solution by dissolving a small amount of saponin in distilled water
    a. Vortex gently and place on rocker until ready for use
3. Fill all permeabilization tubes with 1.5 mL of freshly thawed BIOPS and *40 ug/mL saponin (6 uL in 1.5 mL BIOPS).
    a. * Different saponin concentrations may be used depending on species/tissue type but 40 ug/mL is standard for rodent
4. Fill all wash tubes with 1.5 mL freshly thawed Buffer Z
5. Fill all 0.5 mL tubes with 500 uL of BIOPS
6. Using a 50 mL falcon tube, weigh out creatine (this number will change based on the number of chambers you need with creatine), add the correct amount of Buffer Z to make a 20 mM Creatine-Buffer Z Solution
    a. Place on rocker as creatine takes some time to dissolve
7. Label and fill a 5 mL tube with 3.5 mL BIOPS for every muscle that will be harvested during surgery

Post-surgery

1. Separate fibres in BIOPS as quickly and carefully as possible
    a. Remember to change ice block/ice pack frequently as buffer should never be allowed to warm up
2. Place separated fibres in corresponding 0.5 mL tube with BIOPS and proceed to wet weight procedure

Bundle wet weights

1. Fill a 1.5 mL tube with BIOPS until a dome of liquid covers the top
2. Place tube in holder on scale and tare the scale
3. With fine forceps remove first bundle from Eppendorf and using a Kim wipe, blot the bundle to remove excess liquid
4. Very carefully place bundle in liquid on scale, making sure the forceps to not draw up any liquid
5. Wait for scale to stabilize and record weight
6. When done weighing, place back in 0.5 mL Eppendorf tube until all bundles have been weighed

Permeabilization

1. Once all bundles are weighed, switch bundles to permeabilization tubes (the ones that have saponin) using forceps or a gel loading pipette tip
2. Place on nutator in the fridge for 30 minutes

    a. Make sure all Eppendorf's have the liquid mixing by ensuring that the air bubble is moving
    b. If air bubble appears stuck, invert Eppendorf 1-2 times to allow for movement and place back on nutator
3. After 30 minutes, transfer bundles to corresponding wash tubes using gel loading pipette tip
4. Place bundles in wash back on nutator in the fridge for 15 minutes
    a. Permeabilized bundles can remain in fridge in wash for up to 2 hours but will start to lose viability after that point so use bundles ASAP
5. After 15-minute wash proceed to "Running an Experiment"

Running an Experiment

1. When fibres are done washing and chambers have been air phased, remove stoppers and place on top of O2k
2. Add 5 uM blebbistatin and stop the stir bar pressing F11 for Chamber A and F12 for Chamber B
3. Add fibre and loosely place stopper in chamber (do not push down at all)
4. Turn stir bar back on by clicking F11 and F12
5. Add a very small amount of O_2 with syringe through capillary in stopper
6. Wait until O_2 concentration reaches ~350 and remove stopper, O_2 concentration will continue to rise, when the levels begin to fall push stopper in all the way so there is a tight seal between the chamber and stopper
7. Ensure there is no air bubble in the chamber
8. If no air bubble, press F10 to shut off lights
9. If there is an air bubble, remove stopper, add more buffer and repeat steps 5-8
10. Wait for background to reach a steady state…this usually takes 10+ minutes
11. To record when you add each substrate, by clicking "Control" and Left Clicking your mouse on the spot on the graph that you added a substrate you can make an event

BIOPS BUFFER (Extracellular)

Chemical	Stock Solution	Molecular Weight (g/mol)	Final Concentration	Addition to 2 Litre Final Volume
CaK_2EGTA*	100 mM		2.77 mM	55.4 mL
K_2EGTA*	100 mM		7.23 mM	144.6 mL
Na_2ATP		605.24	5.77 mM	6.98 g
$MgCl_2 \cdot 6H_2O$		203.3	6.56 mM	2.67 g
Taurine		125.1	20 mM	5.02 g
Na_2Phosphocreatine		327.14	15 mM	9.81 g
Imidazole		68.1	20 mM	2.72 g
Dithiothreitol (DTT)		154.2	0.5 mM	0.154 g
MES Hydrate		195.2	50 mM	19.52 g

*__**ALWAYS**__ double check molecular weights for supplier-specific chemicals (n=m/M.W.)

BIOPS contains the following ion concentrations		EXTRACELLULAR RANGE
Ca^{2+} free	0.1 uM	Rat: 7.6 mM Mouse: 1.3 mM
Mg^{2+} free	1 mM	
Na^{+}	41 mM	Human: 133-143 mM
K^{+}	20 mM	Human: 4.5 mM
Cl^{-}	13 mM	Rat: 160 mM Mouse: 95-120 mM
MgATP	5 mM	
Ionic Strength	160 mM	
Osmolality	295 mOsm	

BUFFER Z (Intracellular)

Chemical	Molecular Weight (g/mol)	Final Concentration	Addition to 500 mL Final Volume
K-MES	233.33	105 mM	12.26 g
KCl	74.55	30 mM	1.12 g
KH_2PO_4	136.08	10 mM	0.7 g
$MgCl_2 \bullet 6H_2O$	203.3	5 mM	0.51 g
EGTA	380.35	1 mM	0.19 g
BSA		5 mg/mL	2.5 g

*__ALWAYS__ double check molecular weights for supplier-specific chemicals (n=m/M.W.)

Buffer Z contains the following ion concentrations		INTRACELLULAR RANGE
Ca^{2+}	0.0 uM	Human: 30 nM – 60 nM SR: 5.7-20 mmol/L Free Ca^{2+} in SR 0.2-0.5 mM Rat: 7.76-11.11 ueq/g dry wt
Mg^{2+} (total, not free)	5 mM	

Na^+	0.0 mM	Human: 6-13 mM Rat: 7.10-21.9 mmol/L
K^+	145 mM	Human: 130 – 164 mmol/L Rat: 117 – 149 mmol/L
Cl^-	40 mM	Rat: 4.97-16.57 mmol/L
PO_4^{3-}	10 mM	
EGTA free	1 mM	

B.7 Picrosirius Red (PSR) Staining Protocol

Summary

Picrosirius red stains collagen (red) and cytoplasm (yellow). Haematoxylin stains nuclei (brown).

Notes:

- For Brightfield staining, using distilled water is fine. For immunohistochemistry use deionized water. Deionized water is ultra-purified water that has no ions other than H^+ and OH^-.
- Can also use isopropanol as a substitute for ethanol at all steps.
- Stir PSR solution for ~24 hours continuously prior to use. At least 4 hours if you want to use the same day. This helps prevent any precipitate from creating staining artefacts.
- USE A HUMIFIED BOX for staining duration to prevent PSR from drying out

Solutions and Reagents:

Modified Harris Hematoxylin
Harris Modified Method Hematoxylin Stain with Acetic Acid (Fisher Chemical Cat. No. SH26-500D).

Acidified Water:
Glacial Acetic Acid (Fisher Chemical Cat. No. A38-500) ……. 5 mL
Distilled Water ……. 995 mL
Make fresh.

Working PSR:
Direct Red 80 ……. 0.5 g
Saturated aqueous solution of picric acid (1.3% in H_2O) - 500 mL final volume of picric acid (usually can get away with 0.1 g of direct red to 100 mL of picric acid (comes stock)

ALWAYS STAIN ALL YOUR SAMPLES AT THE SAME TIME IF YOU ARE MAKING COMPARISONS BETWEEN THEM.

Procedure:

Deparaffinize Sections

1. Xylene (#1) for 2 minutes.
2. Xylene (#2) for 2 minutes.
3. Xylene (#3) for 2 minutes.
    - Always move the glass slide rack to a new xylene staining dish at each step. Do **not** backtrack
    - Just submerge the slides, no need to agitate
    - Xylene is a clearing agent that removes the paraffin

Re-hydration in Ethanol

4. 100% Ethanol (#1) for 2 minutes.
5. 100% Ethanol (#2) for 2 minutes.
6. 95% Ethanol for 2 minutes.
7. 70% Ethanol for 2 minutes.
8. Distilled water for 2 minutes.

Staining

1. Stain in Modified Harris Hematoxylin for 10 minutes
2. Wash in running distilled water until no more dye comes off
    - Rinse for 10 minutes under running distilled water or rinse with agitation and change water multiple times (i.e. 1-2 min)

Grab histology lid (takeout containers) that has parchment paper taped to it. Add damp paper towel underneath it to keep the slides hydrated. Use uncalibrated 1000 uL pipette to add PSR to slides gently

3. Stain in picrosirius red (pH >4) for 60 minutes.
4. Dip excess PSR off on paper towel
5. Quickly dip in acidified water.
6. Wash in new acidified water with constant agitation for 2 minutes. (2 mL GAA per 398 mL H_2O)
7. Repeat wash in new acidified water with constant agitation for 2 minutes.
    - Physically remove most of the water from the slides by vigorous shaking.
8. 95% Ethanol for 2 minutes.
    - Use the 95% Ethanol from step 6. Discard when finished.
9. 100% Ethanol (#2) for 2 minutes.
    - Use the 100% Ethanol from step 5.
10. 100% Ethanol (#1) for 2 minutes.
    - Use the 100% Ethanol from step 4.
11. Xylene (#4) for 3 minutes.
12. Xylene (#5) for 3 minutes.
13. Keep samples in Xylene until you are ready to mount to keep them hydrated
14. To mount: use glass pasteur pipette to dip into toluene bottle and put 3-4 drops on slide to cover all the sample surface area
15. Place slide cover over the samples and press down gently using pen/pencil/tool with blunt end to remove all air bubbles
16. Let this sit until toluene has stuck the slide cover to the slide (at least 2-3 hours)
17. Mount with xylene-based mounting medium.

B.8 Hematoxylin and Eosin (H and E) Staining Protocol – Myocardial Disorganization

Solutions and Reagents:

Modified Harris Hematoxylin
Harris Modified Method Hematoxylin Stain with Acetic Acid (Fisher Chemical Cat. No. SH26-500D)
1% Acid Alcohol Solution:
1 M Hydrochloric acid (HCl) ……. 1 mL
70% Ethanol ……. 100 mL
Mix well. Make fresh.
0.2% Ammonia Water Solution:
Ammonium Hydroxide (Fisher Chemical Cat. No. A669-500) …… ~8 drops
Distilled water …….. 200 mL
Mix well. Make fresh.

- 1 drop = ~50 µL

Eosin B Stock Solution (1.0%):
Eosin Y (Fisher Chemical Cat. No. E511-25) ……. 10 g
Phloxine B (Fisher Chemical Cat. No. P387-25) ……. 1 g
100% Ethanol …….. 800 mL
Distilled Water ……. 200 mL
Mix to dissolve and store at room temperature.
Eosin B Working Solution (0.25%):
Eosin B stock solution ……. 200 mL
Distilled Water ……. 200 mL
80% Ethanol …….. 600 mL
Glacial Acetic Acid (Fisher Chemical Cat. No. A38-500) ……. 5 mL
Mix well and store at room temperature.

ALWAYS STAIN ALL YOUR SAMPLES AT THE SAME TIME IF YOU ARE MAKING COMPARISONS BETWEEN THEM.

Procedure:

Deparaffinize Sections

9. Xylene (#1) for 2 minutes.
10. Xylene (#2) for 2 minutes.
11. Xylene (#3) for 2 minutes.
    - Always move the glass slide rack to a new xylene staining dish at each step. Do **not** backtrack.
    - Just submerge the slides, no need to agitate.
    - Xylene is a clearing agent that removes the paraffin.

Re-hydration in Ethanol

12. 100% Ethanol (#1) for 2 minutes.

13. 100% Ethanol (#2) for 2 minutes.
14. 95% Ethanol for 2 minutes.
15. 70% Ethanol for 2 minutes.
16. Distilled water for 2 minutes.

Staining

17. Stain in Modified Harris Hematoxylin for 10 minutes.
18. Wash in running distilled water until no more dye comes off.
    - Rinse for 10 minutes under running distilled water or rinse with agitation and change water multiple times (i.e. 1-2 min).
19. 6-10 dips in Acid Alcohol Solution.
20. Wash in running distilled water until no more dye comes off.
    - Rinse for 10 minutes under running distilled water or rinse with agitation and change water multiple times (i.e. 1-2 min).
21. Dip in 0.2% Ammonia Water Solution until slide tissue sections are blue.
22. Wash in running distilled water until no more dye comes off.
    - Rinse for 10 minutes under running distilled water or rinse with agitation and change water multiple times (i.e. 1-2 min).
23. 6 dips in 70% Ethanol to rinse.
    - Use the 70% Ethanol from step 7. Discard when finished.
24. Counterstain in Eosin B Working Solution for 4 minutes.
25. 95% Ethanol for 2 minutes.
    - Use the 95% Ethanol from step 6. Discard when finished.
26. 100% Ethanol (#2) for 2 minutes.
    - Use the 100% Ethanol from step 5. Discard when finished.
27. 100% Ethanol (#1) for 2 minutes.
    - Use the 100% Ethanol from step 4. Discard when finished.
28. Xylene (#4) for 3 minutes.
29. Xylene (#5) for 3 minutes.
30. Mount with xylene-based mounting medium.

B.9 Immunofluorescence (Paraffin-embedded Tissue Processing)

Reagents

1. **TE buffer**: 10 mM Tris/1 mM EDTA, pH=9
2. **3% H_2O_2** (diluted by PBS)
3. **PBST:** 1 L PBS + 1 mL Tween 20
4. 3% BSA, 10% BSA
5. **HCl-EtOH:** 500 uL HCl +200 mL 70% EtOH

Step	Purpose	Operation	Time	Notes
1	De-paraffinizing	Xylene	15 min	
2		Xylene	15 min	
3		Xylene	15 min	
4	Re-hydrating	100% Ethanol	1 min	
5		100% Ethanol	1 min	
6		95% Ethanol	1 min	
7		80% Ethanol	1 min	
8		70% Ethanol	1 min	
9	Wash	ddH_2O	2 min	
10	Antigen Retrieval (microwave)	TE buffer PH=9	10 min	Heating TE buffer vigorously, then place the rack with slides into the buffer and boiling for 10 mins
11	Slow wash	Tap water drip; replace ddH_2O	1 h	Drop the tap water into the buffer very slowly（1 drop/s）
12	Wash	PBS	3x5 min	On rotator
13	Wash	PBS	3x5 min	
14	Wash	ddH_2O	5 mins	
15	Blocking	10% BSA diluted by PBST	1 h	For IF, use appropriate serum corresponding to primary antibody
16	Primary antibody incubation		4° overnight	Keep the container moist, and protect from light
17	Wash	PBST wash	3x5 min	
18	Secondary antibody incubation		1 h	Room temperature
19	Wash	PBST	3x5 min	
20	Wash	ddH_2O	STOP	
21	Mount	Mounting aqueous medium		If using permanent medium, please proceed the following steps.
22		95% Ethanol	1 min	

23	De-hydrating	95% Ethanol	1 min	
24		100% Ethanol	1 min	
25		100% Ethanol	1 min	
26		Xylene	15 min	
27		Xylene	15 min	
28	Mount	Mounting		DAPI

B.10 Spectral Flow Cytometry (Chamber-specific)

Materials list

- 2x 50 mL flasks labelled ‘A #’ (mouse number) and ‘L #’
- 6 mL DMEM
- 4 mL collagenase (2 mg/mL)
- 170 uL hyaluronidase (1 mg/mL)
- 75 uL elastase (1 mg/mL)
- 90 uL DNase (1 mg/mL)
- 30 mL EDTA buffer
    - How to make stock bottle (1 L)
        - Make in 1L ultrapure 18.2MΩ ddH_2O
        - 7.5972 g NaCl
        - 0.37275 g KCl
        - 0.05999 g NaH_2PO_4
        - 2.383 g HEPES
        - 1.8016 g Glucose
        - 1.011 g BDM
        - 1.2515 g Taurine
        - 1.4612 g EDTA
        - Adjust to pH 7.8 using NaOH. Sterile filter.
- 20 mL Perfusion buffer
    - How to make stock bottle (1 L)
        - Make in 1 L ultrapure 18.2MΩ ddH_2O
        - 7.5972 g NaCl
        - 0.37275 g KCl
        - 0.05999 g NaH_2PO_4
        - 2.383 g HEPES
        - 1.8016 g Glucose
        - 1.011 g BDM
        - 1.2515 g Taurine
        - 0.095 g $MgCl_2$
        - Adjust to pH 7.8 using NaOH. Sterile filter.
- 2x 50 mL centrifuge tubes labelled ‘EDTA #’ and ‘Perf #’
- 4x shale plates labelled ‘EDTA #’, ‘Perf #’, ‘Atria #’, ‘LVFW #’
- 4x 2 mL Eppendorf tubes labelled ‘A U #’, ‘A FS #’, ‘L U #’, ‘L FS #’
- 2x 100-micron mesh funnel
- 2x blunt Pasteur pipettes
- 10 mL DMEM + 20% FBS
- 5.2 mL FACS buffer
    - How to prepare stock bottle (made in fume hood):
        - 98 mL DPBS (no calcium or magnesium)
        - 2 mL FBS stock
        - 1 mM EDTA (0.0372 g)
- 4 uL FC block
- 200 uL antibody master mix

- Antibody master mix kept in dark in box in fridge
    - Stock antibody kept in dark in blue box in fridge
- How to prepare stock:
    - 928.68 uL FACS buffer
    - 50 uL SB (super bright complete buffer)
        - Mix until red (homogenized) (sample master mix)
    - 0.83 uL CD45
    - 1.00 uL CD11b
    - 2.50 uL Ly6C
    - 1.25 uL MHCII
    - 1.25 uL CD64
    - 1.00 uL CD22c
    - 10.00 uL CCR2
    - 0.83 uL Ly6G
    - 1.66 uL F4/80
- 2 uL live dead aqua stain

- 800 uL intracellular fixation buffer

Possibly add that this is done within a sterile laminar flow cabinet

Setup

1. Get 2 50mL flasks and label them ‘A #’ (mouse number) and ‘L #’
2. Get 2 50mL centrifuge tubes and label them ‘EDTA #’ and ‘Perf #’
3. Get 4 shale plates and label them ‘EDTA #’, ‘Perf #’, ‘Atria #’, ‘LVFW #’

1. Fill the ice bucket with ice.
2. Place DMEM, collagenase, hyaluronidase, DNase, and 2 50 mL flasks labelled ‘A #’ and ‘L #’ in the ice bucket (to get to 4°C) and leave a parafilm square on top of each flask.
3. Preset centrifuges to 4°C and 500 rcf, and make sure the water bath is set to 37°C.
4. Grab EDTA and Perfusion buffers from the fridge and shake.
5. Grab 2 50 mL tubes and fill 1 with 30 mL of EDTA and the other tube with 20 mL of Perfusion buffer. Place tubes in the 37°C water bath for ~10 minutes until pre-heated. Put your stock buffers back into the fridge.
6. Place the 2 shale plates labelled ‘Atria’ and ‘LVFW’ into the ice bucket and fill each plate with 3 mL DMEM (Do not leave the stock bottle open).
7. Set up your surgical station by taping down at least 2 sheets of paper towel side-by-side. Place a 15 mL centrifuge tube at the top center of the station with the opening facing towards you. Place a cotton swab with isoflurane in the tube.
8. Make the enzyme mix by filling the 2 50mL flasks with (shake enzymes before use and cap the stock bottle each time):

    a. 2 mL collagenase each flask
    b. 85 uL hyaluronidase in each flask
    c. 75 uL elastase **atria flask** (vortex first)
    d. 45 uL DNAse each flask

According to the new Epelman protocol, the enzyme amount and concentration is edited. Each enzyme mix will be made in a 2 mL Eppendorf tube.

a. 1.3 mL DMEM - Atria and Ventricles
b. 150 µL Collagenase (2 mg/mL) (Worthington) - Atria and Ventricles
c. 25 µL Hyaluronidase (1 mg/mL) (Sigma) - Atria and Ventricles
d. 18 µL DNAse I (1 mg/mL) (Sigma) - Atria and Ventricles
e. 75 uL Elastase (stock concentration) (Sigma) - ATRIA ONLY

9. Prepare the mouse by placing the mouse into the weighing container on the balance.
10. Heparin mouse with 0.2 mL per mouse subcutaneous, wait 5 minutes after injection.
11. Label one 2 mL Eppendorf tube per shale plate.

12. Setup a 7 mL EDTA, 10 mL EDTA, and a 3.5 mL perfusion buffer syringe. Place the extras of each buffer in the corresponding plate, making sure to leave enough for the wash.
13. Place the mouse in the anesthesia container and add one cotton swab dipped in isoflurane into it. Place another cotton swab with iso into the surgical pad tube.
14. Once the mouse is fully anesthetized place him onto the surgical pad with his snout in the tube then tape down his limbs. Press on his foot to make sure there is no toe reflex (pedal pain withdrawal reflex). If the mouse begins to wake up, place him back in his cage and reset the surgical pad.
15. Begin surgery by cleaning the mouse's abdomen with ethanol.
16. Lift mouse abdomen skin with forceps and cut open with scissors.
17. Lift mouse abdomen muscle and make a small incision with scissors.
18. Use the incision to cut towards each armpit then open the chest using the clamp.
19. Lift clamp and cut the diaphragm.
20. Twist the clamp to open the chest cavity.
21. Remove the pericardium with the forceps.
22. Lift the right lung with the forceps and cut the arteries connecting it to the heart then remove the lung.
23. Lift the heart with the forceps and cut the inferior vena cava.
24. Insert the 7 mL EDTA syringe bevel side down into the right ventricle, making sure to keep it parallel to the right ventricle as you perfuse. Make sure not to shove the needle in too far and to inject slowly. Afterwards, soak up the excess blood with a Kim wipe. If the perfusion went correctly, the attached lungs should be white, and the liver should be lighter.
25. Use curved forceps to clamp the aorta.
26. Clean up the heart by getting rid of any connective tissue or lungs attached.
27. Lift the heart with the curved forceps and cut the aorta to detach it from the body.
28. Place the heart in the EDTA shale plate and prop it by placing the forceps handle in the container.
29. Inject the left ventricle bevel side up with the syringe of 10 mL EDTA. Make sure to

keep the syringe parallel to the left ventricle and control the flow.

30. Lift the heart out of the EDTA plate and wash the heart with the leftover tube of EDTA buffer, then transfer it into the perfusion buffer shale plate.
31. Inject the left ventricle in the same hole as before with the syringe of 3.5 mL perfusion buffer bevel side down. Make sure to keep the syringe parallel to the left ventricle and control the flow (there should be little to no blood).
32. Once done, release the clamp, put the lid on the plate, and clean any tools you planto use again with ethanol and Kim wipes to prevent contamination with blood.
33. Micro dissect using scissors and forceps until only the heart is left.
34. Cut off each atrium from the rest of the heart and massage out any leftover blood using the forceps. Lift the atria out the plate with forceps and wash them with some of the leftover tube of perfusion buffer. Then place them into the DMEM in the 'Atria' shale plate and place that in the ice bucket.
35. Cut off the top ¼ of the heart. Then cut off and remove the right ventricle. Cut open the left ventricle and remove the thick part (septum) that is leftover. Lift the left ventricle out the plate with forceps and wash it with the rest of the leftover tube of perfusion buffer. Place the left ventricle in the DMEM of the 'LVFW' shale plate and place that in the ice bucket.
36. Weigh the atria by placing both in a weighing boat on the balance and record the result. Place them back in the plate and place the plate back in the ice bucket. Do the same with the left ventricle.
37. Cut up the atria and ventricle into 1-2 mm^2 pieces/ "paste" and funnel them into their respective flasks. Use forceps to place any pieces stuck in the funnel into their flask. Parafilm the flasks/tubes.
38. Digest for 80 minutes at 37°C and 140 rpm by placing the flasks/Eppendorf tubes in the water bath/heated shaker.

    38b. Using the Epelman protocol, Eppendorf tubes with "pasted" chunks of tissue are taped to a shaker at 37°C at 140 rpm for 60 minutes
39. Clean up the workspace with ethanol.
40. After digestion is complete, record how long you let them digest and place the flasks in the ice bucket.
41. Triturate the samples using a blunt pipette for each one. Filter the contents of the flasks into their respective 15 mL tubes through a 100-micron mesh. For the left ventricle, use a homogenizer/glass rods to get excess chunks into the mesh. Washmesh with 5 mL of DMEM + 20% FBS. Shake tubes.
42. Place the 15 mL tubes in the refrigerated centrifuge for 5 minutes at 4°C and 500 rcf. Afterwards, let it incubate on ice in the dark for 15 minutes to let other tissue/cells in suspension gravity settle.
43. Aspirate each tube slowly without touching the side or bottom. Use a 1 mL pipette until 2.2 mL and resuspend fully.
44. Move into prelabeled 2 mL Eppendorf tubes. 200 uL into the respective unstained tube. 2 mL into the respective full stained tube. Place tubes into the centrifuge for 5

minutes at 4°C and 500 rcf.

45. Bring 1000 uL, 200 uL, and 1 uL pipettes and tips to the lab bench by the 2 mL tube centrifuge. Grab the FACS buffer from the fridge and place it in the ice bucket.
46. After centrifuge, pour out liquid keeping the pellet. Resuspend with 100 uL FACS buffer. After resuspension add 1 uL of FC block and shake well. Incubate on ice in the dark for 15 minutes.
47. Gently shake suspension and add 100 uL of the antibody master mix. Incubate for 30 minutes on ice in the dark. Centrifuge for 5 minutes at 4°C and 500 rcf.
48. Resuspend everything in 200 uL of FACS buffer. Add 1 uL of live dead aqua stain (viability stain) to the full stain samples. Incubate for 30 minutes on ice in the dark. Centrifuge for 5 minutes at 4°C and 500 rcf.
49. Aspirate then resuspend everything in 200 uL of FACS buffer. Add 200 uL of intracellular fixation buffer to everything and shake. Incubate for 30 minutes on ice in the dark. Centrifuge for 5 minutes at 4°C and 500 rcf.
50. Aspirate then resuspend the atria samples with 500 uL of FACS buffer and the left ventricle samples with 1 mL of FACS buffer.
51. Store tubes in the dark at 4°C (in the white box in the fridge).

B.11 Western Blotting Protocol

1. Place clean plates washed in methanol in green stands on foam and make sure there is a tight seal
2. Prepare running gel (1 column makes 2 gels) ***DO NOT ADD TEMED UNTIL READY TO LOAD***
3. Using transfer pipette transfer running gel (with TEMED) until top of green door
4. Using new transfer pipette on opposite end of plate add water to top of plate removing any bubbles
5. Let set until left over running gel is hard
6. Make Stacking Gel ***DO NOT ADD TEMED UNTIL READY TO LOAD***
7. Make 1X RUNNING BUFFER (990 mL ddH_20, 110 mL 10X Running Buffer) in graduated cylinder
8. Go get samples in liquid nitrogen and thaw on ice
9. Turn on heat block to 95°C
10. After 30 minutes, turn over gel holder to remove excess water, using square paper towel remove water from corner of gel and wipe plate clean
11. Using Transfer pipette add stacking gel (with TEMED) to top of plate
12. Insert comb starting from one end on angle, careful of splash
13. Let set until left over stacking gel is hard
14. Put standard on bench
15. Vortex thawed samples
16. In fume hood mix Laemmli's buffer and 2-mercaptoethanol (100 uL 2-mer: 900 uL Laemmli)
17. In new labeled tubes mix given quantities of water, Laemmli buffer mix and protein (see excel sheet)
18. Boil for 5 minutes in heat block
19. Remove combs from gels and transfer to tank
20. Fill holders with 1X Running Buffer and then tank
21. Load wells with given volume based on excel sheet with standard in first well always
22. Put lid on at set volts to 160 and time to 40 min, press run
23. Transfer Gels following steps
24. Block for 1 hour at room temp in 15 mL Odyssey Blocking Buffer (50% BB, 50%TBS)
25. Pour out blocking buffer into falcon tube and keep in fridge
26. Cover membrane in Primary in fridge overnight
27. Do 4x5 mins washes in TBST
28. Cover membrane box in foil and wash in secondary at room temp for 1 hour
29. 4x5 min washes in TBST
30. Rinse in TBS then pour out and put fresh TBS to detect

WESTERN BLOTTING – PREPARATION OF BUFFERS

10 X Running Buffer:

	500 mL	1 L	2 L
Tris	15 g	30 g	60 g
Glycine	72 g	144 g	288 g
SDS	5 g	10 g	20 g

1 X Running Buffer: 10 X Running Buffer 100 mL
ddH_2O 900 mL

---

10 X Western Transfer Buffer:

	500 mL	1 L
Glycine	52.5 g	105 g
Tris Base	22.5 g	45 g

1 X Western Transfer Buffer : 10 X Transfer Buffer 80 mL
Methanol 160 mL
ddH_2O 560 mL

---

10 X TBS (Tris Buffered Saline):

	500 mL	1 L
Tris	12.1 g	24.2 g
NaCl	40 g	80 g
Adjust to pH 7.6 with HCl		

1 X TBST:

	1 L	2 L
10 X TBS	100 mL	200 mL
dH_2O	900 mL	1800 mL
Tween 20	1 mL	2 mL

Note: Ensure solution is stirring when adding Tween

	Stacking	Running				
		5%	6%	8%	10%	12%
ddH_2O	6.8 mL	11.4 mL	10.6 mL	9.4 mL	8 mL	6.7 mL
1.5 M Tris-Base, pH 8.8	***	5 mL	5 mL	5 mL	5 mL	5 mL
1 M Tris-HCl, pH 6.8	1.25 mL	***	***	***	***	***
30% Acrylamide	1.70 mL	3.4 mL	4 mL	5.3 mL	6.7 mL	8 mL
10% SDS	100 µl	200 µl	200 µl	200 µl	200 µl	200 µL
10% APS	100 µL	200 µL	200 µL	200 µL	200 µL	200 µL
TEMED	20 µL	20 µL	20 µL	20 µL	20 µL	20 µL

Gel Preparation:

Primary

- Blocking Buffer
- .1% Tween
- .01% SDS

Secondary

- Blocking Buffer
- .1% Tween
- .01% SDS

Isolate Protein from Tissue

50 mL 2xSDS lysis buffer recipe

50 mL	**Final Concentration**
6.8 mL of 1M Tris HCL (pH 6.8)	0.136 M
20 mL of 10% SDS	4%
10 mL of glycerol	20%
13.2 mL of H_2O	
5 protease inhibitor tablets	

Perry Homogenization Buffer: 200 mL solution at pH 7.0

Amount	**Reagent**	**Concentration**	**Molecular Weight**
630.4 mg	Tris/HCL	20 mM	157.60
1.752 g	NaCL	150 mM	58.44
74.48 mg	EDTA	1 mM	372.24
76.07 mg	EGTA	1 mM	380.35
223 mg	$Na_4O_7P_2$	2.5 mM	446.06
36.78 mg	Na_3VO_4	1 mM	183.91
2 mL	Triton X-100	1%	

Backx' Homogenization Buffer

10 uG muscle: 100 uL buffer

Make sure buffer includes:

1. 1 tablet/10 mL phosSTOP
2. 1:200 protease inhibitors (50 uL for 10 mL total buffer)
3. If tissue is less than 2 mg (atria), add 200 uL of 2xSDS lysis buffer and use glass homogenizer
1. For ventricles (cut into ¼ pieces so that it is ~5 mg) and other tissue (over 2 mg, if atria are large), add 400 uL 2xSDS lysis buffer and use glass homogenizer
   - Homogenize using polytron homogenizer for 20 seconds at a time, 3 times (do not need to keep on ice all the time → room temperature is also fine)
2. Boil samples at 100°C for 5 mins
3. Centrifuge samples at 800 g for 10 mins (4°C) and keep supernatant in new tube (store in -80°C freezer)
4. Save 5 uL of sample for protein assay

Protein Assay – BCA

1. Create standards by diluting BSA in homogenization buffer or water
   Standards (BSA):
   0 mg/mL (buffer)
   0.0625 mg/mL
   0.125 mg/mL
   0.25 mg/mL
   0.50 mg/mL
   1.00 mg/mL
2. Dilute 5 uL of each sample in 45 uL of homogenization buffer
3. Using a 96-well plate load in triplicates each standard and each sample
4. Add 190uL of mixed solution (50:1 Solution A:Solution B) into each well of sample
   *Amount needed: (# of standards + # of unknowns) x (3 replicates) x (200 uL)
5. Heat in oven for 30 mins at 37°C

B.12 Peroxiredoxin 3 (Prx3) Western Blot Sample Prep and Bradford Assay (CABG Study)

1. RV and LV must be carefully separated and weighed, then quickly placed in PBS containing the alkylating agent, S-methyl methanethiosulfonate (MMTS) at 75 mM on ice
2. Incubate sample in 75 mM tube for 10 min at room temperature
   Note: Make PBS-75 mM MMTS tubes beforehand (where tissue will incubate for 10 mins at room temperature before being transferred to regular 1.5 ml Eppendorf tube to be flash frozen in liquid N_2). ~400 uL of the PBS-MMTS solution per sample (assuming sample weight is ~15-40 mg)
3. Remove sample from 75 mM MMTS tube and snap freeze in liquid N_2 and store at −80 °C prior
4. Homogenize muscle in 1x RIPA buffer (50 mM Tris-HCl PH 7.4, 150 mM NaCl, 0.25% deoxycholic acid, 1% NP-40, 1 mM EDTA containing MMTS) at 75 mM with protease inhibitor and phosSTOP. For 10 mL homogenization (1x RIPA) buffer, add: 50 uL protease inhibitor and 1 phosSTOP tablet. Mix well to fully dissolve
5. Per sample (~15-30 mg weight), use ~250-400 uL RIPA for homogenization (use Sonicator or polytron homogenizer to homogenize thoroughly)
6. Homogenate will be centrifuged at 12,000 g for 5 min and the supernatant collected (4°C on centrifuge)
7. Protein concentrations determined using the **Bradford assay (Note: BCA will NOT WORK)**

Protein quantification – Bradford

1. Prepare protein standard curve and keep on ice
2. Dilute experimental samples with PBS/ddH_2O/or 75 mM RIPA buffer to fit the standard curve (dilute tissues 1 in 25 in ddH_2O)
3. Pipette 10 µl of each standard and sample solution into separate microtitre plate wells.
4. Protein solutions are assayed in duplicate
5. Add 250 µl of BradfordMX reagent to each well
6. Incubate, at room temperature for 15 min (wrapped in tin foil). Absorbance will increase over time. Samples should incubate at room temperature for no more than 1 h.
7. Run Bradford as you would normal BCA

Calculate total protein in samples using standard curve.

Sample prep:

Sample prep once protein has been calculated using a BRADFORD reagent assay:

- 4x bromophenol blue loading dye:

Reagent	Volume (ml)
1 M Tris-HCL pH 6.8	1.25
Glycerol	3
20 % SDS in dH2O	1
Bromophenol blue	3 – 5 mg (tiny pinch on spatula)
dH2O	3.75

Amount loaded per well previously:
30ug protein/well (15uL at 2ug/uL)

<u>Western Blotting Protocol (Prx3 Oxidation Assay)</u>

Note: Items in red denote deviation from standard Western blotting protocol

Buffers

- Resolving gel buffer - 1.5 M Tris buffer pH 8.8. Makes 1 L.
  181.71 g of Trizma Base dissolved in 800 mL ddH_2O and then pH using HCl, then top up to 1 L (ensure the pH is still correct once at volume). Can be kept at room temperature.
- Stacking gel buffer - 0.5 M Tris buffer pH 6.8. Makes 1 L.
  60.57 g of Trizma Base dissolved in 800 mL ddH_2O and then pH using HCl, then top up to 1 L (ensure the pH is still correct once at volume). Can be kept at room temperature.
- Loading dye buffer – 1 M Tris-HCl buffer pH 6.8. Makes 100 mL.
  12.12 g of Trizma Base dissolved in 80 ml ddH_2O and then pH using HCl, then top up to 100 mL (ensure the pH is still correct once at volume). Can be kept at room temperature.
- 10% SDS. Makes 100 mL.
  10 g of SDS fully dissolved in 80 mL of ddH_2O with gentle stirring and heating (approx. 40-50°C), then top up to 100 mL. Can be kept at room temperature.
- 10% APS. Makes 10 mL.
  1 g of APS fully dissolved in 10 mL of ddH_2O, then divide into 500 µL aliquots and store at -20°C
- 10x Tris Glycine for running buffer. Makes 1 L.
  30 g Trizma Base, 144 g Glycine, dissolved in 800 mL ddH_2O with gentle stirring, and topped up to 1 L if needed.
- 4x bromophenol blue loading dye: **THIS IS <u>NOT</u> THE SAME AS TRADITIONAL HYBRID LAEMMLI BUFFER (NO BETA MERCAPTOETHANOL IN THIS LOADING DYE)**

Reagent	Volume (mL)
1 M Tris-HCL pH 6.8	1.25
Glycerol	3
20 % SDS in ddH_2O	1
Bromophenol blue	3 – 5 mg (tiny pinch on spatula)
ddH_2O	3.75

- Semi-dry transfer buffers:

Reagent	Anode 1	Anode 2	Cathode 1
Trizma base	36.34 g	3.02	
Methanol	200 mL	200 mL	200 mL
ddH2O	800 mL	800 mL	800 mL
6-amino n hexanoic acid			5.24 g
pH	10.4	10.4	7.6

- 10x TBS. Makes 1 L.
  24.2 g Trizma base, and 80 g of NaCl, dissolved in 800 mL, then top up to 1 L.
- 0.1% TBST. Makes 1 L.
  100 mL of 10x TBS, 900 mL ddH_2O, and 1 mL Tween 20, gently mixed.

Cast Bio-Rad gels

8. Set up gel casting frame using 0.75 mm or 1.5 mm plates.
9. Recipe for resolving gel buffer for making 1.5 mm gels. TEMED to be added last and only once ready to cast the gels:

	10%
Reagent	**Vol for 2 x 1.5 mm gels**
ddH_2O	8.14 mL
Acryl/bis buffer (30%)	6.66 mL
1.5 M tris Buffer pH 8.8	5 mL
10 % SDS	0.2 mL
10 % APS	0.1 mL
TEMED	10 µL

	10%
Reagent	**Vol for 2 x 1.5 mm gels**
ddH_2O	9.8 mL
Acryl/bis buffer (40%)	5 mL
1.5 M tris Buffer pH 8.8	5 mL
10 % SDS	0.2 mL
10 % APS	0.1 mL

TEMED	10 µL

10. Pipette resolving buffer into each casting frame until filled to the desired level. Leave enough space for the stacking gel to be double the height of the wells. Add methanol to remove any bubbles, produce a smooth, straight top to the gel, and a seal to enable the gel to polymerise.
11. Any small amount of resolving buffer left in the falcon tube can be used to see when the gel is fully set before adding stacking buffer, approximately 20 mins.
12. Recipe for 3% stacking gel buffer:

Reagent	Vol for 2 x 1.5 mm gels
ddH_2O	4.1 mL
Acryl/bis buffer (30%)	0.9 mL
0.5 M tris Buffer pH 6.8	1.7 mL
10 % SDS	70 µL
10 % APS	50 µL
TEMED	10 µL

Reagent	Vol for 2 x 1.5 mm gels
ddH_2O	4.325 mL
Acryl/bis buffer (40%)	0.675 mL
0.5 M tris Buffer pH 6.8	1.7 mL
10 % SDS	70 µL
10 % APS	50 µL
TEMED	10 µL

13. Pour off the methanol and rinse with water before adding stacking buffer to the brim. Push combs into the frame and leave to set, will take approximately 15 mins.
14. Can store in the fridge for up to 4 days, in a wet paper towel, wrapped in foil/cling film.

Sample preparation

15. Switch on heat block to 95°C
16. Prepare samples and any controls that are running to an appropriate amount of total protein to load, using ddH_20 and loading dye – guideline for most samples is 10-30 µg depending on target looking to detect
    Note - Controls such as recombinant proteins need optimising as usually require very little amounts for detection alongside samples as are pure proteins
17. Heat samples at 95°C for 5 mins
18. Pulse spin samples to bring down any condensation
19. Place gels into green/cream electrophoresis frames - If running 1-2 gels then use the frame with the electrode spikes, and if have 3-4 gels put the others in the frame with the flat electrodes. Ensure short plate is facing inwards. If running just 1 gel, then use the blank dam on the other side, making sure writing faces into the cassette
20. Rest the bottom of the gels on the white semi-circle shelf and snap shut the frame

21. Dilute 10x running buffer with dH_2O to give 1x running buffer (eg. 100ml of 10x running buffer with 900ml dH_2O)
22. Mix & pour into central chamber of electrophoresis unit, and check for leaks. If leaking, open and re-clamp the cassette and plates
23. Fill outside chamber to the mark relevant to number of gels
24. Load molecular weight marker (3-5 uL) and samples into each well
25. Apply lid, connect to power pack and run gel at 160 mV until sample stacks and enters the resolving gel (~ 1 hour)
    Note – Voltage through the stacking and resolving gel is dependent on your sample, running conditions, percentage of gel, and quality of image required

Semi-dry transfer

26. Incubate PVDF membrane in methanol, and filter paper in relevant buffers:

Soak in buffer:	Number of medium filter paper (per gel)
Cathode 1	5
Anode 2	2
Anode 1	4

27. Assemble transfer sandwich on transfer cassette:

Top
Cathode 1 filter paper
Gel
Membrane
Anode 2 filter paper
Anode 1 filter paper
Bottom

28. Tighten the lid of the cassette evenly on both sides and run at 0.3 A for 1 h. If target is heavier than 100 kDa then longer transfer time is likely needed

Antibodies used are Prx1 (Abcam ab41906), Prx2 (Abcam ab109367), Prx3 (Abcam ab73349), Prx4 (Abcam ab184167 and ab59542), Prx3-SO3 (Abcam ab16830). Generally, antibodies are diluted 1:1000 in 1% FSG containing 0.1% Tween-20.

Immunoblotting

29. Fill 2 plastic “biorad” dishes, one with methanol and one with transfer buffer
30. Place 2 transfer packs in dish of transfer buffer and place membrane in dish of methanol
31. After 2-3 minutes place first transfer pack on bottom of transfer case
32. Place membrane in transfer buffer for 10-15 seconds
33. Place membrane on top of transfer pack ensuring no air bubbles
34. Remove short plate from gel and place gel face down on membrane
35. Place second transfer pack on top of membrane
36. Using roller, roll from one side of transfer pack to the other to remove air bubbles
37. Hold firmly down in the middle of the transfer pack and remove excess liquid

38. Put lid on transfer case and run transfer (standard setting is 1.5 mm gel for 10 minutes)
39. Following transfer remove membrane and place in dish with blocking buffer (50% Odyssey Blocking Buffer, 50% TBS) for 1 hour, rocking at room temperature
40. After 1 hour pour blocking buffer back into falcon tube (it can be reused) and add primary antibody
41. Place membrane in primary in fridge overnight, rocking in the morning remove primary and pour back into falcon tube (can be reused)
42. Add TBST to dish and complete 3x5 minute TBST washes rocking at room temperature
43. Add secondary antibody and leave rocking at room temperature for 1 hour
44. Remove secondary and place back in falcon tube (can be reused)
45. Complete 3 more 3x5 minute TBST washes
46. Detect using LiCOR Infrared Imager